KEK Preprint 2016-21
ICRR-Report-701-2016-1

Design Report

(Februry 7, 2016)

K. Abe,[56,58] Ke. Abe,[23] H. Aihara,[58,59] A. Aimi,[18] R. Akutsu,[57] C. Andreopoulos,[27]
I. Anghel,[21] L.H.V. Anthony,[27] M. Antonova,[20] Y. Ashida,[24] M. Barbi,[43] G.J. Barker,[65]
G. Barr,[39] P. Beltrame,[11] V. Berardi,[16] M. Bergevin,[3] S. Berkman,[2] T. Berry,[44] S. Bhadra,[72]
F.d.M. Blaszczyk,[1] A. Blondel,[12] S. Bolognesi,[6] S.B. Boyd,[65] A. Bravar,[12] C. Bronner,[58]
M. Buizza Avanzini,[10] F.S. Cafagna,[16] A. Cole,[49] R. Calland,[58] S. Cao,[24] S.L. Cartwright,[49]
M.G. Catanesi,[16] C. Checchia,[18] Z. Chen-Wishart,[44] J.H. Choi,[8] K. Choi,[14] J. Coleman,[27]
G. Collazuol,[18] G. Cowan,[11] L. Cremonesi,[47] T. Dealtry,[26] G. De Rosa,[17] C. Densham,[42]
D. Dewhurst,[39] E.L. Drakopoulou,[11] F. Di Lodovico,[47] O. Drapier,[10] P. Dunne,[15]
M. Dziewiecki,[64] S. Emery,[6] A. Esmaili,[45] P. Fernández,[30] E. Fernández-Martinez,[30] T. Feusels,[2]
A. Finch,[26] A. Fiorentini,[72] M. Fitton,[42] K. Frankiewicz,[36] M. Friend,[22] Y. Fujii,[22] Y. Fukuda,[32]
D. Fukuda,[37] K. Ganezer,[5] M. Gonin,[10] N. Grant,[65] P. Gumplinger,[61] D.R. Hadley,[65] L. Haegel,[12]
D. Hamabe,[60] B. Hartfiel,[5] M. Hartz,[58,61] Y. Hayato,[56,58] K. Hayrapetyan,[47] J. Hill,[5] S. Hirota,[24]
S. Horiuchi,[68] A.K. Ichikawa,[24] T. Iijima,[33,34] M. Ikeda,[56] J. Imber,[10] K. Inoue,[54,58] J. Insler,[29]
R.A. Intonti,[16] A. Ioannisian,[71] T. Ishida,[22] H. Ishino,[37] M. Ishitsuka,[60] Y. Itow,[34,35]
K. Iwamoto,[46] A. Izmaylov,[20] B. Jamieson,[67] H.I. Jang,[51] J.S. Jang,[13] M. Jiang,[24] P. Jonsson,[15]
K.K. Joo,[7] A. Kaboth,[42,44] C. Kachulis,[1] T. Kajita,[57,58] J. Kameda,[56,58] Y. Karadhzov,[12]
T. Katori,[47] K. Kayrapetyan,[47] E. Kearns,[1,58] M. Khabibullin,[20] A. Khotjantsev,[20] J.Y. Kim,[7]
S.B. Kim,[50] Y. Kishimoto,[56,58] T. Kobayashi,[22] M. Koga,[54,58] A. Konaka,[61] L.L. Kormos,[26]
Y. Koshio,[37,58] K.L. Kowalik,[36] W.R. Kropp,[4] Y. Kudenko,[20] R. Kurjata,[64] T. Kutter,[29]
M. Kuze,[60] L. Labarga,[30] J. Lagoda,[36] P.J.J. Lasorak,[47] M. Laveder,[18] M. Lawe,[26]
J.G. Learned,[14] I.T. Lim,[7] T. Lindner,[61] A. Longhin,[18] P. Loverre,[19] T. Lou,[59] L. Ludovici,[19]
W. Ma,[15] L. Magaletti,[16] K. Mahn,[31] M. Malek,[49] L. Maret,[12] C. Mariani,[68] K. Martens,[58]
Ll. Marti,[56] J.F. Martin,[62] J. Marzec,[64] S. Matsuno,[14] E. Mazzucato,[6] M. McCarthy,[72]
N. McCauley,[27] K.S. McFarland,[46] C. McGrew,[52] A. Mefodiev,[20] M. Mezzetto,[18] J. Migenda,[49]
P. Mijakowski,[36] H. Minakata,[70] A. Minamino,[24] S. Mine,[4] O. Mineev,[20] M. Miura,[56,58]
J. Monroe,[44] D.H. Moon,[7] S. Moriyama,[56,58] T. Mueller,[10] F. Muheim,[11] K. Murase,[40]
F. Muto,[33] M. Nakahata,[56,58] Y. Nakajima,[56] K. Nakamura,[22,58] T. Nakaya,[24,58]
S. Nakayama,[56,58] C. Nantais,[62] M. Needham,[11] T. Nicholls,[42] Y. Nishimura,[57] E. Noah,[12]
F. Nova,[42] J. Nowak,[26] H. Nunokawa,[45] Y. Obayashi,[58] H.M. O'Keeffe,[26] Y. Okajima,[60]
K. Okumura,[57,58] E. O'Sullivan,[9] T. Ovsiannikova,[20] R.A. Owen,[47] Y. Oyama,[22] J. Pérez,[30]
M.Y. Pac,[8] V. Palladino,[17] J.L. Palomino,[52] V. Paolone,[41] W. Parker,[44] S. Parsa,[12] D. Payne,[27]

J.D. Perkin,[49] E. Pinzon Guerra,[72] S. Playfer,[11] M. Posiadala-Zezula,[63] J.-M. Poutissou,[61] A. Pritchard,[27] N.W. Prouse,[47] P. Przewlocki,[36] B. Quilain,[24] M. Quinto,[16] E. Radicioni,[16] P.N. Ratoff,[26] M.A. Rayner,[12] F. Retiere,[61] C. Riccio,[17] B. Richards,[47] E. Rondio,[36] H.J. Rose,[27] C. Rott,[53] S.D. Rountree,[68] A.C. Ruggeri,[17] A. Rychter,[64] R. Sacco,[47] M. Sakuda,[37] M.C. Sanchez,[21] E. Scantamburlo,[12] K. Scholberg,[9,58] M. Scott,[61] Y. Seiya,[38] T. Sekiguchi,[22] H. Sekiya,[56,58] S.H. Seo,[50] D. Sgalaberna,[12] R. Shah,[39] A. Shaikhiev,[20] I. Shimizu,[54] M. Shiozawa,[56,58] Y. Shitov,[15,44] S. Short,[47] R. Simpson,[39,58] G. Sinnis,[28] M.B. Smy,[4,58] S. Snow,[65] J. Sobczyk,[69] H.W. Sobel,[4,58] Y. Sonoda,[56] T. Stewart,[42] J.L. Stone,[1,58] Y. Suda,[59] Y. Suzuki,[58] A.T. Suzuki,[23] R. Svoboda,[3] R. Tacik,[43] A. Takeda,[56] A. Takenaka,[56] A. Taketa,[55] Y. Takeuchi,[23,58] V. Takhistov,[4] H.A. Tanaka,[62] H.K.M. Tanaka,[55] H. Tanaka,[56,58] R. Terri,[47] L.F. Thompson,[49] M. Thorpe,[42] S. Tobayama,[2] T. Tomura,[56,58] C. Touramanis,[27] T. Towstego,[62] T. Tsukamoto,[22] K.M. Tsui,[57] M. Tzanov,[29] Y. Uchida,[15] M.R. Vagins,[4,58] G. Vasseur,[6] C. Vilela,[52] R.B. Vogelaar,[68] J. Walding,[44] C.W. Walter,[9,58] D. Wark,[39,42] M.O. Wascko,[15] A. Weber,[39,42] R. Wendell,[24,58] R.J. Wilkes,[66] M.J. Wilking,[52] J.R. Wilson,[47] T. Xin,[21] K. Yamamoto,[38] C. Yanagisawa,[52] T. Yano,[23] S. Yen,[61] N. Yershov,[20] M. Yokoyama,[58,59] T. Yoshida,[60] M. Yu,[72] J. Zalipska,[36] K. Zaremba,[64] M. Ziembicki,[64] and M. Zito[6]

(Hyper-Kamiokande proto-collaboration)

[1] *Boston University, Department of Physics, Boston, Massachusetts, U.S.A.*

[2] *University of British Columbia, Department of Physics and Astronomy, Vancouver, British Columbia, Canada*

[3] *University of California, Davis, Department of Physics, Davis, California, U.S.A.*

[4] *University of California, Irvine, Department of Physics and Astronomy, Irvine, California, U.S.A.*

[5] *California State University, Department of Physics, Carson, California, U.S.A.*

[6] *IRFU, CEA Saclay, Gif-sur-Yvette, France*

[7] *Chonnam National University, Department of Physics, Gwangju, Korea*

[8] *Dongshin University, Department of Physics, Naju, Korea*

[9] *Duke University, Department of Physics, Durham, North Carolina, U.S.A.*

[10] *Ecole Polytechnique, IN2P3-CNRS, Laboratoire Leprince-Ringuet, Palaiseau, France*

[11] *University of Edinburgh, School of Physics and Astronomy, Edinburgh, United Kingdom*

[12] *University of Geneva, Section de Physique, DPNC, Geneva, Switzerland*

[13] *GIST College, Gwangju Institute of Science and Technology, Gwangju 500-712, Korea*

[14] *University of Hawaii, Department of Physics and Astronomy, Honolulu, Hawaii, U.S.A.*

[15] *Imperial College London, Department of Physics, London, United Kingdom*

[16] *INFN Sezione di Bari and Università e Politecnico di Bari, Dipartimento Interuniversitario di Fisica, Bari, Italy*

[17] *INFN Sezione di Napoli and Università di Napoli, Dipartimento di Fisica, Napoli, Italy*

[18] *INFN Sezione di Padova and Università di Padova, Dipartimento di Fisica, Padova, Italy*

[19] *INFN Sezione di Roma, Roma, Italy*

[20] *Institute for Nuclear Research of the Russian Academy of Sciences, Moscow, Russia*

[21] *Iowa State University, Department of Physics and Astronomy, Ames, Iowa, U.S.A.*

[22] *High Energy Accelerator Research Organization (KEK), Tsukuba, Ibaraki, Japan*

[23] *Kobe University, Department of Physics, Kobe, Japan*

[24] *Kyoto University, Department of Physics, Kyoto, Japan*

[25] *Laboratori Nazionali di Frascati, Frascati, Italy*

[26] *Lancaster University, Physics Department, Lancaster, United Kingdom*

[27] *University of Liverpool, Department of Physics, Liverpool, United Kingdom*

[28] *Los Alamos National Laboratory, New Mexico, U.S.A.*

[29] *Louisiana State University, Department of Physics and Astronomy, Baton Rouge, Louisiana, U.S.A.*

[30] *University Autonoma Madrid, Department of Theoretical Physics, Madrid, Spain*

[31] *Michigan State University, Department of Physics and Astronomy, East Lansing, Michigan, U.S.A.*

[32] *Miyagi University of Education, Department of Physics, Sendai, Japan*

[33] *Nagoya University, Graduate School of Science, Nagoya, Japan*

[34] *Nagoya University, Kobayashi-Maskawa Institute for the Origin of Particles and the Universe, Nagoya, Japan*

[35] *Nagoya University, Institute for Space-Earth Environmental Research, Nagoya, Japan*

[36] *National Centre for Nuclear Research, Warsaw, Poland*

[37] *Okayama University, Department of Physics, Okayama, Japan*

[38] *Osaka City University, Department of Physics, Osaka, Japan*

[39] *Oxford University, Department of Physics, Oxford, United Kingdom*

[40] *Pennsylvania State University, Department of Physics, University Park, PA 16802, U.S.A.*

[41] *University of Pittsburgh, Department of Physics and Astronomy, Pittsburgh, Pennsylvania, U.S.A.*

[42] *STFC, Rutherford Appleton Laboratory, Harwell Oxford, and Daresbury Laboratory, Warrington, United Kingdom*

[43] *University of Regina, Department of Physics, Regina, Saskatchewan, Canada*

[44] *Royal Holloway University of London, Department of Physics, Egham, Surrey, United Kingdom*

[45] *Pontifícia Universidade Católica do Rio de Janeiro, Departamento de Física, Rio de Janeiro, Brazil*

[46] *University of Rochester, Department of Physics and Astronomy, Rochester, New York, U.S.A.*

[47] *Queen Mary University of London, School of Physics and Astronomy, London, United Kingdom*

[48] *Universidade de São Paulo, Instituto de Física, São Paulo, Brazil*

[49] *University of Sheffield, Department of Physics and Astronomy, Sheffield, United Kingdom*

[50] *Seoul National University, Department of Physics, Seoul, Korea*

[51] *Seoyeong University, Department of Fire Safety, Gwangju, Korea*

[52] *State University of New York at Stony Brook, Department of Physics and Astronomy, Stony Brook, New York, U.S.A.*

[53] *Sungkyunkwan University, Department of Physics, Suwon, Korea*

[54] *Research Center for Neutrino Science, Tohoku University, Sendai, Japan*

[55] *University of Tokyo, Earthquake Research Institute, Tokyo, Japan*

[56] *University of Tokyo, Institute for Cosmic Ray Research, Kamioka Observatory, Kamioka, Japan*

[57] *University of Tokyo, Institute for Cosmic Ray Research, Research Center for Cosmic Neutrinos, Kashiwa, Japan*

[58] *University of Tokyo, Kavli Institute for the Physics and Mathematics of the Universe (WPI), Todai Institutes for Advanced Study, Kashiwa, Chiba, Japan*

[59] *University of Tokyo, Department of Physics, Tokyo, Japan*

[60] *Tokyo Institute of Technology, Department of Physics, Tokyo, Japan*

[61] *TRIUMF, Vancouver, British Columbia, Canada*

[62] *University of Toronto, Department of Physics, Toronto, Ontario, Canada*

[63] *University of Warsaw, Faculty of Physics, Warsaw, Poland*

[64] *Warsaw University of Technology, Institute of Radioelectronics and Multimedia Technology, Warsaw, Poland*

[65] *University of Warwick, Department of Physics, Coventry, United Kingdom*

[66] *University of Washington, Department of Physics, Seattle, Washington, U.S.A.*

[67] *University of Winnipeg, Department of Physics, Winnipeg, Manitoba, Canada*

[68] *Virginia Tech, Center for Neutrino Physics, Blacksburg, Virginia, U.S.A.*

[69] *Wroclaw University, Faculty of Physics and Astronomy, Wroclaw, Poland*

[70] *Yachay Tech, Department of Physics, San Miguel de Urcuquí, Ecuador*

[71] *Yerevan Institute for Theoretical Physics and Modeling, Halabian Str. 34; Yerevan 0036, Armenia*

[72] *York University, Department of Physics and Astronomy, Toronto, Ontario, Canada*

Abstract

Hyper-Kamiokande is a next generation underground water Cherenkov detector, based on the highly successful Super-Kamiokande experiment. It will serve as a far detector, 295 km away, of a long baseline neutrino experiment for the upgraded J-PARC beam. It will also be a detector capable of observing - far beyond the sensitivity of the Super-Kamiokande detector - proton decay, atmospheric neutrinos, and neutrinos from astronomical sources.

The detector is much larger than Super-Kamiokande and presents new experimental challenges that are addressed in this report, where a full overview of the cavern and detector design R&D is given. This is also supported by a description of the upgraded beam and near detector suite. Based on the design of the experiment the expected sensitivity for both beam and atmospheric neutrinos, proton decays, solar and astrophysical neutrinos, non standard physics, etc. is shown.

CONTENTS

LIST OF THE ACRONYMS

We introduce here the acronyms used throughout the document:

- AD: Avalanche Diode
- B&L: Box-and-Line dynode
- BSM: Beyond the Standard Model
- CC: charged currents
- CCSNe: Core-Collapse Supernovae
- CCQE: charge current quasi-elastic
- CE: Collection Efficiency
- CPL: Concrete Protective Liner
- DAQ: Data Acquisition
- DR: Design Report
- DT: deuterium-tritium
- EBU: Event Building Unit
- ECal: ND280 Electromagnetic Calorimeter
- FC: Fully Contained
- FCFV: Fully Contained in Fiducial Volume
- FGD: Fine Grained Detector
- FRP: Fiber Reinforced Plastics
- FV: Fiducial Volume
- GUT: Grand Unified Theory
- HDPE: High Density PolyEthylene
- HK: Hyper-Kamiokande
- HPD: Hybrid Photodetector
- HQE: High Quantum Efficiency
- Hyper-K: Hyper-Kamiokande
- IBC: International Board Representatives
- IBD: Inverse Beta Decay
- ID: Inner Detector
- INGRID: Interactive Neutrino GRID
- iSC: international Steering Committee
- LAPPD: Large Area Picosecond PhotoDetector

- LBNE: Long Baseline Neutrino Experiment
- LAr: Liquid Argon calorimeter
- LD: Laser Diode
- LLDPE:Linear Low-Density PolyEthylene
- LV: Lorentz Violation
- MC: Monte Carlo
- MLF: Material Science Facility
- mPMT: Multi-channel Optical Module
- MR: Main Ring synchrotron
- NC: neutral currents
- ND280: Near Detector 280m
- NF: Nano Filter
- OD: Outer Detector
- PC: Partially Contained
- PE: Photo Electron
- PS: Power Supply
- PTF: Photosensor Testing Facility
- MH: neutrino mass hierarchy
- QA: quality assurance
- RBU: Readout Buffer Unit
- RO: Reverse Osmosis
- RCS: Rapid Cycling Synchrotron
- SK: Super-Kamiokande
- SM: Standard Model
- Super-K: Super-Kamiokande
- SUS: Stainless Steel (or Steel Use Stainless)
- TITUS: Tokai Intermediate Tank for Unoscillated Spectrum
- TPU: Trigger Processing Unit
- TS: Target Station
- UF: Ultra Filter
- UPW: Ultra Purified Water
- WAGASHI: Water Grid And SCIntillator detector

EXECUTIVE SUMMARY

On the strength of a double Nobel prize winning experiment (Super)Kamiokande and an extremely successful long baseline neutrino programme, the third generation Water Cherenkov detector, Hyper-Kamiokande, is being developed by an international collaboration as a leading worldwide experiment based in Japan.

It will address the biggest unsolved questions in physics through a multi-decade physics programme that will start in the middle of the next decade.

The Hyper-Kamiokande detector will be hosted in the Tochibora mine, about 295 km away from the J-PARC proton accelerator research complex in Tokai, Japan.

The currently existing accelerator will be steadily upgraded to reach a MW beam by the start of the experiment. A suite of near detectors will be vital to constrain the beam for neutrino oscillation measurements. They will be a combination of upgraded and new detectors at a distance ranging from 280 m to 1-2 km from the neutrino target.

A new cavern will be excavated at the Tochibora mine to host the detector. The corresponding infrastructure will be built. The experiment will be the largest underground water Cherenkov detector in the world and will be instrumented with new technology photosensors, faster and with higher quantum efficiency than the ones in Super-Kamiokande. Pressure tests demonstrate that they will be able to support the pressure due to the massive tank.

The science that will be developed will be able to shape the future theoretical framework and generations of experiments. Hyper-Kamiokande will be able to measure with the highest precision the leptonic CP violation that could explain the baryon asymmetry in the Universe. The experiment also has a demonstrated excellent capability to search for proton decay, providing a significant improvement in discovery sensitivity over current searches for the proton lifetime. The atmospheric neutrinos will allow to determine the neutrino mass ordering and, together with the beam, able to precisely test the three-flavour neutrino oscillation paradigm and search for new phenomena. A strong astrophysical programme will be carried out at the experiment that will also allow to measure precisely solar neutrino oscillation. A set of other main physics searches is planned, like indirect dark matter.

In summary, a new experiment, based on the experience and facilities of the already existing Super-Kamiokande and long baseline neutrino experiment as T2K, is being developed by the international physics community to provide a wide and groundbreaking multi-decade physics programme from the middle of the next decade.

Part I

Introduction

I.1. INTRODUCTION

Recent advances in experimental particle physics have yielded fascinating insights into the inner workings of the smallest-scale phenomena. In 2012, the last missing piece of the standard model (SM) of elementary particles, the Higgs boson, was finally observed by the ATLAS and CMS experiments at the Large Hadron Collider (LHC) in CERN [1, 2]. The SM is highly successful in explaining experimental data, however our current ability to describe nature from a fundamental physics point of view is far from satisfactory, most significantly the fact that neutrino mass cannot be incorporated, and so we need beyond the standard model (BSM) physics.

The Nobel Prize in 2002 was awarded for the detection of cosmic neutrinos (in particular the ones coming from supernova) in Kamiokande and for the pioneering solar neutrino experiment at the Homestake mine. More recently, the 2015 Nobel Prize was awarded for the discovery of neutrino oscillations using data taken by the Super-Kamiokande and the Sudbury Neutrino Observatory collaborations, which has the very profound implication that neutrinos have non-zero but very tiny masses.

Building on the expertise gained from the past and current experiments, Kamiokande and Super-Kamiokande, Hyper-Kamiokande (Hyper-K) is a natural progression for the highly successful Japanese-hosted neutrino program.

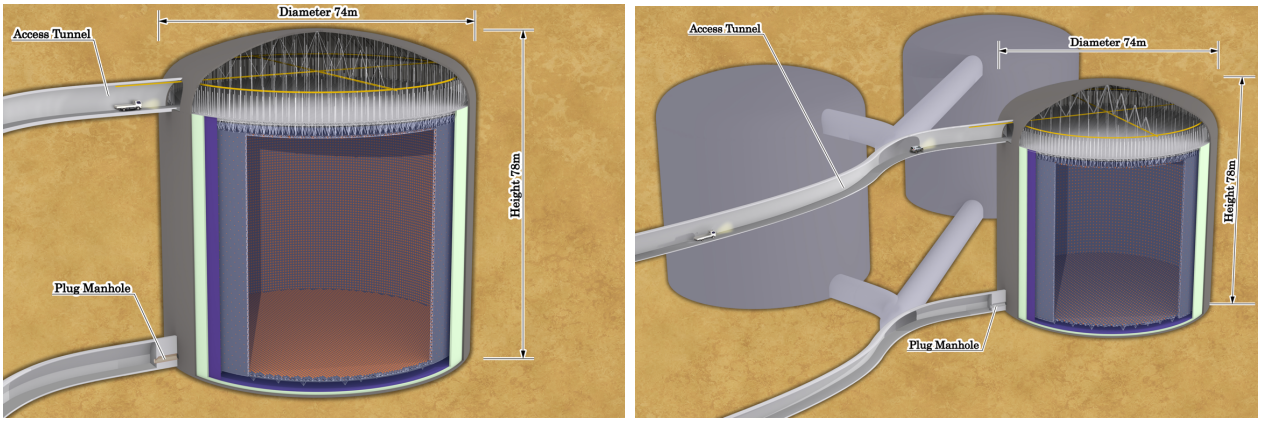

FIG. 1. Illustration of the Hyper-Kamiokande detector with one (left) and three (right) cylindrical tanks.

Hyper-Kamiokande is a next-generation, large-scale water Cherenkov neutrino detector. Three

detector configurations are considered in this report: (1) A single cylindrical detector that is 60 m in height and 74 m in diameter with 40% photocoverage (labeled as 1TankHD throughout the report to denote a single tank with a high photocathode density), see Fig. 18 (left), (2) a configuration of three cylindrical detectors that are 60 m in height and 74 m in diameter with 13% photocoverage (labeled as 3TankLD throughout the report to denote three tanks with a low photocathode density), see Fig. 18 (right) and (3) a configuration of two cylindrical detectors that are 60 m in height and 74 m in diameter with 40% photocoverage, where a staging between the first and second tank is considered (labeled as 2TankHK and 2TankHK-staged throughout the report to denote two tanks with a high photocathode density).

The 1TankHD configuration has the advantage of a higher photon collection efficiency, while the 3TankLD configuration benefits from a higher target mass. Ultimately, the 2TankHK-staged was chosen as the optimal solution by a dedicated task force (TOTF), and it is the one highlighted in the rest of the text. The 3TankLD design serves as a reference design to which the 2TankHK-staged design can be compared.

Candidate sites for the Hyper-K experiment were selected such that neutrinos generated in the J-PARC accelerator facility in Tokai, Japan can be measured in the detector. J-PARC will operate a 750 kW beam in the near future, and has a long-term projection to operate with 1300 kW of beam power. Near detectors placed close to the J-PARC beam line will determine the information about the neutrinos coming from the beam, thus allowing for the extraction of oscillation parameters from the Hyper-K detector. The ND280 detector suite, which has been used successfully by the T2K experiment, could be upgraded to further improve the measurement of neutrino cross section and flux. The WAGASCI detector is a new concept under development that would have a larger angular acceptance and a larger mass ratio of water (and thus making the properties more similar to the Hyper-K detector) than the ND280 design. Intermediate detectors, placed 1-2 km from the J-PARC beam line, would measure the beam properties directly on a water target. Details of the beam, as well as the near and intermediate detectors, can be found in Section II.1.

Hyper-K is a truly international proto-collaboration with over 60 participating institutions from Brazil, Canada, the United States, France, the United Kingdom, Italy, Korea, Poland, Russia, Spain, and Switzerland, in addition to Japan.

Hyper-K will be a multipurpose neutrino detector with a rich physics program that aims to address some of the most significant questions facing particle physicists today. Oscillation studies from accelerator, atmospheric and solar neutrinos will refine the neutrino mixing angles and mass squared difference parameters and will aim to make the first observation of asymmetries in neutrino

and antineutrino oscillations arising from a CP-violating phase, shedding light on one of the most promising explanations for the matter-antimatter asymmetry in the Universe. The search for nucleon decays will probe one of the key tenets of Grand Unified Theories. In the case of a nearby supernova, Hyper-K will observe an unprecedented number of neutrino events, providing much needed experimental results to researchers seeking to understand the mechanism of the explosion. Finally, the detection of astrophysical neutrinos from sources such as dark matter annihilation, gamma ray burst jets, and pulsar winds could further our understanding of some of the most spectacular, and least understood, phenomena in the Universe. These topics will be discussed further in Section III.

This design report is organized as follows. There are three Parts and the Appendices. The remainder of this Part I.1 outlines the theoretical framework for the physics topics contained in this report and discusses the relationships between Hyper-K and other large-scale neutrino experiments. Part II describes the experimental configuration where Section II.1 describes the J-PARC neutrino beam line and near detector facility; Section II.2 discusses the technical details of the experimental design and Section II.3 details the software packages that will be utilized by the Hyper-K experiment. A discussion of pertinent radioactive backgrounds is contained in Section II.4. Finally, Part III explains the physics capabilities for Hyper-K. The Appendices describe the total costs of the experiment and presents its organization.

A. Neutrino oscillations

Neutrino oscillations, discovered by the Super-Kamiokande (Super-K) experiment in 1998 [3], implies that neutrinos have nonzero masses and flavor mixing, providing one of the most convincing experimental proofs known today for the existence of physics beyond the Standard Model (BSM). Indeed neutrino oscillation has been established as a very powerful tool to probe extremely small neutrino masses (or their differences) as well as lepton flavor mixing.

Throughout this design report, unless stated otherwise, we consider the standard three flavor neutrino framework. The 3×3 unitary matrix U which describes the mixing of neutrinos [4] (that is often referred to as the Pontecorvo-Maki-Nakagawa-Sakata (PMNS) or Maki-Nakagawa-Sakata (MNS) [4, 5] matrix) relates the flavor and mass eigenstates of neutrinos as

$$\nu_\alpha = \sum_{i=1}^{3} U_{\alpha i}\nu_i \quad (\alpha = e, \mu, \tau), \tag{1}$$

where $\nu_\alpha(\alpha = e, \mu, \tau)$ and $\nu_i(i = 1, 2, 3)$ denote neutrino fields with definite flavor and mass,

respectively.

Using the standard parameterization, found, e.g. in Ref. [6], U can be expressed as,

$$U = \begin{pmatrix} 1 & 0 & 0 \\ 0 & c_{23} & s_{23} \\ 0 & -s_{23} & c_{23} \end{pmatrix} \begin{pmatrix} c_{13} & 0 & s_{13}e^{-i\delta_{CP}} \\ 0 & 1 & 0 \\ -s_{13}e^{i\delta_{CP}} & 0 & c_{13} \end{pmatrix} \begin{pmatrix} c_{12} & s_{12} & 0 \\ -s_{12} & c_{12} & 0 \\ 0 & 0 & 1 \end{pmatrix} \begin{pmatrix} 1 & 0 & 0 \\ 0 & e^{i\frac{\alpha_{21}}{2}} & 0 \\ 0 & 0 & e^{i\frac{\alpha_{31}}{2}} \end{pmatrix} \quad (2)$$

where $c_{ij} \equiv \cos\theta_{ij}$, $s_{ij} \equiv \sin\theta_{ij}$, and δ_{CP} — often called the Dirac CP phase —, is the Kobayashi-Maskawa type CP phase [7] in the lepton sector. On the other hand, the two phases, α_{21} and α_{31}, — often called Majorana CP phases — exist only if neutrinos are of Majorana type [8–10]. While the Majorana CP phases can not be observed in neutrino oscillation, they can be probed by lepton number violating processes such as neutrinoless double beta ($0\nu\beta\beta$) decay.

In the standard three neutrino flavor framework, only two mass squared differences, Δm^2_{21} and Δm^2_{31}, for example, are independent. Here, the definition of mass squared differences is $\Delta m^2_{ij} \equiv m^2_i - m^2_j$. Therefore, for a given energy and baseline, there are six independent parameters that describe neutrino oscillations: three mixing angles, one CP phase, and two mass squared differences. Among these six parameters, θ_{12} and Δm^2_{21} have been measured by solar [11–13] and reactor [14–16] neutrino experiments. The parameters θ_{23} and $|\Delta m^2_{32}|$ (only its absolute value) have been measured by atmospheric [17, 18] and accelerator [19–22] neutrino experiments. In the last few years, θ_{13} has also been measured by accelerator [23–26] and reactor experiments [27–31]. Remarkably, the Super-K detector has successfully measured all of these mixing parameters, apart from the CP phase and the sign of Δm^2_{32}. The current best-measured values of the mixing parameters are listed in [6], where the mass hierarchy and CP phase are still unknown though there are some weak preferences by the current neutrino data as will be mentioned later in this section.

By studying neutrino oscillation behaviour, Hyper-K is expected to improve the current bounds obtained by Super-K for various non-standard neutrino properties, such as the possible presence of sterile neutrinos [32], non-standard interactions of neutrinos with matter [33], or violation of Lorentz invariance [34].

1. Mass Hierarchy

The positive or negative sign of Δm^2_{32} (or equivalently that of Δm^2_{31}) corresponds, respectively, to the case of normal ($m_2 < m_3$) or inverted ($m_3 < m_2$) mass hierarchy (ordering). From a theoretical point of view, it is of great interest to know the mass hierarchy to understand or obtain

clues about how the neutrino masses and mixing are generated (see e.g. [35] for a review). Also the mass hierarchy has a significant impact on the observation of the $0\nu\beta\beta$ decay for the case where neutrinos are Majorana particles. If the mass hierarchy is inverted, a positive signal of $0\nu\beta\beta$ is expected in future experiments if the current sensitivity on the effective Majorana mass can be improved by about one order of magnitude beyond the current limit.

In the $\nu_\mu \to \nu_e$ appearance channel, its oscillation probability at around the first oscillation maximum, $O(L/E_\nu) \sim 1$, tends to be enhanced (suppressed) if the mass hierarchy is normal (inverted) due to the matter effect or the so called Mikheev-Smirnov-Wolfenstein (MSW) effect [36, 37] as we will see in Part III. For the antineutrino channel, $\bar{\nu}_\mu \to \bar{\nu}_e$, the effect become opposite, namely, the normal (inverted) mass hierarchy tends to suppress (enhance) the appearance probability. The longer the baseline (L), larger the effect of such enhancement or suppression. Therefore, in principle, the mass hierarchy can be determined by measuring the oscillation probability provided that the matter effect is sufficiently large. This is the most familiar way to determine the mass hierarchy in neutrino oscillation which can be done using accelerator or atmospheric neutrinos.

Independently from this method, it is also possible to determine the mass hierarchy by observing the small interference effects caused by Δm^2_{31} and Δm^2_{32} in the medium baseline ($L \sim 50$ km) reactor neutrino oscillation experiment as first discussed in [38]. The proposed projects such as JUNO [39] and RENO-50 [40] aim to determine the mass hierarchy by this method. Furthermore, in principle, it is possible to determine the mass hierarchy by comparing the absolute values of the effective mass squared differences determined by reactor ($\bar{\nu}_e$ disappearance) and accelerator (ν_μ disappearance) with high precision [41, 42].

It is expected by the time Hyper-K will start its operation, around the year 2025, the mass hierarchy could be determined at $\sim$ (3-4)σ or more by combining the future data coming from the ongoing experiments such as NOvA, T2K and reactor experiments, Daya Bay [43], RENO [44], Double Chooz [45], and proposed future experiments such as JUNO [39], RENO-50 [40], ICAL [46], PINGU [47], and ORCA [48] where the last three projects will use atmospheric neutrinos to determine the mass hierarchy.

2. CP Violation

The magnitude of the charge-parity (CP) violation in neutrino oscillation can be characterized by the difference of neutrino oscillation probabilities between neutrino and anti-neutrino channels [49, 50].

The current data coming from T2K [51] and NOvA [52], when combined with the result of the reactor θ_{13} measurement, prefer the value around $\delta_{CP} \sim -\pi/2$ (or equivalently, $\delta_{CP} \sim 3\pi/2$) for both mass hierarchies though the statistical significance is still small. Interestingly, the Super-K atmospheric neutrino data also prefers similar δ_{CP} values with a similar statistical significance [53].

If CP is maximally violated ($|\sin\delta_{CP}| \sim 1$), CP violation ($\sin\delta_{CP} \neq 0$) could be established at $\sim$ (2-3)σ CL by combining the future data coming from T2K and NOvA as well as with data coming from the reactor θ_{13} measurements.

In Hyper-K the neutrino oscillation parameters will be measured using two neutrino sources which can provide complementary information. Both atmospheric neutrinos, where neutrino oscillations were first confirmed by Super-K, and a long baseline neutrino beam, where electron neutrino appearance was first observed by T2K, will be employed.

With a total exposure of 13 MW $\times$ 10^7 sec integrated proton beam power (corresponding to 2.7×10^{22} protons on target with a 30 GeV proton beam) to a 2.5-degree off-axis neutrino beam, it is expected that the leptonic CP phase δ_{CP} can be determined to better than 21 degrees for all possible values of δ_{CP}, and CP violation can be established with a statistical significance of more than 3σ (5σ) for 78% (62%) of the δ_{CP} parameter space for the 2TankHK-staged design.

Figure 2 shows how both CP-violation and mass hierarchy affect the difference between $\nu_\mu \to \nu_e$ detection probability relative to $\bar{\nu}_\mu \to \bar{\nu}_e$ detection probability for a given set of neutrino parameters.

B. Astrophysical neutrino observations

Hyper-K is also capable of observing neutrinos from various astrophysical objects. One main advantage of the detector is that its energy threshold can be set as low as several MeV; this enables us to reconstruct neutrinos from the Sun and supernovae on an event-by-event basis.

The Sun is an abundant and nearby source of neutrinos. Recently, Super-K showed the first indication of the terrestrial matter effects on ^{8}B solar neutrino oscillations [54]. This was a direct confirmation of the MSW model [37, 55, 56] predictions for neutrino interactions with matter, which is also used to describe neutrino behaviour as it travels through the Sun. Furthermore, terrestrial matter effects hint at an intriguing possibility of using atmospheric and long baseline neutrinos to measure mass hierarchy and CP phase as both these parameters affect how neutrinos interact with matter. Hyper-K hopes to measure terrestrial matter effects with higher precision to better understand neutrino oscillation behaviour in the presence of matter. This also might resolve

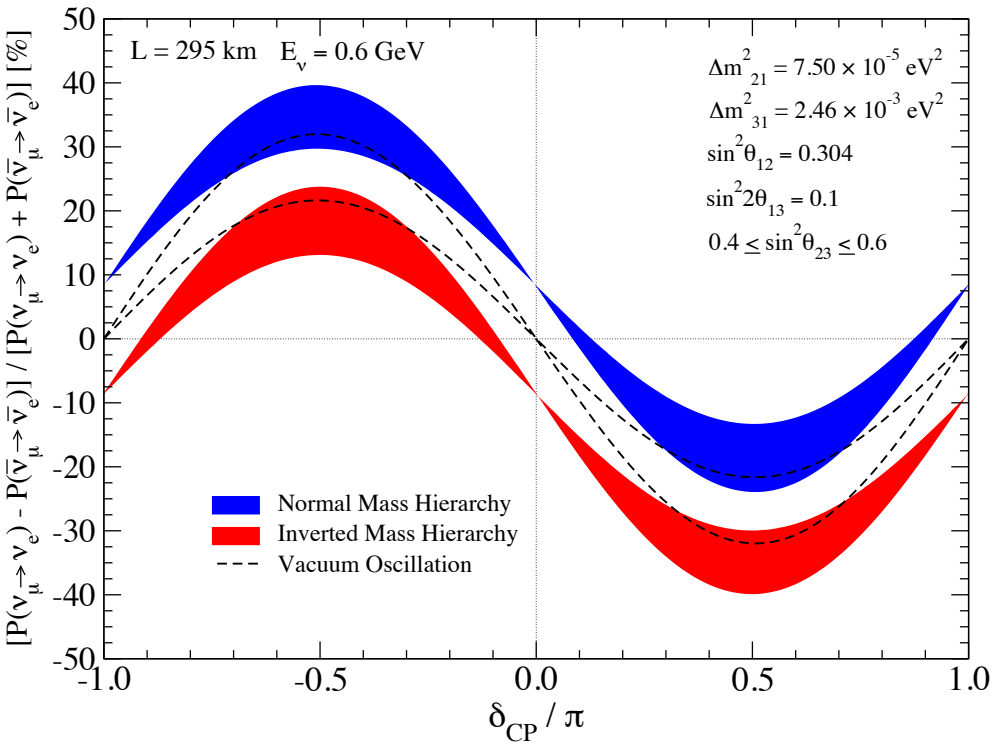

FIG. 2. The effect of neutrino mass hierarchy and CP-violation (δ_{CP}) on the neutrino/antineutrino detection probability, for a specific set of neutrino mixing parameters, neutrino energy(E_ν), and propagation length (L).

the $\sim 2\sigma$ tension between the current best fit values of Δm^2_{21} from solar and reactor neutrino experiments, which is thought to be due to solar neutrino interactions in matter. Additionally, there are several physics goals for the solar neutrino observations in Hyper-K, such as long and short time variation of the ^{8}B flux, the first measurement of *hep* neutrinos, and precise measurement of solar neutrino energy spectrum.

Computational simulations of core-collapse supernovae (CCSN) have failed to successfully reproduce explosions for more than 40 years. However, thanks to the recent advances in modeling techniques and the growth of available computation power, multi-dimensional (2D and 3D) simulations can now produce successful explosions [57–60]. Nevertheless, there are still some puzzles, such as the finding that the total explosion energy of the available multi-dimensional models is small compared to the SN1987A observation. Furthermore, the available 3D models are generally less energetic (or unsuccessful) compared with the more extensively simulated 2D models [59–62].

Clearly, details of the supernova explosion mechanism are still lacking. High statistics observations of neutrinos from a CCSN (along with gravitational waves) are the only way to obtain precious inside information on the dynamics of the CCSN central engine and the explosion mechanism [62, 63]. If a CCSN explosion were to take place near the center of our Galaxy, Hyper-K would observe as many as 250,000 neutrino interactions (see Section III.3 A). Furthermore, Hyper-K will have the ability to precisely determine the arrival time of supernova neutrinos, which will help contribute to the understandings of both neutrino and CCSN properties. For example, by comparing of the number of ν_e and $\bar{\nu}_e$ during the CCSN neutronization burst (first $\sim$10 msec) we will be able to determine the neutrino mass hierarchy (see Section III.3 A). High frequency timing will also provide experimental evidence of the multidimensional dynamics thought to be crucial in the CCSN explosion mechanism [62]. A large target volume like that of Hyper-K is also required to observe neutrinos from CCSN explosions in nearby ($\sim$ few Mpc) galaxies. In this volume, CCSNe occur every few years [64]. Meanwhile, while waiting for a nearby explosion to occur, the continuous flux of relic supernova neutrinos from all past CCSN explosions in the observable universe will guarantee a steady accumulation of valuable astrophysical data.

Thanks to its good low energy performance for upward-going muons, Hyper-K has a larger effective area for upward-going muons below 30 GeV than do cubic kilometer-scale neutrino telescopes. Additionally, fully contained events in Hyper-K have energy, direction, and flavor reconstruction and resolutions as good as those in Super-K. This high performance will be useful for further background suppression or studies of source properties. For example, the detector is extremely sensitive to the energy range of neutrinos from annihilations of light (below 100 GeV) WIMP dark matter, a region which is suggested by recent direct dark matter search experiments. Hyper-K can search for dark matter WIMPs by looking for neutrinos created in pair annihilation from trapped dark matter in the Galactic centre or the centre of the Sun. Atmospheric neutrinos are a background to this WIMP search, so spacial cuts are made to determine if there is an excess of neutrinos coming from the Galactic centre or the Sun. Hyper-K will have the ability to detect both ν_e and ν_μ components of the signal, making it more sensitive to this type of analysis.

The detection of neutrinos from solar flares is another astrophysics goal for Hyper-K. This will give us important information about the mechanism of the particle acceleration at work in solar flares. There have been some estimations of the number of expected neutrinos. Although it has large uncertainties, about 20 neutrinos will be observed at Hyper-K during a solar flare as large as the one in 20 January 2005. Hyper-K also has the potential to see neutrinos from astrophysical sources such as magnetars, pulsar wind nebulae, active galactic nuclei, and gamma

ray bursts. The large target volume of Hyper-K, combined with the potential for these sources to emit neutrinos with energy at the GeV-TeV scale, could make Hyper-K an interesting experiment for observing these neutrinos. As with dark matter searches, the most significant background for detecting neutrinos for these astrophysical sources are atmospheric neutrinos. Spacial, and in some cases temporal, cuts need to be utilized to disentangle the astrophysical neutrino signal from the atmospheric neutrino background.

C. Nucleon decay searches

The stability of everyday matter motivated Weyl, Stueckelberg, Wigner, and other early quantum physicists to introduce a conserved quantity, baryon number, to explain the observed and unobserved particle reactions. Baryon number violation is believed to have played an important role during the formation of the universe, and comprises one of the famous Sakharov Conditions to explain the baryon asymmetry of the universe. Proton decay and the decay of bound neutrons are observable consequences of the violation of baryon number.

The Standard Model Lagrangian explicitly conserves baryon number, although anomalous quantum effects do violate baryon number at an unobservably tiny level. Nevertheless, there are reasons to believe that the Standard Model is part of a more expansive theory. Baryon number violation is a generic prediction of Grand Unified Theories (GUTs) that combine quarks and leptons and include interactions that allow their transition from one to the other. These theories are well motivated by observations such as the equality of the sum of quark and lepton charges, the convergence of the running gauge couplings at an energy scale of about 10^{16} GeV, and frequently have mechanisms to generate neutrino mass. If new forces carrying particles have masses at this GUT scale, the lifetime of the proton will be in excess of 10^{30} years, where past, present, and future proton decay experiments must search.

Baryon number violation has never been experimentally observed and lifetime limits, mainly by Super-Kamiokande, greatly restrict allowable Grand Unified theories and other interactions of interest to model building theorists. In Fig. 3, we show 90% CL lifetime limits by Super-Kamiokande and earlier experiments compared with representative lifetime ranges predicted by various GUTs. We also show the improvement in lifetime limits expected for 10 years of Hyper-Kamiokande exposure. The complementary experiment DUNE, assumed to be a 40 kt liquid argon time projection chamber (LArTPC) is also a sensitive to nucleon decay. Due to its smaller mass compared to Hyper-K, it is competitive mainly in modes with distinctive final state tracks such as

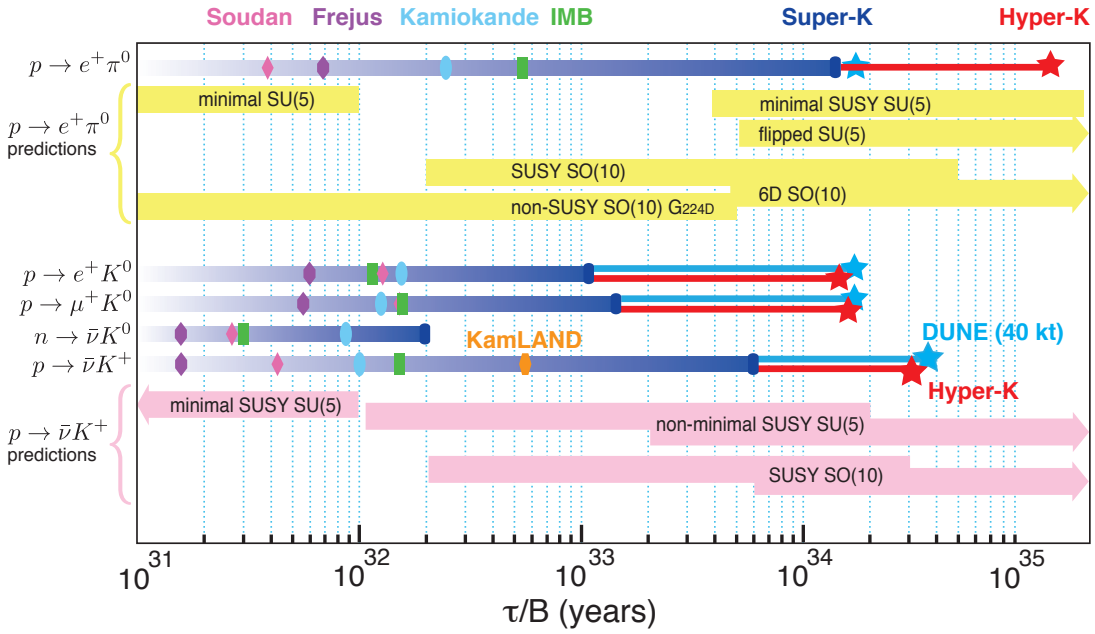

FIG. 3. A comparison of historical experimental limits on the rate of nucleon decay for several key modes to indicative ranges of theoretical prediction. Included in the figure are projected limits for Hyper-Kamiokande and DUNE based on 10 years of exposure.

those involving kaons.

The message the reader should conclude from this figure is that 10 years of Hyper-K exposure is sensitive to lifetimes that are commonly predicted by modern grand unified theories. The key decay channel $p \to e^+\pi^0$ has been emphasized, because it is dominant in a number of models, and represents a nearly model independent reaction mediated by the exchange of a new heavy gauge boson with a mass at the GUT scale. The other key channels involve kaons, wherein a final state containing second generation quarks are generic predictions of GUTs that include supersymmetry. Example Feynman diagrams are shown in Fig. 4.

Generally, nucleon decay may occur through multiple channels and ideally, experiments would reveal information about the underlying GUT by measuring branching ratios. It is a strength of Hyper-K that it is sensitive to a wide range of nucleon decay channels, however the few shown here are sufficient to discuss the details of the search for nucleon decay by Hyper-Kamiokande later in this document.

Practically, because of the stringent limits from more than 300 kt·y of Super-K running, the next generation experiments will have to concentrate on the discovery of nucleon decay, perhaps by one or a small number of events. The predictions are uncertain to two or three orders of magnitude,

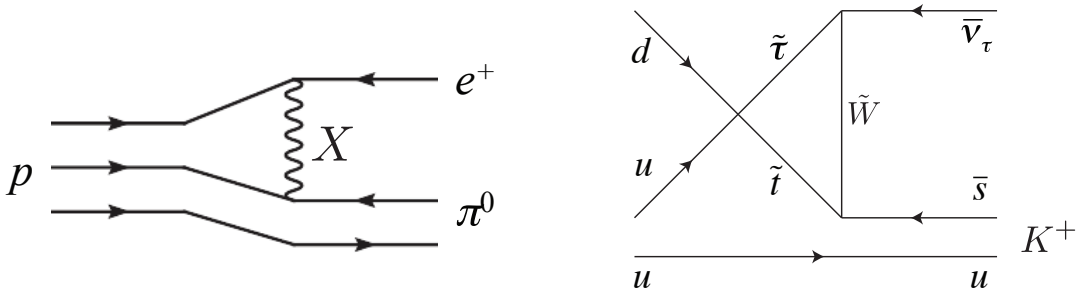

FIG. 4. Two sample Feynman diagrams that could be responsible for proton decay. The left diagram is a $d = 6$ interaction mediated by a heavy gauge boson, X, with mass at the GUT scale. The right diagram contains superymmetric particles and a $d = 5$ operator that is predicted in many SUSY GUTs.

and one should not expect a negative search to definitively rule out the idea of GUTs. To excel in the search for proton decay, Hyper-Kamiokande requires the largest mass that is affordable in combination with sufficient instrumentation to minimize experimental background.

D. Synergies between Hyper-K and other neutrino experiments

This section will focus on understanding how Hyper-K will fit into the context of the global neutrino community. This includes currently operating experiments such as T2K and Super-K, as well as future experiments like DUNE.

1. T2K

T2K [23] is a currently-operating experiment which uses Super-K to measure neutrinos produced in the J-PARC beam line. Hyper-K will use much of the existing infrastructure used by T2K, particularly the beam line and near detectors. Hyper-K will also benefit from any improved data analysis techniques developed for T2K. Several important T2K upgrades and improvements are planned for the coming years, and this will have a direct impact on improved Hyper-K performance.

- **Near detector improvements**: The T2K experiment uses the ND280 near detector suite. Future analysis improvements in the ND280 detector aim to reduce the cross section and flux uncertainties. Hardware upgrades, particularly to the time projection chamber component has also been proposed. The reader should refer to Section II.1 D 1 for the full details of the current and future status of the ND280 detector.

- **Increased beam power**: J-PARC is planning an upgrade of the proton drivers in the neutrino beam. The near-term goal is to improve the beam power from 365 kW to 750 kW. After the proton driver upgrade, beam power is projected to reach 1300 kW. See Section II.1 for more details.

- **Better data analysis techniques**: T2K demonstrated in its publications about ν_e appearance that aspects of the data analysis such π^0 rejection can be improved. Other improvements to the data analysis technique are under development, including ν_e detection efficiency, precision of the vertex determination (which could allow for an increased fiducial volume), and an improvement in π/μ separation.

In addition to benefiting directly from the upgraded hardware and analysis techniques, Hyper-K will also benefit from the expertise gained through implementing these upgrades. Furthermore, these upgrades can serve as a test bed for new near detector designs that have been proposed for Hyper-K (see Section II.1).

2. Super-K

In June 2015, the Super-Kamiokande Collaboration approved the SK-Gd project. This project is an upgrade of the detector's capabilities, achieved by dissolving 0.2% gadolinium sulfate into Super-K's water in order to enhance detection efficiency of neutrons from neutrino interactions. One of the main motivations of SK-Gd is to discover supernova relic neutrinos (SRN), the diffuse flux of neutrinos emitted by all supernovae since the beginning of the universe. SRN primarily interact in Super-K via inverse beta decay (IBD). Therefore, following the prompt detection of a positron, the accompanying IBD neutron can be identified in SK-Gd by a delayed gamma cascade, the result of the neutron's capture on gadolinium. As a result of this positive identification of true IBD events, a much improved separation between signal and background can be achieved.

As Super-K will be the first example of gadolinium loading in a large-scale water Cherenkov detector, this will be a template for any future possibility of loading gadolinium into Hyper-K. In addition to determining the physics performance of gadolinium-loaded water, Hyper-K will also benefit from the extensive research done to optimize the water purification system, as well as the tests for material compatibility that was required to upgrade the Super-K detector.

3. DUNE

The Deep Underground Neutrino Experiment (DUNE), formerly LBNE [65], is a 40 kilotonne liquid argon neutrino experiment that is projected to begin taking data around the same time as Hyper-K. Because DUNE will use a different target material than Hyper-K (liquid argon rather than water), many complementary measurements can be made, including nucleon decay measurements (as described in Section I.1 C) and supernova neutrino detection.

As mentioned in Section I.1 B, information about the neutrino signature from supernovae is much sought after, and Hyper-K and DUNE will each add to the overall picture. The primary reaction channel for these neutrinos in Hyper-K is the inverse beta decay channel, in which only electron antineutrinos will take part. In DUNE, the reaction channel will be the charged-current reaction on ^{40}Ar, which measures electron neutrinos. Taken together, these measurements will be able to determine the relative abundance of neutrinos to antineutrinos. Furthermore, DUNE will be able to better determine some features of the neutrino spectrum which are dominated by the neutrino signal, such as the neutronization burst that occurs during early times, while Hyper-K will better measure features where there is an antineutrino signal, such as the accretion and cooling phases that occur at late times.

Due to the fact that the baseline between the accelerator facility and Hyper-K will be shorter than the proposed baseline for the DUNE experiment, the two experiments will have some complementarity in the information they can extract from their accelerator programs. The longer baseline to the DUNE experiment means their measurement will be more affected by matter effects, which will give them more sensitivity to the mass hierarchy. The shorter baseline of Hyper-K experiment means less sensitivity to matter effects, which should lead to an increased sensitivity to the measurement of the CP-violation phase. This is further described in Section III.1 A.

Part II

Experimental Configuration

II.1. J-PARC NEUTRINO BEAM FACILITY

The accelerator neutrinos at detected by Hyper-K are produced at the Japan Proton Accelerator Research Complex (J-PARC) [66]. The proton accelerator chain, neutrino beamline and near detectors are located within J-PARC. Proposed intermediate detectors would be located near the J-PARC site at a distance of 1-2 km from the production target. This section, describes the proton accelerator chain, neutrino beamline, near detectors and proposed intermediate detectors. In each case, the current configuration and future upgrades are described.

A. Neutrino beam and near detectors in long baseline oscillation measurements

The T2K neutrino beam is produced by colliding 30 GeV protons extracted from the J-PARC accelerator chain with a 91 cm long graphite target. Three magnetic horns focus secondary charged particles that are produced in the proton-target collisions. The polarity of the horns' currents determine which charge is focused and defocused, allowing for the creation of neutrino or antineutrino enhanced beams. The secondary particles are allowed to decay in a 96 m long decay volume. The dominant source of neutrinos is the decay of $\pi^{\pm}$. Most $\mu^{\pm}$ are stopped in the absorber located at the end of the decay volume before they decay, and $\nu_e(\bar{\nu_e})$ from $\mu^{\pm}$ decays contribute less than 1% to the total neutrino flux at at the peak energy.

The J-PARC beam is aimed 2.5° away from the Super-K and Hyper-K detectors to take advantage of the pion decay kinematics to produce a narrow band beam [67] with a spectrum peaked at 600 MeV, at the first oscillation maximum for a baseline of 295 km. Fig. 5 shows the calculated energy dependent neutrino fluxes in the absence of neutrino oscillations impinging on Hyper-K for 320 kA horn currents in both horn polarities. Neglecting oscillations, neutrino detectors located near the neutrino source observe a similar neutrino spectrum to the far detector spectrum, but the peak of the spectrum is broader since the beam appears as a line source for near detectors, compared to a point source for far detectors.

The neutrino flux is calculated using a data-driven simulation that employs primary proton beam measurements, hadron production measurements, beamline element alignment measurements and horn current and field measurements [68]. The dominant uncertainty on the flux calculation arises

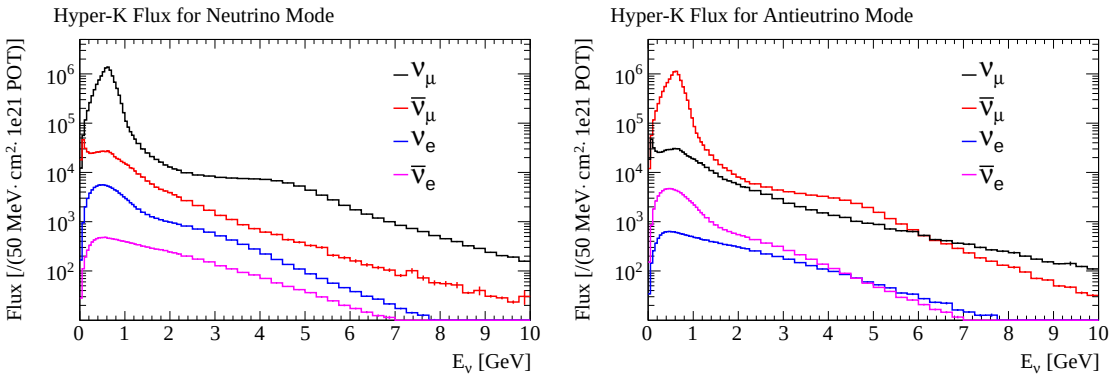

FIG. 5. The neutrino spectra at Hyper-K for the neutrino enhanced (left) and antineutrino enhanced (right) horn current polarities with the absolute horn current set to 320 kA.

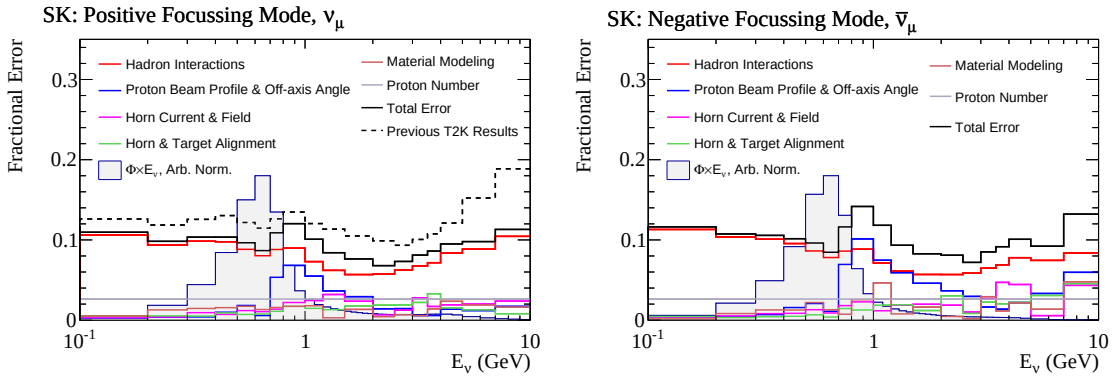

FIG. 6. The uncertainties on the T2K flux calculation at Super-K for neutrino enhanced (left) and antineutrino enhanced (right) beams.

from modeling of hadron production in the graphite target and surrounding material. To minimize the hadron production uncertainties, the NA61/SHINE experiment [69] has measured particle production with 30 GeV protons incident on a thin (4% of an interaction length) target [70, 71], and a replica T2K target [72]. The thin target data have been used in the T2K flux calculation, and a 10% uncertainty on the flux calculation has been achieved, as shown in Fig. 6. Much of the remaining uncertainty arises from the modeling of secondary particle re-interactions inside the target. Preliminary work suggests that the hadron production uncertainty can be reduced to $\sim 5\%$ by using the NA61/SHINE measurement of the particle multiplicities exiting the T2K replica target [73]. In the context of Hyper-K, the thin target data from NA61/SHINE are applicable to the flux calculation, and the replica target data may also be used if the target geometry does not change significantly.

The near neutrino detectors of T2K are located 280 m from the pion production target and they

include the INGRID on-axis detector [74] and the ND280 off-axis detector [75–79]. The INGRID detector is used primarily to measure the beam direction, while ND280 measurements provide constraints on the neutrino flux and interaction models that are used to predicted the event rate at the far detector after oscillations. Measurements with the ND280 detector are used for both dedicated neutrino cross-section measurements and event rate constraints that are used directly in neutrino oscillation measurements. For neutrino cross-section measurements, the neutrino flux is derived from the previously described flux calculation and the neutrino cross-section is inferred from the event rate and particle kinematics measured with the ND280 detector. The cross-section measurements provide constraints on the building of models of neutrino-nucleus interactions that are ultimately used in oscillation measurements. For the oscillation measurements themselves, nuisance parameters are introduced to describe the uncertainty on the neutrino flux and interaction models. A fit to a subset of the ND280 data simultaneously constrains the flux and interaction model nuisance parameters, and the predicted event rate and uncertainty at the far detector are updated [51]. The beam direction measurement, neutrino cross section measurements and direct constraints on the neutrino event rate for oscillation measurements are all necessary for long baseline oscillations measurements at Hyper-K.

B. The J-PARC accelerator chain

The J-PARC accelerator cascade [66] consists of a normal-conducting LINAC as an injection system, a Rapid Cycling Synchrotron (RCS), and a Main Ring synchrotron (MR). H^- ion beams, with a peak current of 50 mA and pulse width of 500 μs, are accelerated to 400 MeV by the LINAC. Conversion into a proton beam is achieved by charge-stripping foils at injection into the RCS ring, which accumulates and accelerates two proton beam bunches up to 3 GeV at a repetition rate of 25 Hz. Most of the bunches are extracted to the Materials and Life science Facility (MLF) to generate intense neutron/muon beams. The beam power of RCS extraction is rated at 1 MW. With a prescribed repetition cycle, four successive beam pulses are injected from the RCS into the MR at 40 ms (= 1/25 Hz) intervals to form eight bunches in a cycle, and accelerated up to 30 GeV. In fast extraction (FX) mode operation, the circulating proton beam bunches are extracted within a single turn into the neutrino primary beamline by a kicker/septum magnet system.

In the MR FX mode operation, a beam intensity of 1.9×10^{14} proton-per-pulse (ppp) has been achieved, corresponding to a 365 kW beam power. The accelerator team is following a concrete upgrade scenario [80] to reach the design power of 750 kW in forthcoming years, with a typical planned

TABLE I. Main Ring rated parameters for fast extraction, with numbers achieved as of May 2015. The columns show (left to right): the currently achieved operation parameters, the original design parameters, the projected parameters after the MR RF and magnet power supply upgrade, and the projected parameters for the maximum beam power achievable after the upgrade.

Parameter	Achieved	Original	Doubled rep-rate	Long-term Projection
Circumference			1,567.5 m	
Beam kinetic energy	30 GeV	50 GeV	30 GeV	30 GeV
Beam intensity	1.9×10^{14} ppp	3.3×10^{14} ppp	2.0×10^{14} ppp	3.3×10^{14} ppp
	2.4×10^{13} ppb	4.1×10^{13} ppb	2.5×10^{13} ppb	4.1×10^{13} ppb
[RCS equivalent power]	[575 kW]	[1 MW]	[610 kW]	[1 MW]
Harmonic number			9	
Bunch number			8 / spill	
Spill width			$\sim 5\,\mu$s	
Bunch full width at extraction	~50 ns	–	~50 ns	~50 ns
Maximum RF voltage	280 kV	280 kV	560 kV	560 kV
Repetition period	2.48 sec	3.52 sec	1.28 sec	1.16 sec
Beam power	365 kW	750 kW	750 kW	1367 kW

parameter set as listed in Table I. This will double the current repetition rate by (i) replacing the magnet power supplies, (ii) replacing the RF system, and (iii) upgrading injection/extraction devices. Based on high intensity studies of the current accelerator performance, it is expected that 1-1.3 MW beam power can be achieved after these upgrades [81, 82]. The projected beam performance up to 2030 is shown in Fig. 7. For operation larger than 2 MW beam power, conceptual design studies are now underway [83], and they include approaches such as raising the RCS top energy, enlarging the MR aperture, or inserting an emittance-damping ring between the RCS and MR.

C. Neutrino beamline

Fig. 8 shows an overview of the neutrino experimental facility [84]. The primary beamline guides the extracted proton beam to a production target/pion-focusing horn system in a target station (TS). The pions decay into muons and neutrinos during their flight in a 96 m-long decay volume. A graphite beam dump is installed at the end of the decay volume, and muon monitors

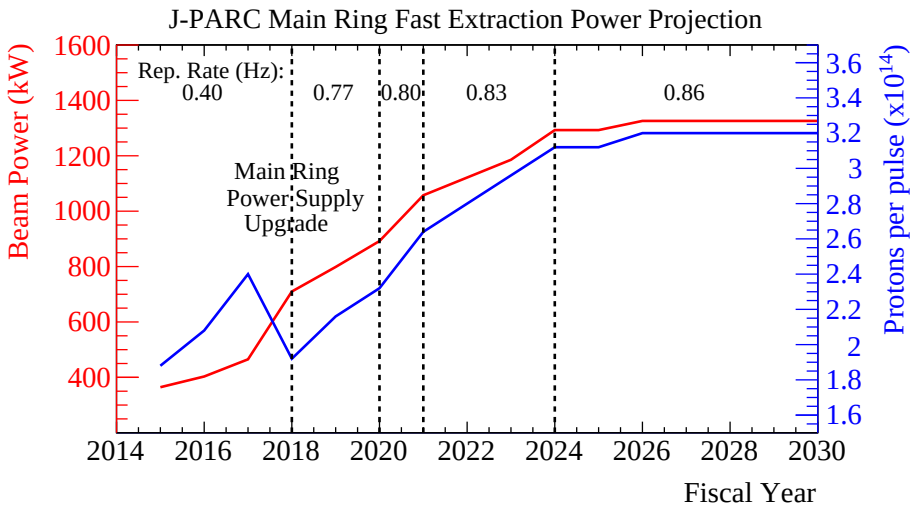

FIG. 7. The projected Main Ring fast extraction performance up to 2030, including the beam power, the protons per pulse, and the repitition rate.

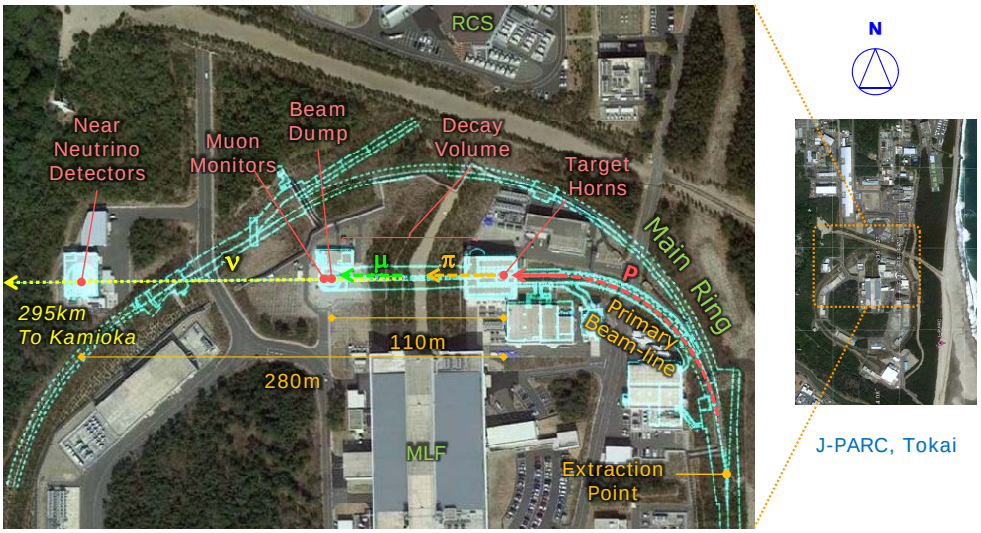

FIG. 8. The neutrino experimental facility (neutrino beamline) at J-PARC.

downstream of the beam dump monitor the muon profile. The beam is aimed 2.5° off-axis [85] from the direction to Super-K and the beamline has the capability to vary the off-axis angle between 2.0° to 2.5°.

The centreline of the beamline extends 295 km to the west, passing midway between Tochibora and Mozumi, so that both sites have identical off-axis angles.

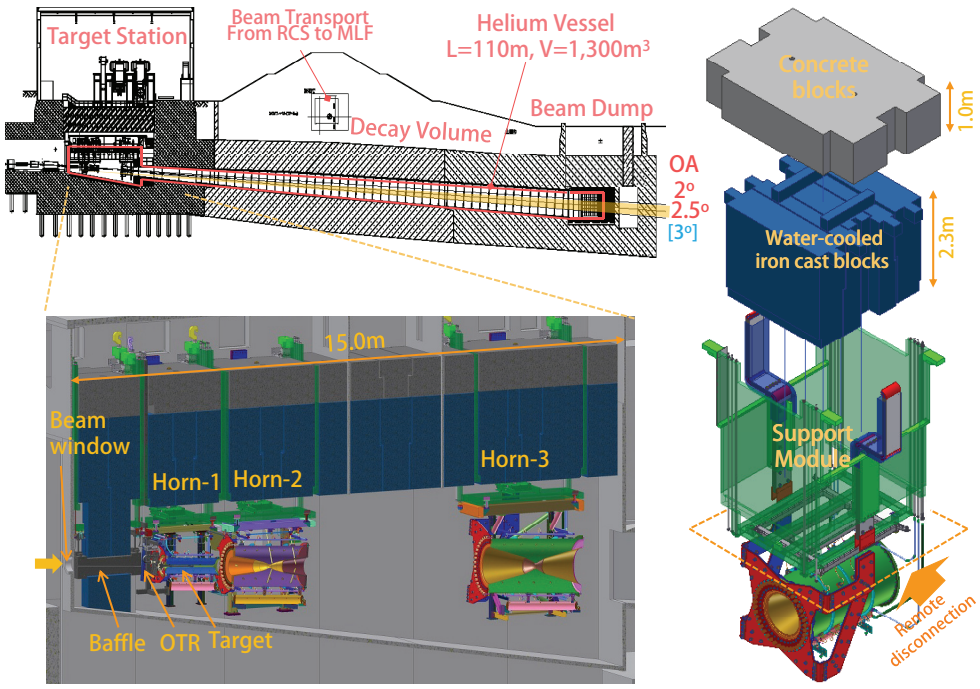

FIG. 9. (Left) Side view of the secondary beamline, with a close up of the target station helium vessel. (Right) A schematic view of a support module and shield blocks for horn-3. If a horn fails, the horn together with its support module is transferred remotely to a purpose-built maintenance area, disconnected from the support module and replaced.

1. *Secondary beamline*

The secondary beamline consists of the beamline from the TS entrance to the muon monitors. Fig. 9 shows a cross section of the secondary beamline, and a close-up of the TS helium vessel. The secondary beamline components and their capability to accept high power beam are reviewed here.

A helium cooled, double skin titanium alloy beam window separates the helium environment in the TS vessel (∼1 atm pressure) from the vacuum of the primary beamline. The proton beam collides with a helium-cooled graphite production target that is inserted within the bore of the first of a three-horn pion-focusing system. At 750 kW operation, a ∼20 kW heat load is generated in the target. The neutrino production target and the beam window are designed for 750 kW operation with 3.3×10^{14} ppp (equivalent to RCS 1 MW operation) and 2.1 sec cycle. In the target, the pulsed beam generates an instantaneous temperature rise per pulse of 200 C° and a thermal stress wave of magnitude 7 MPa. Given the tensile strength, the safety factor is ∼5. Although the tensile

strength and safety factor will be reduced by cyclic fatigue, radiation damage and oxidization of the graphite, a lifetime of 2−5 years is expected.

The horns are suspended from the lid of the TS helium vessel. Each horn comprises two co-axial cylindrical conductors which carry up to a 320 kA pulsed current. This generates a peak toroidal magnetic field of 2.1 Tesla which focuses one sign of pions. The heat load generated in the inner conductors by secondary particles and by joule heating is removed by water spray cooling. So far the horns were operated with a 250 kA pulsed current and a minimum repetition cycle of 2.48 sec. To operate the horns at a doubled repetition rate of ∼1 Hz requires new individual power supplies for each horn utilizing an energy recovery scheme and low inductance/resistance striplines. These upgrades will reduce the charging voltage/risk of failure, and, as another benefit, increase the pulsed current to 320 kA. The horn-1 water-spray cooling system has sufficient capacity to keep the conductor below the required 80°C at up to 1.85 MW.

All secondary beamline components become highly radioactive during operation and replacements require handling by a remotely controlled overhead crane in the target station. Failed targets can be replaced within horn-1 using a bespoke target installation and exchange mechanism.

Both the decay volume and the beam dump dissipate ∼1/3 of the total beam power, respectively. The steel walls of the decay volume and the graphite blocks of the hadron absorber (core of the beam dump) are water cooled and both are designed to accept 3∼4 MW beam power since neither can be upgraded nor maintained after irradiation by the beam.

Considerable experience has been gained on the path to achieving 365 kW beam power operation, and the beamline group is promoting upgrades to realize 750 kW operation, such improving the activated air confinement in TS, and to expanding the facilities for the treatment of activated water. Table II gives a summary of acceptable beam power and/or achievable parameters for each beamline component [86, 87], for both the current configuration and after the proposed upgrades in forthcoming years.

D. Near detector complex

The accelerator neutrino event rate observed at Hyper-K depends on the oscillation probability, neutrino flux, neutrino interaction cross-section, detection efficiency, and the detector fiducial mass of Hyper-K. To extract estimates of the oscillation parameters from data, one must model the neutrino flux, cross-section and detection efficiency with sufficient precision. In the case of the neutrino cross-section, the model must describe the exclusive differential cross-section that

TABLE II. Acceptable beam power and achievable parameters for each beamline component after proposed upgrades. Limitations as of May 2015 are also given in parentheses.

Component	Acceptable beam power or achievable parameter	
Target		3.3×10^{14} ppp
Beam window		3.3×10^{14} ppp
Horn		
cooling for conductors		2 MW
stripline cooling	(400 kW $\rightarrow$)	1$\sim$2 MW
hydrogen production	(300 kW $\rightarrow$)	1$\sim$2 MW
power supply	(250 kA $\rightarrow$)	320 kA
	(0.4 Hz $\rightarrow$)	1 Hz
Decay volume		4 MW
Hadron absorber (beam dump)		3 MW
water-cooling facilities	(750 kW $\rightarrow$)	$\sim$2 MW
Radiation shielding	(750 kW $\rightarrow$)	4 MW
Radioactive air leakage to the TS ground floor	(500 kW $\rightarrow$)	$\sim$2 MW
Radioactive cooling water treatment	(600 kW $\rightarrow$)	$\sim$2 MW

includes the dependence on the incident neutrino energy, E_ν, the kinematics of the outgoing lepton, momentum p_l and scattering angle θ_l, and the kinematics of final state hadrons and photons. In our case, the neutrino energy is inferred from the lepton kinematics, while the reconstruction efficiencies depend on the hadronic final state as well.

The neutrino flux and cross-section models can be constrained by data collected at near detectors, situated close enough to the neutrino production point so that oscillation effects are negligible. Our approach to using near detector data will build on the experience of T2K while considering new near detectors that may help address current limitations in reducing flux and cross section modelling uncertainties with the current near detector system.

The near detectors should be capable of measuring the signal and background processes relevant for neutrino oscillation measurements made using the accelerator produced neutrinos. The processes include:

- The charged current interactions with no detected final state pion (CC0π) that are the signal channel for the oscillation measurements in Hyper-K.

- The intrinsic electron neutrino component of the beam from muon and kaon decays, which is a background for the electron (anti)neutrino appearance signal.

- The neutral current interactions with π^0 production (NCπ^0) that are a background for the electron (anti)neutrino appearance signal.

- The wrong-sign charged current processes (neutrinos in the antineutrino beam and vise versa) which are a background in the CP violation measurement.

In addition to measuring these processes, the near detectors should be designed to maximize the cancellation of systematic uncertainties when extrapolating from measured event rates in the near detector to predict the event rate at Hyper-K. Hence, the near detector should be able to make measurements with the same angular acceptance (4π) and target nuclei (H_2O) as Hyper-K. Another source of uncertainty in the extrapolation is the difference between the near and far detector neutrino spectra due to oscillations, which can amplify systematic errors related to the modeling of the relationship between the final state lepton kinematics and the incident neutrino energy [88–90]. The near detectors should be able to sufficiently constrain the modeling of the dependence of lepton kinematics on neutrino energy over the relevant neutrino energy range.

The near detectors can also be used to constrain important neutrino interaction modes for atmospheric neutrino and nucleon decay measurements at Hyper-K. For example, Hyper-K may use neutron captures on Gd or H to statistically separate neutrinos and antineutrinos in the atmospheric measurements, or to reject atmospheric neutrino backgrounds in the nucleon decay measurements. The neutron multiplicities produced in the interactions of neutrinos and antineutrinos with energy of $\mathcal{O}(1$ GeV) can be measured in the near detectors. The dominant sources of uncertainty in the determination of the mass hierarchy and θ_{23} quadrant with atmospheric neutrinos are uncertainties in the neutrino to anti-neutrino cross section ratio for both CCQE and single pion production modes, the axial vector nucleon form factor, the neutrino-tau cross section, and the DIS cross section model. Near detector measurements that would constrain these uncertainties for interactions on water, have the potential to significantly improve the sensitivity of these atmospheric neutrino measurements. The near detectors can also be used to measure the interaction modes for nucleon decay backgrounds, including the CCπ^0 background to the $e^+(\mu^+)\pi^0$ mode and the kaon production background to the $K^+\nu$ mode.

1. The ND280 Detector Suite

The T2K ND280 detector suite, shown in Fig. 10, comprises two detectors: INGRID [74], which consists of 16 iron-scintillator modules in a cross pattern centered on the neutrino beam axis, and ND280, a multi-component detector at an angle of 2.5° from the beam direction. The primary purpose of the INGRID detector is to constrain the neutrino beam direction, whilst the off-axis detector is used to characterise the neutrino beam before oscillation.

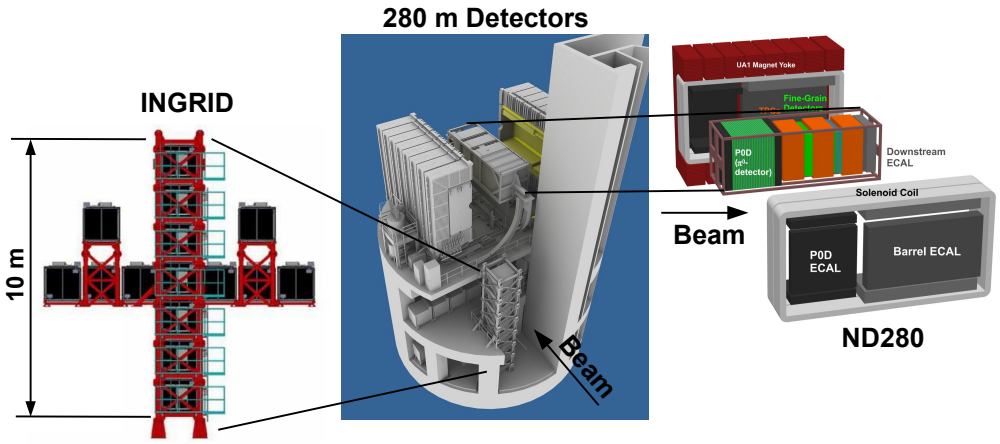

FIG. 10. The ND280 detector complex (center) including the INGRID (left) and ND280 (right) detectors.

The ND280 off-axis detector is composed of an inner tracking region surrounded by an upstream Pi-zero detector [75], electromagnetic calorimeters [76] and side muon range detectors [77], all of which are held inside the UA1 magnet. The 0.2 T magnetic field allows for momentum measurement and sign selection of charged particles, and is important for operation in antineutrino mode where the neutrino background is large. The tracking region is composed of three time projection chambers (TPCs) [79] separated by two fine grained detectors (FGDs) [78], the second of which contains passive water layers to allow for neutrino interaction rate measurements on oxygen. The FGDs are the neutrino target whilst the TPCs provide precise momentum measurements, particle identification and sign selection.

T2K has successfully applied a method of fitting to ND280 data with parameterized models of the neutrino flux and interaction cross-sections, as described in [51]. Using the ND280 measurements, the systematic uncertainties on the parts of the models constrained by ND280 have been reduced to ∼3% on the Super-K (SK) predicted event rates, as shown in Table III.

Current limitations and future analysis improvements

TABLE III. Current systematic uncertainty contributions to the T2K oscillation measurements taken from [51]

Source of uncertainty	ν_μ *CC*	ν_e *CC*
Flux and common cross sections		
(w/o ND280 constraint)	21.7%	26.0%
(w/ ND280 constraint)	2.7%	3.2%
Independent cross sections	5.0%	4.7%
SK	4.0%	2.7%
FSI + SI(+ PN)	3.0%	2.5%
Total		
(w/o ND280 constraint)	23.5%	26.8%
(w/ ND280 constraint)	7.7%	6.8%

As shown in Table III, the dominant sources of systematic uncertainty in the oscillation analyses are the cross section model parameters unconstrained by the near detector ("Independent cross sections" in Table III), which contribute a 5% systematic error to the predicted event rates at SK. These uncertainties are largely related to the modeling of the nuclei in the neutrino-nucleus interactions and cover the variation of nuclear models, such as the relativistic Fermi gas [91] and spectral function [92]. These systematic effects are unconstrained by the ND280 data since T2K has not yet incorporated the water targets in the analysis and only uses measurements on plastic scintillator. It is expected that this source of systematic error will be reduced with the inclusion of measurements on the water targets, but the eventual size of the systematic uncertainty is not yet known. FGD2 is split 40:60 by mass between water and scintillator and isolating events on water requires the subtraction of scintillator events from the sample. This subtraction introduces an additional systematic on the SK prediction, proportional to the relative fraction of carbon to water in the detector.

Another limitation of the current ND280 analysis is the difference in acceptance between ND280 and SK. These differences in accessible phase space mean that ND280 and SK are sensitive to different parts of the neutrino interaction model, which introduces additional uncertainty when performing oscillation analyses. The current ND280 analyses have a 50% efficiency for CC events with the muon traveling at angles of up to 53° relative to the detector Z axis, which is roughly aligned with the neutrino beam direction. Future analysis improvements will provide some acceptance of events at greater angles and with backward-going muons, but will not provide the same

coverage as a true 4π detector, such as SK.

A fundamental limitation of near detectors in oscillation analyses is that the near and far detectors do not sample the same neutrino spectrum due to the neutrino oscillations. Since the observed final state particle distributions are produced by different spectra in the near and far detectors, the interaction models are necessary to extrapolate the rate observed with the near detector spectrum to the rate expected with the far detector spectrum. This extrapolation is sensitive to the modeling of the observed final state particle kinematics for each incident neutrino energy. For water Cherenkov detectors such as Hyper-K, the relation of the final state lepton kinematics and neutrino energy for events with only a visible lepton is critical since the neutrino spectrum is infered from the lepton kinematics, and the signal sample is chosen by the presence of a single lepton candidate ring. If this relationship is not properly modeled, systematic biases will arise in the extrapolation. This effect has been studied for both muon neutrino disappearance and electron neutrino appearance measurements and found to be a potentially limiting source of systematic uncertainty for the oscillation measurements [88–90, 93]. Measurements of neutrino interactions from multiple neutrino spectra peaked at different energies may be used to constrain and improve the models to the level necessary for Hyper-K. This may be done at different experiments or with a single experiment by using the off-axis dependence of the neutrino beam. Alternatively, measurements at many off-axis angles may also be used to directly predict the expected event rate for the oscillated spectrum, as discussed in Section II.1 D 3. The models may also be improved with better measurements of exclusive final hadronic states.

Taken together, future analysis improvements at ND280 will decrease the uncertainty in the event rate prediction from the flux and cross section model (current value $\sim$6%), although the exact level of improvement is not yet known. These improvements will be driven by the inclusion of measurements on water and new samples with leptons produced at large angles. However the inherent limitations of ND280, including the limited efficiency for high angle reconstruction and 40:60 water:scintillator ratio, may ultimately limit the extent of these improvements, suggesting alternative paths for potential upgrades to ND280.

ND280 Hardware Upgrade possibilities

Within the T2K collaboration, discussions are taking place to upgrade ND280: the target is to reduce systematic errors on the prediction of far detector interactions in the presence of oscillations to better than 3%.

One possibility is to replace part of the existing detectors with a high pressure TPC, as was

proposed for the LBNO design study [94]. This would allow full angular coverage and a very detailed view of the vertex as well as superb particle identification and sensitivity to low momentum protons. The drawback in the case of T2K and Hyper-K is that it is difficult to find a suitable set of gases that would allow measurements of cross-sections for interactions on H and O. Another option to probe the hadronic final state and enhance our understanding of neutrino-nucleus interactions and to measure the low energy ν_e interaction cross-section is to add an emulsion detector to the ND280 suite. Emulsions provide 3D tracking with sensitivity to protons down to $\approx$20 MeV, and $> 3\pi$ sub micrometer position accuracy through offline scanning [95].

Another possibility is to improve the FGD+TPC combination by placing the targets in the plane constituted by the beam axis and the magnetic field axis, or by using a target with high water content (80%) such as the WAGASCI detector described below. This would allow a full 4π acceptance and would reduce the uncertainty on the water sample due to the subtraction of events on carbon as described above. An example of such a reconfiguration is shown in Figs. 11 and 12.

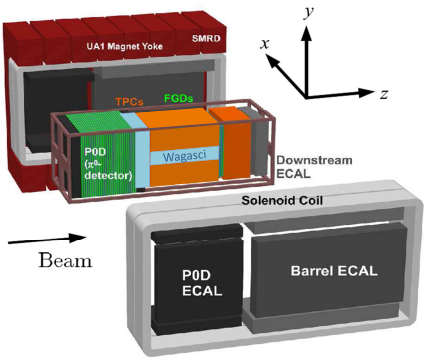

FIG. 11. A possible reconfiguration of the ND280 off-axis detector, with rotated TPCs and an FGD or WAGASCI type detector oriented parallel to the beam.

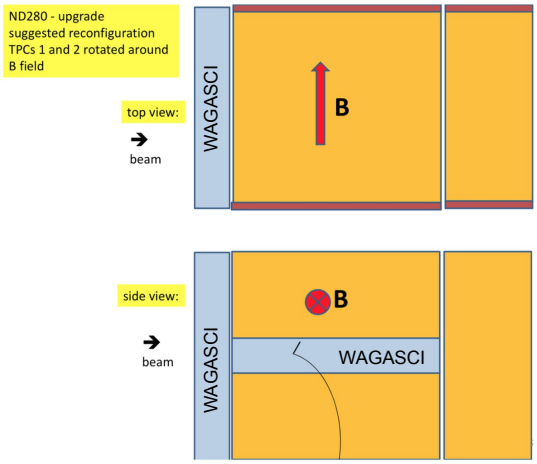

FIG. 12. An example event with the reconfigured target detectors. The acceptance of low energy quasi-elastic neutrino events is considerably improved compared to the current detector orientation.

WAGASCI

A new neutrino detector with a water target, WAGASCI (Water Grid And SCIntillator detec-

tor), is under development to measure neutrino interactions with high precision and a large angular acceptance. It uses a 3D grid-like structure of scintillator bars to track charged particles across the full 4π solid angle (Fig. 13 and 14). This structure provides WAGASCI with a larger angular acceptance and larger mass ratio of water to scintillator bars (80:20) than the current off-axis ND280 detector. A side muon range detector and magnetised baby-MIND detector surrounding a stand-alone WAGASCI will serve to range out the muons [96].

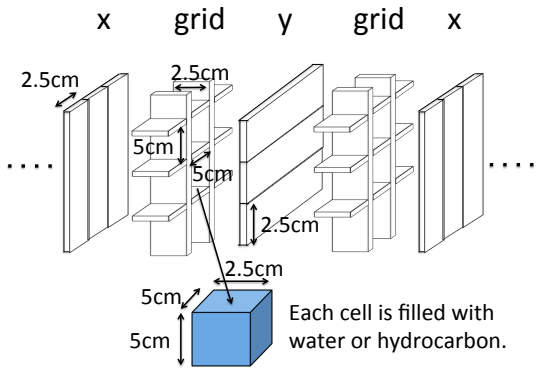

FIG. 13. Schematic view of 3D grid-like structure of plastic scintillator bars inside the WAGASCI detector.

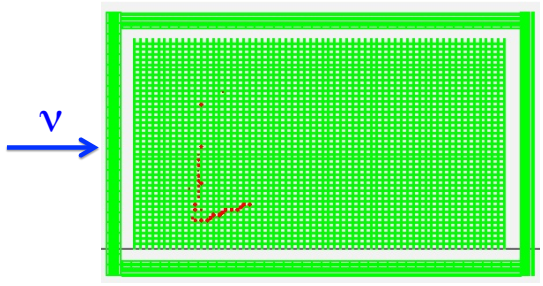

FIG. 14. MC event display of a charged current neutrino event in the WAGASCI detector.

As a first step, WAGASCI modules with water and hydrocarbon targets will be installed on the B2 and SS floors of the near detector hall at J-PARC. The detector on the B2 floor will be surrounded by massive muon range detectors. These detectors have been approved by the J-PARC PAC as test experiment T59 and will measure neutrino cross sections on water and hydrocarbon [97]. By comparing the observed interaction rate in the two targets, the inclusive water to hydrocarbon charged current cross section ratio can be measured with better than 3% precision, an established technique that has been shown to work by the current INGRID detector [98].

2. Intermediate detector

A water Cherenkov near detector can be used to measure the cross section on H_2O directly, with the same solid angle acceptance as the far detector with no need for a subtraction analysis. This approach was taken by K2K [19] and was proposed for T2K [99]. The MiniBooNE experiment has also employed a mineral oil Cherenkov detector at a short baseline to great success [100].

Additionally, WC detectors have shown excellent particle identification capabilities, allowing for the detection of pure ν_μ-CC, ν_e-CC and NCπ^0 samples. The CCπ^0 rate and kaon production in neutrino interactions, which are backgrounds to nucleon decay searches, can also be measured.

These additional WC measurements are essential to achieve the low systematic errors required by Hyper-K, but are complemented by the ND280 magnetised tracking detector, which has the capabilities to track particles below the threshold to produce Cherekov light in water and to separate neutrino and antineutrino charged current interactions via the lepton charge measurement. Hence a combination of a magnetized tracking detector such as ND280 and the WC detector should have the largest impact to reduce systematic uncertainties.

A WC near detector design should be large enough to contain muons up to the momentum of interest for measurements at the far detector and should be far enough from the neutrino production point that there is minimal pile-up of interactions in the same beam timing bunch. These requirements lead to designs for kiloton size detectors located at intermediate distances, 1-2 km from the target, for the J-PARC neutrino beam.

Here we present the three main features that are being considered for the WC detector:

- A detector that spans an off-axis angle range of $1^\circ - 4^\circ$ to measure the final state leptonic response over a range of neutrino spectra peaked at different energies. Measurements at multiple off-axis angles can be used to address the limitation of different neutrino spectra at the near and far detectors.

- Gd loading in the WC detector allows for the measurement of neutron multiplicities in neutrino and antineutrino interactions. These measurements can be used for statistical separation of neutrino and antineutrino interactions as well as different interaction modes and may be applied to the atmospheric and accelerator neutrino analyses in Hyper-K. The measurements can also be used to predict the rejection of nucleon decay backgrounds in Hyper-K with neutron tagging.

- A magnetized muon range detector allows for the extension of the muon momentum acceptance of the WC detector and for muon charge identification of muons escaping the WC detector. The muon charge identification can be used as an independent calibration of the statistical neutrino/antineutrino separation from the neutron tagging.

Finally, the WC detector has its own physics program independent from the measurements in service to Hyper-K. At a 1-2 km baseline, it can search for neutrino oscillations through sterile

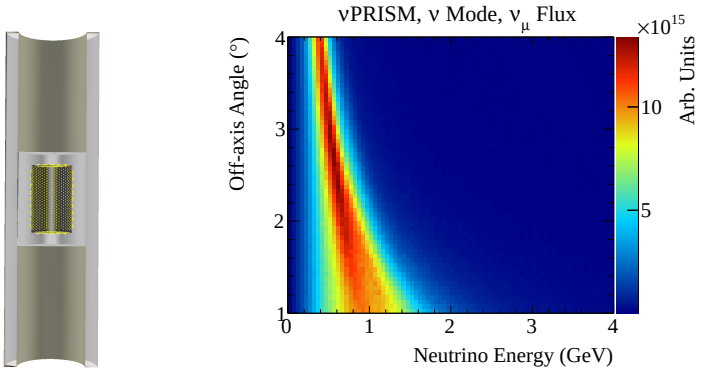

FIG. 15. Left: A conceptual drawing of the nuPRISM detector. Right: the ν_μ flux energy dependence for the $1^\circ - 4^\circ$ off-axis angle range.

neutrinos, on its own and in combination with ND280. The WC detector can also be used as an independent supernova alarm, and with the addition of gadolinium, would provide valued neutrino-type discrimination in the event of a supernova in the local galaxy.

In the following text, the above main features of the intermediate detector will be described in more detail, making use of the studies from other detectors.

3. Off-axis angle spanning configuration

The intermediate WC detector can be oriented with the polar axis of the cylinder in the vertical direction and the detector extending from the ground level downward. This configuration is employed by the proposed NuPRISM detector [101], which is located at a baseline of 1 km and fills a 10 m diameter, 50 m deep pit. By orienting the long axis of the detector perpendicular to the beam direction, the detector covers a range of angles relative to the beam direction. Hence, each vertical slice of the detector samples a different neutrino spectrum due to the decay kinematics of the pions and kaons producing the neutrinos, the so-called off-axis beam effect. Fig. 15 shows the conceptual drawing of the NuPRISM detector and the ν_μ spectra for the $1^\circ - 4^\circ$ off-axis angle range spanned by the detector. The baseline design for the detector is an instrumented structure with a 10 m tall inner-detector containing 3215 8 inch inward facing photomultiplier tubes to detect the Cherenkov light, giving 40% photo-coverage. A crane system will move the detector structure vertically in the 50 m pit to make measurements at different off-axis angles.

There are three primary motivations for making neutrino measurements over a range of off-axis angles. First, the change in the neutrino spectrum with off-axis angle is well known from the flux model, so the predicted off-axis spectra can be combined in a linear combination to produce almost

arbitrary neutrino spectra. Measured distributions at different off-axis angles can be combined in the linear combination to produce the predicted measured quantity for the neutrino spectrum of interest. In this way, it is possible to measure the muon spectrum for a nearly mono-chromatic neutrino spectrum, or a spectrum that closely matches the oscillated spectrum that is expected at the far detector. This approach can nearly eliminate the main model dependent uncertainty in near to far extrapolations, which arises from the combination of two factors: the near and far detector do not see the same flux due to oscillations, and the relationship between the true neutrino energy and final state lepton kinematics strongly depends on nuclear effects, which are not well modelled [101].

The second physics motivation is the measurement of the electron neutrino cross section relative to the muon neutrino cross section. At further off-axis positions, the fraction of intrinsic $\nu_e, \bar{\nu}_e$ in the beam becomes large, making the selection of pure candidate samples possible. By taking advantage of the enhanced purity at large off-axis angles, a measurement of the cross section ratio, $\sigma_{\nu_e}/\sigma_{\nu_\mu}$ with 3% precision or better may be possible. A measurement of the $\sigma_{\bar{\nu}_e}/\sigma_{\bar{\nu}_\mu}$ ratio is also possible, although the precision is expected to be degraded due to the larger neutral current background rate for electron antineutrino candidates and the presence of a larger wrong-sign background for both muon and electron antineutrino charge current interactions.

The third physics motivation is the search for sterile neutrino induced oscillations that are consistent with the LSND [102] and MiniBooNE [103] $\bar{\nu}_e$ and ν_e appearance anomalies. At a 1 km baseline, the L/E of the neutrino spectrum peak varies between 1.1 km/GeV at 1° off-axis to 2.5 km/GeV at 4° off-axis. Since the neutrino spectrum varies with off-axis angle, it is possible to search for the oscillation pattern not only through the reconstructed energy of the neutrino candidate events, but also through the reconstructed off-axis angle. This method provides a significant improvement in the electron neutrino appearance search sensitivity, and preliminary studies with a non-optimal detector configuration already show that much of the LSND allowed region can be excluded at 5σ [104].

4. Gadolinium Loading

Recent developments in the addition of gadolinium (Gd) [105] and Water-based Liquid Scintillator (WbLS) compounds [106] to water raise the possibility to separate neutrino and antineutrino interactions by detecting the presence of neutrons or protons in the final state.

Final state proton tagging has been studied intensively for an application for LArTPC detec-

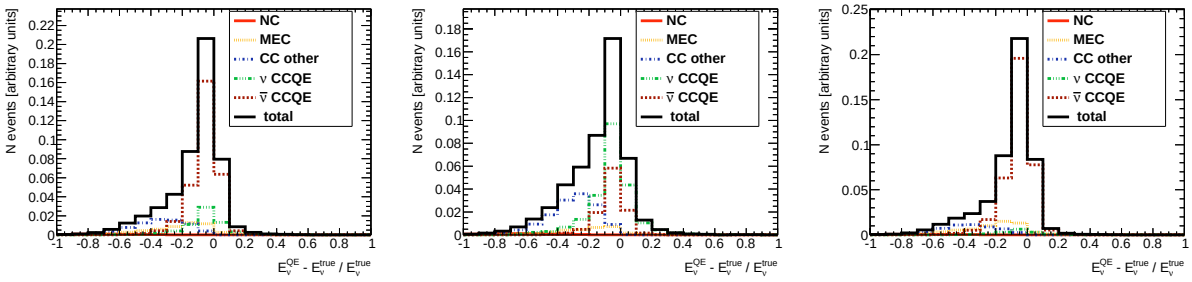

FIG. 16. The neutrino energy resolution due to the QE assumption in water Cherenkov near detector simulation for the TITUS detector [110] during anti-neutrino mode running. The effect of different neutron selections is shown. From left to right, no neutron tagging, neutron number =0, and neutron number > 0.

tors [107], where final state protons can be counted to further purify the sample to improve the oscillation sensitivity [108]. An analogous approach is possible for the larger Water Cherenkov detectors. Namely, Gd-doped water Cherenkov detectors possess neutron tagging ability on top of the 4π detector coverage [109], which allows statistical separation of primary interaction modes, otherwise impossible. Figure 16 shows an example of a water Cherenkov near detector simulation from the studies using the TITUS detector [110]. In this example, selecting "neutron≥1" increases the selection purity for $\bar{\nu}$CCQE interactions and hence improves the energy resolution. This technique will be also applied to the ANNIE experiment [111] in the next years.

The ability to tag neutrons also provides charge separation information due to the enhanced presence of neutrons in the final state for $\bar{\nu}$ charged current interactions. This will allow studies of neutrino:anti-neutrino cross-section ratios on water, thus reducing a critical systematic uncertainty in both the beam δ_{CP} and atmospheric neutrino oscillation analyses. Neutron tagging also allows more detailed studies of the interaction modes, and in particular final state interaction effects, for the main backgrounds to proton decay.

One aspect of the intermediate detector's design that needs to be carefully considered with Gd-doped water is how to veto incoming neutrons from beam-induced interactions in the material surrounding the detector which will be the dominant contributor for the number of particles entering the detector. Vetoing most of these particles requires at least 1 m of water to reduce the low energy tail, plus a fiducial cut on the reconstructed capture vertex. Preliminary studies using spallation rates induced by muons [112] and interactions in the material surrounding the detector show this veto can reduce the number of neutrons entering the detector's ID to just 10% of all the events entering the tank and the fiducial region further reduces this to approximately 7% of the entering particles.

In principle, Gd loading is compatible with the off-axis spanning detector configuration described in the previous section. The off-axis spanning detector should be as near as possible to the beam origin to reduce the depth of the excavated volume, while the Gd loaded detector should be far enough away to limit the beam induced entering neutron background to the necessary level. Preliminary studies suggest that the entering neutron rate is sufficiently low for the off-axis spanning detector located at 1 km from the neutrino production point.

5. Muon Range Detector

An additional magnetized muon range detector (MRD) would serve to range out muons and measure their momentum and charge, complementing the WC detector by both increasing sample size and directly constraining the wrong-sign components in the beams. A design to accompany a horizontally orientented WC cylidrical tank, as illustrated in Figure 17 for the TITUS detector, has been investigated, allowing the forward scattered muons which escape the tank to be included in the oscillation fit up to a momentum of 2 GeV/c. The smaller side-MRD, which is also magnetized, allows a measurement of the less well understood high-Q^2 region of phase space: useful for testing and discriminating neutrino interaction models.

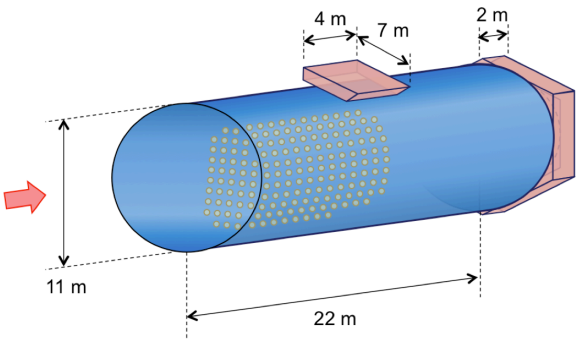

FIG. 17. A large magnetized MRD, with radius 11 m to match the Cherenkov tank, and thickness 2 m is placed downstream of the WC tank, to stop the large numbers of forward-scattered muons. A smaller magnetized side-MRD is placed on the side of the tank to allow low-background measurements of the anti-neutrino cross-section in this high-angle region of phase-space. This figure comes from the TITUS detector studies.

6 cm thick planes of iron are interleaved with orthogonally arranged pairs of scintillator planes that sample the position of particle tracks with position resolution of 1 cm for precise measurements

of the curvature and a strong, well-understood particle identification (PID) via the direction of curvature. To optimize for the the 0.6 GeV spectral peak, double scintillator planes and 10 cm air gaps are used in the first 3 planes giving 90% charge reconstruction efficiency for these shorter tracks. Higher energy muons ($p_\mu \gtrsim 1\,\mathrm{GeV/c}$) will travel through many iron planes and their charge can be measured with very high efficiency by reconstructing their curved trajectories in the 1.5 T magnetic field inside the iron. This sample is particularly interesting with regard to the validation of the complementary gadolinium charge reconstruction technique. The mean charge reconstruction efficiency for all events in the downstream MRD is estimated to be 95%.

By combining the gadolinium and MRD techniques it will be possible to obtain $\sim 96\%$ pure ν_μ and $\bar{\nu}_\mu$ samples from events in the oscillation peak.

E. Summary

This section has outlined the performance and requirements of the accelerator complex, neutrino beamline and near detectors at J-PARC that will be required for the Hyper-K physics program. The J-PARC accelerator chain has achieved 365 kW beam power extracted to the neutrino beamline. The accelerator upgrade plan, which includes the upgrade of the MR magnet powers supplies and RF is expected achieve 1.3 MW beam operation with 3.2×10^{14} protons per pulse, as early as 2018.

The neutrino beamline components require some upgrades to accept the repetition rate, proton intensity and total beam power necessary to achieve 1.3 MW at 3.2×10^{14} protons per pulse. To achieve the 1.16 Hz operation, each magnetic horn requires an individual power supply utilizing an energy recovery scheme and low inductance/resistance striplines. The target station activated air confinement will be upgraded to accept up to 2 MW operation. The treatment facilities for activated cooling water will be expanded to accept up to 2 MW operation as well. The current beam window and target are rated to 3.3×10^{14} ppp, however their lifetime at 3.2×10^{14}ppp and 1.16 Hz will be studied and upgrades may be necessary.

The current T2K near detectors, including ND280 and INGRID, are used to control neutrino flux and cross-section systematic errors at the $\sim$6% level. Further upgrades to the ND280 data analyses with water target measurements and large angle tracks will reduce the systematic error, although the ultimate performance may be limited by the relatively low water fraction and low efficiency for large angle track reconstruction. Upgrades to ND280 are being considered by T2K and these include a high pressure TPC, the WAGASCI water/scintillator 3D grid detector and emulsion detectors. A reconfiguration of the TPC geometry is also being considered to give better

reconstruction at high angles. It is expected that some of these upgrades may be carried out during the T2K experiment and Hyper-K may benefit from their continued use. If they are not implemented during T2K, these ND280 upgrades as well as the continued operation of ND280 are an expected area for international contributions to Hyper-K.

An intermediate water Cherenkov detector provides a necessary complement to the ND280 magnetized tracking detector in order to constrain all the dominant systematics at the precision required. The WC detector requires a new facility off of the J-PARC site and the excavation of a new pit to house the detector.

II.2. HYPER-KAMIOKANDE DETECTOR

A. Introduction of the Hyper-Kamiokande detector

We discuss three detector configurations in this report: (1) configuration of three cylindrical tanks instrumented with low density (13% photocoverage) PMTs (3TankLD) as shown in Fig. 18, (2) configuration of single cylindrical tank instrumented with high density (40% photocoverage) (1TankHD) as shown in Fig. 19 and (3) configuration of two cylindrical tanks instrumented with high density (40% photocoverage) (2TankHK), for which the second tank will start after the first tank (2TankHK-staged). The 3TankLD configuration, as a reference design with three 60 m depth water tanks, has equal total fiducial mass to the original detector design which consists of two horizontally lying 250 m-long tanks [113]. The estimated total construction cost of 3TankLD is smaller mainly due to the smaller ratio of detector surface area to the detector volume that reduces the number of instrumented PMTs. The vertical cylindrical shape would also make the design, construction, and maintenance of the detector simpler and more mature. 1TankHD is an alternative design with only one tank which also has been studied among Hyper-K proto-collaboration. The smaller dimension in the new design would enable us to optimize the actual location of the caverns according to the local geological condition at the site. Finally, the 2TankHK-staged is the optimized tank and should be considered as proposal reference.

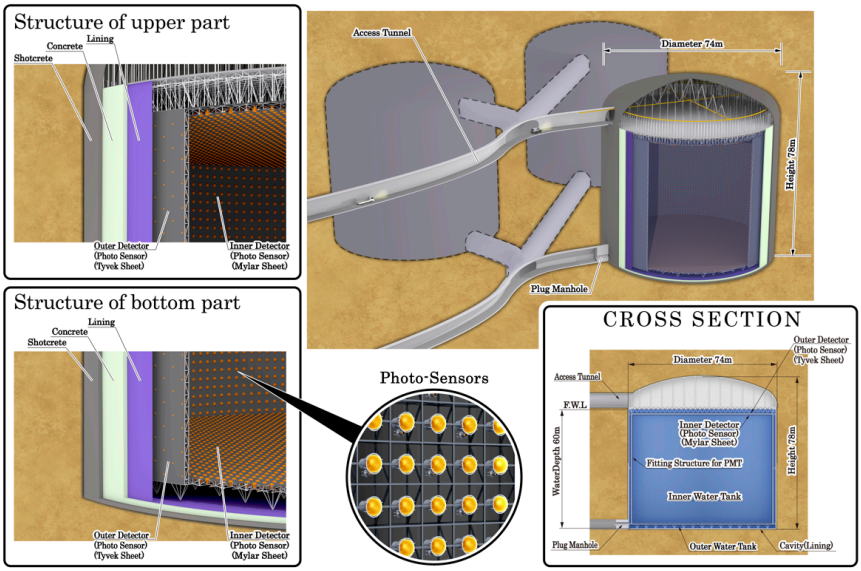

FIG. 18. Schematic view for the configuration of three cylindrical tanks instrumented with low density (13% photocoverage) PMTs. It is referred as 3TankLD in this report.

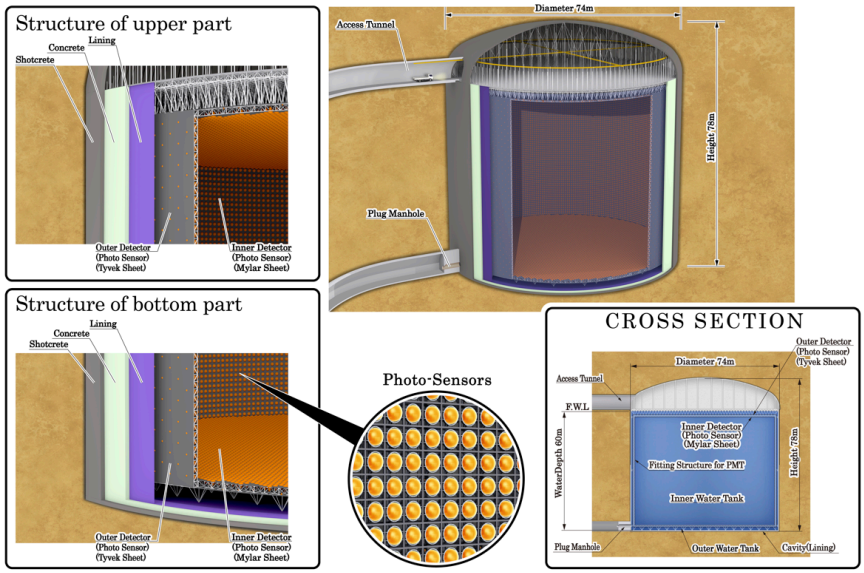

FIG. 19. Schematic view for the configuration of single cylindrical tank instrumented with high density (40% photocoverage) PMTs. It is referred as 1TankHD in this report.

The Hyper-K experiment employs a ring-imaging water Cherenkov detector technique to detect rare interactions of neutrinos and the possible spontaneous decay of protons and bound neutrons. Table IV summarizes the key parameters of the Hyper-K detector compared with other previous and currently operating water Cherenkov detectors. These types of detectors are located deep underground in order to be shielded from cosmic rays and their corresponding daughter particles and thereby to achieve a very low background environment.

The detector mass – or equivalently the underground detector cavern size or water tank size – is one of the key detector parameters that determines the event statistics in neutrino observations and nucleon (proton or bound neutron) decay searches. The detector water plays two roles: a target material for incoming neutrinos and source of nucleons to decay. We need a detector mass of at least $O(10^2)$ kton. in order to accumulate $O(10^3)$ electron neutrino signal events (as shown in Table XXIX) from the J-PARC neutrino beam. This is necessary to measure the CP violation effect with a few % accuracy. This mass of water contains $O(10^{35})$ nucleons (protons and nucleons) which would give an unprecedented sensitivity to nucleon lifetime at the level of 10^{35} years. The location and detailed designs of the Hyper-K cavern and tank are presented in Section II.2 B, II.2 C, and II.2 D.

The detector is filled with highly transparent purified water, as shown in Section II.2 E. A light attenuation length above 100 m can be achieved which allows us to detect a large fraction of the

TABLE IV. Parameters of past (KAM [114, 115]), running (SK [116, 117]), and future (HK-3TankLD and HK-1TankHD) water Cherenkov detectors. The KAM and SK have undergone several configuration changes and parameters for KAM-II and SK-IV are referred in the table. The single-photon detection efficiencies are products of the quantum efficiency at peak ($\sim 400\,$nm), photo-electron collection efficiency, and threshold efficiency. Most right column (HK-1TankHD) shows another design under study which consist of one tank instrumented with high density PMTs.

	KAM	SK	HK-3TankLD	HK-1TankHD
Depth	1,000 m	1,000 m	650 m	650 m
Dimensions of water tank				
diameter	15.6 m ϕ	39 m ϕ	74 m ϕ	74 m ϕ
height	16 m	42 m	60 m	60 m
Total volume	4.5 kton	50 kton	774 kton	258 kton
Fiducial volume	0.68 kton	22.5 kton	560 kton	187 kton
Outer detector thickness	$\sim$ 1.5 m	$\sim$ 2 m	1 $\sim$ 2 m	1 $\sim$ 2 m
Number of PMTs				
inner detector (ID)	948 (50 cm ϕ)	11,129 (50 cm ϕ)	40,000 (50 cm ϕ)	40,000 (50 cm ϕ)
outer detector (OD)	123 (50 cm ϕ)	1,885 (20 cm ϕ)	20,000 (20 cm ϕ)	6,700 (20 cm ϕ)
Photo-sensitive coverage	20%	40%	13%	40%
Single-photon detection efficiency of ID PMT	unknown	12%	24%	24%
Single-photon timing resolution of ID PMT	$\sim$ 4 nsec	2-3 nsec	1 nsec	1 nsec

emitted Cherenkov light around the periphery of the water volume. Radon concentration in the supplied water is kept below $1\,\mathrm{mBq/m^3}$ to control the radioactive background event rate in solar neutrino and other low energy observation. An option being investigated is the Gd-doping of the water. This option, in addition to the nominal water one, is presented in Section II.2 E.

The detector is instrumented with an array of sensors with single-photon sensitivity in order to enable reconstruction of the spatial and timing distributions of the Cherenkov photons which are emitted by secondary particles from neutrino interactions and nucleon decays. The dimension of the photo-sensors and their density are subject to an optimization that takes into account the required signal identification efficiencies, background rejection power, and cost. As a reference, the Super-K detector shown in Table IV covers 40% of the detector wall with Hamamatsu R3600 50 cm diameter hemispherical photomultiplier tubes (PMTs) with the original goal to measure the solar neutrino energy spectrum above $\sim$5 MeV.

The Hyper-K detector is designed to employ newly developed high-efficiency and high-resolution PMTs (Hamamatsu R12860) which would amplify faint signatures such as neutron signatures associated with neutrino interactions, nuclear de-excitation gammas and π^+ in proton decays into Kaons, and so on. This increased sensitivity greatly benefit the major goals of the Hyper-K experiment such as clean proton decay searches via $p \to e^+ + \pi^0$ and $p \to \bar{\nu} + K^+$ decay modes and observation of supernova electron anti-neutrinos. The characteristics of the R12860 tubes are shown in Section II.2 F. The photo-sensors have vacuum glass bulbs and will be located as much as 60 m underwater in the Hyper-K cavern. At this depth, the applied pressure is close to the manufacturers upper specification of the Super-K R3600 PMT (0.65 MPa). Therefore, we need to develop a new bulb design and a quality controlled production method to ensure that the sensors can withstand this pressure. Furthermore, plastic cases will envelop each photo-sensors to avoid a potential chain reaction accident due to the implosion of a glass bulb in the water. The designs of the bulb and case are also described in Section II.2 F.

The detector is instrumented with front-end electronics and a readout network/computer system as shown in Section II.2 G and II.2 H. The system is capable of high-efficient data acquisition for two successive events in which Michel electron events follow muon events with a mean interval of 2 μsec. It is also able to collect the vast amount of neutrinos, which would come from nearby supernova in a nominal time period of 10 sec.

Similar to Super-K, an outer detector (OD) is being envisaged that, in addition to enabling additional physics, would help to constrain the external background. Sparser photo-coverage and smaller PMTs than that for the ID is also planned.

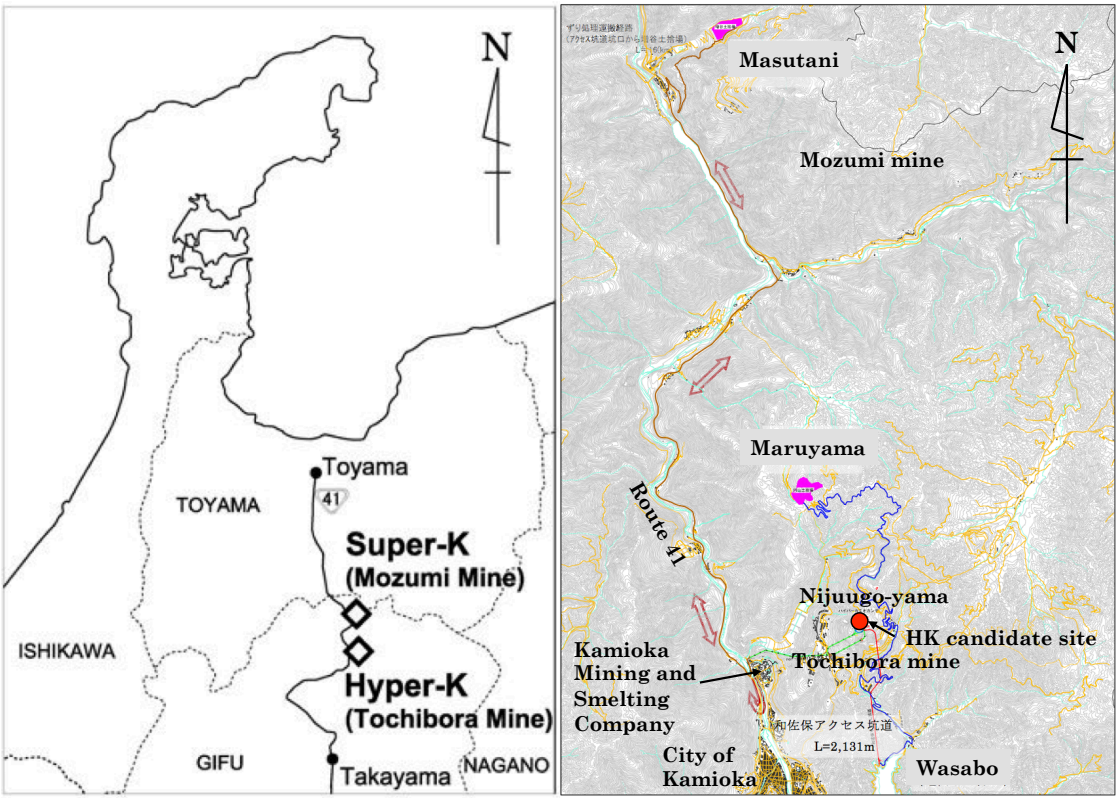

FIG. 20. The candidate site map. Broad area map (left) and detailed map (right).

B. Detector site

1. *Detector location*

The Hyper-K detector candidate site, located 8 km south of Super-K, is in the Tochibora mine of the Kamioka Mining and Smelting Company, near Kamioka town in Gifu Prefecture, Japan, as shown in Fig. 20. The J-PARC neutrino beamline is designed so that the existing Super-Kamiokande detector and the Hyper-K candidate site in Tochibora mine have the same off-axis angle. The experiment site is accessible via a drive-in, ∼2.5 km long, (nominally) horizontal mine tunnel. The detector will lie under the peak of Nijuugo-yama, with an overburden of 650 meters of rock or 1,750 meters-water-equivalent (m.w.e.), at geographic coordinates Lat. 36°21'20.105"N, Long. 137°18'49.137"E (world geographical coordinate system), and an altitude of 514 m above sea level (a.s.l.). The candidate site is surrounded by several faults as shown in Fig. 21 and the caverns and their support structure are placed to avoid a conflict with the known faults. The site has a neighboring mountain, Maru-yama, just 2.3 km away, whose collapsed peak enables us to dispose of more than one million m^3 of waste rock from the detector cavern excavation.

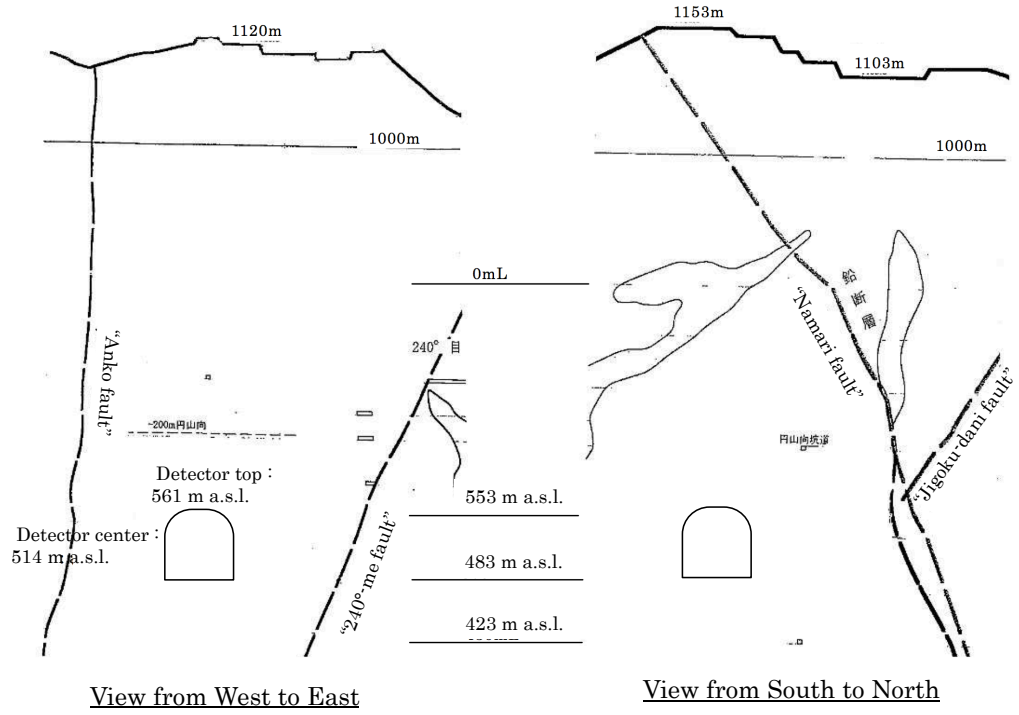

FIG. 21. Location of faults and existing tunnels around the candidate site. The existing tunnels are located at 423, 483, and 553 m a.s.l.

2. Geological condition at the site vicinity

Rock quality is investigated in the existing tunnels and in sampled borehole cores near the candidate site. Fig. 22 summarizes the geological surveys. The rock wall in the existing tunnels and sampled borehole cores are dominated by Hornblende Biotite Gneiss and Migmatite in the state of sound, intact rock mass. This is desirable for constructing such unprecedented large underground cavities. A rock mass classification sytem developed by Central Research Institute of Electric Power Industry (CRIEPI) [118], which is widely used for dams and underground cavities construction for the electric power plants in Japan, is utilized to classify rock quality. The CRIEPI system categorizes rock quality in six groups as A, B, CH, CM, CL, and D (in order of good quality), among which the A, B, and CH classes are suitable for cavern construction. Fraction of rock quality at the measured sites is summarized in Table V. The geological surveys are performed at three different altitudes (423 m, 483 m and 553 m a.s.l.) and better fraction of B and CH classes is observed at higher altitude. The measured fraction of rock quality is used for an assumption of rock quality distribution in cavern stability analyses.

The initial stress of the rock is also measured at three points, two of which are located at the

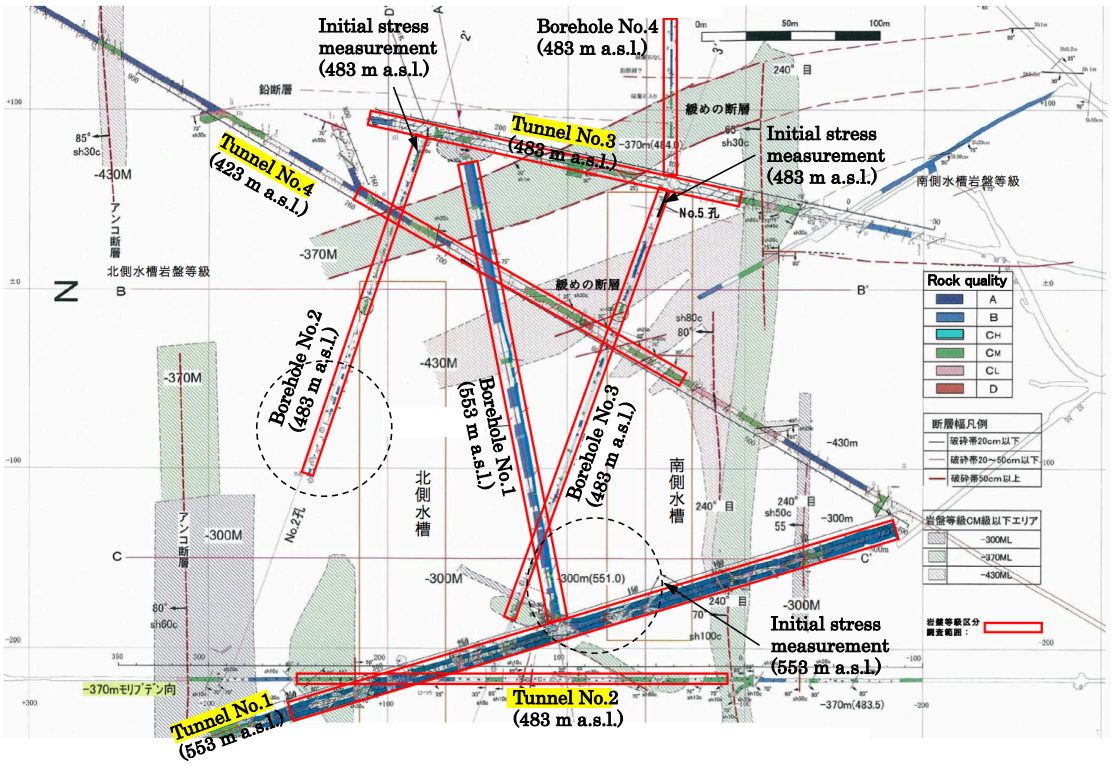

FIG. 22. Location of rock quality measurements in existing tunnels and bore-hole cores at 423 m, 483 m, and 553 m a.s.l. The red rectangulars show the surveyed regions in the measurements. Possible layout of the two caverns is also shown by dashed circles.

bottom of the detector cavern (483 m a.s.l.) and one at top (553 m a.s.l.). The two measurements at 483 m a.s.l. are strongly affected by existing faults and thus the one at 553 m a.s.l. is used for a cavern stability analysis described later. The measured rock stress at 553 m a.s.l. is shown in Fig 23. Based on the *in-situ* measurements of the rock quality and the rock stress, it is confirmed that the Hyper-K caverns can be constructed with the existing excavation techniques (described in latter section).

TABLE V. Summary of measured rock quality fraction. Sum of rock quality fraction in some Bore-holes is not 100% since a small fraction of sampled rock cores was broken during the survey due to a sampling failure.

Place	Rock quality fraction (%)					
	A	B	CH	CM	CL	D
Tunnel No.1	0.0	51.6	43.6	3.0	1.8	0.0
(553 m a.s.l.)	95.2			4.8		
Bore-hole No.1	0.0	67.9	27.7	4.0	0.4	0.0
(553 m a.s.l.)	95.6			4.4		
Tunnel No.2	0.0	11.4	45.4	39.8	3.4	0.0
(483 m a.s.l.)	56.8			43.2		
Tunnel No.3	0.0	4.9	55.7	25.0	14.4	0.0
(483 m a.s.l.)	60.6			39.4		
Bore-hole No.2	2.4	10.5	49.2	29.7	5.7	0.2
(483 m a.s.l.)	62.1			35.6		
Bore-hole No.3	0.0	19.2	59.2	16.5	3.8	0.3
(483 m a.s.l.)	78.4			20.6		
Bore-hole No.4	6.6	20.5	36.4	22.6	7.1	3.1
(483 m a.s.l.)	63.5			32.8		
Tunnel No.4	0.0	18.1	39.0	38.1	1.9	2.9
(423 m a.s.l.)	57.1			42.9		

C. Cavern

1. *Cavern shape*

The Hyper-K detector is composed of two separated caverns, each having a cylindrically shaped barrel region 76 meters in diameter and 62 meters in height with a 16 meter high dome above it. Figure 24 shows the dimension for one cavity. The excavation volume of one cavity is approximately 0.34 Million m^3. It should be noted that the dimension of the excavation volume will be slightly larger than the detector dimension since the water containment system, e.g. a concrete lining, is constructed inside of the excavated cavern surface.

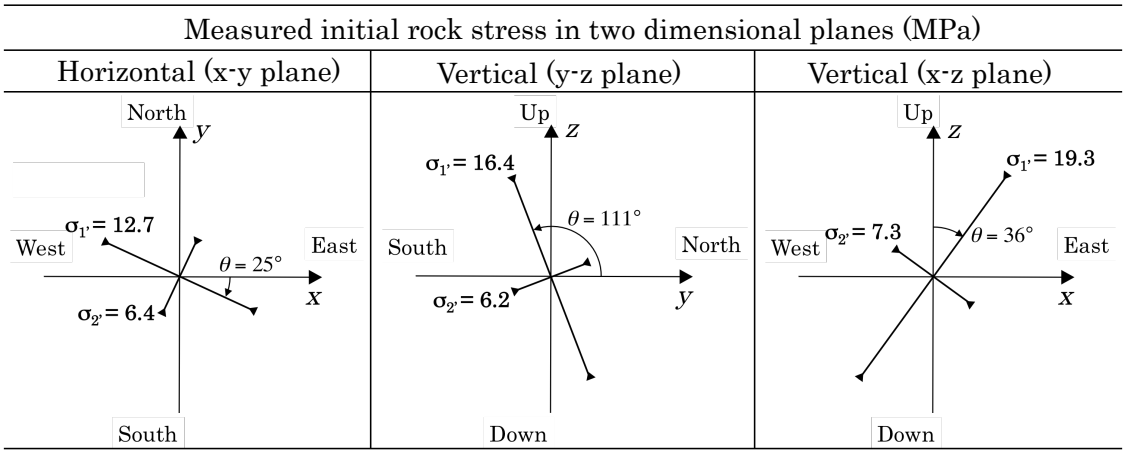

FIG. 23. Results of initial rock stress measurement at 553 m a.s.l.

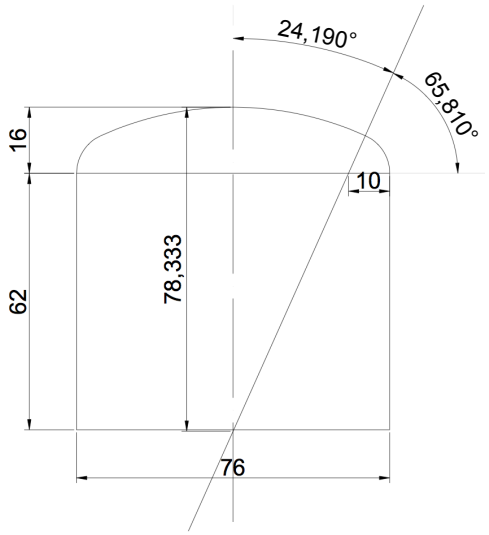

FIG. 24. Cavern shape and dimension. The dimensions in the figure are in meter. The shape of the dome section (top portion of the cavern) is defined with two different curvatures divided in 24.190 degree and 65.810 degree sections denoted in top-right of the figure.

2. Cavern stability and support

The excavated rock wall is supported by rock-bolts, pre-stressed (PS) anchors and shotcrete. A cavern structural stability analysis has been carried out based on the geological condition obtained from the geological surveys. Since the vertical distribution of rock quality has not been examined yet, the vertical profile of rock quality is assumed to have the uniform distribution of the CH-class, which is the major component in the rock quality measurement. The initial rock stress for this analysis is based on the measured stress at 553 m a.s.l. as shown in Fig. 23 and the rock stress

at each depth is corrected by taking into account the depth, overburden. The FLAC3D analysis software, which uses a finete difference method, is adopted to perform a three-dimensional stability analysis. The Hoek-Brown model [119–121] is applied as a dynamic model. The Hoek-Brown model is the method to estimate physical properties of rock by using results obtained from examinations of sampled rock, and is widely used in the world.

Figure 25 shows the plastic region at 45 degree and 105 degree slices in the case of no support (i.e., no rock-bolts, no PS-anchors, and no shotcrete). The plastic region depth is estimated to

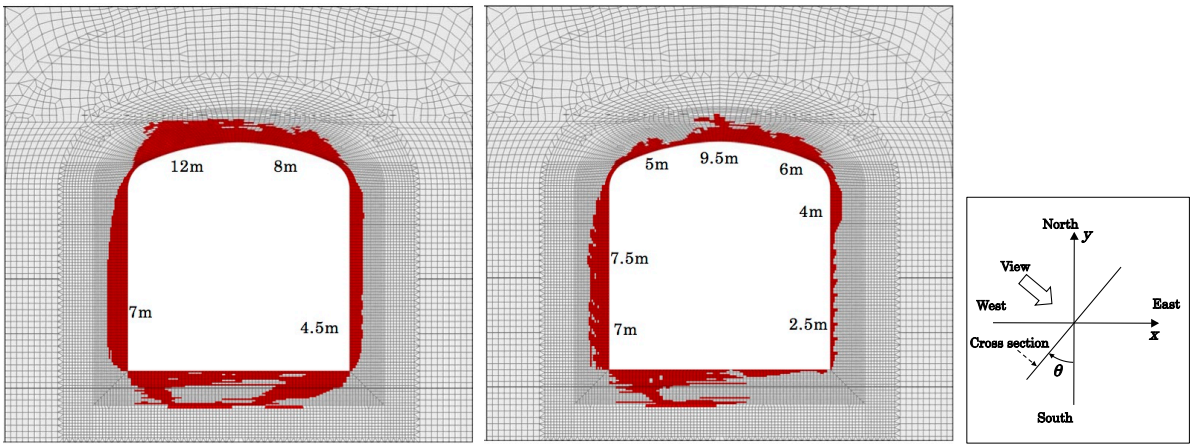

FIG. 25. The plastic region at 45 degree (left) and 105 degree (middle) slices with assumption of uniform CH distribution. The right figure shows definition of the view angle.

be ∼2.5 m to 12 m. The variation of the plastic region depth is due to the geological condition, e.g. initial stress direction. Based on the plastic region obtained, the respective cavern support (PS-anchors) patterns are considered as shown in Fig. 26. The number of PS-anchors and the total length for three caverns are summarized in Table VI. The total length of PS-anchors is estimated

TABLE VI. Summary of total number of PS-anchors and total length for three caverns in case of uniform CH distribution. The number of PS-anchors and total length for one cavern is 1/3 of those in this table.

Section	# of anchors	Total length (m)
Dome	4,611	79,617
Barrel	4,719	71,631
Total	9,330	151,248

to be approximately 151 km.

Another analysis is performed with a different vertical profile of rock quality, as shown in Fig. 27.

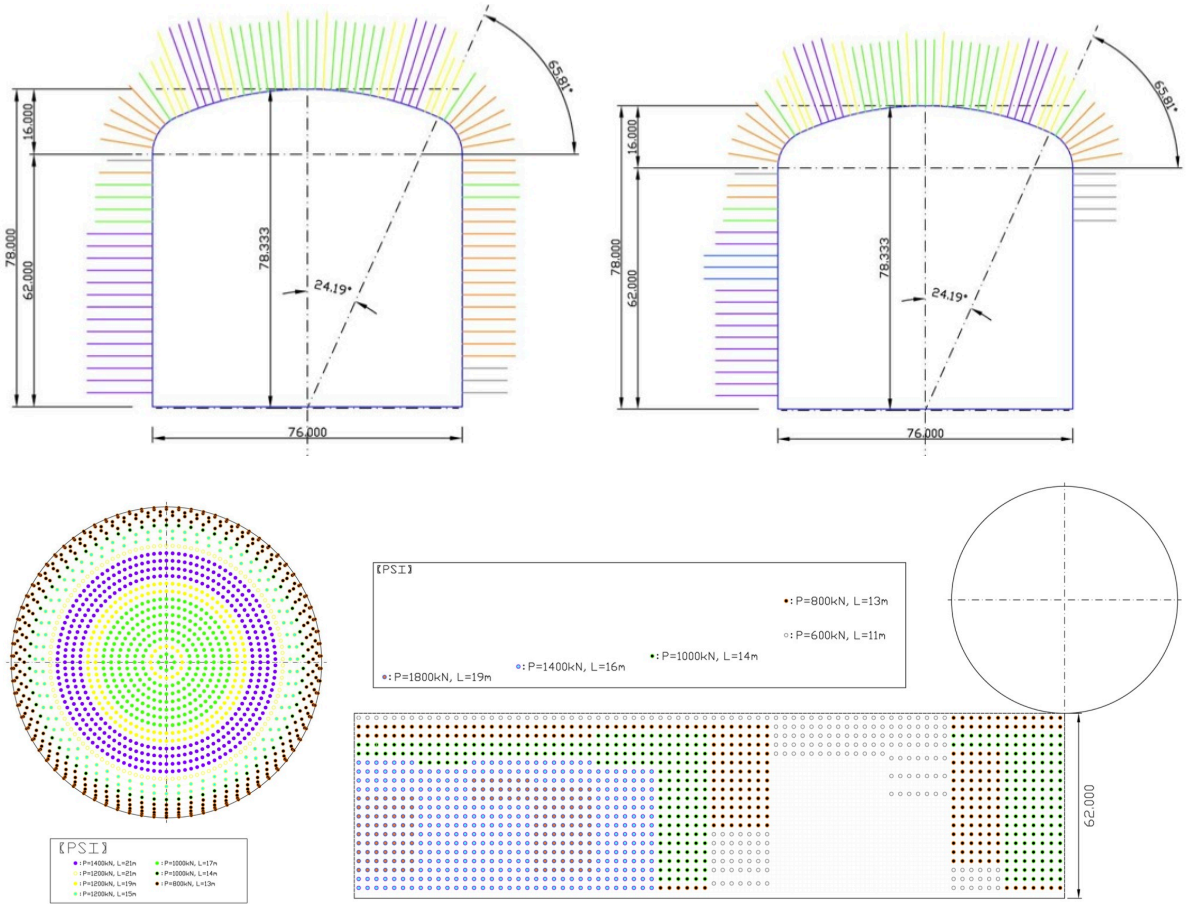

FIG. 26. PS-anchors pattern at 45 degree (top-left) and 105 degree (top-right) slices with uniform CH distribution. Colored lines indicate PS-anchors with different setting of initial force applied to PS-anchors. Bottom figures show developed figures of PS-anchors pattern for dome (bottom-left) and barrel (bottom-right) sections. Initial force and length of PS-anchors are indicated by colored circles.

In Fig. 27, the fraction of rock quality is based on the measurements of rock quality and CM-class is arranged to the dome and bottom sections, which are structurally weaker due to its shape, so as to perform an analysis with a severe condition. Figure 28 shows the plastic region at 45 degree and 105 degree slices with the CH-CM mixed assumption in the case of no support. The plastic region depth is estimated to be ∼10 m to 24 m. In the plastic region at 105 degree, two spikes in the plastic region can be seen at the boundary between CH and CM classes. These sharp spikes are due to the discontinuity of rock quality, which corresponds to a discontinuous change in physical strength, and it is difficult to correctly analyze the plastic region in such a discontinuous condition. PS-anchor pattern is also considered for this case, as shown in Fig. 29. The number of PS-anchors and the total length for three caverns are summarized in Table VII. The total length of PS anchors

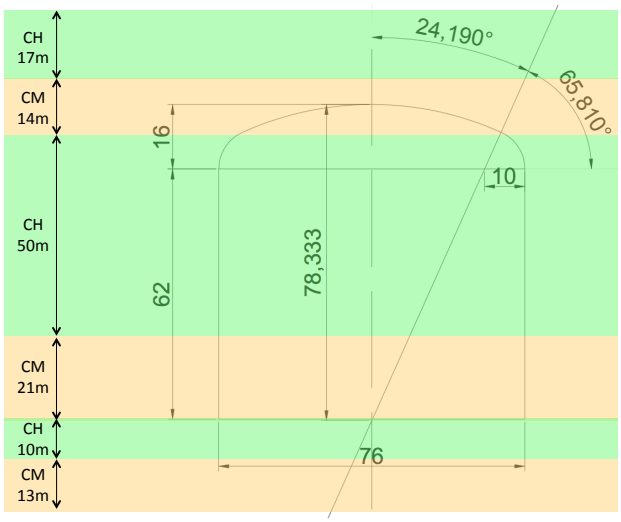

FIG. 27. Assumed rock quality distribution in vertical direction. Rock quality in horizontal plane is assumed to be uniform. Two classes of the rock quality, CH and CM classes, are used for this analysis.

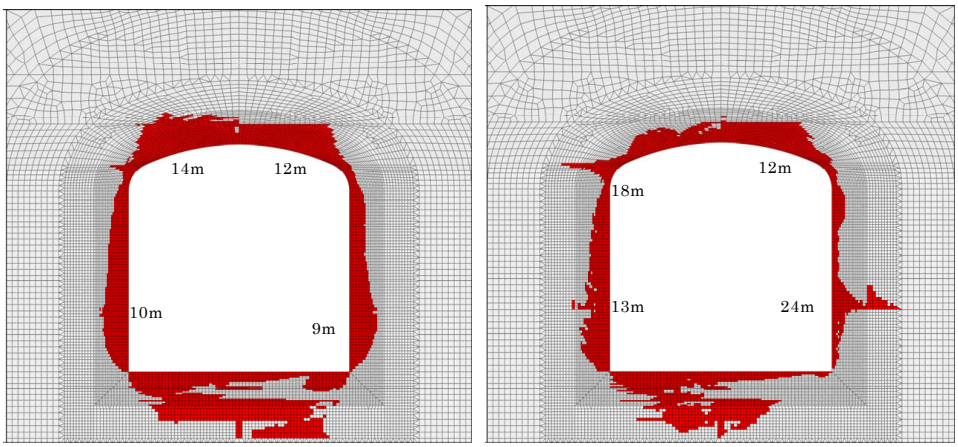

FIG. 28. The plastic region at 45 degree (left) and 105 degree (right) slices with assumption of CH-CM mixed distribution.

TABLE VII. Summary of total number of PS-anchors and total length for three caverns in case of CH-CM mixed distribution. The number of PS-anchors and total length for one cavern is 1/3 of those in this table.

Section	# of anchors	Total length (m)
Dome	5,886	133,437
Barrel	6,060	109,176
Total	11,946	242,613

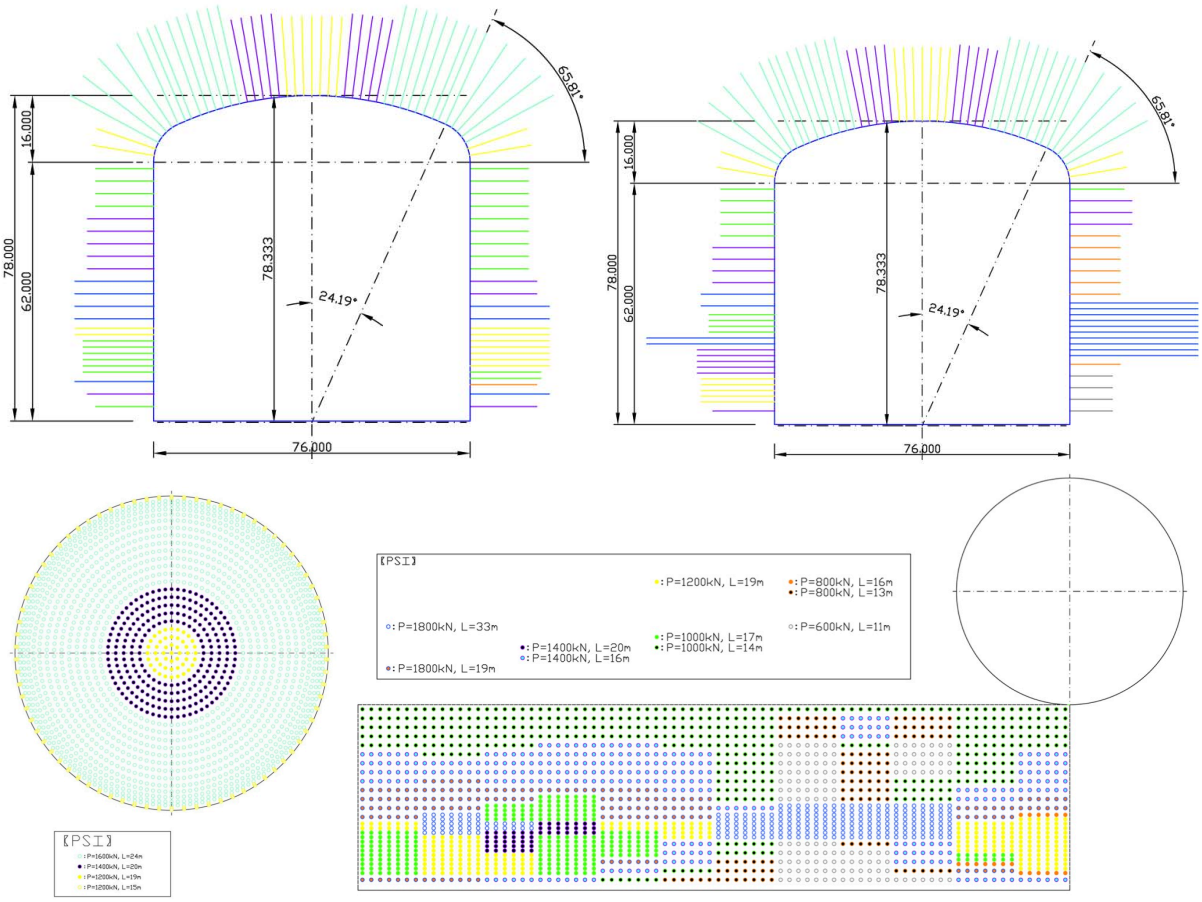

FIG. 29. PS-anchors pattern at 45 degree (top-left) and 105 degree (top-right) slices with assumption of CH-CM mixed distribution. Colored lines indicate PS-anchors with different setting of initial force applied to PS-anchors. Bottom figures show developed figures of PS-anchors pattern for dome (bottom-left) and barrel (bottom-right) sections. Initial force and length of PS-anchors are indicated by colored circles.

is estimated to be approximately 243 km in this assumption. The difference in the total length between two cases can be considered as an uncertainty on the PS-anchors estimation.

While the geological surveys that have been completed already show the feasibility of the required cavern construction, further detailed surveys in the vicinity of the candidate site must be conducted for the final determination of the allocation/layout of caverns and PS-anchors pattern before starting cavern excavation. It should be stressed that structural stability of the detector cavern with the proposed shape can be achieved by using existing cavern construction technologies.

A detailed plan for the additional geological surveys, which need to be done before actual construction begins, has been established. The surveys are divided into three steps: *Step-1* begins with drilling boreholes to sample the rock cores at the existing tunnels at 653 m a.s.l., *Step-2*

is aimed at identifying the geological conditions at the actual cavern locations. This requires additional survey tunnels which can ultimately also be used for final cavern constructions, *Step-3* is the final step of making the detailed cavern design (e.g. PS-anchor pattern) and establishing the actual construction procedure.

3. Cavern construction

The cavern excavation begins with construction of access tunnels and approach tunnels. The tunnels and caverns are excavated with a blasting technique. This section describes the cavern construction method and procedure.

The tunnels leading from the mine entrance into the detector site vicinity are called "access tunnels," and the tunnels leading from the access tunnels into the group of tunnels connected to the caverns are collectively called "approach tunnels." Figure 30 shows overview of the access tunnels. The access tunnel, named as 'Wasabo' access tunnel, is also used to transport the waste

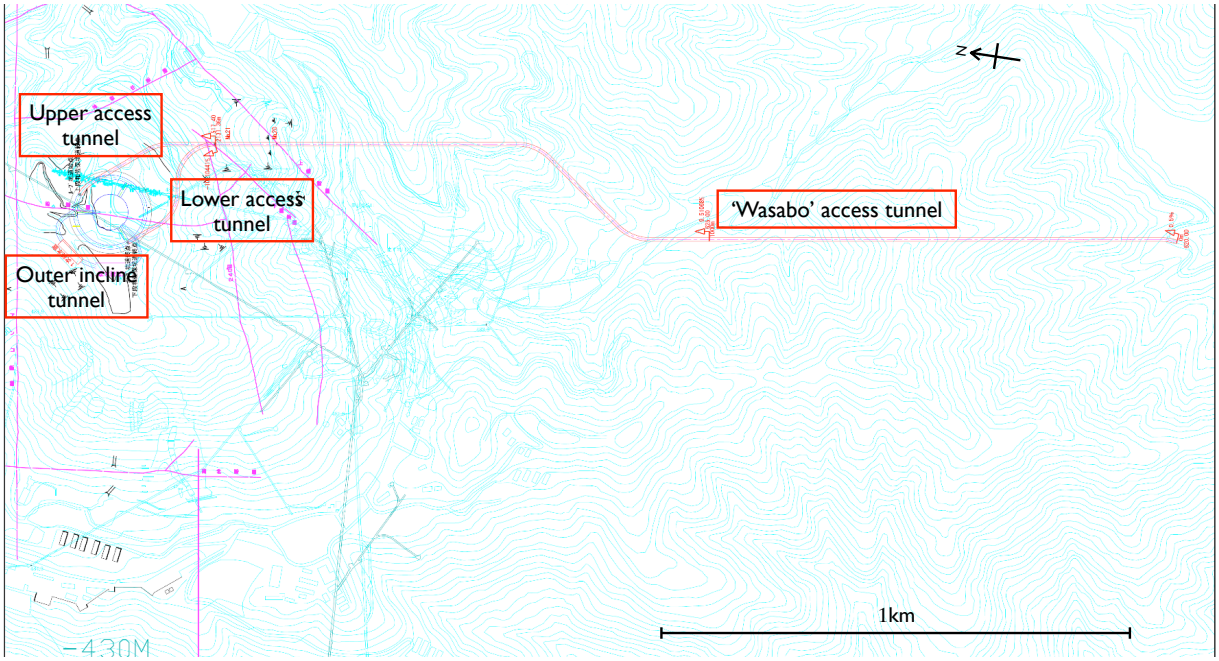

FIG. 30. Overview of the access tunnels. For details of Hyper-K site, one can refer to Fig. 31.

rock to the Wasabo site where waste rock is temporarily accumulated (described in later section).

The caverns are excavated from top to bottom, and there are two general phases in the cavern

construction – excavation of "dome" and "barrel" sections. The dome section is top portion of the cavern, and the barrel section is straight wall section of the cavern (see Fig. 24). The barrel section is further divided into four stages. Each stage has 15.5 m height, and the barrel section is excavated in stage by stage basis. Top and bottom of each stage are connected to approach tunnels, and excavation of each stage proceed from the top approach tunnel to the bottom approach tunnel. Figure 31 and 32 illustrates the layout of the approach tunnels. As shown in the figure, "outer incline tunnel" is helicoidally or spirally arranged around the caverns and the outer incline tunnel works as an interface between access tunnels and approach tunnels. Figure 33 shows schematic of the excavation steps of the cavern construction. The dome section is excavated with thirteen steps (from section "A-1" through section "A-6"). The barrel section is divided into four stages and each stage has three "benches." The excavation of barrel section proceeds from "bench 1-1" through "bench 4-3".

3.1. Waste rock handling and disposal

For the waste rock handling and disposal, three sites are used for different purposes:

- **Wasabo accumulation site**

  Wasabo-site is an intermediate (temporary) waste rock deposition site. All waste rock from cavern excavation is transported and temporary stored at Wasabo-site to sample and analyze heavy metal content in the waste rock.

- **Maruyama cave-in site**

  Maruyama-site is the main waste rock disposal site for waste rock, which do not have heavy metal content. Capacity of the site is more than one Million-m^3. The total distance from Wasabo-site to Maruyama-site is about 14 km.

- **Masutani accumulation site**

  Masutani-site is an additional waste rock disposal site for waste rock which have heavy metal content. Capacity of the site is 0.5 Million m^3 at most. The total distance from Wasabo-site to Masutani-site is about 24 km.

The waste rock from the cavern construction is transported with 25 ton dump-trucks through the Wasabo access tunnel ($\sim$ 2.1 km long) and is temporary deposited at Wasabo accumulation site. At Wasabo-site, the waste rock is sampled and analyzed concerning heavy metal content. The

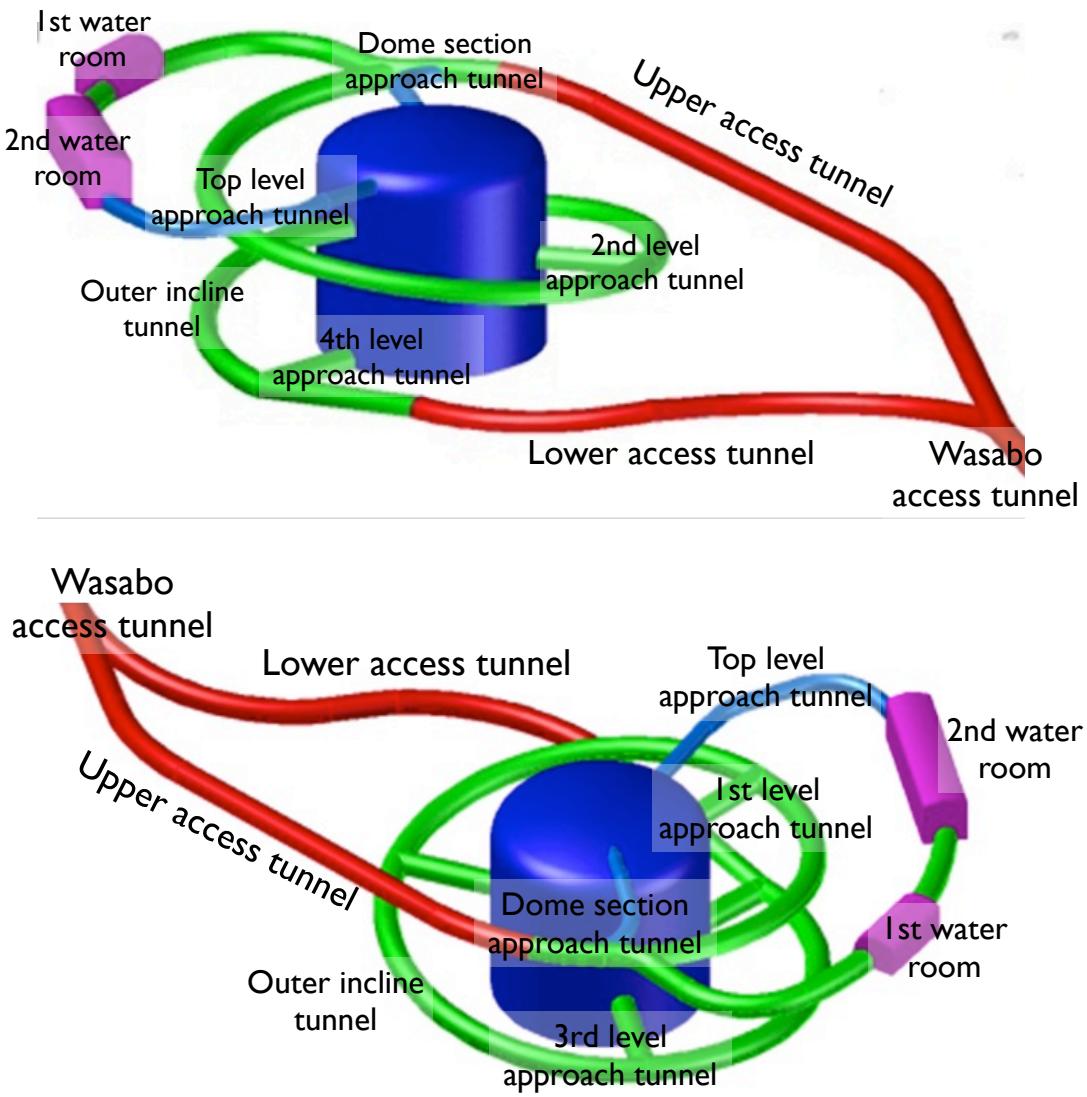

FIG. 31. Layout of approach tunnels (see also Fig. 32). The figure shows the 'water rooms' as well, where the water purification systems are located. The "electronics huts," (a.k.a. counting room) which stores the readout electronics and DAQ computers etc. (not shown in the figure), will be built in the approach tunnel.

rock that is confirmed to have no heavy metal content (below the threshold defined by law and regulations) is transported with 10 ton dump trucks to the final waste rock disposal place, Maruyama cave-in site. The waste rock, which does have some heavy metal components, is transported and treated at the Masutani accumulation site.

Figure 34 shows the route of waste rock transportation from the detector site vicinity to Maruyama-site and Masutani-site. There are the existing roads from Wasabo-site to Maruyama-

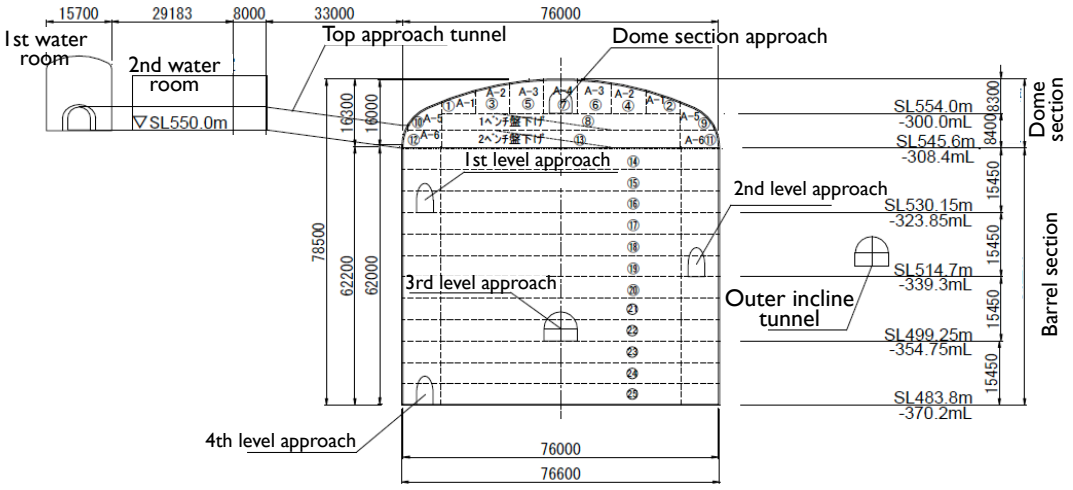

FIG. 32. Layout of approach tunnels.

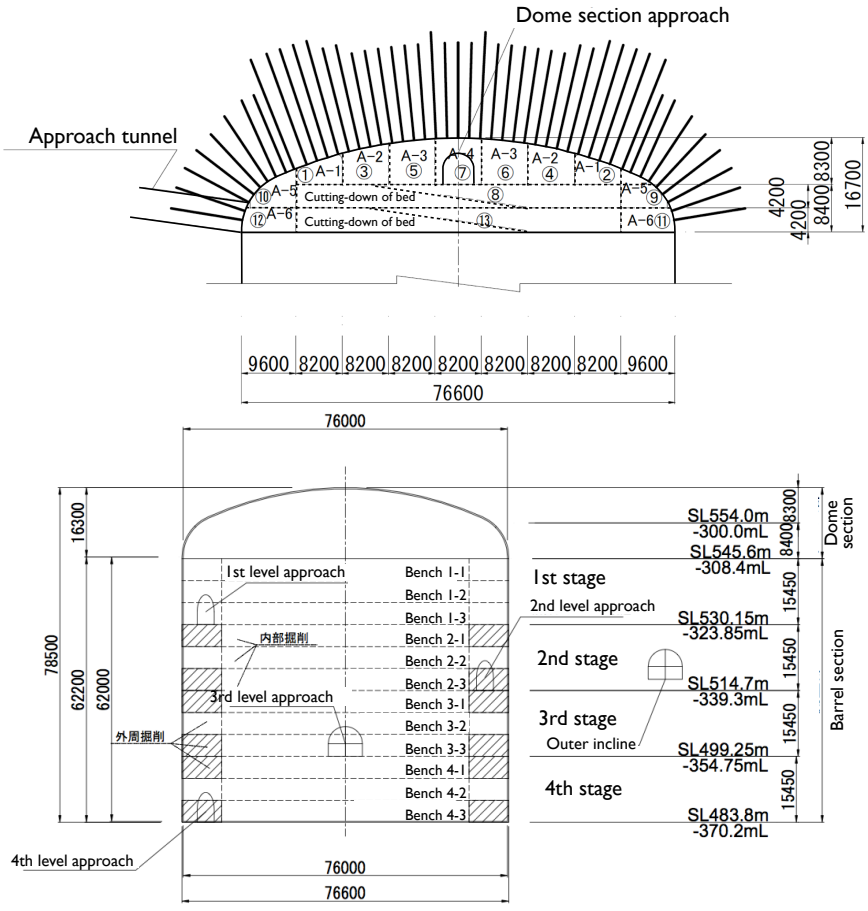

FIG. 33. Illustration of the excavation steps for dome section (upper figure) and barrel section (lower figure).

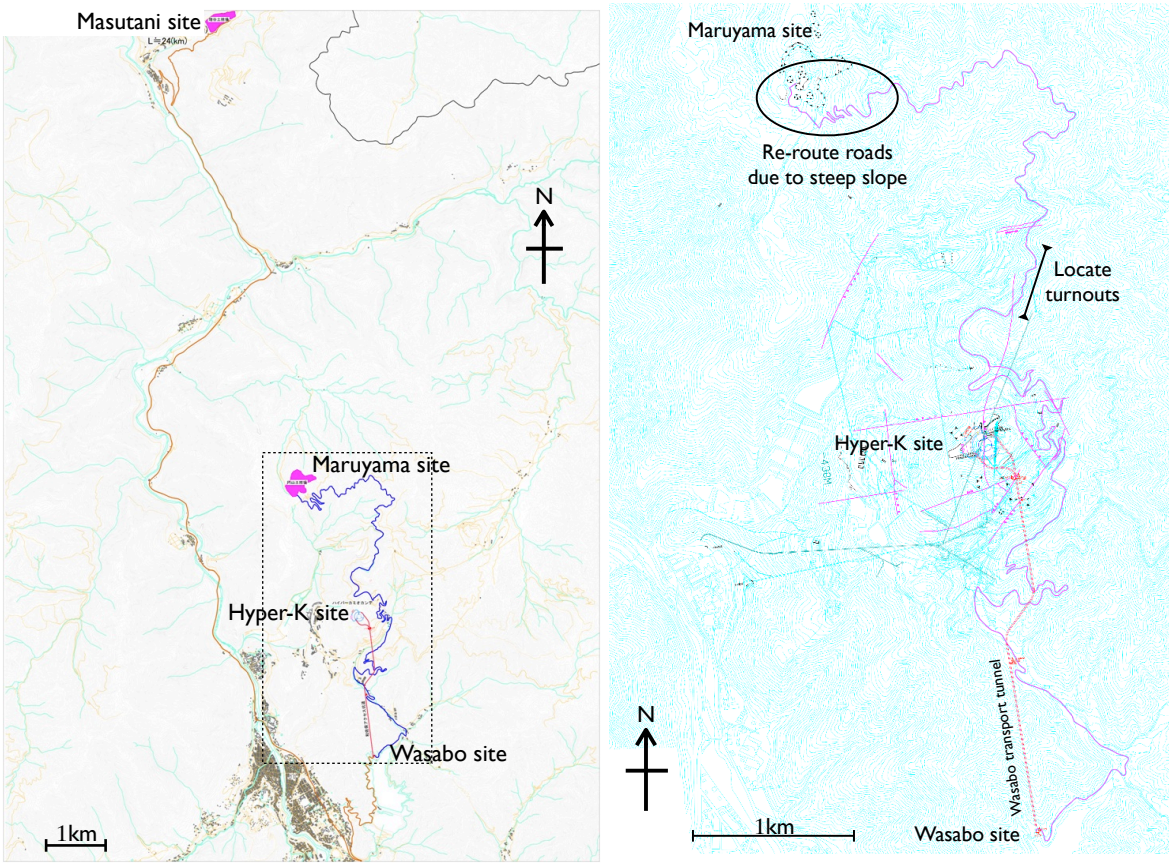

FIG. 34. Left: overview of waste rock transportation routing from Hyper-K site to Maruyama-site and Masutani-site. Orange line indicates the transportation routing from Wasabo-site to Masutani-site, and blue line denotes the transportation routing from Wasabo-site to Maruyama-site. Right: route of waste rock transportation from the Hyper-K detector site vicinity to Maruyama-site. This figure is the enlarged map of the black-dotted rectangular region in the left figure.

site, that can be used for the transportation of waste rock. Some part of the existing roads, however, need to be improved, e.g. widening the roads or allocating turnouts (passing-places), in order to get a large number of dump-trucks pass through. For the waste rock transportation from Wasabo-site to Masutani-site, public roadway is available and no major construction work is required in the path.

3.2. Cavern construction time

The construction sequence has been established by making every effort to minimize the total construction time and construction cost, for example, the approach tunnels construction and cavern

construction run in parallel at different elevations, *etc.*

As described in the previous section, the cavern construction begins with Wasabo access tunnel constructions, and the cavern constructions will follow. The construction of the access tunnels takes ∼23 months, and the cavern excavation takes ∼36 months. The total duration of cavern construction is estimated to be ∼5 years. Figure 35 summarizes an outline of the entire construction processes of one cavern (the first cavern in the two caverns construction in stages).

It should be noted that additional ∼10 months will be required in the cavern construction time if the cavern excavation volume and/or PS-anchor supporting region is near a weak layer, such as a fracture zone, that requires additional construction work. Further detailed surveys in the vicinity of the candidate site is important to minimize such slippage of the cavern construction,

4. Two caverns construction in stages

There are remarks in the two caverns constructions in stages, and they are summarized in this section.

- Waste rock disposal

  It have been confirmed that the waste rock disposal sites have enough capacities to accept all waste rock from the excavation of two caverns.

- Tunnels

  Wasabo access tunnel, which is constructed in the first cavern construction, can be used for the second cavern construction as well. Thus, the cost of access tunnel construction will not be required in the second cavern construction, and the time duration of the access tunnel construction is not needed in the second cavern construction timeline. The approach tunnels, however, need to be newly constructed for the second cavern.

- Distance between cavities

  In the two caverns construction with staging approach, the second cavern excavation runs in parallel with the data taking in the first detector. From the experience at Kamiokande and Super-K, the blasting near the detector does not make any damage in the detector, however the blasting occasionally causes a short-lasting 'PMT flashing' in one or a few PMTs due to vibration from the blasting, which propagates through bedrock. Although the impact of blasting to the physics measurements is limited, since the PMT flashing sinks down within less than a second and the flashing events can be easily identified and eliminated from physics

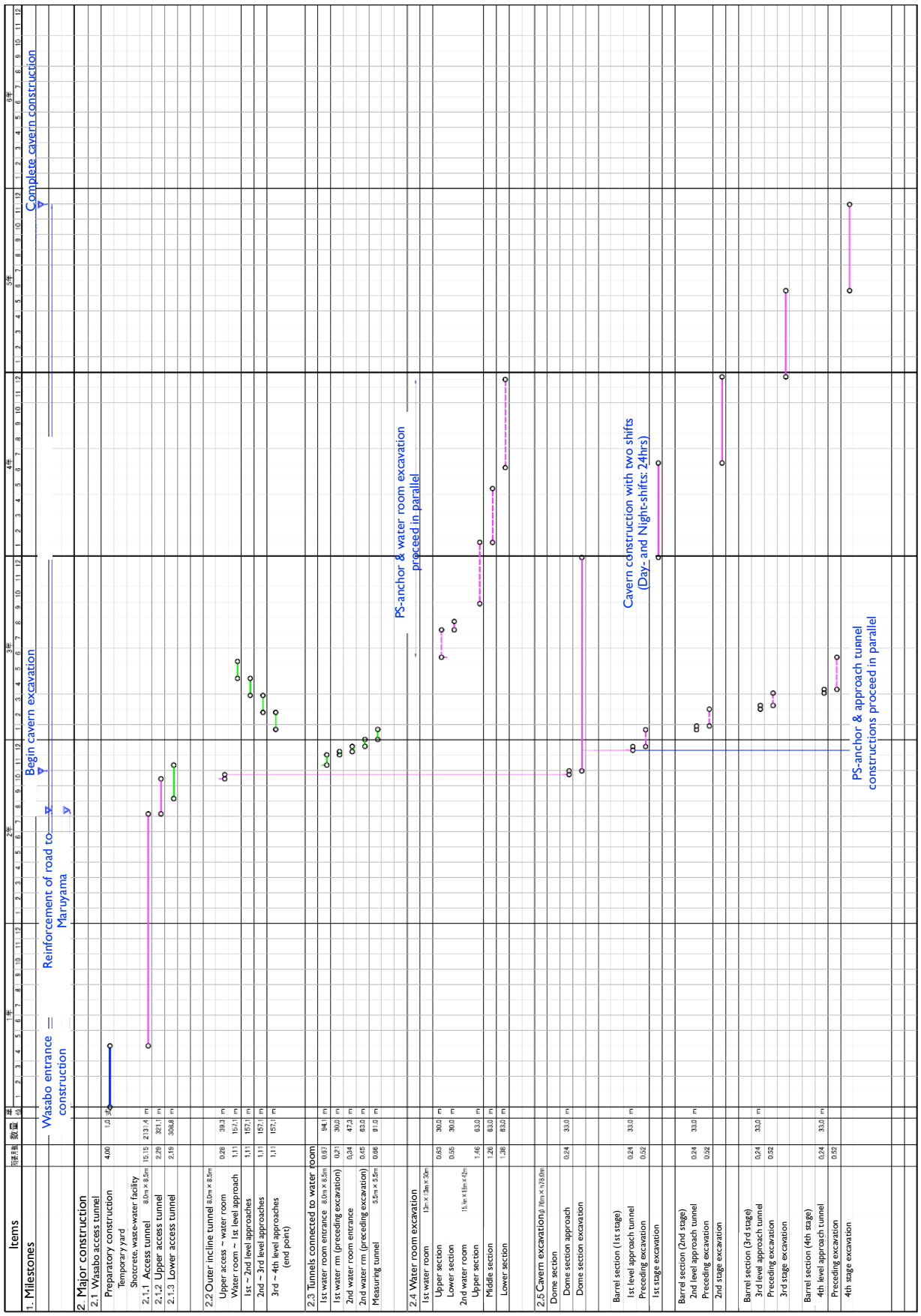

FIG. 35. Outline of the construction processes of one cavern.

data analyses, the second cavern construction requires to have a certain distance from the first detector in order to minimize undesirable influence in physics measurements at the detector[1].

From the experience at Super-K during the blasting for new cavity constructions, e.g. EGADS and new water room for SK-Gd, the distance from second cavern to the first detector needs to be $\sim$200 m at least.

[1] In the cavern construction point of view, regardless the physics data taking, the distance between two caverns must be equal or more than 100 m, which has been estimated based on the cavern stability analyses.

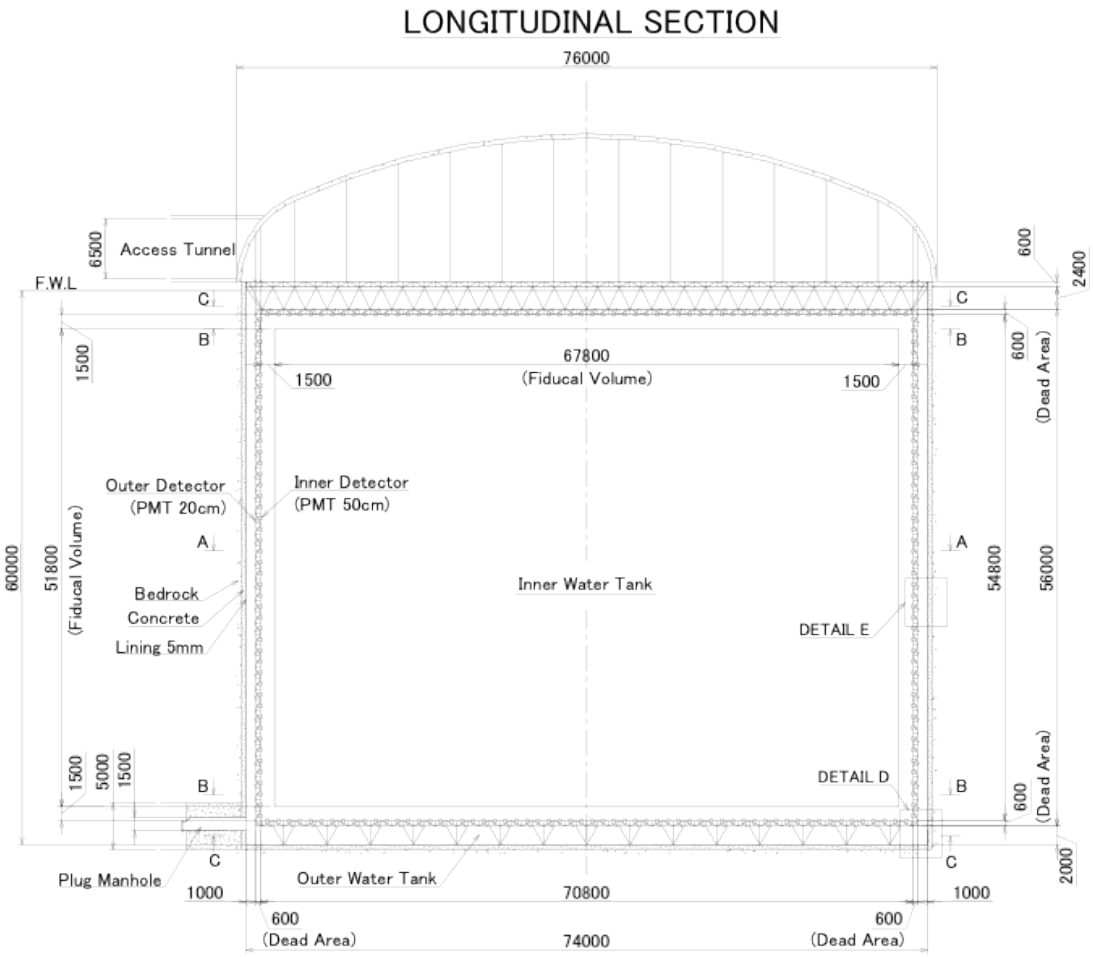

FIG. 36. Schematic view of the Hyper-K water tank.

D. Water Tank

Figure 36 shows a schematic view of the Hyper-K water tank. The excavated cavities for Hyper-K are lined with a watertight liner to contain ultra-pure detector water. The liner surface bounding the detector water is made of waterproof polyethylene sheets, which are stuck on the backside concrete layer. Dimensions of the cylindrical water volume is 74.0 m in diameter and 60.0 m in height, so the total water mass after the two Hyper-K tanks are built is $0.258 \times 2 = 0.516$ million metric tons. The water volume in each of the two tanks contains two photo-sensitive segments optically separated by a 60 cm thick insensitive region.

The inner segment called the Inner Detector (ID) has a cylindrical shape of 70.8 m in diameter and 54.8 m in height. This main active volume for physics measurements is viewed by an array of inward-facing $\sim 40,000$ 50 cm ϕ photosensors per tank. The photocathode coverage in the ID wall

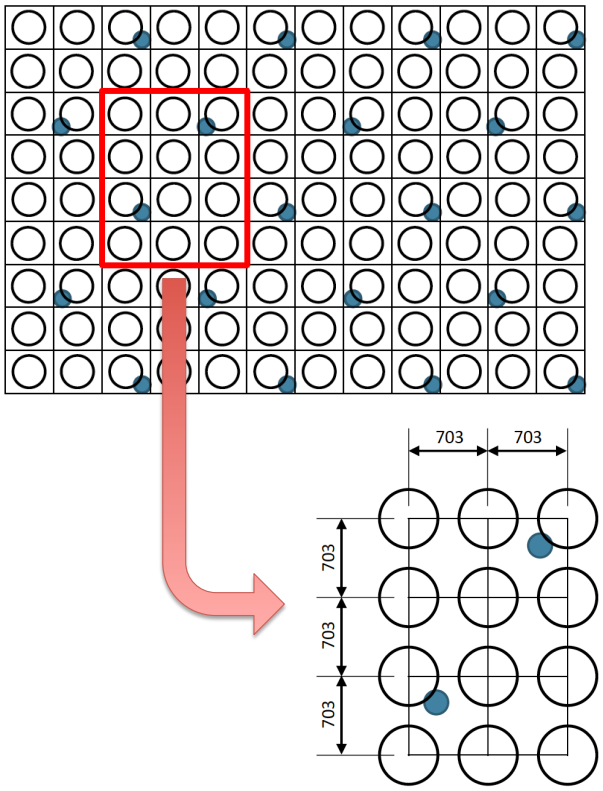

FIG. 37. Arrangement of ID and OD photosensors. The ID photosensors (open circles) are facing inward, and the OD photosensors (blue circles) are facing outward. See also Figure 38.

is 40%, equivalent to that of SK-IV. Since the new 50 cm ϕ PMTs (Hamamatsu R12860) developed for Hyper-K have about twice higher single photon detection efficiency than that of the Super-K PMTs (Hamamatsu R3600), the overall photon detection efficiency in the ID is almost double that of SK-IV. A standard fiducial volume in each tank, defined as the region inside a surface drawn 1.5 m from the ID wall, is 0.187 million tons, The Hyper-K total fiducial volume, $0.187 \times 2 = 0.374$ million tons, is about 17 times the fiducial volume of Super-K.

The outer segment monitored by outward-facing $\sim 6,700$ 20 cm ϕ photosensors per tank is called the Outer Detector (OD), which acts mainly as a veto for entering particles such as cosmic ray muons. Another important task of the OD is to determine whether a particular event occuring within the ID is fully contained in the ID or not. The OD water thickness is 1 m in the barrel region and 2 m in the top and bottom regions. The number density of the OD photosensors is about (1 photosensor)/(3 m^2), one sixth of that of the ID photosensors, making the photocathode coverage of about 1%.

The photosensors for the ID and OD are mounted on stainless steel supporting framework. The

arrangement of ID and OD photosensors is shown in Figure 37. The grid size of the ID photosensor array is about 70 cm, while the grid size of the OD photosensor array is roughly 2 m. The space between the ID photosensors is lined with opaque black sheets to prevent light leaks, while the gaps between the OD photosensors are lined with reflective sheets to enhance light collection in the OD. The stainless steel framework and the photosensor cables are located in the 60 cm thick insensitive region between the ID and the OD.

Every component of the Hyper-K tank, such as the waterproof tank liner and the photosensor supporting framework, was designed so that the tank can be built with a construction cost as low as possible, while fulfilling the requirements from the Hyper-K physics programs. The design of each component and the tank construction procedure will be described later in this section.

1. Tank-Cavern Interface

After the cavity is excavated, shotcrete is sprayed onto the bedrock surface. The tank liner, made of waterproof polyethylene sheets lying on a backfill concrete layer, is constructed inside of the shotcrete surface. The backfill concrete layer is reinforced by steel rods to ensure the integrity of the water tank. In between the shotcrete layer and the backfill concrete liner, waterproof sheets are placed to prevent both the leakage of the detector water to the outside and the penetration of external sump water into the tank.

The boundary between the cavern excavation and the water tank construction is shown in Figure 38. As illustrated in the figure, the shotcrete spraying process is included in the cavern excavation work, while the liner installation, including the middle waterproof sheet layer, is included in the tank construction.

2. Tank Liner

The lining covers inner surface of the Hyper-Kamiokande tank. It is to contain ultra purified water (UPW) or gadolinium sulfate ($Gd_2(SO_4)_3$) water solution inside of the tank ideally without any leakage and without any dissolution of impurities into the medium. Durability should be ∼30 years. The lining structure is to be constructed inside of the cavern bedrock coated with shotcrete. Between the shotcrete and the lining, a backfill concrete is to be employed. As a former example, a 4 mm-thick stainless steel membrane, backfilled with a reinforced concrete, was adopted as the lining material for the Super-Kamiokande tank [116]. In designing a similar lining structure for

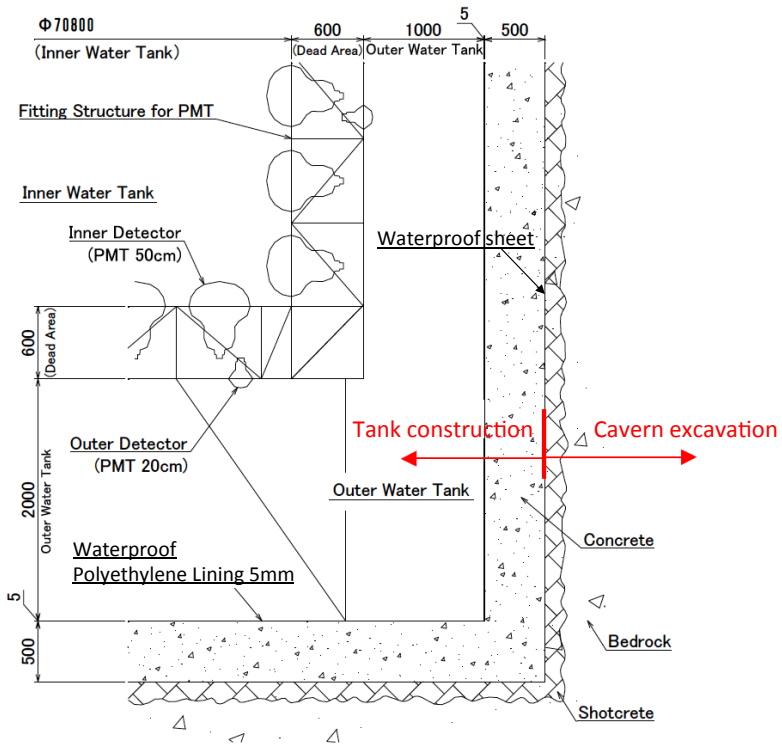

FIG. 38. Boundary between the cavern excavation work and the water tank construction work.

Hyper-K, we assume the following conditions:

- Physical properties of the bedrock surrounding the tank are the same as those used for the Super-Kamiokande designing. For example, elastic modulus of the bedrock is 51 (20) GPa for non-damaged (damaged) region, respectively.
- Physical properties of the backfill concrete are taken from *Standard Specification for Concrete Structure*[122].
- The surrounding bedrock will not be displaced during/after tank construction.
- The backwater is controlled so that there is no water pressure on the lining structure from the bedrock side. To satisfy this critical condition, location of the entire detector cavern(s) is to be chosen at the -370 mL above the main water drainage level of the candidate mine site (-430 mL).

2.1. Liner sheet characteristics As a lining material for the gigantic Hyper-K, firm adhesion to the backfill concrete wall and enough elongation to follow possible deficits and cracks of the

concrete wall are both desirable characteristics. To fulfill these functionalities, concrete embedment liner, or the Concrete Protective Liner (CPL), made of High Density PolyEthylene (HDPE), has been chosen as the baseline candidate lining material. Figure 39 shows schematic views of the candidate CPL (Studliner, GSE Environmental). It has a 2.0∼5.0 mm thick section of HDPE with a number of studs protruding from one side, that lock the liner into the surface of concrete to prolong the service life of concrete structures.

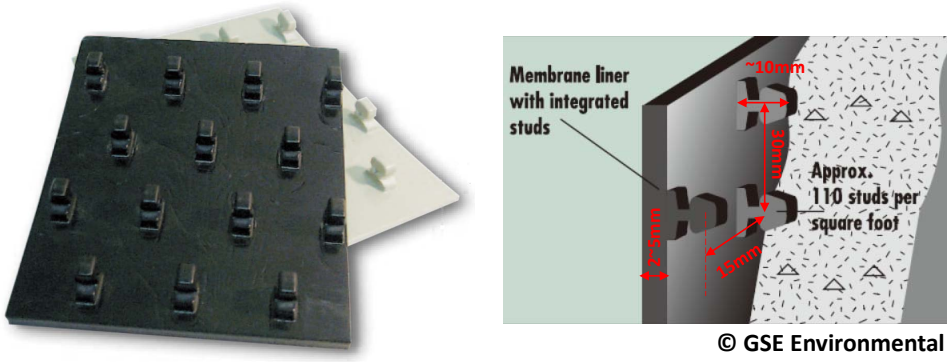

FIG. 39. Concrete Protective Liner made of High Density PolyEthylene, considered as the baseline tank lining material of Hyper-Kamiokande (Studliner, GSE Environmental).

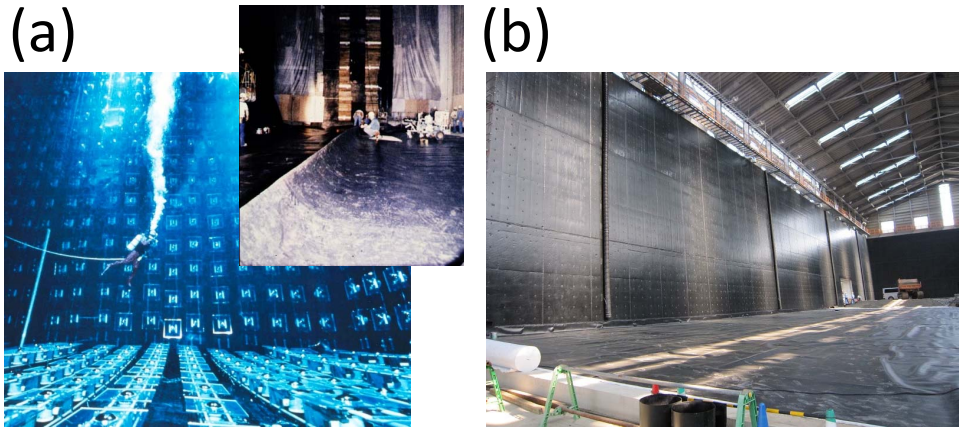

FIG. 40. Former examples of the HDPE lining. (a) IMB detector's 8 kt water tank lined with HDPE geomembrane sheets (product of Schlegel Lining Technology, a precursor of GSE Environmental). (b) The CPL (GSE Studliner) applied to water-sealing walls of a large industrial waste processing trench.

HDPE is a thermoplastic resin, a linear polymer prepared from ethylene (C_2H_4) by a catalytic process. The absence of branching results in a more closely packed structure with a higher

density (greater than 0.94), and somewhat higher chemical resistance than Low Density Polyethylene (LDPE). HDPE is also harder and more opaque, and it can withstand higher temperatures (120° Celsius for short periods, 110° Celsius continuously). Advantages of HDPE as the lining material are: impact/wear resistance, flexibility (very high elongation before breaking), good chemical resistance, very low water permeability, good plasticity (particularly well to blow molding), and low price. On the contrary, disadvantages of HDPE are: it may have voids, bubbles or sink in the thick sections, poor dimensional accuracy, and low mechanical and thermal properties.

A former example to apply HDPE liner to large water tank can be found in the IMB detector[123] as shown in Fig.40(a). The 8 kt water tank ($22.5\times17\times18\,\mathrm{m}^3$) utilized 2.5 mm -thick double layered non-reflective black HDPE liners, separated by a plastic drainage grid allowing water to flow between the liners. They were produced and installed by Schlegel Lining Technology, one of the precursors of GSE Environmental. Figure 40(b) shows an application of the CPL as the water-sealing walls of a large industrial waste processing trench. Table VIII shows material parameters of the candidate CPL, GSE Studliner. It is also to be noted that the LBNE far-site Water Cherenkov Detector (WCD) with 200 kt volume adopts the water containment system option with use of 1.5∼2.5 mm-thick Linear Low-Density PolyEthylene (LLDPE) geomembrane.[124]

TABLE VIII. Material parameters, taken from specification of the candidate CPL (Studliner, GSE Environmental).

Material property		Nominal Value
Thickess	(mm)	5.00
Density	($\mathrm{g/cm^3}$)	0.94
Yield strength	(MPa)	15.2
Elongation at break	(%)	500
Carbon black content	(%)	2−3
Pigment content	(%)	1.5−2.5
Notched constant tensile load	(hours)	400
Thermal Expansion Coefficient	(C°)	1.20E-04
Low temperature brittleness	(C°)	-77
Dimensional stability in each direction	(%)	±1.0
Water vapor transmission	($\mathrm{g/m^2/day}$)	< 0.01
Typical roll dimension	(m)	2.44(W)×59.73(L)

The planned procedures of the CPL installation into cavern are illustrated in Fig.41: At first CPL is fastened to the inside of molds before concrete is poured to create a surface lined with

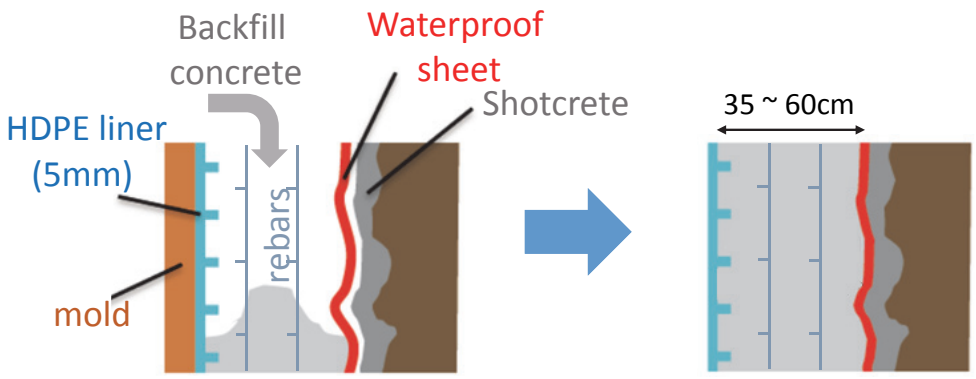

FIG. 41. Schematics of the planned procedures for CPL installation into the cavern with shotcrete surface.

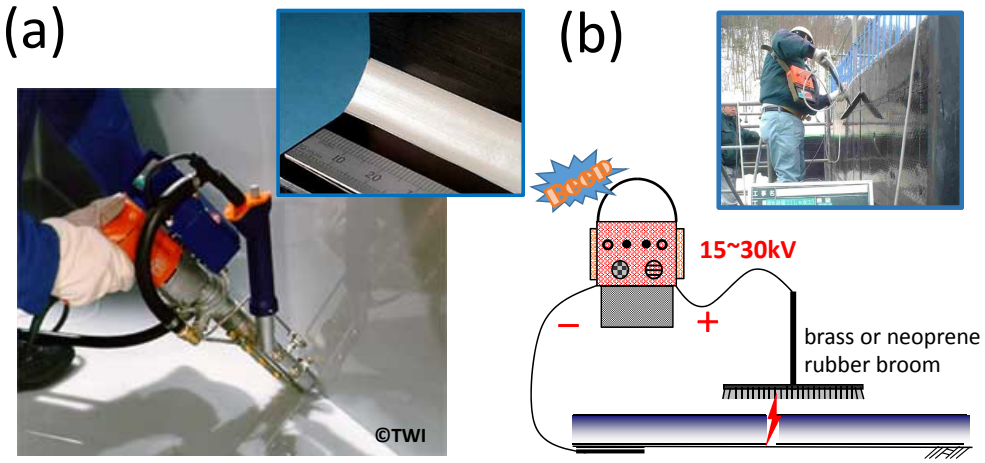

FIG. 42. (a) The extrusion welding and a welded seam. (b) The high-voltage pin-hole test.

HDPE. The backfill concrete flows around the studs anchoring CPL firmly in place, and fastens it securely to the surface of the concrete. The waterproof sheet between bedrock-covering shotcrete and backfill concrete aims conveyance of water, coming from tiny leakage of water through the CPL and backfill concrete structure, if any, and/or penetrating underground backwater from bedrock.

The adjacent CPLs are welded by the extrusion welding of thermoplastics, which is used typically for assembly of large fabrications (such as chemical storage vessels and tanks) with wall thicknesses up to 50 mm. Figure 42(a) shows an extrusion welding work and close-up to the welded seam. In this method, molten thermoplastic filler material is fed into the joint preparation from the barrel of a mini hand-held extruder based on an electric drill. For the CPL welding the same HDPE is used as the filler material. The molten material emerges from a PTFE shoe shaped to match the

profile being welded. At the leading edge of the shoe a stream of hot gas is used to pre-heat the substrate prior to the molten material being deposited, ensuring sufficient heat is available to form a weld.

For the quality control of the lining, the holes in the CPL sheets with size of >0.5 mm, including those on the welded seams, can be identified by a high-voltage pin-hole testing method [125], as illustrated in Fig. 42(b): It utilizes a charged metal or neoprene-rubber broom above the liner. The power source is grounded to the conductive deck and creates a high potential difference (∼30 kV at maximum) with tiny current. When the metallic broom head is swept over a breach or a hole in the insulating membrane surface, current is detected by the test unit which turns off the power to the broom and emits a beep sound to alert the test operator. The area is then carefully swept again at ∼90 degrees to the original sweeping direction to pinpoint the exact location of the breach/hole. This process is continued until all areas of the CPL have been tested. Occasionally negative pressure tests with a vacuum box can be applied on the possible breaches and the welded seams. The leakage water through the holes less than 0.5 mm diameter, if any, can be collected and controlled by a leakage detection and drain system, as described later.

2.2. Liner sheet tests Various material tests were carried out for the candidate CPL, as are described in Appendix B. To see the change of light absorbance and elusion of impurities, specimens of the lining sheet were soaked both into ultra-purified water and into 1% gadolinium sulfate solution: increase of the light absorbance were observed at the wavelength lower than 300 nm, and certain amount of material elution, i.e. total organic carbon, anions and metals, were observed. The relation between material elusion and change of light absorbance should be studied carefully. Meanwhile, since PMT is sensitive for higher wavelength, the effect to the experiment can be limited.

Measurements on material strength, i.e. tension test and creep test, were performed: the candidate CPL sheet has basically enough strength. If cracks or rough holes happen in the backfill concrete, the liner should locally stand for water pressure. To simulate the situation, tests to apply localized water pressure on the lining were performed with variety of slits and holes: For all cases, the liner survived without breaking.

The water leak can happen around components which penetrate the water tank lining, such as anchors and water pipes. A possible design of the penetration structure was developed. Its prototype was exposed to series of pressure tests, which showed no leaks.

2.3. Leakage detection and drain system The water leakage, if it happens, will be not through the sheets themselves, but through small holes, which are undetectable by the pin-hole/vacuum

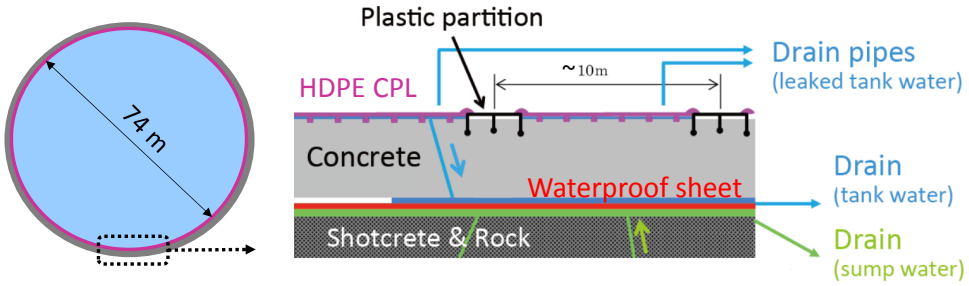

FIG. 43. Conceptual diagram of water leak detection/drain system.

tests, or breaches, which are caused unavoidably by works after the tests. To be prepared for these possible failures, a leak detection/drainage system is to be developed. Figure 43 shows preliminary concept of the system. HDPE plastic moldings are embedded together with the CPL in the backfill concrete, to work as partition at a pitch of about 10 m in the direction of circumference of the tank. Water leaks from the CPL(s) or seam(s) in each partition are to be collected individually, so that leak detector installed at the bottom can identify the partition with the problem. Occasionally, water leak through the CPL can flow into bedrock side through cracks of the backfill concrete. Water-proof sheets (high panel signal sheet), installed between bedrock and backfill concrete, can separate leakage of inside (tank) water and sump water coming from outside bedrock. These water will be drained separately, and tank water will be treated with care especially for the case with gadolinium sulfate solution is used in the tank.

3. Photosensor Support Framework

The structural framework on which ID and OD photosensors are mounted is basically made of commercially available SUS304 shaped steels, like Super-K. The stainless steel framework has been designed to support the weight loads listed in Table IX.

The PMT supporting framework in the tank bottom part is constructed on the floor, independently from the top/barrel frameworks. The supporting frameworks in the top and barrel parts are truss structures hung from the ceiling, unlike the Super-K's framework whose barrel part is freestanding on the ground, while the top roof is supported at the edge contacting the side concrete wall. A suspension structure can usually be built with relatively thinner and lighter steel members, resulting in a lower construction cost, while a freestanding structure usually needs thicker and heavier framework members to avoid a buckling. Figure 44 shows part of the top and barrel

TABLE IX. List of the major weight loads taken into account for designing the supporting framework.

ID photosensor	(/ PMT)
50 cm ϕ PMT	13 kg
Protective cover	39 kg
Cable (for readout/power supply, 10 m)	2 kg
OD photosensor	(/ PMT)
20 cm ϕ PMT	2 kg
Protective cover	8 kg
Wavelength shifting plate	5 kg
Cable (for readout/power supply, 10 m)	2 kg
Underwater electronics (for readout/power supply)	47 kg / unit
Network cables connecting adjacent underwater electronics units	2 kg/ unit
Water system pipes (65A PVC)	1.4 kg/m
Calibration system (w/ 200A SUS pipe holes)	1000 kg/m^2 $\times$ 4
	100 kg/m^2 $\times$ 16
Other distributed load on the roof	100 kg/m^2

frameworks along with their suspension parts. The weight load at each suspension point is about 110 kN for the top structure including the photosensors and other instruments on the top deck and about 70 kN for the barrel structure including the photosensors etc. The anchor bolts for the suspension points are embedded in the ceiling rock during the excavation of the dome part of the cavern.

The top floor of the tank on which people can walk is made of the stainless steel plates placed on the truss framework. On this top deck, the following penetrating components are built; the "calibration holes" through which various instruments for the detector calibration are inserted into the water tank, the "water pipes" for the tank water supply/drain, and the "cable holes" for the photosensor/electronics cables. As described in Section II.2 G, unlike the Super-K detector in which all the PMT cables are directly connected to the readout electronics placed on the top deck, the photosensor cables in Hyper-K are connected to nearby electronics submerged to the water tank. The underwater electronics modules are connected to each other and only the top modules are connected to the readout computers, thus the size of the cable holes can be reasonably small. The top deck will be designed to also allow the penetration of the pipes to hang the barrel supporting structure.

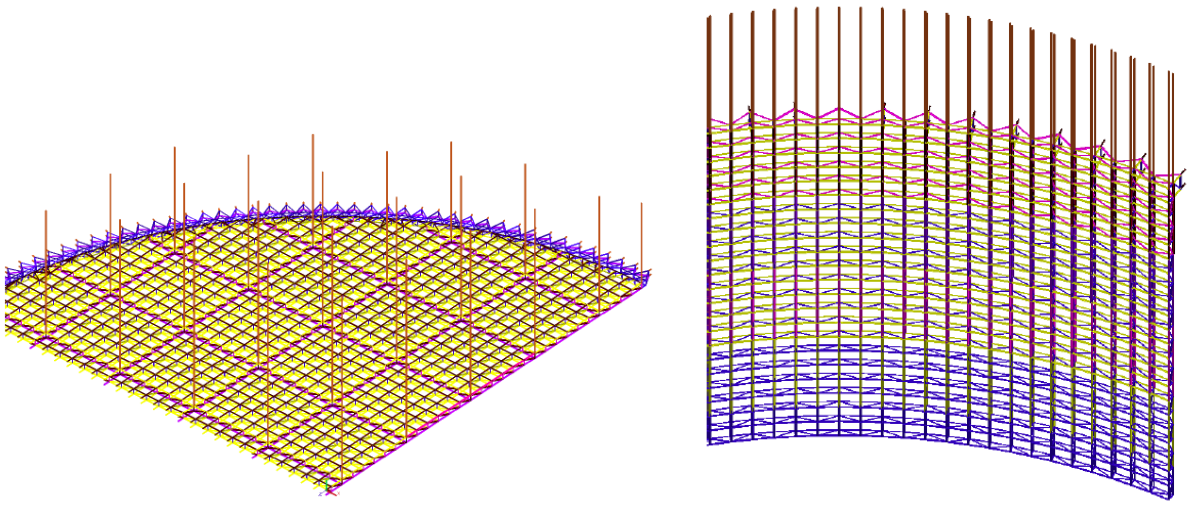

FIG. 44. Schematic view of the top and barrel frameworks. The lines extending upward show the vertical pipes which are anchored to the dome ceiling for suspending the top/barrel frameworks.

When the tank is filled with water, the overall load to the framework is reduced by the buoyancy of the various components such as photosensors. Therefore, the design of the structural framework has been made so that it has sufficient strength when the tank is empty (i.e. no water inside). As for the horizontal load in the case of an earthquake, the peak horizontal acceleration is set as $0.15\,g$ ($g = 9.8\,\mathrm{m}^2/\mathrm{s}$), although there is no official regulation for considering the effect of an earthquake in "the Law on Special Measures related to Public Use of Deep Underground". The peak horizontal acceleration of $0.15\,g$ is equal to that used for designing the Super-K water tank, which is a conservative assumption as it is derived based on "the Seismic Design Code for High-Pressure Gas Facilities of Japan" , a standard for facilities on the ground.

For the designed tank structure, a seismic response analysis has been performed to estimate the maximum displacement of the tank structure during an earthquake assuming various seismic waveforms. The result shows that the framework displacement becomes maximum at the bottom end of the suspended structure and its size is estimated to be smaller than 50 cm. Since the Hyper-K water tank is built deep underground, the actual displacement of the framework during an earthquake is expected to be much smaller. To ensure safety in the case that people work inside the empty tank during construction or future detector maintenance, the possibility of setting some temporary stopper rods is being investigated.

Finally the tank will have an enough air space below the top deck so that a water sloshing in the tank caused by an earthquake does not damage detector components.

4. Geomagnetic Field Compensation Coils

4.1. Introduction Photon collection efficiency (CE) decreases when a magnetic field is applied on a PMT especially perpendicular to the PMT direction. For example, the CE for box and line PMT decreases by about 1%, 2%, and 3% at 100 mG, 150 mG, and 180 mG, respectively. On the other hand, decrease of the CE is negligible when a magnetic field is applied parallel to the PMT direction even at 200 mG. An initial goal of the geomagnetic field compensation coil design is to keep the remaining magnetic field perpendicular to the ID PMT (B_{perp}) smaller than about 100 mG.

4.2. Calculation of remaining geomagnetic field The remaining geomagnetic field at each ID PMT is calculated for a 60 m height and 74 m diameter vertical cylindrical tank. The geomagnetic field compensation coils are located along the tank inner wall. To compensate for the geomagnetic field (x, y, z) = (-303, 0, -366) mG, vertical rectangular coils along the x-axis and horizontal circular coils along the z-axis (vertical direction) are assumed. For simplicity after several initial studies, the interval between each coil is set to be 2 m for both vertical and horizontal coils, and the following three currents are used to minimize B_{perp}: a common constant current for all the vertical coils (I_V), a common constant current for all the horizontal coils (I_H), and additional currents only at the top and bottom horizontal coils ($I_V \times n$, where n is a positive integer and corresponds to the number of winding of the coils). The last parameter n is found to be effective to reduce B_{perp} at around both the top and bottom tank corners. Distances between the tank inner wall and the ID surface are (2+0.6) m at the top and bottom and (1+0.6) m at the barrel, where 2/1 m are for the OD regions and 0.6 m is for a dead region. Note that the OD region is reduced from 2 m to 1 m at the barrel (SK and the baseline tank) to minimize cost. This is one of the HK detector design parameters to be evaluated from this calculation of the remaining geomagnetic field.

The ID PMTs are mounted on the ID inner wall (54.8 m height and 70.8 m diameter cylinder). The interval between each PMT is 70.7 cm except in the horizontal direction at the barrel ($7080 \cdot \pi / 314 = 70.84$ cm, where 314 is an appropriate integer value to make the interval close to 70.7 cm). There are 39,424 ID PMTs in total. The coil locations are shown in Figure 45.

A current set to (I_V, I_H, n) = (60A, 67A, 7) is the best case (the minimum fraction with B_{perp} >100mG). Figure 46 shows the B_{perp} distribution for all the ID PMTs at the best currents. The fraction of the number of the ID PMTs with B_{perp} <100 mG is 97.8%. Even though the OD region at the barrel is reduced from 2 m to 1 m, the fraction with B_{perp} <100 mG is large enough. Figure 47 shows the location of the ID PMTs with B_{perp} >100 mG at the best currents, along with

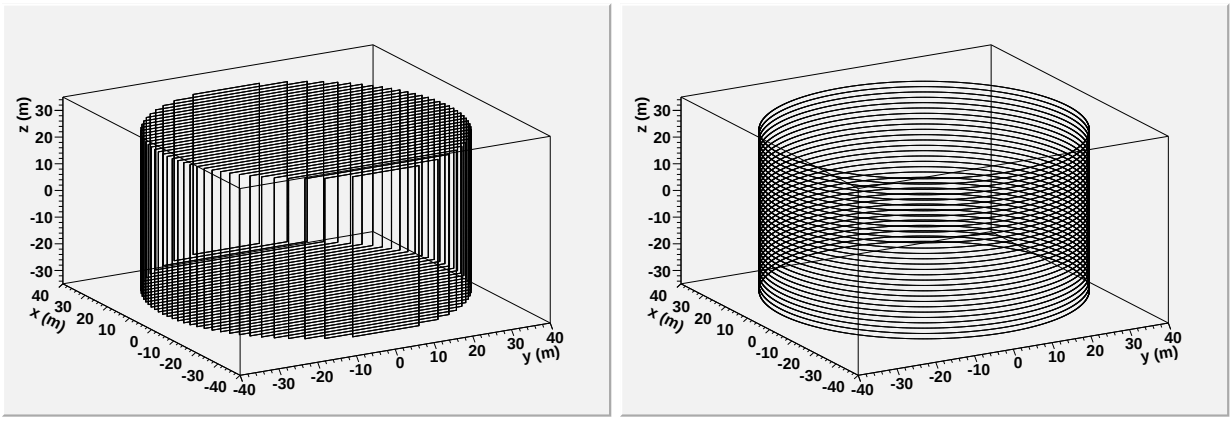

FIG. 45. Location of vertical rectangular coils (left) and horizontal circular coils (right).

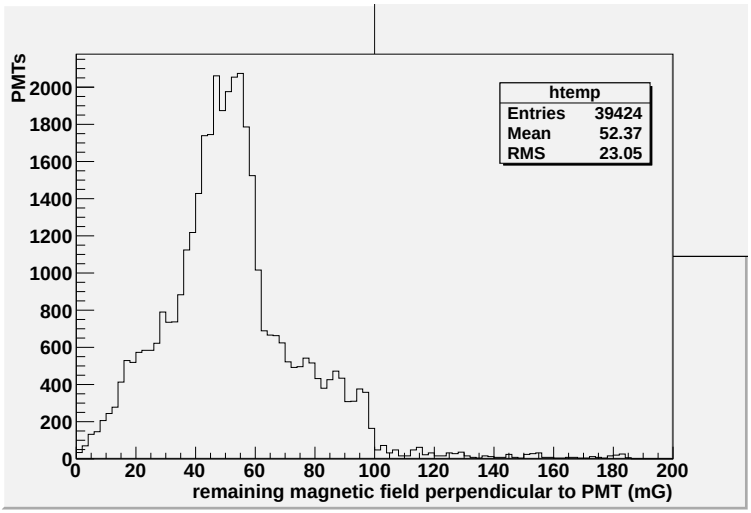

FIG. 46. B_{perp} distribution for all the ID PMTs at the best current set.

positions of all ID PMTs.

From Figure 46, decrease of CE is at most 1% on average. This satisfies the initial goal. If necessary, B_{perp} at the tank corners could be reduced by adding more coils and so on.

4.3. Cables and power supplies (PSs) The cables for the geomagnetic field compensation coils are installed near the lining surface of the tank. We are considering of placing the cable inside tubes embedded in the backfill concrete layer. In an alternative design, the cables are located in the tank water, like those of the magnetic coils in Super-K, supported by the fixtures attached to the lining sheets. We are investigating which design is better for Hyper-K.

A 4-conductor cable ($0.491\,\Omega$/km) is assumed for the total power consumption estimation. Table X and Table XI show PSs used for the estimation and their consumption for the horizontal and vertical coils, respectively. For the horizontal (vertical) coils, PSs are assigned for 7 circles (6

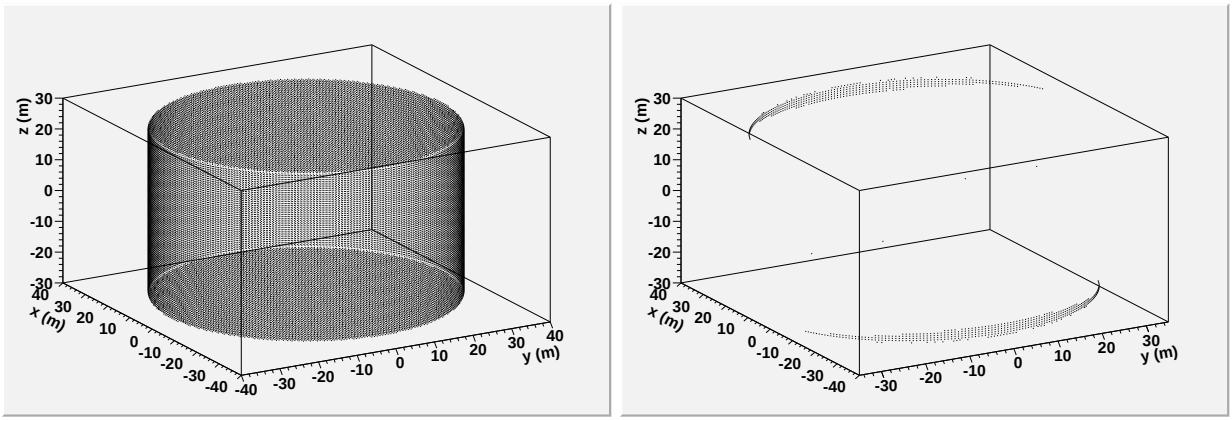

FIG. 47. Location of all the ID PMTs (left) and ones with B_{perp} >100 mG(right).

TABLE X. Power supply (PS) for horizontal circular coils per tank. The PS number is assigned along the z-axis of tank.

PS #	Coil length [km]	Voltage [V]	I_H [A]	consumption [kW]
1 (bottom)	1.62	53.4	67	0.894
2	1.62	53.4	67	0.894
3	1.62	53.4	67	0.894
4 (z=0)	0.23	7.6	67	0.127
5	1.62	53.4	67	0.894
6	1.62	53.4	67	0.894
7 (top)	1.62	53.4	67	0.894
Total				5.49

rectangular) along the z-axis (x-axis) except 1 PS for 1 circle (rectangular) at z (x) = 0, respectively. The total power consumption for the tank is 5.49 kW (horizontal coils) + 3.88 kW (vertical coils) = 9.37 kW. This is higher than that for SK (about 6.5 kW with 7 PSs in total) but reasonable.

Note that the coils between PSs and both horizontal/vertical coils are neglected (about 2/1%, respectively).

5. Construction

The water tank construction work includes laying the liner, building the photosensor support framework, and the installation of the underwater instruments (photosensors, electronics, light shielding sheets, magnetic coils, etc.). The planned construction procedure is similar to that of the

TABLE XI. Power supply (PS) for vertical rectangular coils per tank. The PS number is assigned along the x-axis of tank.

PS #	Coil length [km]	Voltage [V]	I_V [A]	consumption [kW]
1	1.18	34.8	60	0.522
2	1.48	43.6	60	0.654
3	1.59	46.8	60	0.702
4 (x=0)	0.27	7.9	60	0.119
5	1.59	46.8	60	0.702
6	1.48	43.6	60	0.654
7	1.18	34.8	60	0.522
total				3.88

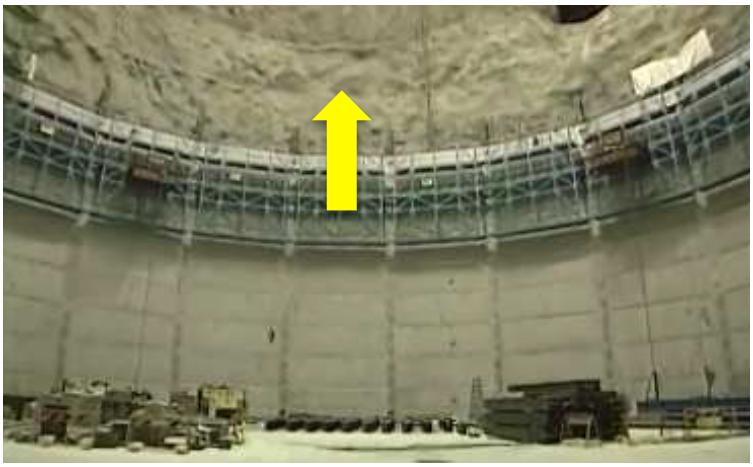

FIG. 48. A photograph of the Super-K tank liner construction using mobile scaffoldings.

Super-K water tank.

First, the drainage structure and the leveling concrete layer are constructed at the bottom of the cavern. Then, the side-wall liner is constructed ring-by-ring from bottom to top using mobile scaffoldings built along the whole circumference. Such a barrel liner laying using elevating scaffoldings was successful in the Super-K water tank construction (see Figure 48). To fasten HDPE sheets on the concrete layer by their studs, the backfill concrete is poured after setting a form with a HDPE sheet attached. After the concrete sets hard, the form is disassembled.

After the barrel liner construction is completed, building the photosensor support framework

starts.

First, the roof structure and the support framework for the photosensors in the top region are built on the bottom floor. The installation of the top photosensors is also done on the bottom floor. Then the top framework with photosensors mounted is lifted up from the bottom floor to its final destination by using the jacks. The total lifting load of the top structure with the photosensors mounted is about 9,400 kN. The number of hanging points is about 150, and the weight load per jack is about 70 kN.

The construction of the barrel framework and the photosensor installation are performed layer-by-layer on the bottom floor. Once the first stage of the barrel units with photosensors is completed, the whole structure is lifted up by using jacks, and then the second stage of barrel units with photosensor is hung just below the first stage one. The total lifting load of the barrel structure with the photosensors mounted is about 21,000 kN. The number of hanging points is about 320, and the weight load per jack is about 70 kN.

Finally, after the barrel framework construction and the photosensor installation is completed, the support framework in the bottom region is built and the photosensors are mounted.

During the tank construction, most of the components such as the liner sheets, the framework members, the photosensors are transported into the tank through the bottom approach tunnel. After the construction of the support framework is completed, the tunnel is closed by using the concrete and the waterproof liner sheets. The plug manhole made of the stainless steel is built there so that people can enter the tank through this manhole for future maintenance works (see Figure 36).

As for the tank construction time, the liner laying work will take 20 months, then the support framework construction in parallel with the photosensor installation will take 13 months. In the current estimation, the time for the framework construction and the photosensor installation is determined by the speed for supplying the photosensor assemblies. In total, about three years will be needed for the tank construction.

E. Water purification and circulation system

1. Introduction

Water is the target material and signal-sensitive medium of the detector, and thus its quality directly affects the sensitivity. In order to realize such a huge Cherenkov detector, achieving good water transparency is the highest priority. In addition, as radon emanating from the photosensors and detector structure materials is the main background source for low energy neutrino studies, an efficient radon removal system is indispensable.

In Super-Kamiokande the water purification system has been continually modified and improved over the course of SK-I to SK-IV. As a result, the transparency is now kept above 100 m and is very stable, and the radon concentration in the tank is held below 1 mBq/m^3. Following this success, the Hyper-Kamiokande water system design will be based on the current Super-Kamiokande water system.

Naturally, ever-faster water circulation is generally more effective when trying to keep huge amounts of water clean and clear, but increasing costs limit this straightforward approach so a compromise between transparency and re-circulation rate must be found. In Super-Kamiokande, 50,000 tons of water is processed at the rate of 60 tons/hour in order to keep the water transparency (the attenuation length for 400 nm-500 nm photons) above 100 m, and 20 Nm^3/hour of radon free air is generated for use as a purge gas in degas modules, and as gas blankets for both buffer tanks and the Super-Kamiokande tank itself. For the 0.258 million tons of water in one tank of Hyper-Kamiokande, these process speeds will need to be scaled-up to 310 m^3/hour for water circulation and 50 Nm^3/hour for radon free air generation.

2. Source water

As for the initial water filling, the speed of the filling is restricted by the amount of the source water in the mine. In Mt. Nijuugo-yama, the baseline location of Hyper-Kamiokande, the total amount of the spring water is about 600 tons/hour. (It varies seasonally between 300 tons/hour and 800 tons/hour and it is above 600 tons/hour except Winter (December-March).) However, as the mine company uses the water for their smelting factory, the available Spring water for Hyper-Kamiokande is limited. In Mt. Ikeno-yama, the location of the Super-Kamiokande, there are sufficient mine water and no mining/smelting activities. The water quality of Tochibora spring water is compared with that of Mozumi spring water in Table XII. Obviously, they are quite similar.

		Tochibora used cooling water as of 11 Nov. 2015	Tochibora Spring water as of 1 Mar. 2011	Mozumi Spring water as of 16 Mar. 2011
Temperature(Typical)	°C	17	11	12
pH (25°C)		7.7	7.8	7.8
Conductivity	μS/cm	142	170	221
Turbidity	degree(Kaolin)	< 1	< 1	< 1
Acid consumption (pH 4.8)	mg $CaCO_3$/L	43.1	40.0	75.8
TOC	mg/L	< 0.1	< 1	< 1
Phosphate	mg/L	< 0.1	< 0.1	< 0.1
Nitrate	mg/L	2.1	1.0	1.6
Sulfate	mg/L	21.9	36.4	30.2
Fluoride	mg/L	0.3	0.3	0.4
Chloride	mg/L	1.7	1.6	1.8
Sodium	mg/L	4.4	4.9	6.2
Potassium	mg/L	0.5	0.5	0.5
Calcium	mg/L	22.2	25.2	32.0
Magnesium	mg/L	1.8	1.5	2.9
Ammonium	mg/L	< 0.1	< 0.1	< 0.1
Ionic silicon dioxide	mg/L	14.9	17.1	11.8
Iron	mg/L	< 0.01	< 0.01	< 0.01
Copper	mg/L	< 0.01	< 0.01	< 0.01
Zinc	mg/L	0.07	0.09	< 0.01
Lead	mg/L	< 0.1	< 0.1	< 0.1
Aluminum	mg/L	< 0.01	< 0.01	< 0.01
Boron	mg/L	< 0.01	< 0.01	0.2
Strontium	mg/L	0.16	0.18	0.52
Barium	mg/L	< 0.01	< 0.01	0.03

TABLE XII. Source water quality.

3. Main system flows and layouts

Water systems for the case of 2 x 258 m^3 tanks are shown here. The HK main water purification system consists of a 1st stage system (filling) and each 2nd stage (re-circulation) system for each water tank as shown in Figure 49. Figure 50 shows the flow of 1st and 2nd stage systems and Figure 51 shows their layouts. The process power of the 1st stage system is 240 m^3/h, so it takes 46 day to fill one tank and 92 days to fill two tanks. Here 320 t/h of source water availability is assumed. Preferably, additional 118 t/h of 11 °C cooling water is required for the heat exchangers.

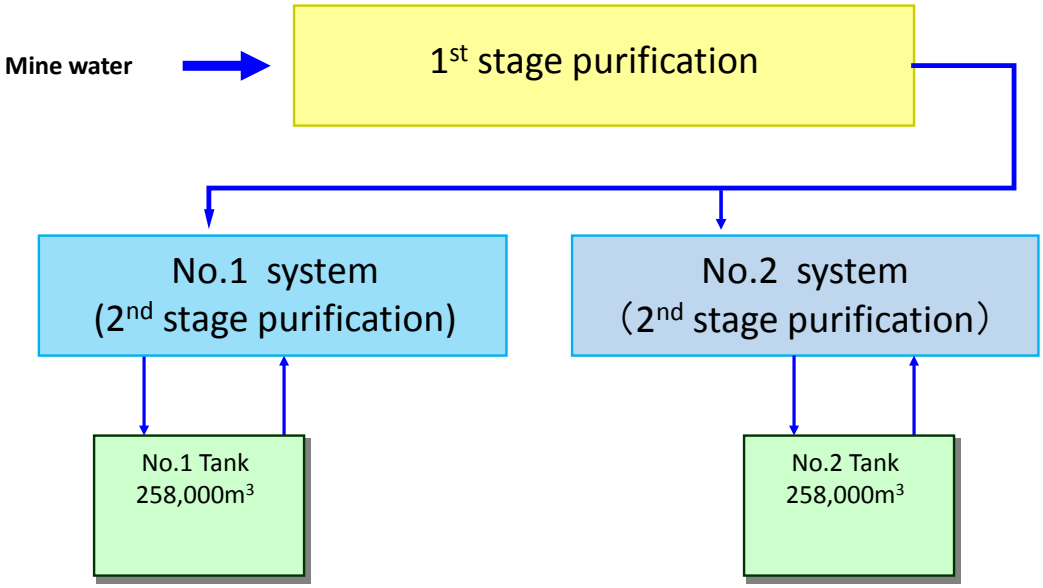

FIG. 49. Hyper-K water system overview.

4. Water flow simulation in the tank

Water flow in the tank directly affects the water quality and the physics results, therefore water flow simulations for the baseline design tank were conducted. Water flow is determined not only by the total water flow rate but also by detector geometry, the configuration of water inlets and outlets, supply water temperature, heat sources in the tank, surrounding rock temperature and so on. The input parameters are summarized in Table XIII, and the main results are shown in Figure 52. When cold water is supplied from the bottom of the tank, convection in the tank is suppressed and the flow becomes laminar. As the result, the water replacement goes effectively. When cold water is supplied from the top of the tank, large convection is evoked and the water quality in the tank becomes uniform, while the water replacement becomes worse. Actually these behaviors were confirmed in Super-Kamiokande's 50 kton tank and seem to be identical to cylindrical tanks; thus the water flow in Hyper-Kamiokande should be controlled like Super-Kamiokande.

5. Radon in the water

The dominant low energy background is expected to be radon and the dominant radon source in the tank is expected to be the PMTs themselves. The radon emanation from Hyper-Kamiokande

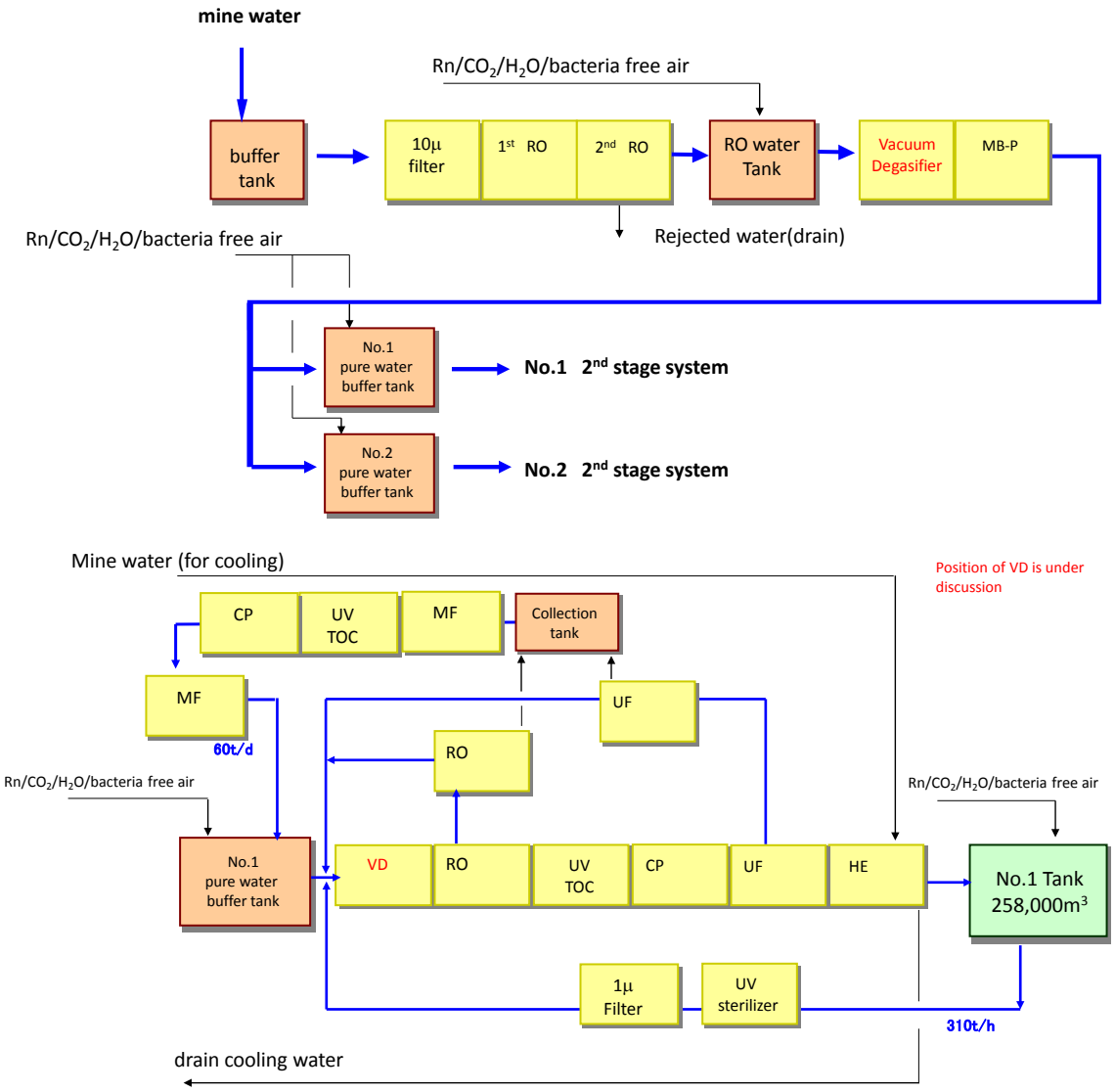

FIG. 50. 1st stage and 2nd stage water systems.

photon sensors have not been measured yet, but each Super-Kamiokande ID PMT emanates about 10 mBq and the measured radon concentration in the Super-Kamiokande water is 2 mBq/m^3. Super-Kamiokande has 11129 ID PMTs and 50 ktons of water, therefore the average radon concentration should be around 10 mBq/PMT $\times$ 11129 PMTs / 50000 tons = 2.2 mBq/m^3. Accordingly, the radon concentration expected in one Hyper-Kamiokande HD tank is 10 mBq/PMT $\times$ 40000 PMTs / 258000 tons = 1.6 mBq/m^3.

Regarding radon suppression, the Hyper-Kamiokande water system includes Super-Kamiokande-based vacuum degasifiers which reduce radon by about one order of magnitude as shown in Fig-

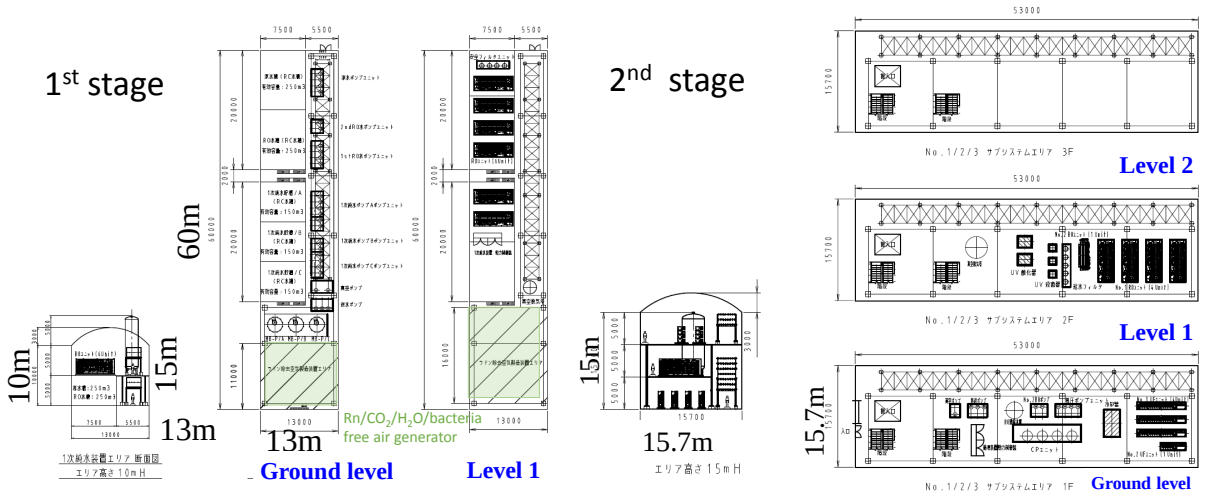

FIG. 51. Necessary space for the main systems.

Tank shape	Baseline C shape
ID flow rate	271.8 m^3/h
OD flow rate	37.9 m^3/h
Inlets/Outlets	65A×37/65A×37
ID boundary condition	Inlet: 0.61 m/s, 286K Outlet: 0Pa
OD boundary condition	Inlet: 0.67 m/s, 286K Outlet: 0Pa
Supply water temperature	13.0 °C
Top level rock temperature	16.7 °C
Bottom level rock temperature	17.7 °C
Heat flux from the PMT/electronics/coil	3.2W/m^2
Total heat form ID top and bottom	2100W and 2100W
Total heat from ID wall	6502W
Total heat from OD wall(rock)	5384W
Water density @ 286K	999.4 kg/m^2
Water heat conductivity @286K	0.587 W/m/K
Water viscosity @286K	0.0012 kg/m/s

TABLE XIII. Input parameters for the water flow simulations.

ure 50. That being said, in the experience of Super-Kamiokande the best way to reduce radon is by inducing a gentle laminar flow in the fiducial volume, allowing the radon to primarily decay close to the PMTs (i.e., not in the fiducial volume) where it can do the least harm.

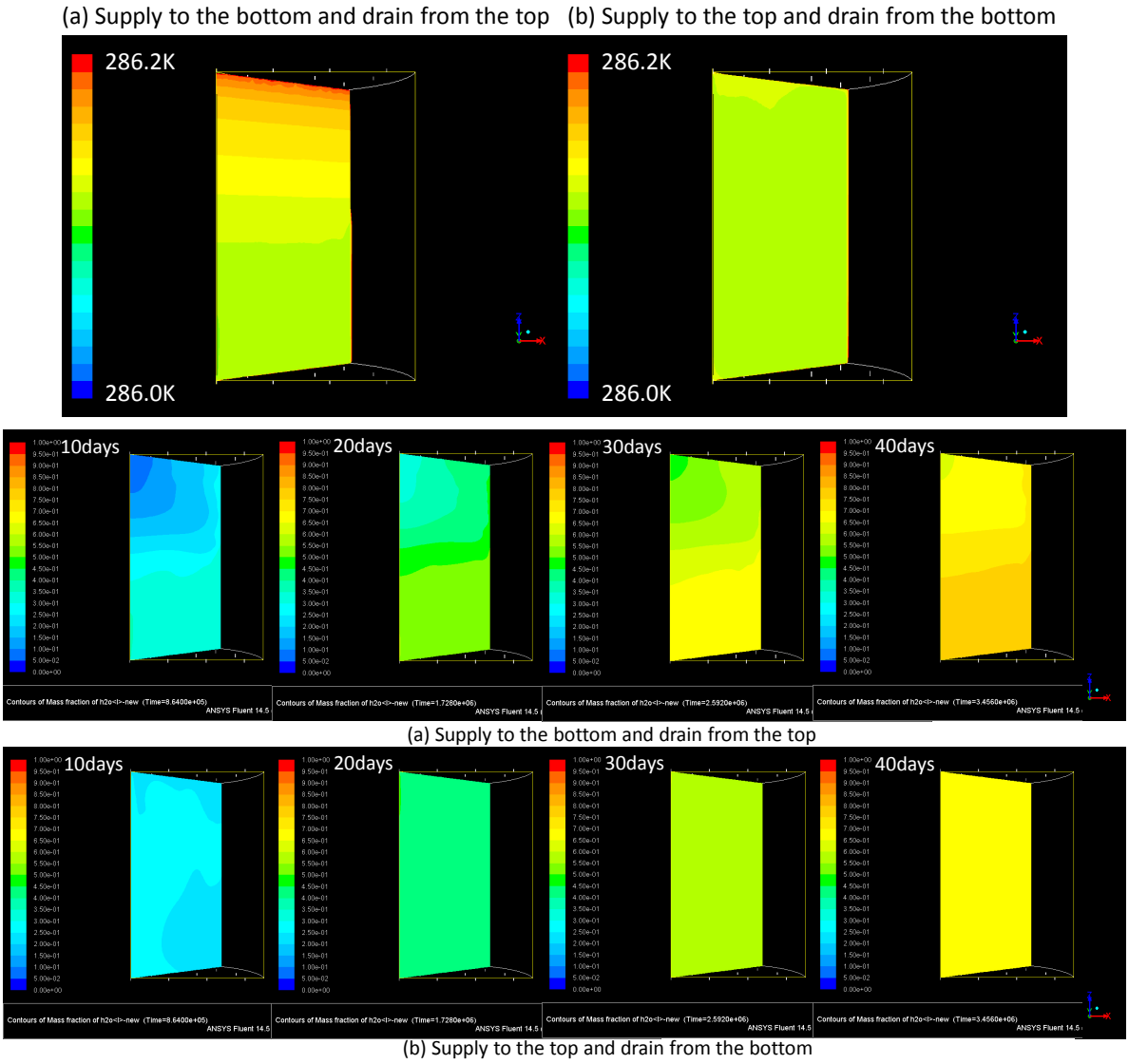

FIG. 52. Water temperature distributions (top 2 figures) and water replacement efficiencies as the result of water flow simulations. (a) The case for supplying water from the bottom of the tank and draining water from the top of the tank. (b) The case for supplying water from the top of the tank and draining water from the bottom of the tank. The elapsed days since the recirculation starts are indicated. In this simulation, at first the tank was filled with old water (= 0), then new water (= 1) was supplied to the tank, therefore the color scale in the figures corresponds to the water replacement efficiency.

6. Gd option

In order to realize the many physics benefits provided by efficient tagging of neutrons in water, it has been proposed to add dissolved gadolinium sulfate to Super-Kamiokande. As a result, over a period of years much effort has gone into the design and demonstration of a specialized water system

capable of maintaining the exceptional water transparency discussed above, while at the same time maintaining the desired level of dissolved gadolinium in solution. In other words, somehow the water must be continuously recirculated and cleaned of everything *except* gadolinium sulfate.

Starting in 2007 with a 0.2 ton/hour prototype at the University of California, Irvine, since 2009 the Kamioka-based EGADS (Evaluating Gadolinium's Action on Detector Systems) project has shown that such a selective water filtration technology - known as a "molecular band-pass filter" - is feasible at 3 tons/hour. It continuously improves and then maintains the transparency of water loaded with $Gd_2(SO_4)_3$ to SK ultrapure water levels, removing unwanted impurities while simultaneously and indefinitely retaining the desired levels of both the gadolinium and sulfate ions.

Since EGADS was built specifically to show that gadolinium loading would be feasible in Super-K, scalability was always an important design criterion. Therefore, from the beginning the EGADS band-pass system was conceived of as a modularized design. It uses cost-effective, readily available components operating in parallel to achieve the desired throughput and assure serviceability.

As the band-pass design is modular and uses off-the-shelf equipment, albeit in novel ways, scaling it up from the current 3 tons/hour to 60 tons/hour for Super-Kamiokande, or 310 tons/hour for each tank of Hyper-Kamiokande, is straightforward. Figure 53 indicates how one rack of filtration membrane housings, the modular unit around which the Hyper-K band-pass system is designed, is derived from the operating EGADS selective filtration system.

Figure 54 depicts how the modular rack from Figure 53 may be duplicated and operated in parallel to provide the needed throughput. Further design simplification and cost savings are achieved by using this standardized membrane housing array and filling the housings with a variety of filter membranes, each of which handles a different cleaning task. These components include nanofilters (NF), ultrafilters (UF), and reverse osmosis (RO) membranes; in each case there are two stages. Note that the layout shown in Figure 54 is schematic in nature. Due to space constraints underground the illustrated system will likely be split into two levels, one atop the other.

Using the baseline Hyper-K design, the system shown in Figure 54 represents what is needed for selective filtration of the water in one tank following the addition of gadolinium sulfate to the Hyper-K water. It is assumed that pure water for filling the detector will be provided by the main, non-Gd-capable water system described above. The Gd-specific "molecular band-pass" system described here will be augmented with additional Gd-capable water handling equipment – also demonstrated by and scaled up from a working EGADS version – known as a "fast recirculation" system. The Hyper-K fast recirculation system will be used in conjunction with HK's band-pass to maintain the Gd-loaded water's quality.

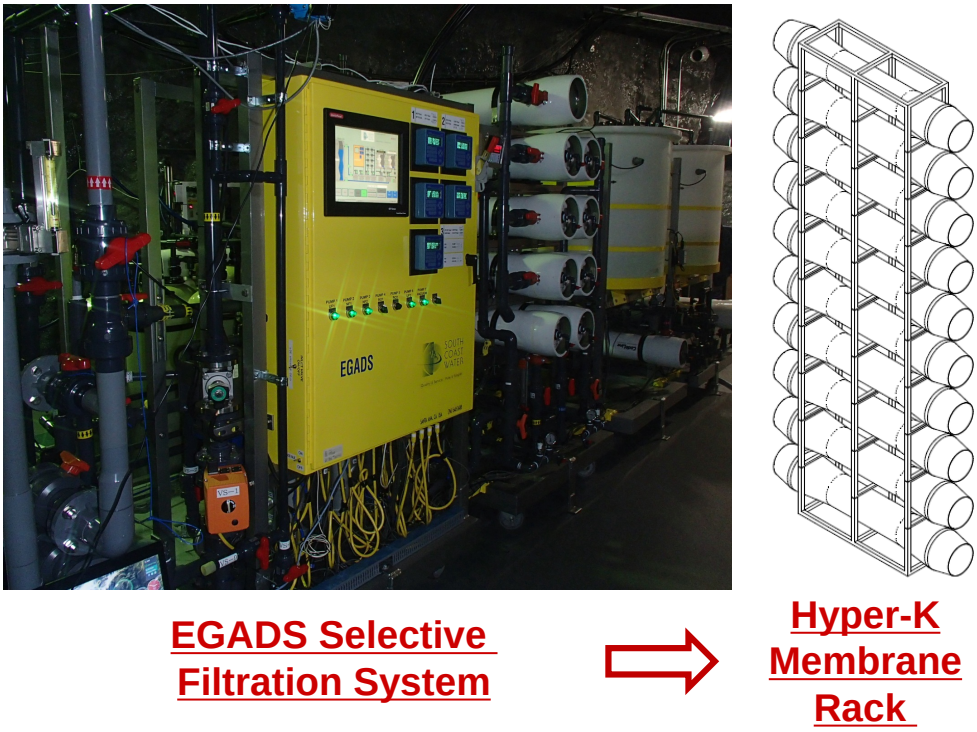

FIG. 53. Scaling the modular EGADS selective filtration band-pass for Hyper-Kamiokande. One rack of filtration membrane housings is shown here; Figure 54 shows many of them arranged into a functional selective filtration system.

Due to gadolinium sulfate's benign nature with regards to the usual detector components (materials compatibility was another component of the EGADS study), retaining the ability to add gadolinium to Hyper-Kamiokande primarily means retaining the option of adding gadolinium filtration capability to the Hyper-K water system. Indeed, if gadolinium works as well as expected in Super-Kamiokande over the next few years, it is hard to imagine that a next-generation detector like Hyper-K would not also want to enjoy the physics advantages a gadolinium-loaded Super-K would already have. Therefore, we have been careful to keep the possibility of gadolinium loading in mind when designing the overall Hyper-Kamiokande water system.

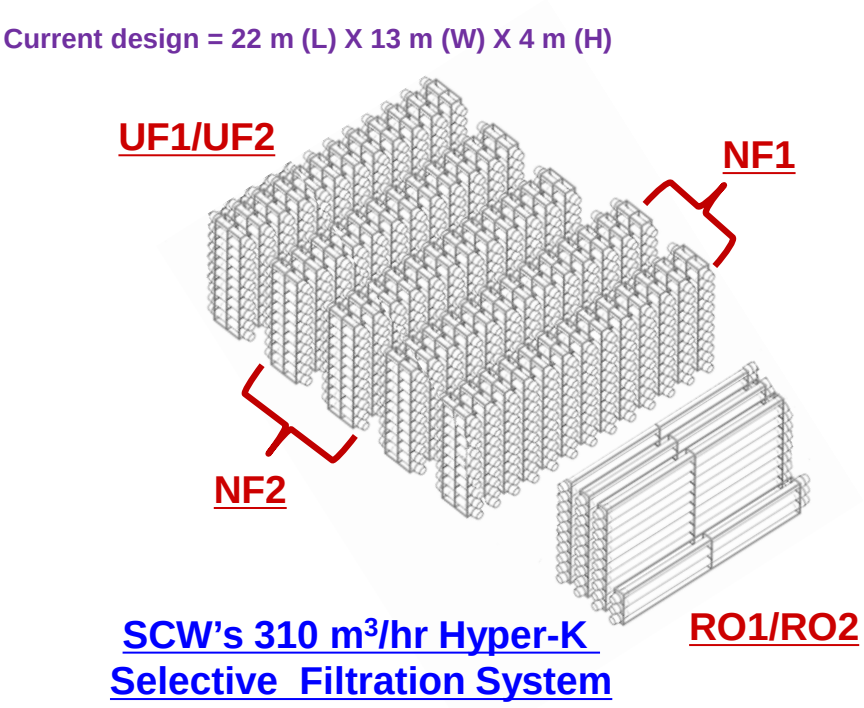

FIG. 54. Gadolinium-capable water system for Hyper-Kamiokande. Two stages each of nanofilters (NF), ultrafilters (UF), and reverse osmosis (RO) membrane racks are shown, sufficient to provide selectively filtered water for one tank (∼258 ktons) of Hyper-K. Please note that this figure contains proprietary design elements and is the property of South Coast Water, a Division of Hannah Industries; prior approval must be granted by SCW for redistribution.

F. Photosensors

1. *Introduction*

Photosensors for Hyper-K are subdivided into the ID and OD photosensors, to detect the Cherenkov ring pattern and to tag in-coming or out-going particles such as a cosmic ray background, respectively.

The ID photosensor was newly developed for Hyper-K to meet the requirements listed in Table XIV. The new photosensor is based on the well established and reliable design of the 50 cm R3600 PMT by Hamamatsu Photonics K.K. with a Venetian blind dynode type, which was used for Super-K, and the 43 cm PMT with a box-and-line dynode (Hamamatsu R7250), which was used for the KamLAND experiment. Further improvements were achieved by a higher quantum efficiency and optimized box-and-line dynode, resulting in the new photosensor, a Hamamatsu R12860-HQE

PMT.

Requirements	Value		Conditions
Detection efficiency	16%	Typ.	Quantum Efficiency × Collection Efficiency
Timing resolution	2.2 nsec	σ, Typ.	Single Photoelectron (PE)
Charge resolution	50%	σ, Typ.	Single PE
Signal window	200 nsec	Max.	More than 95% of a total signal area
Dynamic range	2 photons/cm^2	Max.	Per detection area on wall
Gain	$10^7 \sim 10^8$	Typ.	
Afterpulse rate	15%	Max.	For single PE, relative to the primary pulse
Rate tolerance	10 MHz	Max.	Single PE pulse, within 10% change of gain
Magnetic field tolerance	100 mG	Typ.	Within 10% degradation
Life time	20 years	Typ.	Less than 10% dead rate
Pressure rating	0.8 MPa	Min.	Static, load in water

TABLE XIV. Minimum requirements of the Hyper-K ID photosensors, mostly from Super-K with the R3600 PMT. The dark rate is also an important parameter, but its required value depends on the photosensor specification and each physics topic. Thus it is judged in the Hyper-K simulation later assuming the photosensor performance. Better performance than the values listed is obtained in the newly developed ID photosensors described in this section.

The OD photosensors can be the same as the Super-K OD photosensors using a 20 cm Hamamatsu R5912 PMT, which can also stand the 60 m deep water pressure in Hyper-K.

This section describes the characteristics and related accessories of these photosensors. In addition, we present prospects for alternative options, which may be adopted in future.

2. Photosensor for Inner Detector

2.1. Performance

A newly developed R12860-HQE PMT (HQE, high quantum efficiency) for Hyper-K by Hamamatsu, or so-called "50 cm high-quantum-efficiency box-and-line PMT (HQE B&L PMT)", has a faster time response, better charge resolution and a higher detection efficiency with a stable mechanical structure, compared to the existing large aperture PMTs. This section describes the specifications of the HQE B&L PMT and a safety design for a long operation.

2.1.1. Design and Specifications

Figure 55 shows a side view of the HQE B&L PMT, whose shape is similar to the PMT used in Super-K. Hence, the supporter system developed in Super-K to attach the PMT is also appropriate for the HQE B&L PMT in Hyper-K. The dynode inside the bulb shape and the surface curvature were improved. A typical bias voltage of 2,000 V is divided to each dynode by a bleeder circuit such as in Figure 57. The specification of the typical HQE B&L PMT is listed in Table XV.

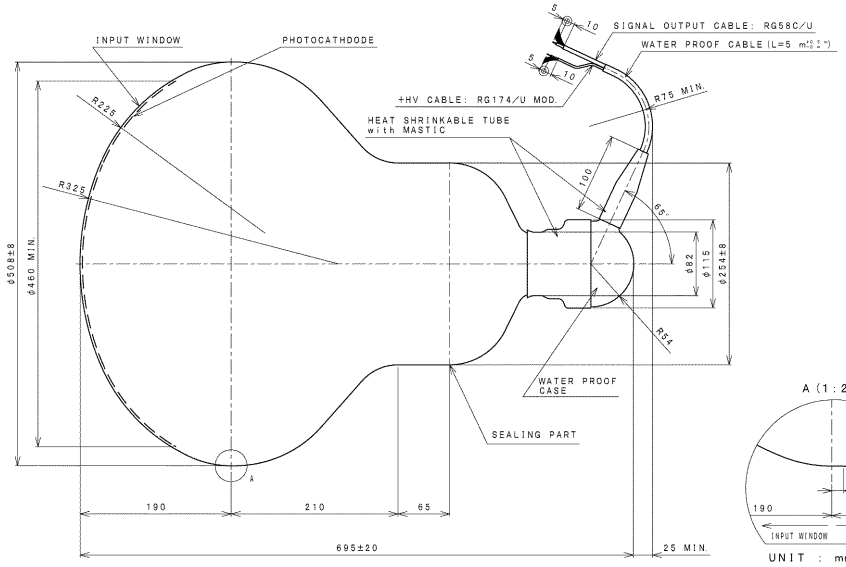

FIG. 55. Design of the HQE box-and-line R12860 PMT.

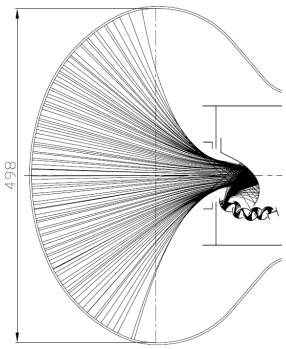

FIG. 56. Focus lines of photoelectrons to the box dynode and amplification paths of electrons to the line dynodes.

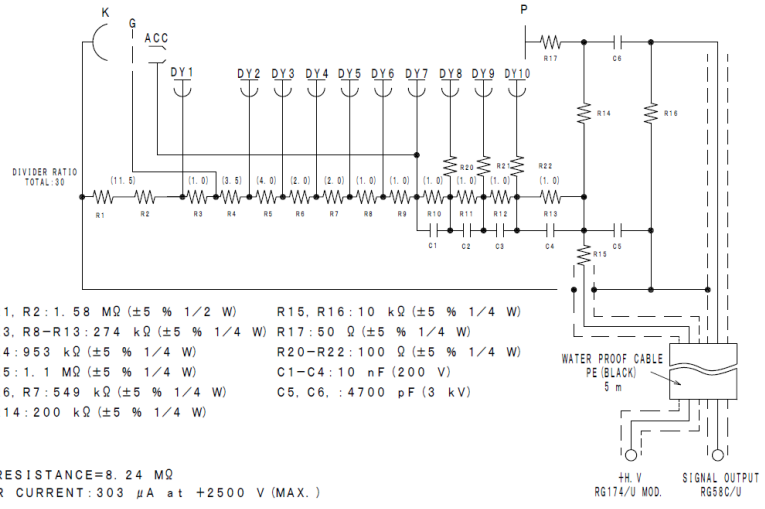

FIG. 57. Bleeder circuit of the HQE box-and-line R12860 PMT, used in the performance evaluation.

Shape	Hemispherical
Photocathode area	50 cm diameter (20 inches)
Bulb material	Borosilicate glass (~ 3 mm)
Photocathode material	Bialkali (Sb-K-Cs)
Quantum efficiency	30 % typical at $\lambda = 390$ nm
Collection efficiency	95 % at 10^7 gain
Dynodes	10 stage box-and-line type
Gain	10^7 at ~ 2000 V
Dark pulse rate	~ 8 kHz at 10^7 gain (13 Celsius degrees, after stabilization for a long period)
Transit time spread	2.7 nsec (FWHM) for single photoelectron signals
Weight	7.5 kg (without cable)
Volume	61,050 cm^3
Pressure tolerance	9 kg/cm^2 water proof

TABLE XV. Specifications of the 50 cm R12860-HQE PMT by Hamamatsu.

2.1.2. Detection Efficiency

The total detection efficiency of the HQE B&L PMT is twice as high as the conventional R3600 (Super-K PMT). Figure 58 shows the measured quantum efficiency (QE) of several HQE B&L PMTs as a function of wavelength compared with a typical QE of the Super-K PMT in dotted line. After several iterations to improve the QE of the large 50 cm bulb by Hamamatsu, a QE of 30% was achieved at peak wavelength of 390 nm, compared to the 22% of the Super-K PMT.

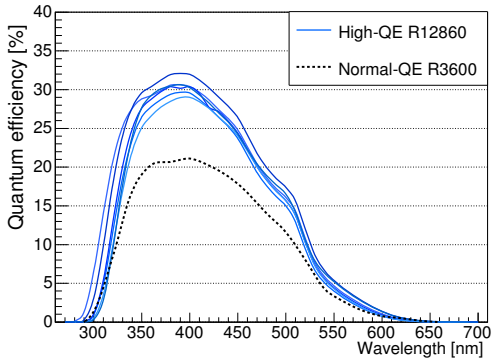

FIG. 58. Measured QE for six high-QE R12860 (solid lines) and a normal R3600 (dashed line).

If the sensitive photocathode area with a collection efficiency (CE) greater than 50% is compared, the HQE B&L PMT has an increased area with a diameter of 49.2 cm, compared to 46 cm in case of the Super-K PMT and 43.2 cm in the KamLAND PMT. Compared with 73% CE of the

Super-K PMT within the 46 cm area, the HQE B&L PMT reaches 95% in the same area and still keeps a high efficiency of 87% even in the full 50 cm area. This high CE was achieved by optimizing the glass curvature and the focusing electrode, as well as the use of a box-and-line dynode. In the Super-K Venetian blind dynode, the photoelectron sometimes misses the first dynode while the wide first box dynode of the box-and-line accepts almost all the photoelectrons. This also helps improving the single photoelectron (PE) charge resolution, which then improves the hit selection efficiency at a single PE level. By a measurement at the single PE level, we confirmed the CE improvement by a factor of 1.4 compared with the Super-K PMT, and 1.9 in the total efficiency including HQE. Figure 59 shows that the CE response is quite uniform over the whole PMT surface in spite of the asymmetric dynode structure.

A relative CE loss in case of a 100 mG residual Earth magnetic field is at most 2% in the worst direction, or negligible when the PMT is aligned to avoid this direction on the tank wall. The reduction of geomagnetism up to 100 mG can be achieved by active shielding by coils.

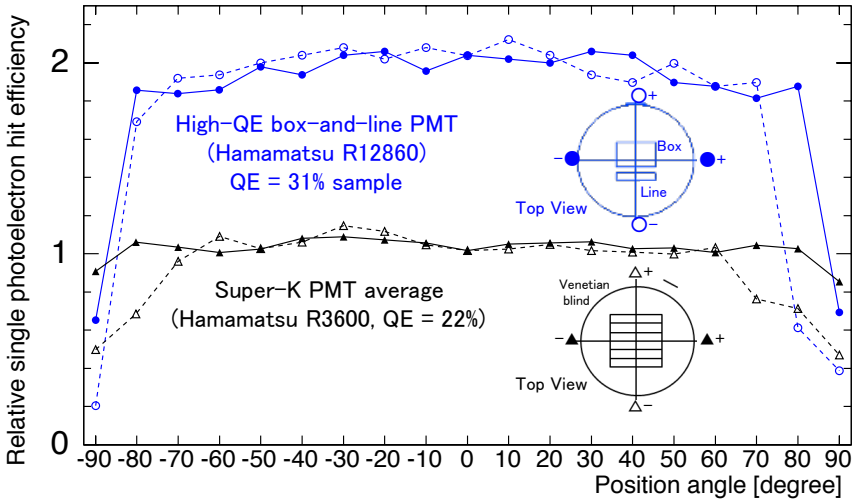

FIG. 59. Relative single photoelectron detection efficiency as a function of the position in the photocathode, where a position angle is zero at the PMT center and $\pm 90^\circ$ at the edges. The dashed line is the scan along the symmetric line of the box-and-line dynode whereas the solid line is along the perpendicular direction of the symmetric line. The detection efficiency represents QE, CE and cut efficiency of the single photoelectron at 0.25 PE. A HQE B&L PMT with a 31% QE sample shows a high detection efficiency by a factor of two compared with normal QE Super-K PMTs (QE = 22%, based on an average of four samples).

2.1.3. Performance of Single Photoelectron Detection

The single photoelectron pulse in a HQE B&L PMT has a 6.7 ns rise time (10%–90%) and 13.0 ns FWHM without ringing, which is faster than the 10.6 ns rise time and 18.5 ns FWHM in the Super-K PMT. The time resolution for single PEs is 1.1 ns in σ for the fast left side of the transit time peak in Figure 60 and 4.1 ns at FWHM, which is about half of the Super-K PMTs. This would be an important factor to improve the reconstruction performance of events in Hyper-K.

The nominal gain is 10^7 and can be adjusted for several factors in a range between 1500 V to 2200 V. Figure 61 shows the charge distribution, where the 35% resolution in σ of the single PE is better compared to the 50% of the Super-K PMT. The peak-to-valley ratio is about 4, defined by the ratio of the height of the single PE peak to that of the valley between peaks.

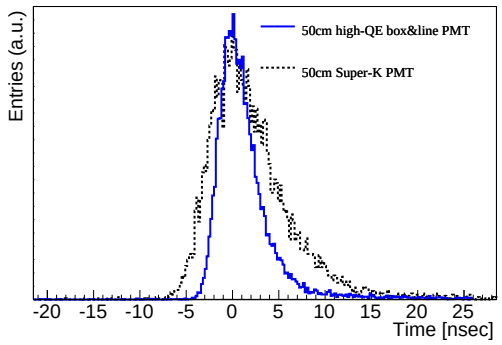

FIG. 60. Transit time distribution at single photoelectron, compared with the Super-K PMT in dotted line.

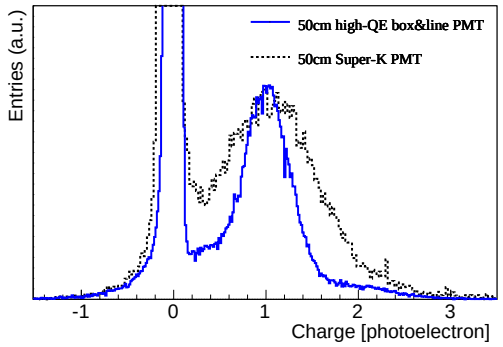

FIG. 61. Single photoelectron distribution with pedestal, compared with the Super-K PMT in dotted line.

2.1.4. Gain Stability

Because the Hyper-K detector is sensitive to a wide energy range of physics, the PMT is required to have a wide dynamic range. The Super-K PMTs have an output linearity up to 250 PEs in charge by the specifications and about 700 PEs measured in Super-K (with up to 5% distortion) [117], while the linearity of the HQE B&L PMT was measured to be within 5% up to 340 PEs as seen in Figure 62. Even with more than 1,000 PEs, the output is not saturated and the number of PEs can be calculated by correcting the non-linear response. The linearity range depends on the dynode current, and can be optimized with changing the resistor values in the bleeder circuit. This result demonstrates sufficient detection capabilities in the wide MeV–GeV region as in Super-K, as long as it is corrected according to the response curve.

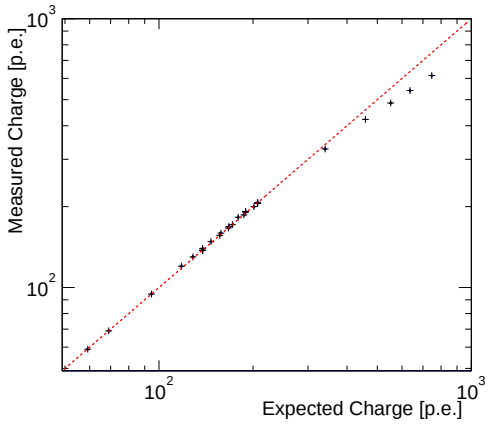

FIG. 62. Output linearity of the HQE B&L PMT in charge, where a dotted line shows an ideal linear response. It is derived by measurements of a coincident emission by two light sources compared with an expectation by sum of individual detections.

A fast recovery of gain for high signal rate is needed by supernova observation, decay electrons from muons, and any accidental pileup events. The nearest time depends on the charge integration range, that is 200 nsec or more depending on the electronics.

The rate dependence of the output charge was measured at several light intensities while varying the constant interval time of light pulses (as shown in Figure 64). A 5% drop is observed at the output current of 170 μA. It corresponds to 87 MHz in the single PE intensity or 1 MHz in most of detected intensities like at the level of few tens of PE. This is sufficient to detect possible burst physics events (Section III.3 A).

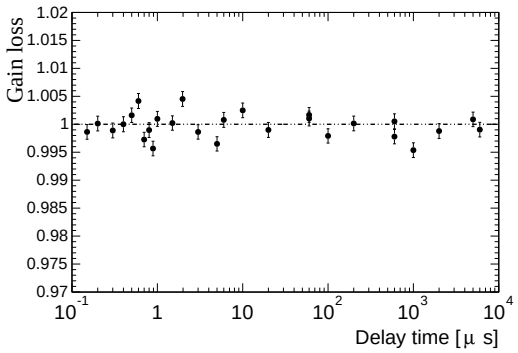

FIG. 63. Gain stability of a delayed pulse after a primary pulse, compared with no primary pulse. The charge set is about 150 PEs at 10^7 gain for both primary and delayed pulses in various delayed time.

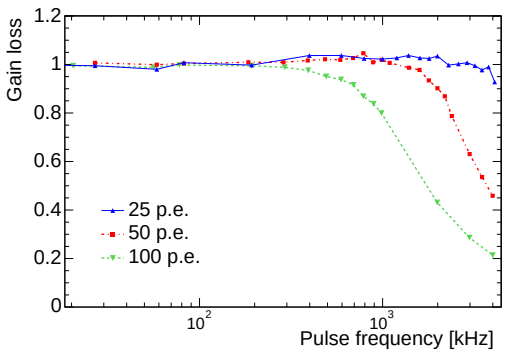

FIG. 64. A measured gain stability as a function of the pulse rate in three light intensities of 25, 50 and 100 photoelectrons, relative to outputs at 100 Hz. Each charge is calculated using the baseline just before the pulse.

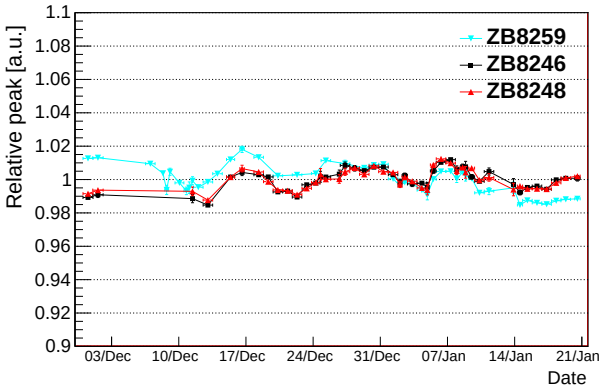

FIG. 65. Relative charge of three HQE B&L PMTs for two months in a 200 ton water Cherenkov detector. Signals of several tens photoelectrons from a xenon light pulse were monitored.

Even in the case of a detection of two near continuous events like a decayed particle accompanied, no loss of charge was observed for the second delayed pulse. By measuring two continuous pulses of about 150 PEs in both, the observed loss of gain is stable within 0.5% as shown in Figure 63. Therefore, tagging of the delayed particles will be stable in the HQE B&L PMT.

A long term feasibility test was performed on the three HQE B&L PMTs in a 200 ton water Cherenkov detector at the Kamioka mine, which was constructed to evaluate an anti-neutrino tagging with doping gadolinium in water. All the HQE B&L PMTs function over a year, and the gain measuring the charge peak from a constant light was stable within 1% RMS (Figure 65).

2.1.5. Backgrounds

The dark hit rate originates from a thermionic emission on the photocathode, and depends on the environmental temperature, the bias high voltage and the accumulated operating time for stabilization. For Hyper-K, the minimum detection energy is determined by the dark hit rate, because the dark hits creates more fake triggers which are generated by the sum of PMT hits.

The dark rate of several HQE B&L PMTs were measured to be 10 kHz at room temperature after stabilization for a few days. With the 13 °C temperature expected in Hyper-K and a long time stabilization, we expect the dark rate to be 8–9 kHz in Hyper-K. It is high compared to the Super-K PMT (4.2 kHz), but the dark hit rate per photon detection efficiency is about the same because of the double detection efficiency. Section III discusses the adequacy of this dark hit rate on the physics sensitivities.

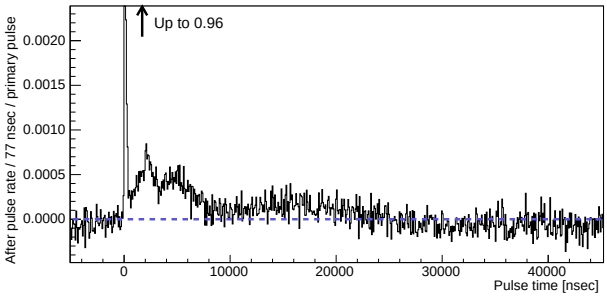

FIG. 66. Time distribution of hits, where the primary single PE signal comes at zero and others are afterpulses. The dotted line represents the level of the dark hit which is set to zero. The expected value of the number of afterpulses is measured to be 0.05 for one primary pulse in this sample.

The afterpulse has a long delay of several microseconds order after the primary PE, and confuses event reconstruction for tagging delayed particles. It is caused by a feedback of the ionized residual gas to the photocathode, and several timing peaks appear by different gas molecular masses. The HQE B&L PMT shows afterpulse peaks in Figure 66. Typically in five measured samples, the afterpulse rate is in total less than 10% relative to the main pulse at single PE observation. It is comparable to the Super-K PMT.

The radioactive contamination in the surface glass was measured by a germanium semiconductor detector using a block sample. It is listed in Table XVI by Uranium series, Thorium series and Potassium-40. Because the glass is provided from the same manufacturer as in Super-K, the expected number of background events in Hyper-K will be similar as in Super-K.

	U-chain	Th-chain	K^{40}
Bq/kg	5.5	1.8	18.2
Bq/PMT	27	9.4	95

TABLE XVI. Radioactive contamination in glass for the HQE B&L PMT (Hamamatsu R12860-HQE).

2.2. Mechanical Characteristics

In 2001, a chain implosion of 6,779 PMTs out of 11,146 took place at Super-K. It was triggered by an accidental implosion which was transmitted to other PMTs as pressure pulse. In order to avert a similar accident, a protective cover made of a UV transparent acrylic cover for the detection area and an FRP (Fiber Reinforced Plastics) for the rear was introduced in Super-K.

The HQE B&L PMT bulb has been improved for a test and its specification allows the bulb to survive under 60 meter water, which is better than Super-K PMT specified for 40 meter deep water (Section II.2 F 2 2.2 2.2.2). However, we expect it is very hard to ensure no glass failure of so many photosensors at all, even with a pre-selection (using a quick pressure test, etc.) before the installation into Hyper-K. Therefore, a protective cover is needed to avoid any cascade implosion of the photosensors, making up for the difficult control of the glass quality in the production.

The cover needs to be re-designed to further reduce the impact of pressure pulse, because a 60 meter water depth boosts the peak pressure caused by the implosion by a factor of 1.6 from Super-K, corresponding to 2–3 MPa. The new design of the ID photosensor cover and its validation are explained in this section.

2.2.1. Design and Confirmation Test

The weakest point of the Super-K PMT around the largest reverse curvature (Neck in Figure 67) was improved for the HQE B&L PMT. Based on a stress analysis, the first bulb shape, R12860-A, was designed to reduce a stress concentration around the neck. Further improvement was achieved as R12860-B by optimizing the curvature because there was a crack observed on the photocathode surface of R12860-A (in Figure 67) by a high pressure water test.

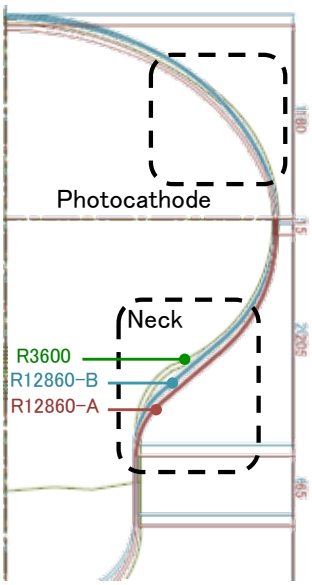

FIG. 67. Comparison of the glass bulb curvature between R3600 and R12860 PMTs.

To validate the degree of improvement, a dedicated test of the PMT in water under high pressure

was performed. In a high pressure vessel filled with water, one PMT was tested with increasing the pressure by a step of 0.1 MPa above 0.5 MPa and waiting for 7 minutes in each step.

At first, we have tested 35 samples of the initial prototypes (R12860-A), and the depth range of implosion or crack was between 70 and 155 meters pressure water (Figure 69). According to a survey of the glass thickness before the test, weak samples imploded around shallow 70–100 meters are found to have a thin thickness of around 2.0–2.5 mm at the thinnest point as in Figure 68. Such a bulb with a thin thickness will be rejected by measuring the thickness during quality control. The glass quality, as for bubbles, foreign matters, cracks and thickness, is expected to be improved after training a bulb blowing over a year before the mass production.

The R12860-B PMT improved with the new shape was also tested. The 21 R12860-B PMTs out of 25 did not implode up to 1.5 MPa (Figure 68). All tested PMTs got a sufficient high pressure resistance for the 60 meter water depth of Hyper-K. It should be noted that the test performed this time was in several different conditions of PMT length or waterproofing, in order to find the best design with high pressure bearing.

One of the two PMTs imploded between 1.2 and 1.3 MPa has the thinnest thickness of glass around the neck part in the tested 25 R12860-B PMTs and another one got a crack around the metal pins in the back where is the weakest part in R12860 by the stress analysis. The latter has a waterproofed guard cover around the pins with the same design as the R3600's, while its material made of Polyethylene is not sufficiently hard to guard the glass against a high pressure water above 1 MPa level. Thus, the guard cover was improved with a new hemisphere design made of PPS (Poly Phenylene Sulfide Resin) and adopted for the test of a hundred of PMTs as described in Section II.2 F 2 2.2 2.2.2.

2.2.2. Quality Control of the PMT Glass Bulb

The glass bulb is manufactured by hand; therefore it is difficult to expect uniform thickness throughout the mass production. In order to reject a possible failure, the glass thickness is checked by an ultrasonic thickness gauge at measurement points. Also the bulb is inspected by eye to find an unexpected crack, foam and foreign matter. As indicated in Figure 68, it would be effective to minimize the failure.

Eventually after the production, individual PMTs will be tested before the installation. It is planned to load a high pressure in water quickly before the installation to the Hyper-K tank, in order to reject a bad bulb. In case of Super-K, 4,727 PMTs were checked with 0.65 MPa high

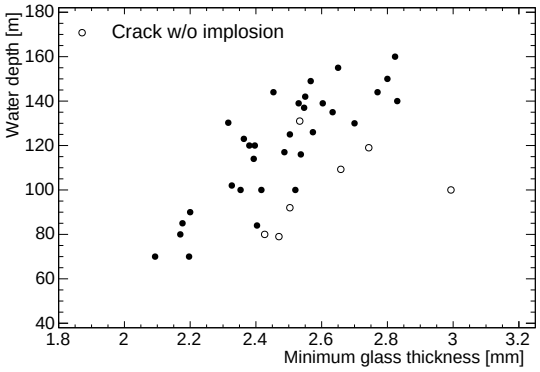

FIG. 68. Relation between a broken pressure in water depth and minimum glass thickness around the neck and photocathode of R12860-A. Several PMTs without imploded but cracked are shown in a blank circle.

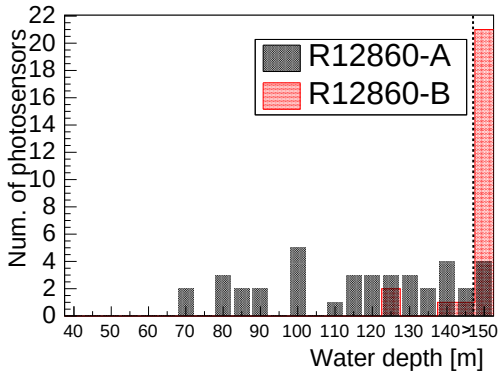

FIG. 69. Broken pressure in tested R12860-A and R12860-B samples up to 1.5 MPa.

pressure water to be safely used up to 40 m water depth for the reconstruction after the accident. Sixteen PMTs of 4,727 were rejected by the test, that is 0.3% fraction.

Before the mass production of photosensors for Hyper-K, we performed the quality check similar to that in Super-K using a hundred of R12860 PMTs. At this time, the load pressure is assumed to be 0.95 MPa for the use in 60 meter water corresponding to 0.65 MPa for 40 meter in Super-K. So far, fifty PMTs were tested after the production and there was no damage at 0.95 MPa. All of 50 PMTs were also tested up to 1.25 MPa for further investigation, but there is no damage in all PMTs as well. The PMTs are used for the chain implosion test.

In order to set the best criteria for the mass production, the checks were done in detail.

- Remarkable failures such as bubbles, foreign matters and striae were recorded and taken by pictures during the quality check with measuring the size and counting the number of those.
- The glass thickness was measured at 57 points.
- Waiting time at high pressure is a little long for 10 minutes.

For the mass production, the selection criteria and condition will be optimized according to this test. It is noted that the photocathode and dynode are absent, but it does not matter because we only investigated the mechanical characteristics without measuring the detection performance.

We plan to test another 50 PMTs by the end of 2016 fiscal year. Although the design of the R12860 PMT is same as the previous test, the production will be improved as below.

- The metal mold will be renewed in order to use much glass as possible.
- The amount of glass will be controlled to suppress an individual difference with much glass by an automated machine.
- The measurement of glass thickness will be automated precisely and quickly with preparing a dedicated setup.

We could have a prospect of the yield ratio according to the test in an order of one percentage. The efficient criteria of the quality check will be considered for the mass production later.

2.2.3. Degradation of the PMT Glass Bulb

As for a degradation of the glass material, the HQE B&L PMT uses stable glass made of borosilicate like Super-K, which is highly resistant to an aqueous corrosion. test for the glass plate, in 100% humidity air at 121°C and 0.2 MPa for 17 hours, showed almost no optical degradation, where the largest degradation is about 1% only seen at around 350 nm wavelength and negligibly small. A test to immerse a glass powder in 98°C boiled pure water for an hour showed a small 0.03% dissolution in weight, which is very low compared to existing glass.

Mechanical characteristics were evaluated on PMT sampling glasses of four different points in PMT, taken from the bottom of the Super-K tank after 5-year running. A composition ratio of material and bending strength are surveyed, and found to be comparable with other Super-K PMTs stored in air at atmospheric pressure. The high pressure test was also performed on nine sample PMTs from Super-K – three each from the top, bottom and barrel sections after 5-years in water – and there was no implosion with a 0.65 MPa load.

As for a possibility of a degradation by a glass crystallized, the glass surface was surveyed using X-ray diffraction at the four different points as well. There was no diffraction peak confirmed, which is originated from the crystallized glass, in both two samples; one was stored in air and another picked up from the bottom in Super-K.

The number of dead channels of the ID photosensors is 0.4% after seven years of Super-K operation, including the ones getting wrong cable connections. It might also include PMTs with an unknown crack or implosion, and therefore we would expect a similar rate of glass damage in Hyper-K, 1% at maximum for twenty years.

It is concluded that the borosilicate glass used in the HQE B&L PMT is quite stable by material characteristics for twenty years, and several mechanical tests for the Super-K PMTs after the long

run could find no degradation. The mass production and selection should be well managed such that the physical damage rate is suppressed to 1% level, while few unexpected failures are acceptable because the protective cover definitely avoids a chain implosion.

2.2.4. Shockwave Prevention Covers for PMTs

Necessity of PMT covers As described in previous sections, every effort has been and will be made to avoid a PMT implosion inside the Hyper-K water tank. Based on the knowledge of the mechanical characteristics of the Super-K PMT, the new 50 cm PMT has been designed to have enough strength for the safe use at a water depth of 60 m, and its performance has been demonstrated by hydrostatic pressure tests. The production of the forty thousand PMTs for Hyper-K will be carried out under a strict quality control, and the total inspection of the products including a pressure test will get rid of any individual PMTs having a higher risk of an implosion before their installation.

However, the possibility of a single PMT implosion cannot be zero. To prevent a chain reaction of imploding PMTs caused by the failure of a single one, all PMTs in Hyper-K are housed in the shockwave prevention covers, as are the 50 cm PMTs in Super-K after the catastrophic accident.

Basic design concept The PMT cover for Hyper-K is designed on the same basic concept as that for the Super-K PMT cover design. In both detectors, the PMT cover has several small holes, and the gap between the PMT surface and the cover is filled with the tank water. Since the covers themselves are not usually exposed to the water pressure, there is no need to care about any deformations caused by a long-term exposure to the high water pressure. On the other hand, the PMTs are constantly exposed to the water pressure. In the unlikely event of an imploding PMT, the water pressure is immediately applied to the cover housing the broken PMT. The PMT cover is designed to have enough strength so that it can keep its shape even in such a case. The tank water slowly flows in through the small holes on the cover and fills up the vacuum region made by the PMT implosion. Thus, the peak amplitude of the pressure shockwave is significantly reduced outside the PMT cover and thus cannot cause a chain reaction. The cover also functions as a protector for the PMT in the very unlikely event that a large pressure shockwave occurs.

Super-K PMT covers In developing the Super-K PMT cover, there were strict restrictions on its weight and shape, since the PMT supporting framework constructed in the tank had originally been designed to support the bare PMTs. Among three major candidate designs, the PMT cover formed by combining an acrylic front window and a backside cover made of fiber-glass reinforced

plastic (FRP) was selected in Super-K, since it had been demonstrated by a hydrostatic test and a PMT implosion test that the cover would not be crushed even if the PMT inside would implode. Thus, we determined that the combination of the acrylic and FRP parts with flange coupling bolts was suitable for a possible future PMT replacement work and that the components can be readily produced.

A cover formed by combining two half bodies of a molded acrylic product was another candidate. This full-acrylic cover also was found to have enough mechanical strength for withstanding the water pressure in the case of a PMT implosion, but it was not adopted due to its mass production difficulty and a higher manufacturing cost. A cover composed of an acrylic front cover and a stainless steel (SUS) backside cover was also a candidate, but the SUS cover with a thickness of 2 mm could not pass a PMT implosion test. Due to the restriction on the cover weight in Super-K, PMT covers with a thicker SUS component were not possible.

Cover design selection for Hyper-K Since the depth of the Hyper-K water tank (60 m) is about 1.5 times larger than that of the Super-K water tank (41.4 m), the Hyper-K PMT covers have to withstand the higher pressure in case of an implosion of the PMT inside. The three cover designs which had been studied for Super-K (i.e. acrylic+FRP, full acrylic, and acrylic+SUS covers) can also be candidates for the Hyper-K PMT cover.

However, it is now known that FRP does not just contains much more radioisotopes than those in the PMT glass but FRP itself also emits the feeble light by a chemiluminescence, as observed in Super-K. Since these unwelcome things can produce more background events for low energy physics, we have decided not to use any FRP-made covers in Hyper-K. As for the PMT cover formed by combining two half bodies of a molded acrylic product, there still exist the problems of lower productivity and higher cost. If these problems could be solved within a reasonable time scale, the full-acrylic cover can be an alternative design for Hyper-K.

The cover made of the stainless steel contains less radioisotopes and is suitable for mass production. Unlike the Super-K case, in which SUS-made PMT covers were not adopted due to the weight limit coming from the existing tank framework specification, the Hyper-K tank framework can be designed so that it can support the PMT system including the SUS covers of a sufficient strength. Therefore, we have adopted the PMT cover design of a combination of acrylic and SUS components for Hyper-K.

Hyper-K cover design Figure 70 shows the shape of the Hyper-K PMT cover. The front-side cover with a partial spherical shape is made of a UV transparent acrylic with thicknesses of 14 mm at the center position and 20 mm at the flange part (Figure 71), which is about 1.5 times thicker

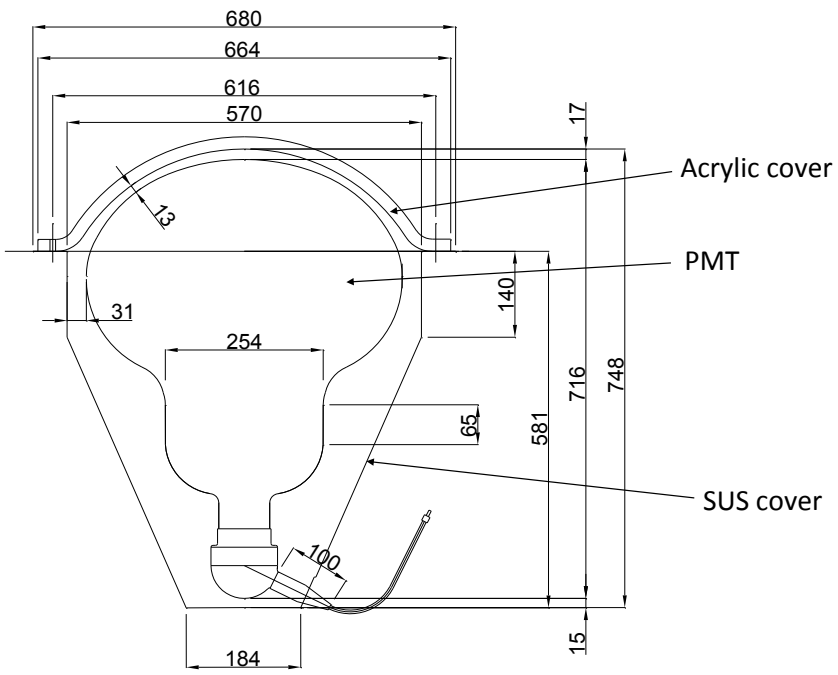

FIG. 70. A schematic view of the shockwave prevention cover for the Hyper-K ID PMTs.

than the acrylic part of the Super-K PMT cover. The light transmittance of the acrylic cover measured in water is more than 95% for a wavelength longer than 350 nm, which is reasonably good considering the quantum efficiency of the 50 cm Hyper-K PMT. Since the section modulus is proportional to the square of the thickness, the Hyper-K acrylic cover could have about twice the strength of the Super-K one, though this is just a crude estimation. The backside cover with a combination of ring and circular truncated cone shapes is made of stainless steel with a thickness of 4 mm. The front acrylic part and the backside SUS part are connected to each other by flange coupling bolts.

The detailed design of the cover, such as a thickness of each part, has been determined based on a dynamic behavior analysis, simulating the situation after a PMT implosion. The analysis has shown that the PMT cover of the design mentioned above (i.e. 14–20 mm acrylic + 4 mm SUS) will not be crushed even if the PMT inside would implode at a water depth of 100 m. The PMT implosion simulation should have some uncertainties, but we think they cannot change the conclusion that the cover will be functioning well at the depth of 60 m. This will be confirmed by the performance demonstration tests described later.

On the acrylic cover, five holes with a diameter of 10 mm are formed; one at the center and four

FIG. 71. Acrylic window part of the PMT cover.

near the flange. These number, diameter and position of the holes on the acrylic cover are the same as those for the Super-K PMT cover. In developing the Super-K PMT cover, the soundness of the holes on the acrylic cover against the water stream caused by a PMT implosion had been checked. The test had shown that the holes were not affected at all by a water stream of 0.65 MPa hydraulic pressure. Therefore, the hole design should be applicable also to the Hyper-K PMT cover. The design of the holes (number, diameter and position) will be optimized if it is found to be necessary by the PMT implosion test described later.

It is known that acrylic resin is a water-swelling material, but it has been demonstrated that its impact strength did not degrade even if the water absorption was saturated. Therefore, if it is confirmed by the PMT implosion simulation that the covers have enough performance to prevent a chain implosion pf PMTs, they are expected to be functioning during a long time use in Hyper-K.

2.2.5. Demonstration Test of Shockwave Prevention Covers

The Hyper-K PMT cover has been designed so that it will not be crushed in the unlikely event of a PMT implosion and will prevent the occurrence of the shockwave causing a chain reaction of imploding PMTs. A simulation shows that the cover will not break even if the PMT inside would implode at a water depth of 100 m. We plan to carry out the following tests to demonstrate that the cover works well in Hyper-K to prevent a chain reaction of imploding PMTs.

One is a hydrostatic pressure test of the PMT covers. In this test, a plastic bag containing a set of the PMT cover is deaerated, sealed, and then pressurized in a pressure vessel filled with water. This test does not completely simulate the situation that the PMT inside the cover implodes but mimics the moment that the open vacuum region is instantly produced inside the cover by a PMT

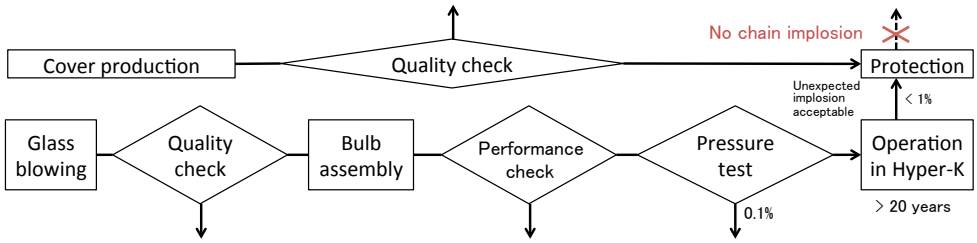

FIG. 72. Flow from the bulb manufacture to the operation in Hyper-K.

implosion. We will confirm that the sealed cover surely withstands the water pressure at a depth of 60 m.

The other is a mock test simulating the event of a PMT implosion in Hyper-K. In developing the PMT cover for Super-K, similar tests were carried out in the actual Super-K water tank. In the tests in Super-K, nine PMTs aligned in 3×3 were mounted on a framework with the same spacing and mounting bracket as those in the Super-K detector. After this mock PMT module was sunk into the Super-K water tank, the center PMT was forced to implode. The design of the covers attenuated the amplitude of the shockwave sufficiently such that adjacent tubes did not break, while the chain implosion of PMTs happened if a bare PMT was broken first. To understand well what was going on, each event was recorded by a high-speed video camera, pressure gauges, and strain meters. We will perform the similar implosion simulation test in a vertical shaft filled with water to demonstrate the cover prevent the PMT implosion at the Hyper-K water depth.

2.2.6. Summary

A possible damage of the PMT bulb is minimized by the improved bulb design, quality check and pre-test in the high pressure vessel before the installation. A schematic flow diagram of various measures to avoid a chain reaction of imploding PMTs is summarized in Figure 72. In general, it is hard to expect there is no implosion occurred in Hyper-K for a long operation of decades. Thus, the protective cover is conservatively designed to avoid any chain implosion by suppressing the shockwave, and this design will be tested in advance of final production.

3. Photosensor for the Outer Detector

The primary function of the Outer Detector is to reject the incident cosmic ray muons that make up part of the background in the measurement of nucleon decays and neutrino interactions occurring in the Inner Detector. The photosensor design for the Hyper-K Outer Detector will be similar to that of the Super-K Outer Detector. The photosensors are Hamamatsu R5912 PMTs with a 20 cm diameter photocathode. The OD PMT array will be sparse relative to the ID PMT array, resulting in a 1% photocathode coverage on the inner wall of the OD. To improve the light collection efficiency by about a factor of 1.5, an acrylic wavelength shifting plate of a 60 cm × 60 cm square shape is placed around the glass bulb of each of the 20 cm OD PMTs.

The pressure tolerance tests have demonstrated that R5912 PMTs could stand enough the water pressure at a depth of 60 m. The risk of a single implosion cannot, however, be zero, therefore the OD PMTs can be also housed in protective covers to avoid making a chain implosion if it is required according to the implosion test.

4. Alternative Designs

There is still a room to improve the Hyper-K performance with new possible photosensors which are under development. The key of the alternative options is to realize sufficient or superior physics sensitivities with proving a long safe use in the water tank at a reasonable cost. All the listed alternative candidates are expected to be ready soon and on time before the Hyper-K construction, but shown as options because the products are not provided as a final design yet.

4.1. 50 cm High-QE Hybrid Photodetector

Another new 50 cm photosensor with the better time and charge resolution in existing 50 cm photosensors is a combination with a semiconductor device, called a hybrid photodetector (HPD) made by Hamamatsu (R12850-HQE). It is almost ready and waiting for a proof test in water. In very near future, the HPD would be a superior option to the PMTs with a low cost, after successful long-term tests of all performance and usability criteria.

The HPD uses an avalanche diode (AD) instead of a metal dynode for the multiplication of PEs emitted from a photocathode. A simple AD structure will realize a good quality control in mass production, and a lower production cost than the complex of metal dynodes. In order to collect

PEs in a small 20 mm diameter area of the AD, a high 8 kV is applied. Related items such as a cable, connector and power supply were also developed.

Figure 73 shows that electrons are multiplied by a factor of 10^5 with a combination of a bombardment gain and then avalanche gain. The gain is adjusted by the bias voltage applied on the AD, around a few hundred volt, while the 8 kV is fixed. The HPD is equipped with a pre-amplifier, so the resulting gain is equivalent to PMTs. The size and surface material are almost the same as that of the 50 cm PMT as shown in Figure 74, thus the same support structure and protective cover as the PMTs can be used.

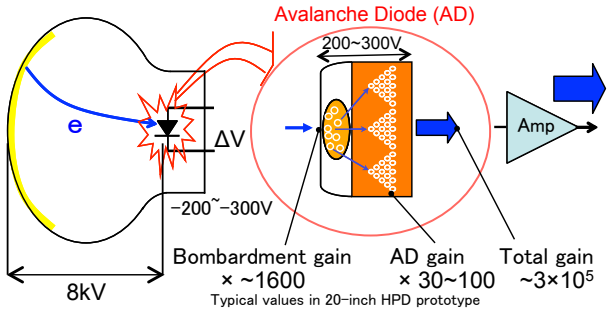

FIG. 73. Schematic view of amplification system on the HQE 50 cm HPD.

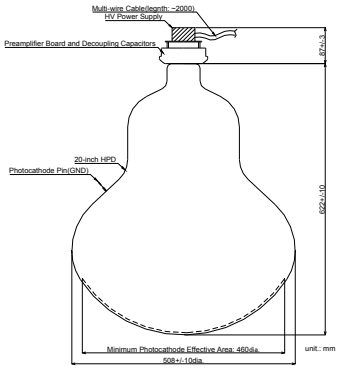

FIG. 74. Design of the HQE 50 cm HPD (before waterproofing).

The single PE detection is quite better, though it is still limited by the pre-amplifier. By using a 5 mm AD in a prototype 50 cm HPD, a 16% charge resolution and a time resolution of 1.0 ns in σ of the faster half from the peak and 3.6 ns at FWHM are obtained at single PE. In the actual application, the 20 mm AD divided into five pixels is considered while improving and optimizing the pre-amplifier in the ongoing R&D.

4.2. Smaller Photosensors

Photosensors with a 20–30 cm aperture can also be an alternative option with the HQE, HPD, and PMT provided by another manufacturer.

4.2.1. 20–30 cm Hybrid Photodetector

A 20 cm HPD (Hamamatsu R12112) was developed with the 5 mm diameter AD, prior to the 50 cm HPD. Most of components such as electronics, design and principle are similar to the 50 cm

HPD.

Using the eight 20 cm HPDs with a design shown by Figure 75, a long time operation of the HPD was established by a test for two years in the 200 ton water Cherenkov detector by monitoring its stability. The dark rate is around 1 kHz and sufficiently low as confirmed in the test. Due to the high single PE resolution, multi-photoelectron peaks can be identified as shown in Figure 76.

Though the 20 cm HPD has already achieved a high CE of 95%, the high QE (30% typical) was also applied for a next upgrade as R12112-HQE with a slightly longer size of the bulb. The total improvement of the photon collection efficiency will be comparable or superior to the conventional OD PMT attached with the wavelength shifting plate.

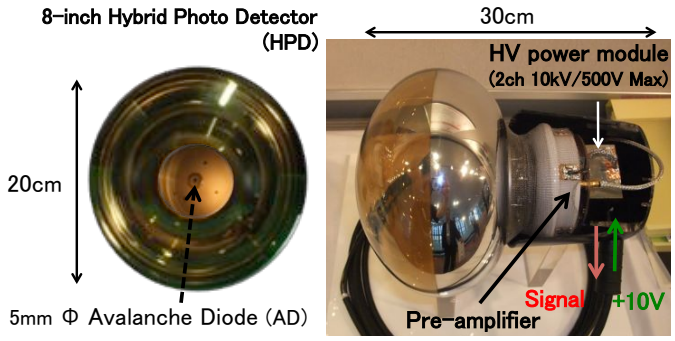

FIG. 75. Picture of the 20 cm HPD layout. The 5 mm diameter AD was located at the center of the HPD face.

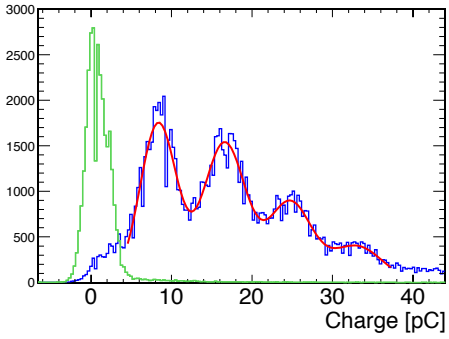

FIG. 76. Photoelectron peaks from one to four in a blue line and pedestal peak in green observed by the 20 cm normal-QE HPD.

4.2.2. 20-30 cm High-QE PMTs

Based on the successful development of the 50 cm HQE B&L PMT, 20 cm or 30 cm PMTs can obtain superior performance to existing small PMTs. By applying the same techniques, the 20 cm and 30 cm PMTs with a high QE box-and-line dynode and improved performance will be available easily by scaling the 50 cm PMT down with a similar design. The performance is expected to be equivalent or better compared with the 50 cm HQE B&L PMT.

Prior to that, the HQE 30 cm PMT, R11780-HQE by Hamamatsu, was developed aimed at a large water Cherenkov detector planned in US for the LBNE project. It reached a QE of 30% and pressure rating over 1 MPa. Further improvement was tried, and a new bulb design of the HQE 30 cm PMT based on the R12860-HQE and R11780-HQE was made. In order to validate the high pressure tolerance, a test in a high pressure water was performed on three samples at Kamioka.

As a result, all the samples got no implosion up to 150 meter water equivalently. hour.

Until recently, photomultiplier tubes with an aperture over 25 cm have been almost exclusively supplied to the market by Hamamatsu. It is important that additional vendors come in the marketplace for price competition and for additional supply capacity.

ET Enterprise Limited ADIT, now a US-based PMT manufacturer in Texas, has been developing a large area PMT, financially supported by NSF. Testing of the operational first generation 28 cm HQE PMTs have been performed at Pennsylvania, UC Davis, etc. showing comparable efficiency and charge measurement performance to those of similarly-sized Hamamatsu HQE PMTs.

If successfully produced, the PMTs can be a cost-effective alternative to Hamamatsu for Hyper-K OD PMTs.

4.3. Multi-Channel Optical Module

The concept of an optical module with a 20 to 40 cm PMT housed in a glass pressure vessel has been developed the past decades for neutrino telescopes in water and ice (DUMAND [126], Baikal [127], NESTOR@ [128, 129], ANTARES [130, 131], AMANDA [132] and IceCube [133]). For KM3Net [134], the km^3 neutrino observatory under construction in the Mediterranean, a single large area phototube has been replaced by 31 7.7 cm PMTs packed in the same glass pressure vessel. This new concept, in which small PMTs replace a single PMT, has been dubbed "multi-PMT Optical Module (mPMT)". the major advantages is that the price per photocathode area is much cheaper than for the 20 to 40 cm PMTs. While the total photocathode area is the same or even larger than in the case of a single, large PMT, one gets an increase in segmentation by a factor of 30. This helps in distinguishing single-photon hits from multi-photon hits from coincident signals in neighboring PMTs. As the single PMTs all have different orientations, the mPMT carries information on the direction of each detected photon which can be used for triggering and improved signal-to-noise separation for low energy signals (eg. neutron tagging as in Section III.2 B). The increased granularity and directionality will also improve the reconstruction performance, especially close to the inner detector wall. An additional advantage of small PMTs is their much lower sensitivity to the Earth's magnetic field, which makes magnetic shielding unnecessary [135]. The failure rate of small PMTs is of the order of 10^{-4}/year. Any loss of a single PMT would affect the detector performance minimally compared to the loss of one large area PMT.

The technology of mPMTs for neutrino detection is mature and well tested by the KM3Net collaboration, while it is currently being explored by the IceCube-Gen2 collaboration [47]. In

addition to its performance, the cost effectiveness of this design is a major driver for both neutrino experiments. The design of a KM3Net mPMT module is restricted by the size of commercially available transparent pressure vessels: borosilicate glass spheres with a diameter of 33.3 cm and 43.5 cm. Hence, one of the main challenges existed in the maximal mechanical packing of as many cheap, high quality 7.7 cm PMTs as possible inside these spheres [136]. For IceCube-Gen2, the maximum size of the borehole and the temperature in Antarctic Ice add additional challenges to the development of a different type of a mPMT module [137]. Both neutrino telescopes instrument the water or ice up to about 2,500 m depth and therefore have pressure requirements up to 700 bar on their pressure vessels. Ref: Lew Classen ICRC for PINGU: Used PINGU-LoI and Kappes's latest talk at VLVnT15.

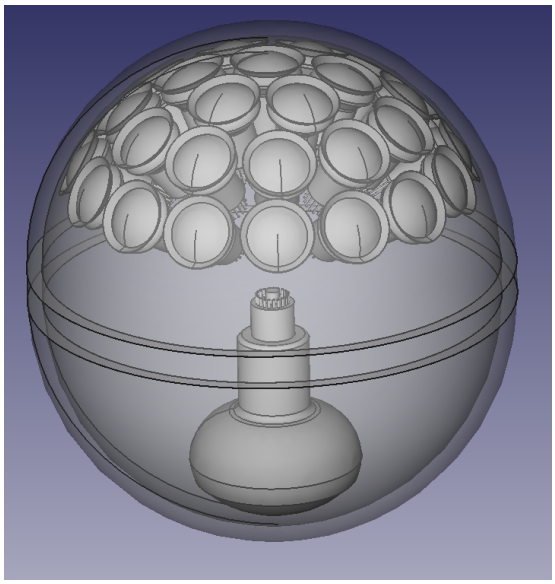

FIG. 77. Multi-PMT conceptual drawing with 33 7.7 cm PMTs as ID detectors and one 20 cm PMT in the OD half. While each small ID PMT has a reflector cone, many light enhancement options are possible for the OD PMT. A 16 mm thick acrylic vessel is used as pressure vessel. The ID PMT orientation is chosen such that shadowing from nearby modules is limited.

FIG. 78. A Hamamatsu R12199-02 7.7 cm PMT that is currently used in KM3Net and considered for IceCube-Gen2 modules. As this passed the Hyper-K PMT requirements, it is also a good candidate for a Hyper-K mPMT.

For Hyper-K the pressure requirements are not as stringent as for deep neutrino telescopes. However, a pressure vessel in either glass or acrylic would protect the PMTs from any external water pressure. The lower pressure requirements also and limit shock waves do not restrict the vessel to either 33.3 cm or 43.5 cm diameter glass spheres. The baseline design of a Hyper-K mPMT

would replace each 50 cm PMT by 33 7.7 cm PMTs in a half sphere with a radius of about 26 cm in order to fit them mechanically as illustrated by Fig. 77. When reflector cones are added to each 7.7 cm PMT to increase the effective photocathode area by about 30%, we get the same effective photocathode area as a single 50 cm PMT. The 7.7 cm PMTs will be supported by a 3D printed foam structure and optically and mechanically coupled by Silicon Gel to a 16 mm thick acrylic pressure sphere. The angle of the first circle of 7.7 cm PMTs with respect to the base plane of the hemisphere is chosen such that their main viewing angle is above the neighboring mPMTs to minimize shadowing effects. According to the design of the OD, explained in Section II.2 F 3, OD PMTs can now be encased in the opposite hemisphere and use the same electronics as the 33 ID PMTs. In between both hemispheres a 40 mm cylinder exists for OD PMT base and the electronics. The penetrator, which connects the signal and power cable to the module, would be connected to the cylindrical side of the mPMT module. An additional advantage of this design is the increase of the fiducial volume by reducing the dead space between the ID and OD while a standard black sheet can still maintain the optical separation.

Currently, there are two main candidates for 7.7 cm PMTs that have been developed specifically for KM3Net, the Hamamatsu R12199-02 (see Fig. 78) and the ET Enterprises D792KFL/9320KFL. They have been measured in detail [138–140] and would be adequate for Hyper-K. Both PMTs use standard quantum efficiency photocathodes but have a high peak QE of $\sim$ 27% at 404 nm. Their collection efficiency is more than 90%. The transit time spread is about 4 ns at FWHM and the dark rate is 200-300 Hz. Active development of these PMTs is still in progress, which will reduce the cost and increase their performance in the next years.

The price for $\sim$30 7.7 cm PMTs is comparable to the price of one large area 50 cm HQE B&L PMT. In addition, the cost could be reduced due to the competition between several companies like Hamamatsu and ET Enterprises in the next couple of years. Additional cost savings come from the reduced magnetic field sensitivity of small PMTs, which make the magnetic field coil described in Section II.2 D 4 redundant. The front-end electronics will be situated in modules in the water near the PMTs which need to be pressure tolerant, water-tight and use water-tight connectors (see Section II.2 G 1). This cost can be reduced by encasing the front-end electronics inside the same pressure vessel as the ID and OD PMTs. The HV generation for each ID PMT can be done on a board attached to the PMT base. Only one water-proof cable for both communication, LV and signal can then be connected to the whole module through a penetrator, as done in previous deep water neutrino experiments. The glass or acrylic pressure vessel is cheaper than the vessels used in deep underwater or ice neutrino telescopes and similar in price as the protective cover required

for the single large PMTs.

A flexible implementation in the simulation software WCSim (see Section II.3 A) makes optimization of the reference design possible and will be the main topic for further study together with further improvement of small photosensors. Based on the results of the optimization studies facilities a prototype mPMT will be built and tested.

5. Schedule

Before the photosensor mass production, it takes 0.5 year to complete a design of a production line, and 1-1.5 years for the setup and startup of the equipment in the factory. The capacity of the factory production is expected to be 11k 50 cm and 4k 20 cm photosensors per year.

Remaining items on research and development are validations on final designs. The validation of the ID protective cover requires a year from early 2016 by performing chain implosion tests in deep water. Necessity of the OD cover is also judged with the test.

A Hyper-K prototype test using two hundreds of the photosensors starts from 2017 to validate the photosensor, its cover and supporter in water. Moreover, criteria for the quality control including a selection with high pressure load will be established.

Table XVII summarizes the default design and improved alternatives as for photosensors described in this section. Even without the alternatives, Hyper-K would gives the sufficient performance with the realistic time line in the default options. Further improvements would be surveyed in near future and ready on time of the Hyper-K construction to consider the improvement.

Items	
ID photosensor	**HQE 50 cm B&L PMT (Hamamatsu R12860-HQE)**
(Alternative)	HQE 50 cm HPD (Hamamatsu R12850-HQE)
OD photosensor	**20 cm B&L PMT (Hamamatsu R5912)**
(Alternative)	HQE 20 cm HPD
(Alternative)	HQE 20-30 cm PMT
(ID and OD photosensor alternative)	Multi-channel optical module
ID cover	**Acrylic and stainless steel**
(Alternative)	Full acrylic (or acrylic and other resin)

TABLE XVII. Summary of the current base design in bold type and alternative options related with photosensors.

G. Frontend electronics

1. General concept of the baseline design

If we want to detect the neutrino from nature, it is not possible to tell when and where a neutrino interacts in the detector. Therefore the front-end electronics modules for this kind of detectors are required to digitize the signal from a photosensor above certain threshold channel by channel without any external signal. The digitized information are read out appropriately or discarded depending on the design of the trigger system.

Current design of the HK detector is quite similar to the SK detector, in terms of the required specifications and the number of photosensors in one detector. Therefore, it is reasonable to start with the system used in the SK detector.

The signal shape from the photo-sensor for HK are expected to have similar shape from the 20 inch PMT, R3600, used in the SK detector. The dark (noise) rate is required to be $\sim$ 5-10 kHz, which was set to be higher than R3600. Under the current baseline design, the number of PMTs in one detector is 50,000 PMTs. We have estimated the total data rate and concluded it is possible for us to design the data acquisition system using almost the same concept to develop the one for SK-IV.

As already realized in the SK-IV DAQ system, it is possible to read out all the hit information from the photosensors including the dark noise hits. There is no technical problem in selecting the actual events to be recorded for the analyses.

One difference is the size of the detector. The total amount of photo-sensors in one entire detector is expected to be up to $\sim$ 50,000. If we locate the front-end electronics modules on the top of the detector, it is necessary to run the cable from the PMT to the roof and the detector structure has to support the weight of the cable. The amount of the cable weight is non-negligible and thus, it would be helpful if it is possible to reduce the length of the cables. Also, the maximum length of the cable is $\sim$ 30% longer than SK. This also reduces not only the signal height but also the quality of the signal. Considering these issues, we are now planning to place the front-end electronics module with the power supply for the photo-sensor in the detector water, close to the photo-sensor. This configuration makes it possible to have shorter signal cables from the photo-sensors and to reduce the weight, which has to be supported by the photo-sensor support structure. Of course, it is necessary to make the enclosure of the front-end module pressure tolerant water tight and also to use the water-tight connectors. This kind of "water-tight" casing has been studied

in the other experiments and there are several possible options. One concern is the cost of the special cables and connectors but the number of these components are fairly large and once we start mass production, the price is expected to be reduced.

The other thing we have to keep in mind is the fact that it is almost impossible to fix the module in case of failure. When a failure of one module affects the data transmission from other modules, a much larger region of the detector could be lost . Therefore, the system must be redundant in various ways; for example, avoiding a single point failure and minimizing the affected number of photo-sensors in case of the failure of one module. Also, careful design of the data transport connections and the timing distribution system are essential.

The current baseline design of the front-end module is prepared considering these requirements. The schematic diagram of the front end module is shown in Fig. 79.

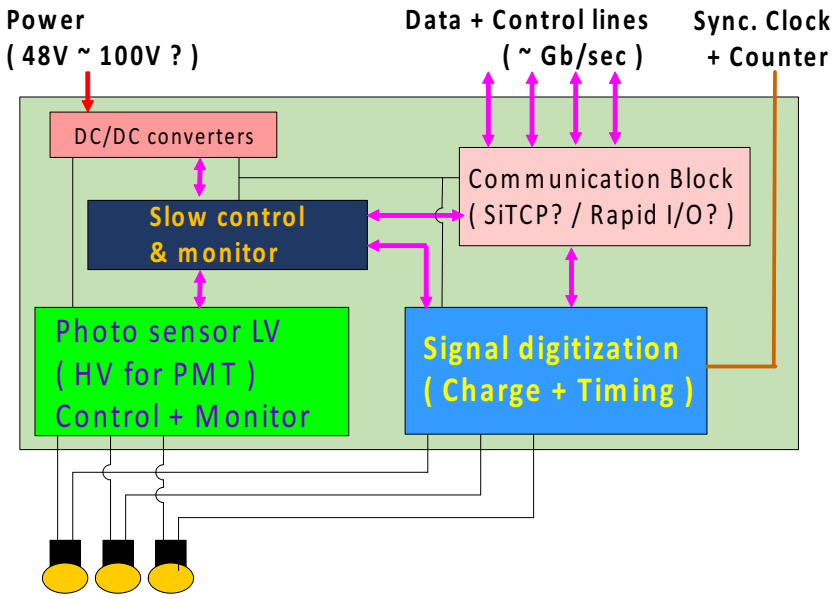

FIG. 79. Schematic diagram of the front-end module.

There are 4 main function blocks in the front end board. The signal digitization block, the photo-sensor power supply block, the slow control block and the communication block. In this design, one module accepts signals from 24 photo-sensors, digitize them and sends out the data.

In the following sections, some details of each component in the front-end module and the data readout and processing part are described.

2. Signal digitization block

The signal digitization block accept the signals from the photo sensors and convert them to the digital timing and charge data. As mentioned in the previous section, there is no way to tell when a neutrino or a nucleon decay event happens. Therefore, the front-end electronics module is required to have self-triggered analog to digital conversion mechanism and to be deadtime-free. The actual event rate is expected to be smaller than a tens of kHz even with the background events from gamma-rays from the surrounding wall or cosmic-rays. Also, the number of PMT hits in the gamma-ray events is quite small, much less than 1% of the PMTs in a compartment. Therefore, the time interval to detect photons in the single photo- sensor is rather long, much longer than the dark rate of the sensor. However, muons decay into electrons in the detector and photons from both of them may hit a single PMT. Therefore, it is necessary to have the capability to detect both photons, generated by the parent muons and the decay electrons. The lifetime of muons are rather long, $\sim 2\,\mu$ sec and thus, it it not necessary to be completely deadtime free but the deadtime should be as short as possible.

One possible way to satisfy these requirements is to employ the Charge to time conversion (QTC) chips. This QTC chip receives the signal from the photo-sensor and produce the digital signal, whose width is linear to the amount of the input charge. Also, the rise time of the output digital signal corresponds to the timing when the input signal exceeded the threshold to produce output digital signal. The digital output signal from the QTC chip is read out by a TDC. The maximum width of the output signal may be slightly longer than the charge integration gate width. Therefore, there is a small deadtime after the first signal but it is no larger than a several hundreds of ns and thus, acceptable to be used in the water Cherenkov detector.

The requirements of the charge and timing resolution is summarized in the Table II.2 G 2.

The QTC chips used in the front-end module of SK-IV called QBEE is a good reference and satisfy all the requirements. Unfortunately, this QTC chip is discontinued and thus, we have to design a new one but should not be difficult. As for the TDC chip used in QBEE, called AMT3 designed for the ATLAS muon chamber, was also discontinued. However, there is a new FPGA-based TDC designed in FNAL. The performance of this TDC is expected to be better than AMT3 and thus, we are considering to employ this TDC design.

As described, current baseline design is to use the QTC with TDC but it is also possible to satisfy the requirements with the Flash ADC (FADC) chips. For this case, a FADC chip has to run continuously and digitizes the input signal all the time. The output data is processed by FPGA

items	required values
Built-in discriminator threshold	1/4 p.e ($\sim$ 0.3 mV)
Processing speed	$\sim 1\mu$sec. / hit
Charge resolution	$\sim$ 0.05 p.e. (RMS) for $<$ 5 p.e.
Charge dynamic range	0.2 $\sim$ 2500 pC (0.1 $\sim$ 1250 pe.)
Timing response	0.3 ns RMS (1 p.e.)
	0.3 ns RMS ($\geq$ 5 p.e.)
Least time count	0.52 ns
Time resolution	0.25 ns
Dynamic range	$\geq$ 15 bits

TABLE XVIII. Specification of the signal digitization block.

to identify whether there is a significant pulse. When a pulse is found, the timing of the signal is calculated using the shape of the wave form to achieve better timing resolution than the sampling speed of the FADC.

The advantage of FADC digitization is that it is completely deadtime free. We would be able to detect photons from both the prompt muon and from decay electrons, even if the decay electron happen only 100 ns after the initial interaction. We may also be able to distinguish photons from direct vs reflected light. However, this system requires larger power consumption and the cost might be higher than the QTC-TDC configuration. Also, it might be necessary to have multiple FADCs per channel to satisfy the requirements of the dynamic range.

In either case, it is necessary to be prepared the failure of the digitization components. We have considering to have a set of spare channels and also, insert analog switches between the signal inputs and the digitization block. With this configuration, we have some flexibility to change the configurations of signal inputs and digitization blocks. This also allows us to check additional way to calibrate the digitization blocks. Of course, analog switch is known to degrade the quality of the signal and thus, we have to be careful before implementing this scheme.

Because the relative timing is used to reconstruct the event vertex in the detector, all the modules have to be synchronized. Therefore, it is necessary to drive the TDC or FADC by a clock synchronized to the reference clock fed externally. Also, the system-wide counter is attached to the data to combine the data from different modules in the later stage.

3. The timing synchronization block

Synchronization of the timing of each TDC or FADC is crucial in measuring the arrival timing of photons precisely. Also, fluctuation of the clock makes the timing resolution worse. In Hyper-Kamiokande, timing resolution of the photosensor is expected to be largely improved. Therefore, we have to be careful in the timing synchronization of the modules. We are planning to distribute the common system clock and the reference counter to all the modules. We have not started the actual design of this system but there are several existing examples. The first method is to send the clock and serialized 32 bit counter information using special STP cable, called nano-skew cable, whose skew is less than a few nano seconds for 100 m cable. This system has been used in current SK DAQ system and the skew is measured to be much smaller than 100 ps. This system requires intermediate timing distributer and thus, need to be modified to be used in Hyper-Kamiokande but it is not difficult. The other possibility is to use the idea of White Rabbit. The White Rabbit system is designed for the synchronization in the accelerator complex and correct the timing differences with measured delay in each node. It is not necessary to implement entire functionality of White Rabbit for our case but employ the main part of the timing synchronization and stabilization.

4. The photo-sensor power supply block

If HPDs are used as the photo-sensor, it is necessary for the front-end module to control the acceleration and the APD bias voltages on HPD base.

If the normal PMTs are used as the photo-sensor, we are considering to put the high voltage module in the same enclosure as front-end module. In this case, the control signal is fed not to the sensor but the internal high voltage modules.

The configuration of control signals to HPD or the internal high voltage modules are configured externally through the communication block.

5. The slow control and monitor block

It is important to control and monitor the status of the power supply for the photo-sensors. Also, the voltage, the current and the temperature in the front-end module has to be monitored. This slow control and monitor block is prepared for this purpose. This block accepts the command from the communication block and also keep the current status, which are accessed externally through the communication block.

6. The communication block

The communication block can be divided into two parts, the data transportation part and the slow control and monitor part. In order to reduce the amount of cables, we are planning to connect the modules each other and only the top modules are connected to the readout computers. Of course, it is necessary to avoid the single point failure, and to secure the communication path even if one of the module fails, we are planning to have several communication ports and connect more than one module as shown in the Fig. 80. With this configuration, we always have alternative route to transfer the data by skipping the failed module.

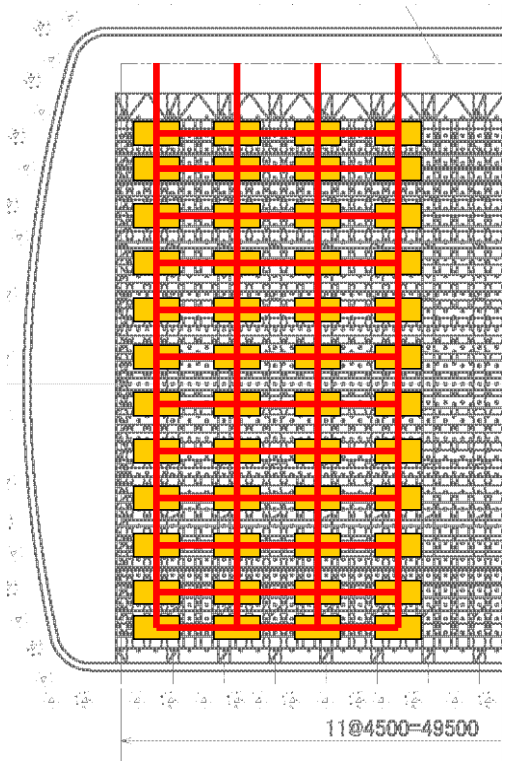

FIG. 80. Schematic diagram of the connections between front-end modules.

There are several possibilities for the connection but one of the promising one is SiTCP, FPGA based TCP/IP stack. This TCP/IP stack does not require CPU core in FPGA and accessed like a simple FIFO buffer. SiTCP acts as either TCP/IP server or client, it is possible to receive data from the other module and add the data from its own and send them to the next module. Also, SiTCP has registers, which can be accessed via UDP commands. With this functionality, it is possible to realize the slow control and monitor system, such as setting the high voltage or monitoring the status like the read-back voltages of the power supply. Recently, CPU cores are

embed in the FPGA chip. With this kind of chips, TCP/IP communication part is also possible to be handled with the embed CPU. We will investigated this possibility. Apart from TCP/IP, there are several other industry standard communication protocols available. One example is the Rocket-I/O. Rocket I/O is the standard in interface supported in Xilinx FPGA. This allows us to transfer data more than a gigabit per second. We are also investigating this possibility for the faster communication between the modules.

7. Timeline

Currently, we are studying two possible digitization scheme, QTC+TDC and FADC. Simultaneously, two communication method, SiTCP and Rocket I/O, are also under testing. We are planning to develop the evaluation boards from the next year (2016) to be used in the Hyper-Kamiokande test detector and evaluate the performance with the actual detector system. It is expected to take 2 to 3 years to finalize the design of the modules after deciding the digitization method and the communication scheme, including the test production and evaluation. Once the mass production starts, it is expected to take another 2 years to prepare all the modules. In total 5 years are necessary. This means that all the preparation has to be finished just after the actual excavation starts.

H. Data acquisition system

1. Data acquisition and triggering

All PMT hits from the detector (above a threshold of ~ 0.25 p.e.) will be delivered to the data readout and processing system where they will be formed into events and recorded on disk for further processing offline. The overall rate of hits (mostly from dark noise) from the inner detector will be about 460 MHz, leading to a total input data rate of 5GB/s including additional data, in the absense of waveform information. The OD adds less than 10% to this data load. To reduce the data recorded, trigger decisions will be made using real-time processing of the hits in the detector. Events will be formed from all hits within a time-window surrounding the trigger and recorded to disk for offline study.

The main trigger will be the same as that used in SK-IV; a trigger will be generated when the total number of hits seen (NHITS) in a sliding time-window exceeds a certain threshold (e.g. 27 hits). This trigger will accept all the necessary data for studies of proton decay, atmospheric neutrinos, beam neutrinos and cosmic ray muon events. It is important that there is no dead time in the triggering or data collection so that delayed energy depositions following a triggered event, such as from a Michel electron or neutron capture, are recorded, either as part of the same event or separately. More sophisticated trigger algorithms, which can be added into the architecture, are being studied to increase sensitivity to lower energy events (by distinguishing events with fewer hits from random combinations of dark-noise hits) and detection of supernova bursts (by observing elevated trigger rates). As in Super-K, an additional trigger input will be derived from the J-PARC beam-spill gate to define readout windows around the beam spill time, independent of the number of hits observed. Triggers will be defined to receive calibration events. Also, external trigger inputs are necessary to take the calibration data with synchronized timing. The estimated rate of events is shown in Table XIX for readout with the hit-only electronics, which require 12 bytes per hit (the waveform option needs a factor four higher bandwidth, ~ 50 bytes of information per hit).

A requirement of the data acquisition system is to reliably trigger and collect information from a supernova burst. This is one of the more challenging design aspects and benefits from the large memory buffers available in modern commodity hardware, sufficient to retain all raw hit information for around 100 s of detector operation. Two modes of operation are foreseen. In the first, the detector will self-trigger on a supernova burst by searching for an elevated rate of individual triggers in a sliding time-window e.g. 0.1 s. If such a trigger occurs, all raw hit information in a large time

TABLE XIX. Estimates of data rates. The rate for each physics process is given: "pre-trigger" is the rate before the trigger, Post-(a) is the data in the physics hits after the trigger and Post-(b) is the total data after triggering, including the dark-noise in the trigger window. In all cases, the dark noise dominates the data throughput requirements.

Data source	Event rate (gate width)	Hits/event	Data rate Pre-trigger	Data Rate Post-(a)	Data Rate Post-(b)
Dark noise	10 kHz each in 46,700 PMT	1	5.6 GB/s	–	–
very low energy background	10 kHz (1.5 μs)	25	3 MB/s	3 MB/s	87 MB/s
low energy background	35 Hz (40 μs)	50	21 kB/s	21 kB/s	7.8 MB/s
Cosmic muons	100 Hz (40 μs)	46,700	56 MB/s	56 MB/s	78 MB/s
Beam events	1 Hz (1 ms)	0	0 MB/s	0 MB/s	5.6 MB/s
Calibration	2 Hz	46,700	2 MB/s	2 MB/s	2 MB/s
Pedestal	1 Hz	46,700	2 MB/s	2 MB/s	2 MB/s
Total rate				63 MB/s	183 MB/s

window around the supernova trigger would be saved in the local hardware and then slowly written to disk. Note that even a close supernova burst yielding 100,000 events per second of 50 PMT hits each (5 million hits/s) will not overwhelm the readout which is designed to continuously read 460 MHz of dark noise hits. In the second mode of operation, a large storage buffer on hard disk drives is used to save all the hit data, overwriting the oldest data. An external observation may reveal up to a few hours after the event that a supernova signature was seen, perhaps in a neighbouring galaxy, in which only a few events are expected to be observed in Hyper-K.

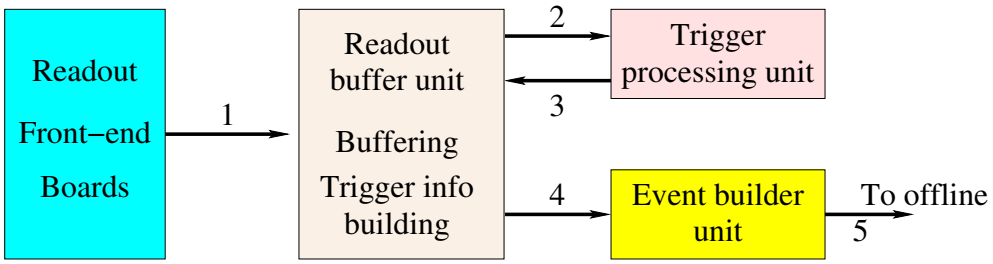

FIG. 81. Simplified block diagram of the readout showing the sequence of data transfers.

Figure 81 is a schematic diagram of the data readout and processing system showing the five steps in the sequence of readout operations. The main components are readout buffer units (RBU) that receive PMT hit (and possibly waveform) data from the front-end boards, trigger processing

units (TPU) and event building units (EBU). The sequence of operation is indicated by the numbers 1-5 on Figure 81: (1) Data on hits in a group of channels are streamed into buffers in the RBUs, where they are retained for the duration of the trigger decision. (2) A summary block of information for triggering is sent to the TPUs. (3) Trigger decisions are delivered back to the RBUs to extract event data from the buffer. (4) The event data are sent to the EBUs. (5) Built events are written to disk for later processing offline. A description of each of the blocks shown is given in the following sections. The DAQ system will be designed to be homogeneous, flexible and scalable.

Parameters of the readout system, including data rates at each point in the sequence of readout operation are shown in Table XX. Since the architecture is flexible, the additional data generated by the waveform option is easily accommodated, although with a larger number of RBUs.

TABLE XX. Parameters of the readout design.

Parameter	Hit-only option	Waveform option
Pre-trigger input data rate	5,600 MB/s	23,400 MB/s
Number of RBUs	38	122
Input rate to each RBU	150 MB/s	188 MB/s
Latency provided by RBU (pre-trigger buffer length)	109 s	87 s
Trigger info output rate per RBU	50 MB/s	15 MB/s
TPU data input rate (for 16 TPUs in detector)	117 MB/s	117 MB/s

2. Readout buffer unit (RBUs)

The RBUs receive continuous streams of data from the front-end cards and perform three main tasks. First they store incoming data in buffer storage. A short-term store of the most recent data is retained whilst trigger decisions are made and a long-term storage area is reserved in case of a supernova event until it can be read out. Second, it forms a compressed block of data which is handed to the TPU for trigger decision making. Finally, the RBU handles trigger requests to dispatch complete event data to the event builder unit, and supernova trigger requests to move data to the long term storage area. Since the detector is large, and to allow scalability, there are many RBUs working in parallel, each responsible for processing data from a designated region of the detector. In the current design of 45,000 PMTs, between about 40 and 120 RBUs will be required depending on the amount of data received per hit, and each will use 16 GB of memory to provide the necessary storage. The RBU design is largely independent of whether there is one

40%-coverage detector or several 14%-coverage detector caverns.

The final design of the RBUs depends on the layout and interface of the upstream electronics. Possible implementations use either commodity computers with commodity network switches to direct the data, or hardware receiver cards in a communication-crate such as ATCA with a commodity computer as a controller. The RBU may also include an interface to the upstream link for monitoring information.

3. Trigger processing unit

The Trigger Processing Units (TPUs) will accept compressed trigger data blocks from the RBUs and use these to form trigger decisions, such as the simple, robust NHITS trigger. Hooks will be provided to allow for more sophisticated triggering. The trigger will also search for large collections of individual events, which may indicate a burst of neutrinos from a supernova explosion in the galaxy.

The trigger will operate using windows of fixed time duration (e.g. 60 per second) in order to allow the trigger processing to be parallelized. This allows for a scalable design that can be extended easily should e.g. the noise be larger than expected. One TPU is allocated for a given time window and will process all the data in that time window. The TPUs are connected to the RBUs by a switched Ethernet network to allow the data from the different RBUs (one for each section of the detector) to be routed to the correct TPU. The data is transferred asynchronously and the TPU starts processing when all data packets have arrived.

The trigger information can be compressed into a 32-bit word per hit to identify the channel number within the RBU (10 bits) and the time within the window (21 bits) to 10 ns accuracy (better time resolution is not needed in the trigger) and one spare status bit. The trigger information can be truncated if it is clear that the NHITS trigger will be satisfied from the data in that one RBU alone, as in this case, the event is guaranteed to be collected without further transfer or processing of trigger data. For this level of packing, the output rate per RBU will be about 30 MB/s and if a farm of 16 TPUs is used, the input rate to each will be around 100 MB/s. The final design of the TPUs is largely independent of the choice of front-end electronics, because the RBUs provide the trigger data in the same format regardless.

The TPU design depends on the type of processing required for the sophisticated triggers. One possible implementation is for the Ethernet packets to be received in FPGAs housed in ATCA crates or similar where the data are processed. A second possibility to implement the TPU on

a commodity computer. In this implementation data packets would be received into the main memory of a commodity computer and the processing to occur in FPGAs or GPUs that read the data over PCIe links and deliver the trigger verdict for a given time block back to the main memory.

4. Event Building Unit

Once the trigger decision has been made for a time-window, the decision is reported back to a central trigger control process, from where it is delivered to the RBUs. The request contains an event number, and the definition of the position and width of the trigger window. The central trigger control process also looks for an increased rate of positive triggers, which would be indicative of a supernova burst, and in such case sends the RBUs an instruction to save the relevant data in the long-term part of the buffer memory.

On receipt of a normal trigger, the RBUs send all the hits in the trigger window to a designated event-building node, which puts the event together and writes it to the output file. Once the file reaches a certain size, it is closed and released for offline processing, and new events are recorded in a new output file without interruption. The event builders also allow events to be read by monitoring and event display programs. Once a supernova trigger has occurred, a separate event-building stream is used to gather the data in the long-term part of the RBU memory and output it to a separate file. There will be one file per supernova trigger. A straightforward implementation of the event builders is to use commodity computers.

5. Redundancy and partitioning

Different architectural schemes are being considered for increasing the robustness of the acquisition of data, in particular to avoid a situation that no data are collected in the event of a supernova. If the chosen detector is a 14%-coverage, three-tank design, then the three detectors will be partitioned and thus have independent data acquisition systems, however it will be possible to take common triggers across all detectors for high energy events such as those from beam interactions or supernova.

If the single 40%-coverage detector design is chosen, one possible option is to also have three (almost) independent DAQ systems. In this case, the PMTs are divided into three groups which are read out by different readout cards, have independent time distribution networks and are powered by separate low and high voltage supplies. This redundancy yields a DAQ architecture that is

functionlly the same as the three-tank design described above. The performance can be enhanced in this case by correlating the data for the trigger between the three groups, something which we believe can be achieved by careful design of the networking protocols to allow continuous detector operation if parts of the system go offline.

I. Detector calibrations

The Hyper-Kamiokande detector consists of an Inner Detector and an Outer Detector and both detectors need to be calibrated. The Super-Kamiokande detector has been successfully operated for about two decades and established several techniques to calibrate a large water Cherenkov detector [117]. Hyper-Kamiokande calibrations are designed based on and extension of the Super-K calibrations. This section describes the calibration strategy and methods for Hyper-K detector.

1. Inner Detector Calibration

Hyper-K detector calibrations consists of two major phases: calibrations of the detector system, e.g. PMTs, and calibrations dedicated for physics analyses. The calibrations for the detector system is to characterize the PMT responses, including readout electronics, and the optical properties of detector material, e.g. water, PMT (glass bulb and housing material), black sheet, and tyvek sheet. The calibrations for physics analyses are designed to satisfy the requirements from Hyper-K physics program which consists of variety of physics topics covering wide range of energy region, from a few MeV to several hundred GeV. For these calibrations, various calibration techniques have been developed and established by Super-K and they are applicable to Hyper-K calibrations without major technical difficulties.

Table XXI summarizes the calibration items and the calibration sources used in Super-K calibrations for a reference. These calibration items are important to characterize the Hyper-K detector responses, and the calibration results need to be implemented in the detector simulation. As shown in the Table XXI, the detector calibrations require various calibrations sources: light sources, radioactive sources and natural sources. Note that "Nickel source" listed in Table XXI is a calibration source to generate single photo-electron (p.e.) level of light, which isotropically emits $\sim$9 MeV gamma rays from thermal neutron capture on nickel with the reaction of $^{58}\mathrm{Ni}(n,\gamma)^{59}\mathrm{Ni}$, where $^{252}\mathrm{Cf}$ source is used as neutron source. With the use of a Nickel source, for example, "relative" photo-detection efficiency, (quantum efficiency times collection efficiency) of each single PMT is calibrated by evaluating relative differences of the hit rates between PMTs for single photon level of light. The "low-energy physics" events like solar neutrinos mostly consist of 1 p.e. hits and thus the relative photo-detection efficiency calibration plays an important role for the low energy physics analyses. On the other hand, PMT/electronics linearity calibration for the full dynamic range is important for "high-energy physics" events like atmospheric neutrinos, which involves TeV-scale

TABLE XXI. Calibration items for the detector systems and calibration sources used in Super-K.

Calibration items	Calibration sources used in SK
Photosensor & electronics calibrations	
High-voltage tuning	Xe flash lamp
Single photo-electron charge (gain)	Nickel source
Electronics threshold effect	Nickel source
Photo-detection efficiency	Nickel source
Non-linearity (photosensor and electronics)	Nitrogen-dye laser
Overall charge scale	Cosmic-ray muons
'Time-walk' correction (TQ map)	Nitrogen-dye laser
Timing resolution	Nitrogen-dye laser
Dark noise	Off-timing hits
Optical properties of detector material	
Light transparency of water (absorption, scattering)	Nitrogen laser, laser diodes
Optical properties of PMT glass & housing material	(Nitrogen laser, laser diodes, Xe lamp)
Calibrations dedicated for physics analyses	
Solar and supernova ν etc.: energy scale and vertex	LINAC, DT generator, Nickel source
Beam and atmospheric ν etc.: energy/momentum scale and PID	Cosmic-ray muons, decay-e's, π^0

muons. For the linearity calibration, a nitrogen-dye laser is used in Super-K, which is utilized with a variable light attenuation filtering system to obtain a variety of light intensities covering the full dynamic range of PMT and readout electronics ($\sim$0.25 p.e. to 1000's p.e.). In addition to calibrations of PMT and electronics, understanding of optical properties of water plays a key role in all physics analyses of Hyper-K. The water optical properties, absorption and scattering of light, are calibrated as a function of time and position in the detector volume using a series of laser diodes with various wavelengths. Since the detector condition can change from time to time, the continuous monitoring and periodical calibrations of these detector components are also indispensable over the lifetime of the experiment. There are many other calibrations to characterize/monitoring the detector system, as explained in Ref. [117] for further details.

The Hyper-K physics program consist of various physics topics which cover a wide range of energy from a few MeV to several hundred GeV. For example, low energy events like solar neutrinos and supernova neutrinos are in a few MeV up to tens of MeV, J-PARC neutrino beam are around 1 GeV, and atmospheric neutrinos are in a range between $\sim$1 GeV and several hundred GeV. For

physics analyses in each energy regime, there are a series of dedicated calibrations, e.g. energy scale, which are described in the later sections.

For all necessary detector calibrations in Hyper-K, the calibration methods and techniques established in Super-K are sufficiently good enough, and we do not see any technical difficulty to apply them to Hyper-K. We have, however, been developing more sophisticated calibration sources/systems for Hyper-K in order to minimize the detector downtime and manpower required for the detector calibrations since Hyper-K detector consists of multiple detectors and a larger detector volume than Super-K. The following sections discuss the status of research and development for Hyper-K calibrations.

1.1. Detector Calibration Systems

In order to achieve the level of calibration required for the Hyper-Kamiokande physics program we require an extensive calibration infrastructure. Data from in situ sources such as cosmic muons or Michel electrons will be used to supplement the information from these systems, but they cannot replace them. In Hyper-Kamiokande we propose two systems, a source deployment system to allow the deployment of calibration sources across the detector inner region and an integrated light injection system for the inner and outer detector regions. These two calibration systems provide the data that will be required to characterise the detector and reduce the systematic uncertainties to the required level. The integrated calibration system allows for calibration and monitoring of the detector without the deployment of specialised manpower while calibration sources can be used for more extensive calibrations during the time when the neutrino beam is off.

1.1.1. Calibration sources and deployment system

Similar to other water Cherenkov detectors the ability to deploy calibration sources is essential to understand the Hyper-Kamiokande detector. The Hyper-Kamiokande source deployment system will consist of a number of source deployment points above the detector down which calibration sources may be lowered down to any required detector level with high precision. In addition to the z-axis option, that these points provide optionally a full 3D manipulator system may be developed allowing sources to be deployed over a wider range of the detector volume.

In order to calibrate the multiple detectors simultaneously, a computer-controlled source deployment system is desirable. The first prototype of the source deployment system has been developed

(Fig. 82). The system will be installed in Super-K in 2016, and we plan to further develop the source deployment system for Hyper-K based on the Super-K operation experience.

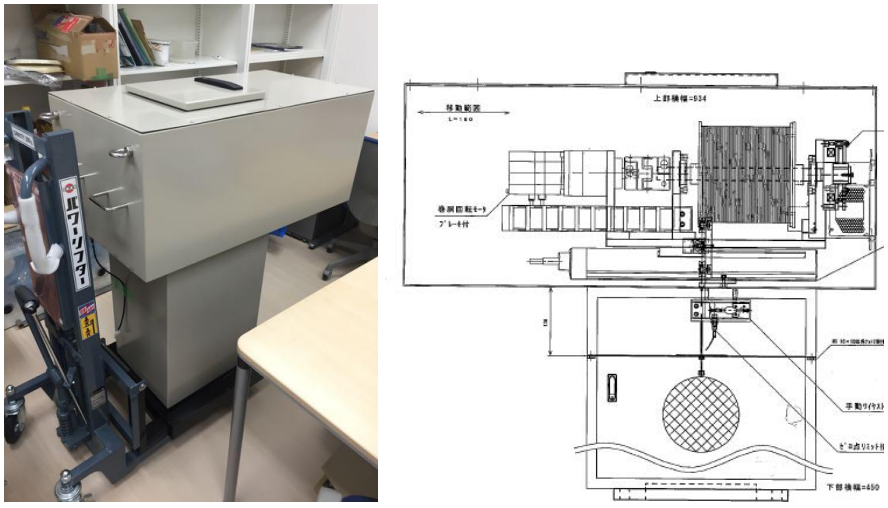

FIG. 82. Photograph (left) and sketch (right) of the first prototype of the calibration sources deployment system.

A variety of sources can be deployed through this system including optical sources for PMT and measurements of detector optical properties, and various radioactive sources. Based on previous experience at Super-K this would include a deuterium-tritium base reaction pulsed neutron generator (DT generator) to create ^{16}N for calibration in the solar neutrino energy regime. A number of sources can be developed to provide neutrons for calibration. These include ^{252}Cf and AmBe sources that were previously used to calibrate the neutron response of the SNO detector. In addition to the conventional neutron sources, we currently explore ideas for compact and pulsed neutron generator [141] for Hyper-K detector calibrations, that uses a similar technology to DT generator but is a palm-size portable neutron generator and can manoeuvre more effectively in detector calibrations. These sources produce neutrons at a known rate, and comparing the rate of measured Gd captures to this rate the neutron detection efficiency and any possible variation across the detector can be measured, should Gd be deployed in Hyper-Kamiokande. Neutron captures on Gd also provide a source of events inside the detector of known energy providing a further calibration of the detector response in addition to the neutron response of the detector. Development of additional calibration sources to exploit this system can be expected over the lifetime of Hyper-Kamiokande.

1.1.2. Integrated light injection system

Hyper-Kamiokande will include an integrated light injection system for optical (extinction and scattering) and PMT (timing, gain and multi-photon) calibrations. This system consists of a number of light injection points connected via optical fibres to light pulsers in the electronics. Light pulses of 1-2 ns can be produced using LEDs, laser diodes (LDs) or similar solid state optical devices can be produced relatively inexpensively. This allows multiple optical sources to be deployed around the edge of the detector that can then be used for calibration. This system consists of an LED (or similar) coupled to an optical fibre, which is then connected to an optical diffuser on the PMT support structure. The optical diffuser is used to shape the light inside the detector and designs can provide different calibration pulses for different needs.

In order to maintain fast light pulses over the order 100 m distance of optical fibres required for Hyper-Kamiokande graded index fibre is required rather than the step index fibre used in for example SNO+. Graded index fibre has a small active core complicating the challenge of light collection. The key challenges of this system are the coupling of the LEDs to the optical fibre, minimising dispersion in the fibre to maintain short optical pulses and achieving the required dynamic range without compromising the fast optical pulses. Research and development is currently underway in the UK to solve these problems. Figure 83 shows first prototype of LED and LD driver unit and light monitoring system with MPPC.

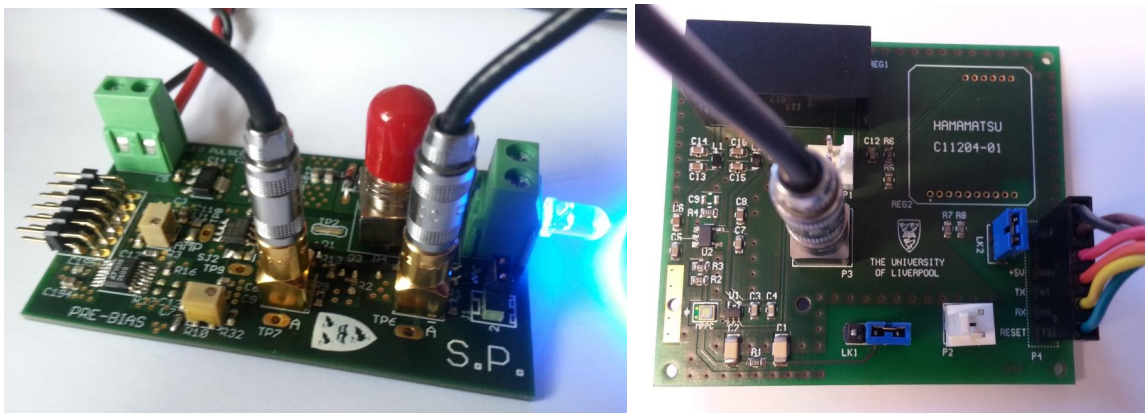

FIG. 83. Photograph of the prototype of LED/LD driver board (left) and MPPC front-end board (right).

For some calibrations, it will be essential to monitor the light injected into the detector. There are two points at which monitoring of the light produced can be done and Hyper-Kamiokande will monitor both. The optical coupling between the LED and fibre is imperfect and the light that does

not enter the fibre can be monitored by a solid state device such as an MPPC or photo diode. The monitoring path will be built into the LED-fibre coupling system. A return fibre from the optical diffuser can also be implemented and monitored. These two systems will allow for pulse by pulse and long term monitoring of the light entering the detector.

This system allows PMT and optical calibration data to be taken without manpower intensive calibration source deployment that has been previously used in water Cherenkov detectors. These data either can be collected in either dedicated high rate calibrations or interspersed during data taking. This system also allows calibration to be conducted during extended periods of beam running where deployment of calibration sources would otherwise result in detector downtime. Given the systematic error budget of Hyper-Kamiokande this system will mean we do not have to compromise between efficiency and the collection of sufficient calibration data.

The calibration of the PMT timing requires a short duration light pulse of known origin and time. The integrated light injection system, from any given fibre, provides this but clearly cannot illuminate the entire PMT array at once. To minimise the number of fibres required the optical diffuser for the PMT calibration is required to provide a wide opening angle, to illuminate of order 1000 PMTs on the far side of the detector. The diffuser must be carefully designed to ensure that there is no time dependence as a function of angle. To achieve the overall calibration of global time offset of the array PMTs must be illuminated by at least two fibres to allow the fibre times to be cross calibrated. We target a six-fold degeneracy of the PMT calibration fibre points to allow to for improved cross calibration and to provide redundancy against single point failures in the fibres. This system will allow for the calibration of PMT timing, the dependence of time on charge and the PMT time response.

The integrated calibration system can also be used to measure optical scattering, extinction and the PMT response. While the basic elements of the system are the same as that used for PMT calibration, a number of changes are required meaning that fibres and diffusers used for these calibrations are different. These properties are required as a function of wavelength, thus several LED types will be used to provide light at six different wavelengths between 320 nm and 500 nm. To measure scattering a narrow beam is required from the optical diffuser; the scattering length is measured by monitoring the light level of PMTs outside the narrow beam as a function of the path length of the beam through the detector. Optical extinction is measured by monitoring the light levels on given PMTs inside the optical beams; unlike scattering wide angle beams are important in this calibration to provide a variety of path lengths. The optical calibration system must be constructed at multiple detector levels to allow for any variation of optical properties with detector

height. The pulse by pulse monitoring of the calibration system is essential for this calibration as the light level at given PMTs is the key measurement of the system. The measured light level at the PMTs is a combination of extinction and PMT response as a function of angle and thus several light paths and angles are required for these to be decoupled in analysis requiring a variety of diffuser points and diffuser directions to be deployed.

1.2. Photosensor calibration ex-situ

As discussed in the previous sections, many of PMT properties can be calibrated *in-situ* by deploying several calibration sources in the detector. We will have additional *ex-situ* measurements to understand further details of PMT properties that are difficult to measure in-situ.

Large photo-cathode area PMTs have non-uniform charge and time responses. The photo-detection efficiency for example can vary depending on the photon incident angle and position on the photo-cathode of the PMT (e.g. [142]). Such non-uniformity of PMT responses need to be understood and are required to build a better model of PMT responses, which is then adopted in the detector simulation. There are some difficulties to measure such non-uniformity of PMT responses after they are installed in the detector since, for example, a small non-uniformity of water transparency can make an apparent variation of PMT responses. Thus, we need to establish a special test stand for the measurements.

A test facility, called 'photosensor test facility (PTF),' has been built at TRIUMF. Figure 84 shows a photograph and schematic diagram of PTF. The PTF has two manipulator arms (gantries)

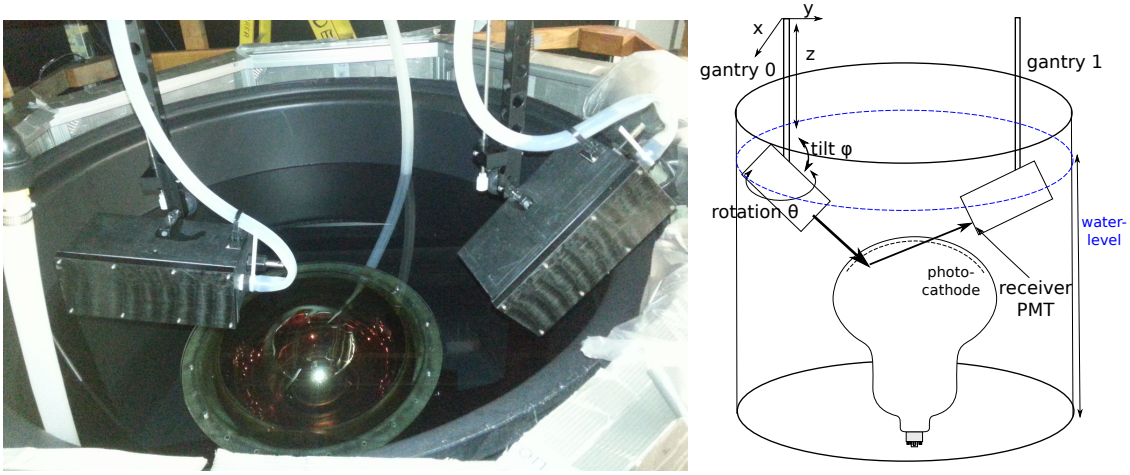

FIG. 84. Photograph (left) and schematic diagram (right) of the photosensor test facility at TRIUMF.

which are motorized and move independently in the x-, y-, z-direction, rotation, and tilt. Each gantry is equipped with an optical box that contain a light source with a chosen wavelength, a (monitor) PMT to measure the intensity of the injected light and a (receiver) PMT which is used for measurement of reflectivity. The PTF is equipped with a water purification system, which generates ultrapure water, and can measure PMT responses under water. As discussed in the photosensor section, Hyper-K PMT will be completely encased in a pressure housing. The optical properties of the PMT housing in ultrapure water will also be measured by the PTF. PTF is now operational and is used for the characterization of new photosensors.

2. Detector Monitoring

To ensure optimal detector performance, minimise systematic uncertainties and facilitate timely responses to detector problems, robust detector monitoring is essential. This will be enabled by the integrated light injection system. The integrated light injection system is being designed to allow calibration of PMT response and detector optical properties. A dedicated calibration can be performed using the system at high rate (1-10kHz) collecting sufficient statistics for each calibration channel in a short period of time. However, the system can also operate at low rate, (0.1-10 Hz) cycling through calibration channels allowing lower statistics calibration samples to be collected over the period of a few hours. Using these low statistics samples the detector calibration can be monitored for changes that might require a dedicated calibration from the inbuilt system to update the detector calibration. These monitoring pulses will also allow the health of other detector systems such as the PMT efficiency to be monitored, tracking any changes to the system as a function of time. Data from this system can be used both by experts, automated systems and detector shifters to track detector performance and understand the health of the detector.

3. Calibrations dedicated for physics analyses

3.1. Calibrations for low energy physics

In this section, detector calibration methods for so-called 'low energy' physics, which is a range from a few MeV to a few tens' MeV energy region, are described. The physics targets are solar neutrinos, supernova neutrinos and geo neutrinos *etc.*

3.1.1. Review of calibration in Super-K

In the low energy physics, electrons generated by neutrino-electron elastic scattering and positrons by inverse beta decay are the detection particles. It is essential to reconstruct their vertex, direction and energy accurately for a precise observation. For this purpose, Super-K employed multiple calibration techniques.

First, an electron LINAC is used to calibrate the absolute energy scale, energy resolution, vertex and direction resolution. Single electron with mono-chromatic energy, from 5 to 16.3 MeV, is injected from LINAC to the detector downward at nine different detector heights. A comparison between the observed LINAC data and the Monte Carlo simulation is shown in Fig. 85. As shown in the figure, Monte Carlo prediction and data are in good agreement. From the results, the energy scale uncertainty is estimated to be less than 0.5%. Since the LINAC calibrations require a longer detector downtime and manpower, LINAC data are taken once per year or two years. Detail of the LINAC system and its performance can be found in reference [143].

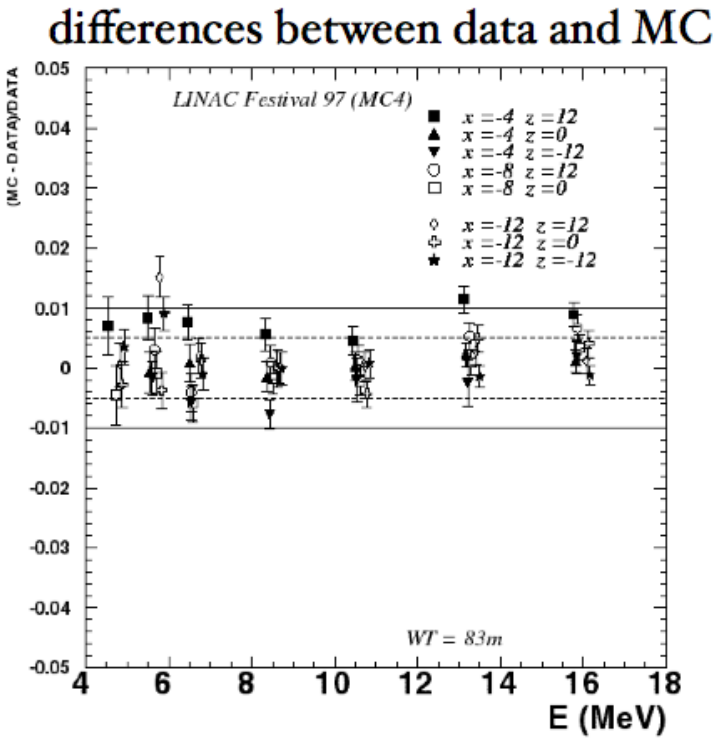

FIG. 85. Comparison of absolute energy scale between LINAC calibration data and Monte Carlo simulation.

The decay of ^{16}N is also used for the absolute energy calibration. ^{16}N decay is dominated by an electron with a 4.5 MeV maximum energy, coincident with a 6.1 MeV γ ray. To create ^{16}N, a DT generator is employed to generate the (n,p) reaction on ^{16}O in the water. The DT

calibrations are carried out more frequently than LINAC, that is three or four times per year. The DT calibration results are good agreement with LINAC calibration. Since ^{16}N decay generates electrons and gammas isotropic unlike LINAC, the DT calibration technique allows to estimate the different systematic uncertainty from the LINAC calibration, which is the angular dependence of the energy scale uncertainty, for example. Detail of the ^{16}N calibration system can be found in reference [116].

'Nickel source' is used for the calibration of event vertex and detector uniformity. This is a $\sim$9 MeV γ source generated by thermal neutron capture on nickel. Neutrons are produced by the spontaneous fission of ^{252}Cf, and a 20 cm diameter 'nickel ball', which consists of 6.5 kg of NiO and 3.5 kg of Polyethylene, is used. Since nickel source is easy to handle and can be deployed in the detector with good position accuracy (less than 1 cm uncertainty), nickel source calibration is carried out about every month by deploying the source at multiple locations in the detector. From this calibration, the vertex reconstruction uncertainty is estimated to be less than 5 cm. The monthly nickel source calibration measures the variation of the detector uniformity which is caused by the water quality change.

3.1.2. Toward Hyper-K

For the solar and supernova neutrino detection, the similar level of precise calibration to Super-K is needed for Hyper-K. Many of calibration sources used in Super-K, like nickel source, can also be used in Hyper-K, however, employing an electron LINAC system requires further considerations since Hyper-K consists of multiple detectors and have a larger volume than Super-K, that causes a much larger burden to operate LINAC calibration system at Hyper-K. Thus, alternative approaches to the LINAC calibration are being developed. One possible approach can be the following. Super-K detector simulation is tuned with LINAC calibration data, and the LINAC-tuned simulation reproduces DT calibration data very well, as described above. By adopting the tuning parameters of the LINAC-tuned Super-K simulation in Hyper-K, DT calibration data of Hyper-K can provide a good calibration of the absolute energy scale without employing LINAC calibrations in Hyper-K. This way does not requires LINAC calibrations at Hyper-K but requires an intensive DT calibrations. For the purpose, a compact DT generator or an alternative neutron generator would be desirable. In order to calibrate the energy regime, up to a few tens MeV, which is higher energy than DT calibration, we need to develop new calibration sources. These new systems are under development.

There is an option in Hyper-K detector to dope gadolinium in water, that is aimed to increases a sensitivity of antineutrinos detection, e.g. supernova relic neutrinos, by using 'delayed coincidence' detection technique for inverse beta-decay process. For the calibrations of gadolinium doped water Cherenkov detector, the standard calibration techniques, described previous sections, are still valid. In addition to the standard calibrations, however, it would be desirable to calibrate the neutron capture rate in gadolinium doped water using with a neutron sources with *known* neutron emission rate, e.g. AmBe source, a pulsed neutron sources described previous sections. We will further develop the calibration techniques for the gadolinium doped water Cherenkov detector based on the SK-Gd project experience.

3.2. Calibrations for high energy physics

In this subsection, the energy scale calibration of the inner detector for the higher-energy physics analysis (atmospheric neutrino oscillation, proton decay search, T2K, *etc.*) is described.

3.2.1. Review of calibration in Super-K

The charge scale of the SK detector simulator (SKDETSIM) is initially calibrated by measuring each PMT quantum efficiency, single photo-electron charge distribution, *etc.* by using various control samples such as the nickel source. Then, a global correction factor which scales the total photo-electron yield is tuned in SKDETSIM by using cosmic-ray through-going muons.

The momentum is reconstructed as follows: the total integrated corrected charge from all the hit PMTs within a 70 degree cone from the reconstructed vertex with respect to the reconstructed ring direction is measured for each ring. The correction of the charge is done for each hit PMT by taking into account the photon acceptance as a function of the incident angle to the PMT and the light attenuation length in water. The corrected charge is converted to momentum by using a conversion table made with MC for each particle type assumption. For multi-ring events, the momentum for each ring is determined by separating charge for each hit PMT to maximize agreement of observed and expected ring charge pattern according to the particle type assumption determined by PID. For the expected charge calculation, photon scattering in water and reflection at the inner detector wall are taken into account. Time variation of the attenuation length and PMT gain is taken into account and the momentum is corrected in the real data.

Figure 86 shows the result of a comparison of the energy scale between data and MC from

around 10 MeV/c to 10 GeV/c, using cosmic-ray stopping muon and associated decay electron data, and π^0 data produced in atmospheric neutrino interactions in SK-IV. The absolute scale

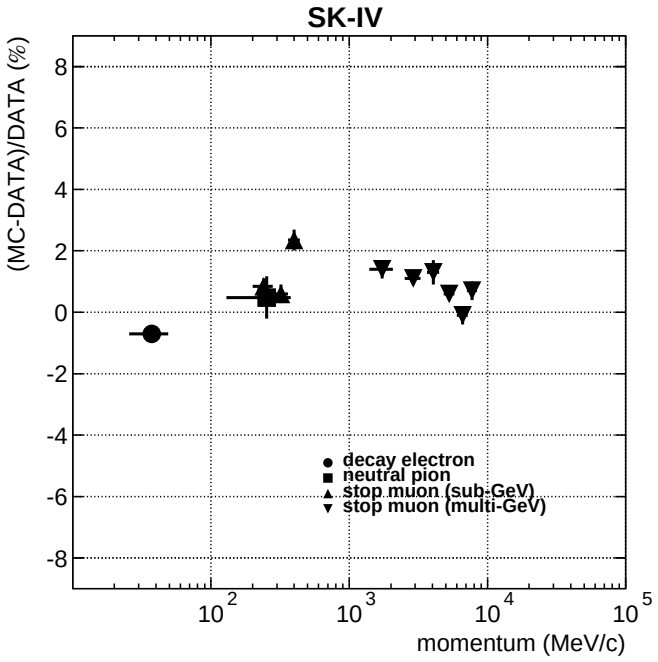

FIG. 86. The absolute energy scale check in SK-IV.

error is estimated to be 2.4% from the largest difference between data and MC which occurs for the sub-GeV stopping muon sample. Note that the global momentum scale for data was adjusted typically in the end of each SK detector period to minimize the absolute scale error but has not been done yet in SK-IV. The time variation of reconstructed momentum is shown in Fig. 87 and Fig. 88. For the entire SK-IV time period, the momentum has been stable within 1% and the time variation (RMS/mean) is estimated to be about 0.4%, taken as the largest value between these two calibration sources. By taking the quadratic sum of the absolute scale error and the time variation, the energy scale error is estimated to be 2.4% in SK-IV. Further, the directional dependence of decay electron momenta is used to estimate the asymmetry of the energy scale. The asymmetry was estimated to be 0.8% in SK-IV.

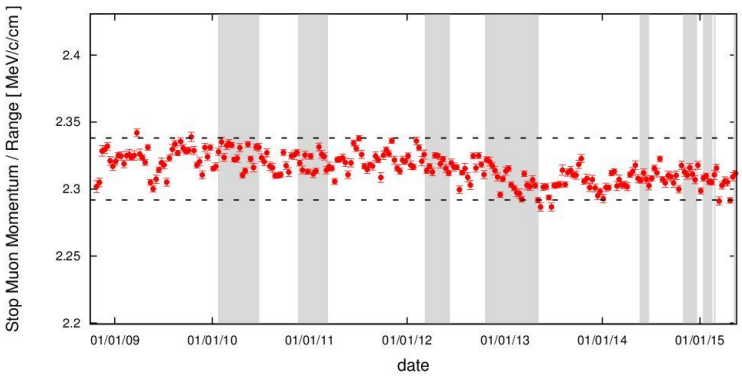

FIG. 87. The momentum time variation for cosmic-ray stopping muon in SK-IV. The horizontal broken lines correspond to ± 1% with respect to the average. The shaded regions correspond to T2K run periods.

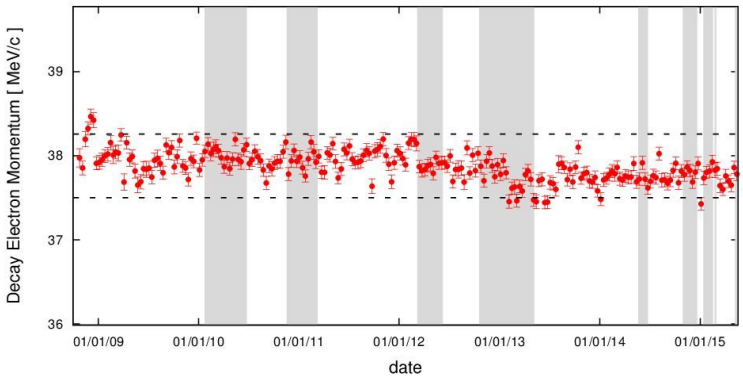

FIG. 88. The momentum time variation for decay electron in SK-IV. The horizontal broken lines correspond to ± 1% with respect to the average. The shaded regions correspond to T2K run periods.

Fig. 89 shows the absolute energy scale checks from SK-I to SK-III. From SK-I to SK-II, the PMT photo-coverage changed from about 40% to 20%. Starting from SK-II, each PMT was covered by an acrylic cover. Starting from SK-III, the photo-coverage was back to about 40%. Starting from SK-IV, new readout electronic modules were installed. Despite these changes, the absolute scale error remains at about 1-2% from SK-I through SK-IV. The absolute energy error is estimated to be 0.74%, 1.60%, and 2.08% for SK-I, SK-II, and SK-III, respectively.

Figure 90 shows the result of the momentum time variation from SK-I to SK-III. The time variation during SK-I, SK-II, and SK-III was 0.88%, 0.55%, and 1.79%, respectively. The time variation in SK-III was relatively larger due to worse water quality and it is at a minimum in SK-IV due to improved momentum time variation correction for SK-IV. During SK-I, SK-II, and SK-III, the energy scale asymmetry was estimated to be 0.6%, 0.6%, and 1.3% respectively.

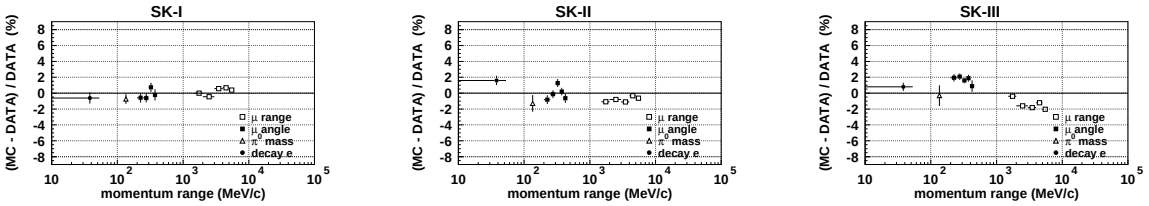

FIG. 89. Comparison of absolute energy scale checks from SK-I to SK-III.

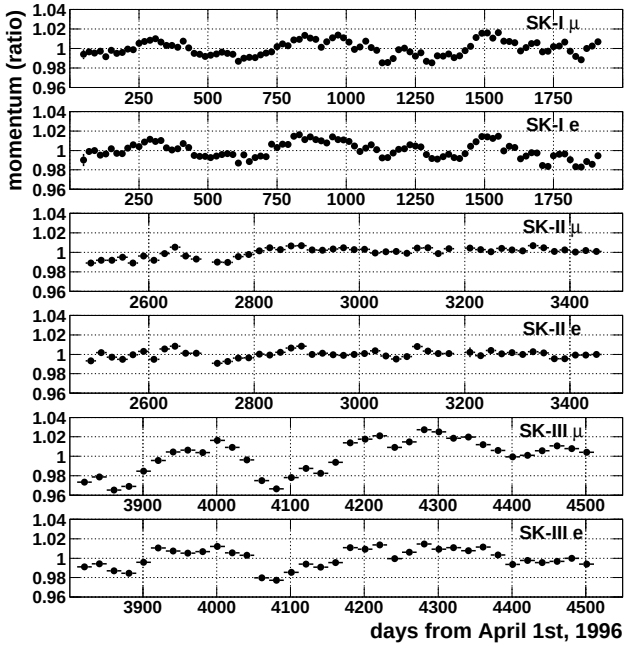

FIG. 90. Comparison of the momentum time variation from SK-I to SK-III.

3.2.2. Toward Hyper-K

Thanks to the similar vertical cylindrical tank, there is no major concern which makes the energy scale error significantly larger in HK.

The current energy scale error in SK-IV comes from the unknown momentum dependence of the absolute scale, especially as seen in the sub-GeV stopping muon sample. The muon momentum of the sub-GeV sample is below about 500 MeV/c where the Cerenkov angle significantly depends on the momentum. Each sub-sample of the sub-GeV sample is defined by using the reconstructed Cerenkov angle. The Cerenkov angle reconstruction depends on the charge profile shape which is especially affected by the tuning of the scattering parameters in SKDETSIM. Therefore, better understanding of the water quality is important.

Any improvement of the existing momentum reconstruction such as time variation correction as well as new sophisticated algorithm such as fiTQun would reduce the energy scale error.

4. OD calibration system

The major task of the OD part of the Hyper-K (HK) detector is not to obtain the exact energy deposited but to identify the neutrino events out of the cosmic-ray muons. For example, "fully contained" events are identified by requiring no energy deposition in OD, and "partially contained" events and "upward-going muon" events, which are important sub-samples in atmospheric neutrino analyses, are identified with OD hits coinciding with ID hits. For these physics analyses, an 'inter-calibrations' between OD and ID, e.g. timing calibrations between OD and ID, is also important in addition to the calibrations of OD itself.

Compared the ID part, the OD has various disadvantages in having a calibration system. They are: 1) many light injection points are necessary to illuminate all the light sensors in the OD area to an intensity level of a few 100 PE's, 2) there is sensor support structures which can hinder the delivery of calibration light, and 3) there is no easy way to deploy additional light injection points to replace non-functional ones once the detector is filled with water. The latter 2 points can be mitigated by having redundant light injectors, but this will certainly increase the total cost of the system.

In the case of Super-Kamiokande experiment, the OD calibration system consists of a N_2 and a dye laser, monitoring PMT's, a variable attenuation wheel, optical switches, and 52 fibers. Each fiber is equipped with a light diffusing tip at the end. Of these fibers, 24 are placed in wall section

and 14 each are placed in top and bottom sections. They are 72 m long, except for those placed in the bottom section which is 110 m long. In average, each wall fiber covers 160 m^2 of OD sensor area and about 2.5 m away from the OD PMT plane. Top and bottom fibers cover 64 m^2 per fiber and about 1.6 m away. These fibers are reasonably redundant and a little over a half of them are actually used to calibrate all the OD PMT's.

For the SK OD calibration system to be adopted to the HK detector, 79 fibers are required to achieve the same fiber density as the SK for the HK wall section. For top and bottom, 61 each is necessary. In total, 201 fibers are needed for the entire HK detector. In terms of length, 200 m fibers for bottom and 120 m ones for other sections are necessary to compensate the linear dimension difference between the SK and HK detectors.

J. Computing

Hyper-K adopts a Tiered computing model where Kamioka and KEK sites form the Tier-0 due to the distributed nature of the experiment. A general overview of a future Hyper-K tiered system is shown in Fig. 91.

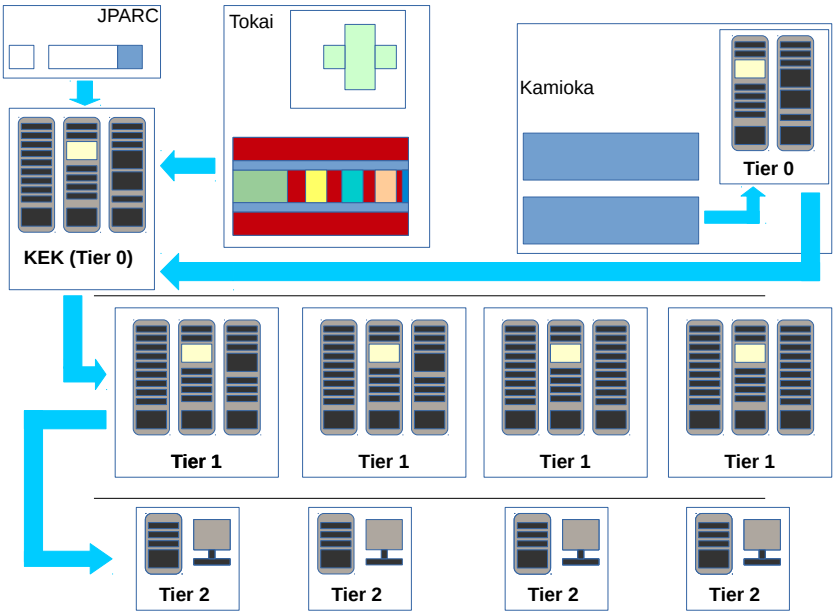

FIG. 91. General overview of a possible Hyper-K tiered system.

The Tier0 sites will hold the raw experiment data as well as the processed data. The KEK Tier0 will also contain a The Tier1 centres (such as RAL, TRIUMF, ccin2p3) would hold portions of the raw, processed and simulated data and provide computational resources for the simulation, processing and reprocessing. The Tier2 sites which typically consist of universities will provide computational and storage resources (the storage is usually used to hold specific subsets of the data or simulation). The model makes efficient use the available computing resources that exist at collaborating sites. The model will be regularly reviewed as changes to the computing landscape take place.

A current estimate of the rate of raw data to be stored is 20 TB/day. About 80 PB of the disk space is necessary to store the raw data for the 10 years operation.

Reduction and reconstruction software will be applied to all the data in the Kamioka Tier0 as soon as the data are taken to provide different samples for different energy regions or different analysis groups, i.e. low energy region mainly for the study of solar neutrinos, higher energy for

the study of nucleon decay and atmospheric neutrinos, downward going muons for the background study of solar neutrinos, the data during the beam timing from the accelerator for the beam neutrino analyses. These data sets also provide timely feedback to the experiment and beam operations groups on the quality of the beam and performance of the detector. Also, early detection of a supernova burst is crucial and dedicated realtime analysis has to be performed in the independent system. The required computing power for data reduction and reconstruction at this level, together with the supernova detection system, is not so huge and 1000 cores of the current Intel IA64 CPUs will be sufficient.

1. Simulation production

Mass production of the simulation data sets and their analyses are expected to be performed in the Tier-1 centres because the required CPU resource for the huge amount of simulation data is expected to be at least a few tens of times larger than the ones necessary for the real time data processing. On the other hand, the simulated data set is not extremely large and the cost of the storage could be less than 10% of the storage for the real data sets. All the data sets after reduction and the processed simulation data sets are shared among the geographically distributed analysis working groups. The Tiered model ensures results in a more scalable architecture capable of meeting the computational and storage demands of the experiment.

The Monte Carlo simulation production currently makes use of existing HEP computational Grid resources to produce sufficient quantities of physics events necessary to optimise the detector design for maximum efficiency. The data are managed by the iRODS data management system (`http://irods.org/`) that enables distributed storage to be managed and accessed in an uniform manner. Collaborators access the stored data using the intuitive and simple iRODS client API.

K. Summary of the Hyper-Kamiokande detector

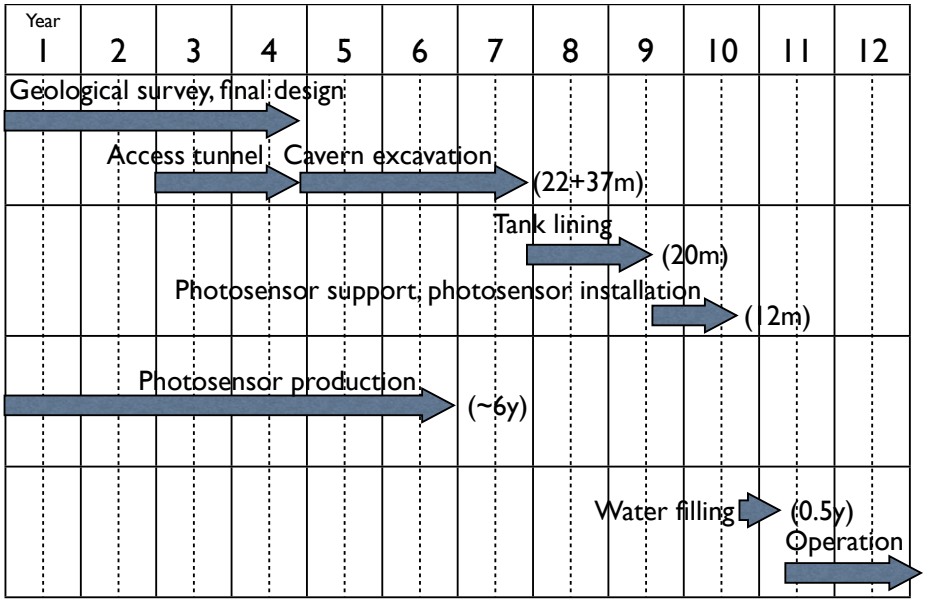

FIG. 92. Construction period for the 1TankHD

Figure 92 shows the estimated construction period of the Hyper-K detector for 1TankHD. The construction is estimated to take about 10 years including the geological survey and final design making.

For the operation of the 1TankHD detector, necessary manpower is estimated to be about 20 full-time equivalent (FTE) by taking into account management and detector calibration in addition to the operation and maintenance of water system, electronics, DAQ system, and computer system. In the case of three tank case, the necessary FTE would be as twice as the single tank case.

II.3. HYPER-KAMIOKANDE SOFTWARE

The Hyper-K software system is designed around the following principles:

- Adaptable. The Hyper-K experiment is expected to run for a decade (or more). This period typically spans more than one generation of software and infrastructure. The Hyper-K offline system is being designed to be flexible enough to accommodate a change in tools or infrastructure.
- Reliable. Each component needs to demonstrate it's reliability by exhibiting well defined behaviour on control samples.
- Understandable. Documentation on what the component does, what it's dependencies are as well as test samples and outputs are essential in being able to use it successfully.
- Low overhead. The management and maintenance should be as automated as possible to free collaborators to focus on the challenge of extracting the high-quality physics measurements.

The software consists of a collection of loosely-coupled packages, some of which are open-source and some of which are specific to Hyper-K. The distributed code management system Git is used to manage the software. Each package is hosted on a third-party central repository (`https://github.com/`) that provides distributed access to the packages. The distributed nature of the code management allows researchers the possibility to develop independently without impacting other researchers. The loose-coupling between packages allows those that reach their end of life to be replaced by better alternatives with minimal impact on the rest of the system. Where possible standard particle physics software libraries are used to reduce the burden of support of experiment-specific code. The working language for the Hyper-K software packages is C++, with the output files being written in ROOT [144] format.

The flow for the simulation is as follows: The events are first modeled by a Monte Carlo detector response code called WCSim, then the event information is reconstructed using either BONSAI (for low energy events) or fiTQun (for high energy events). This is shown schematically in Figure 93. These packages will be described in more detail in the next Sections.

An online workbook is also maintained to provide higher-level documentation on overall procedures and information for new users of the software and developers. An overall software control package allows for the fully automated download, compilation and running of the software, based on user requests.

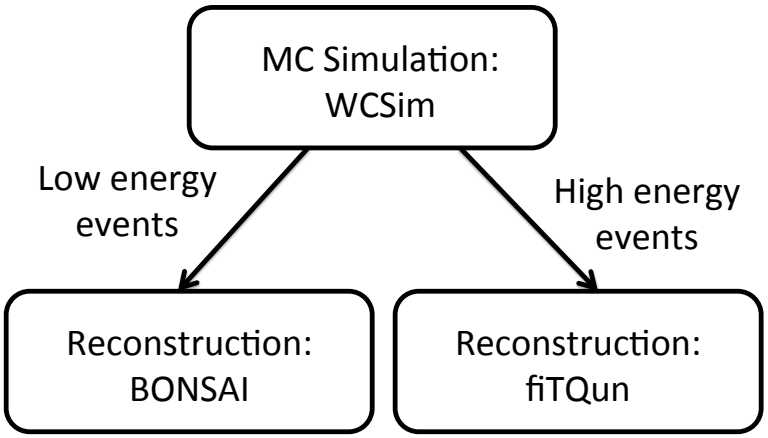

FIG. 93.

A. WCSim

The Water Cherenkov Simulation (WCSim) package is a flexible, Geant4-based code that is designed to simulate the geometry and physics response of user-defined water Cherenkov detector configurations. WCSim is an open-source code and is available for download at `https://github.com/WCSim/WCSim`.

The final performance of the Hyper-Kamiokande detector depends on the detector geometry, the type of photodetectors, and the photocoverage that will be used. WCSim takes these variables as inputs and simulates the detector response, which can then be used to determine the physics potential. WCSim users specify the type of photodetectors, the number of photodetectors, the detector diameter and radius, and whether the water should be doped with gadolinium. The outer detector volume is currently not implemented in WCSim, though it is actively being developed for a future release.

For this report, the relevant photodetectors in WCSim are the R3600 20" diameter PMTs, as well as the R12850 20" and 12" diameter box and line photodetectors. Photodetector parameters in the simulation include the timing resolution, dark noise rate, and the overall efficiency for a photon to register a charge (including the quantum efficiency, collection efficiency, and hit efficiency as described in Section II.2 F). For the R3600 PMTs, the parameters were taken from the Super-Kamiokande simulation code SKDETSIM. The parameters for the R12850 are taken

from measurements as described in Section II.2 F. Some higher-level photodetector effects such as after-pulsing are not currently simulated in WCSim, though this is a planned upgrade for a future releases.

The GENIE [145] and NEUT [146] neutrino interaction packages are adopted to determine the interaction information, while Geant4 [147] is used to track the particles as they the pass through the detector and compute the final deposited energy. Particles that reach the photodetector glass and pass the quantum efficiency and collection efficiency cuts are registered as a hit. The hits are then digitized based on the SK-I electronics scheme.

The output for the WCSim code includes both the raw hit and the digitized information. The raw hit information includes which tubes were hit and how many times each tube was hit. The digitized information includes the number of hits in a trigger window, as well as the charge and time of the hit tubes. WCSim output files can be used for event reconstruction by fiTQun or BONSAI, which are described in the following subsections. Geant4 visualization tools can be used to display the detector geometry. Figure 94 is a rendering of one of the tanks in the 3TankLD configuration.

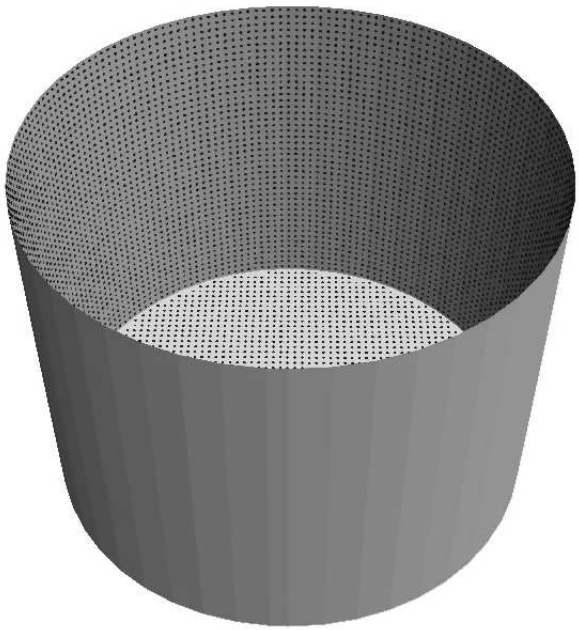

FIG. 94. Geant4 visualization of the Hyper-Kamiokande 3TankLD detector configuration. The top cap of the detector has been removed for visualization purposes. Phototubes are shown in black, while the walls of the detector are shown in medium grey (for the barrel) and light grey (for the bottom cap).

Figure 95 shows the total charge distribution in both the 3TankLD and the 1TankHD configurations for electrons and muons with several momenta. RMS divided by mean charge is plotted in Figure 96 indicating better resolution with 1TankHD than 3TankLD. For lower energy particles, the resolution can be approximated using nhits (the number of phototubes that register a hit). The nhit distribution for both the 3TankLD and 1TankHD configurations is shown in Figure 97.

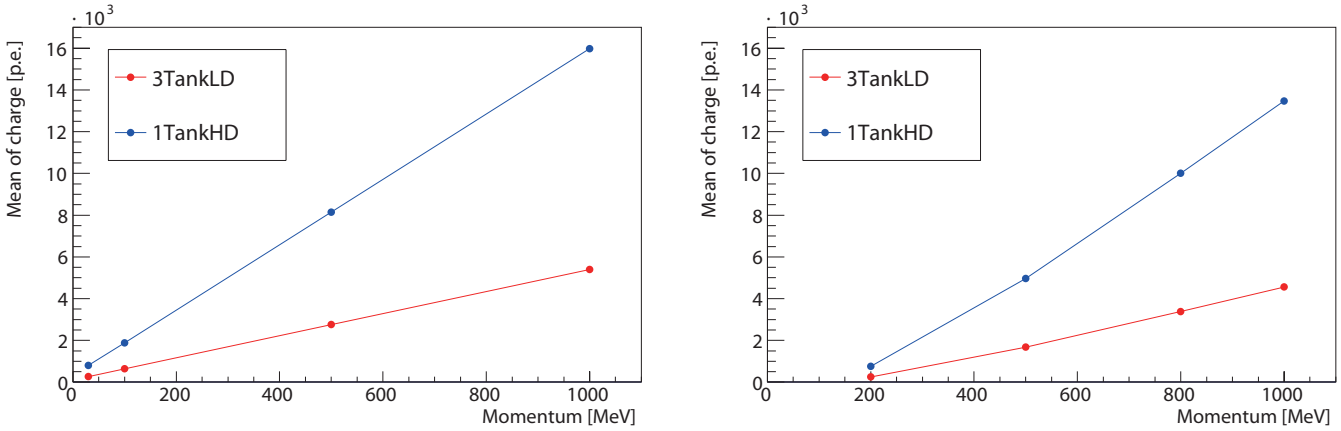

FIG. 95. Total charge distributions for electrons (left) and muons (right) with several momenta. The red line corresponds to the 3TankLD configuration, while the blue line corresponds to the 1TankHD configuration.

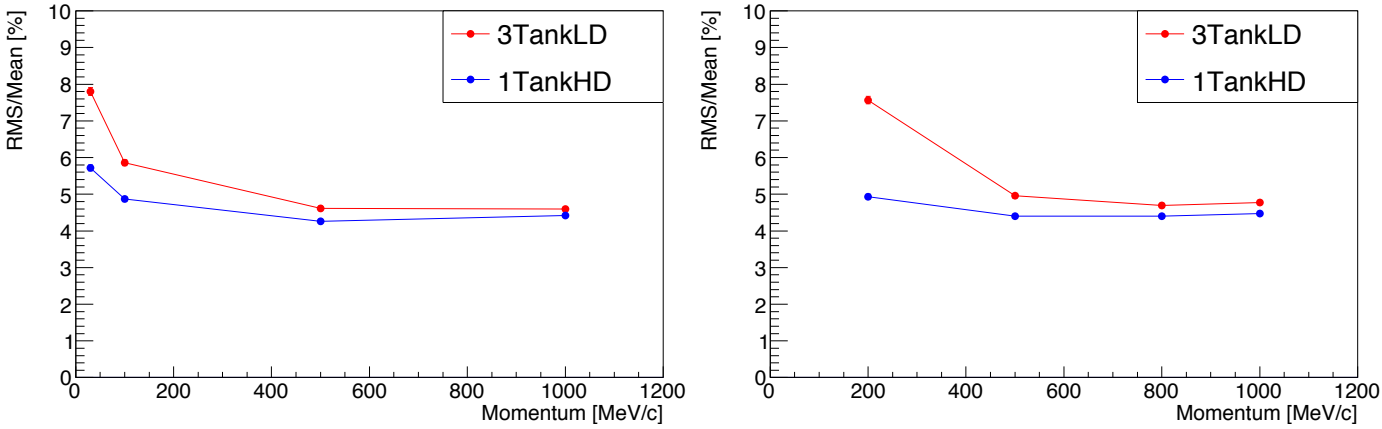

FIG. 96. RMS/Total charge distributions for electrons (left) and muons (right) with several momenta. The red line corresponds to the 3TankLD configuration, while the blue line corresponds to the 1TankHD configuration.

B. FiTQun

FiTQun is an event reconstruction package initially developed for the Super-K detector based on the formalism employed by the MiniBooNE experiment [148]. The reconstruction algorithm allows for single- and multiple-ring event hypotheses to be tested against observed data. For a given event hypothesis, a prediction is made for the complete set of observables at each PMT: whether or not a hit was registered; and in the case of there being a hit, its time and integrated charge. The hypothesis and associated kinematic parameters that best describe a given event are found by maximizing a likelihood function of the predicted hypothesis with respect to the observed data.

FiTQun has been shown to perform well on Super-K data, with significant improvements on

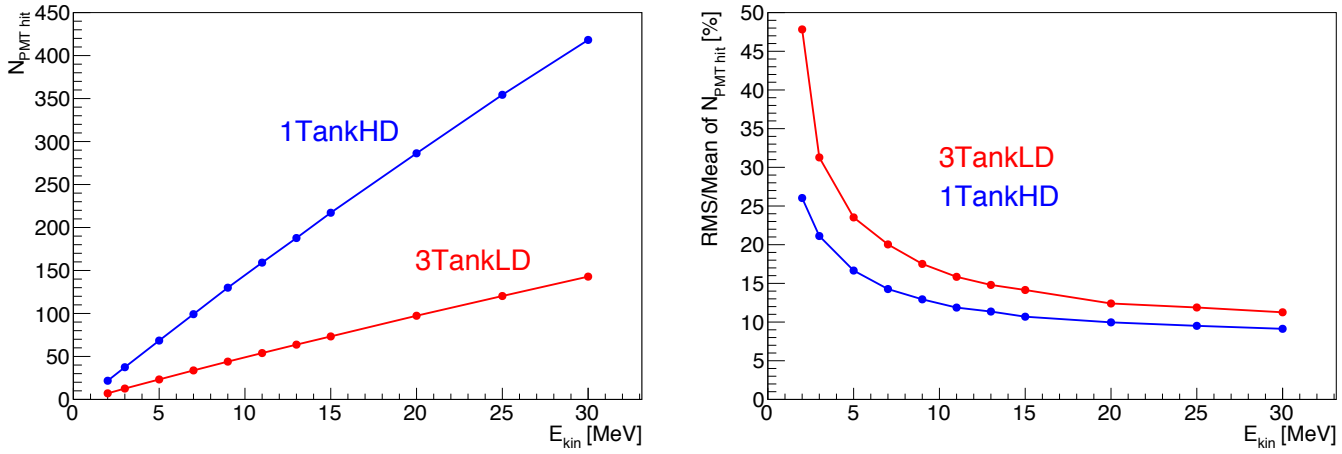

FIG. 97. Expected number of PMT hits ($N_{PMThits}$) and the RMS of the N_{PMThit} distributions. WCsim is used for simulating the injection of electrons with several values of kinetic energy (E_{kin}). The initial position is uniformly distributed inside the fiducial volume (>2 m from inner detector wall). The red line corresponds to the 3TankLD configuration, while the blue line corresponds to the 1TankHD configuration.

vertex, angle and momentum resolutions, as well as particle identification when compared to previous reconstruction algorithms. In particular, fiTQun was successfully deployed to reject π^0 events from the Super-K ν_e sample in the T2K ν_e appearance analysis (Figure 98) [26, 51].

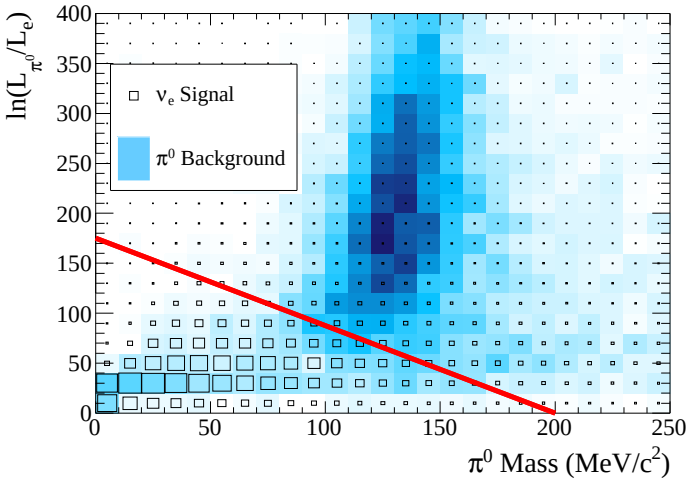

FIG. 98. FiTQun used for π^0 rejection in the ν_e selection for the T2K ν_e appearance analysis[26]. The red line represents the cut, with events above the line being rejected as π^0 background.

1. Reconstruction algorithm

At the core of fiTQun lies a likelihood function, which is evaluated over all the PMTs in the detector:

$$L(\mathbf{x}) = \prod_{j}^{unhit} P_j(unhit|\mathbf{x}) \prod_{i}^{ihit} P_i(hit|\mathbf{x})\, f_q(q_i|\mathbf{x})\, f_t(t_i|\mathbf{x}) \ . \tag{3}$$

Event hypotheses are characterized by $\mathbf{x}$, which includes the time and position of the interaction vertex, momentum and direction of the charged particle tracks, and any other relevant kinematic parameters such as the distance or time interval between tracks, or the energy lost between track segments. For a given $\mathbf{x}$, a prediction of the amount of charge at each PMT, μ_i, is made and the time at which the light is expected to arrive each PMT is calculated.

The detector response is folded into these predictions to give the probabilities P of a PMT being hit and the read-out time and charge probability distribution functions f_t and f_q, respectively. The negative log-likelihood ($-log(L)$) is maximised to obtain the $\mathbf{x}$ that best describe the event according to some event topology (*e.g.*, single electron-like ring).

Once the best-fit parameters have been obtained for several topologies, the ratio between their likelihoods is used to determine which topology gives the best match to the event. This can be used as a particle identification tool if simple one-particle hypotheses are used, or as a more complex selection criterion if multiple final-state particles are included in the hypothesis (*e.g.*, a nuclear de-excitation photon followed by a K^+ decay muon for the selection of $p \to K^+\nu$ events).

2. Integration with WCSim and tuning

FiTQun has been adapted to reconstruct events simulated with WCSim, in the various detector configurations implemented in the simulation software. A class was written (WCSimWrapper) that reads in both detector geometry (positions and radius of PMTs) and event data from the WCSim ROOT output files. A preprocessor flag allows fiTQun to be compiled against WCSim libraries, removing its dependence on Super-K software.

In the context of WCSim, events can be generated in an arbitrary number of detector configurations. For fiTQun to adequately reconstruct events in any given configuration, some of its components have to be re-evaluated. For example, the charge and time response of PMTs must be accurately known in order to obtain unbiased estimates of particle momentum and vertex position. The tuning procedure developed for Super-K and SKDETSIM was translated to be used with WCSim and with generalized cylindrical geometries.

The tunes produced for each simulated detector consist of ROOT files and a number of run-time parameters. A configuration file is given for each tune that contains the information needed by fiTQun to load the appropriate files and parameters. These configuration files are packaged with fiTQun, such that any tune available can be selected for production in a single step.

C. BONSAI

For the event reconstruction at low energy, i.e. few MeV - few tens MeV, a reconstruction algorithm BONSAI (Branch Optimization Navigating Successive Annealing Iterations) is supplied for Hyper-Kamiokande. BONSAI was originally developed for Super-Kamiokande [149] with C++, and has been used for the low energy physics analysis of SK-I to SK-IV. In the low energy region, most of the photosensor signals are single photon hits. BONSAI uses these relative hit time information to reconstruct the position of the Cherenkov light source, i.e. the position of low energy event. For Hyper-K analysis, a wrapper library (libWCsimBonsai) is supplied for ROOT environment.

1. Vertex reconstruction

For the vertex reconstruction, BONSAI performs a maximum likelihood fit using the photosensor hit timing residuals. This likelihood fit is done for the Cherenkov signal as well as the dark noise background for each vertex hypothesis. The likelihood of the selected hypothesis is compared to the likelihood of a hypothesis in an area nearby. Highly ranked hypotheses and new points in the likelihood will survive this step. Finally, after several iterations, the hypothesis with the largest likelihood is chosen as the reconstructed vertex.

The vertex goodness criterion testing the time residual distribution is defined as follows:

$$g(\vec{v}) = \sum_{i=1}^{N} w_i \exp -0.5(t_i - |\vec{x_i} - \vec{v}|/c)/\sigma)^2 \tag{4}$$

where t_i are the measured PMT hit times, $\vec{x_i}$ the photosensor locations, $\vec{v}$ is reconstructed event vertex, σ is the effective timing resolution expected for Cherenkov events (total of photosensor and DAQ resolution) and ω_i are Gaussian hit weights also based on the hit time residuals, but with a much wider effective time resolution. The weights reduces the dark noise contamination of the Cherenkov light.

2. Energy and direction reconstruction

BONSAI and its related subroutines also determine the energy and the event direction reconstruction.

Because most of the photosensor signals consist of single photon hits, the total number of photosensor hits is the leading parameter for reconstructing the energy of events. First, time-of-flight values are subtracted from each of the hit timing values based on the position of each photosensor and the result of the BONSAI vertex reconstruction. Next, the number of photosensor hits around the expected event timing is calculated, considering its cross-section and the local photocoverage with neighboring photosensors. Finally, the number of hits are scaled to energy using the information from detector simulations and calibrations.

The direction reconstruction is performed on the photosensor hit patterns using a circular KS test that checks the azimuthal symmetry around the Cherenkov cone.

As the result, the vertex position, direction and energy of low-energy events are available after BONSAI reconstruction.

Several likelihoods to test mis-reconstruction are also available during the reconstruction. Likelihoods calculated using photosensor hit patterns are also used in particle identification, e.g. to differentiate between electron and gamma events.

II.4. BACKGROUND RATE ESTIMATION

A. Background rate estimation for low energy neutrino study

In this subsection, we will show the background rate estimation used for the study of low energy neutrinos, such as solar neutrinos, supernova neutrinos, and relic-supernova neutrinos. The major background sources are the radioactive isotope of ^{222}Rn contained in water, and radioactive spallation products created by cosmic-ray muons. The ^{222}Rn-induced background concentrates around a few MeV energy region, and impacts the energy threshold of the solar neutrino measurement via neutrino-electron scattering. In this design report, we assume the ^{222}Rn concentration in the Hyper-K water is less than 1.6 mBq/m^3, as described in section II.2 E 5. In that case, we can set the analysis energy threshold in the total energy of recoil electrons at 7.0 MeV, and the 1TankHD of the higher photocoverage configuration will allow us to lower the energy threshold. Other important radioactive isotopes are U and Th in the water, and ^{40}K in the PMT glass; we need to suppress the concentration of those isotopes to the similar level in Super-K as well. On the other hand, the major background sources for the anti-neutrino measurement is anti-neutrino backgrounds from nuclear power reactors, which limit the energy threshold at around 10 MeV; the smaller contribution comes from the radioactive background of (α, n) reactions. In the background estimation, the most complicated task is the estimation of the muon spallation productions and its background reduction by the analyses, because it depends on the detector location and the detector performance. In the following paragraph, we focus on the discussion of the muon spallation backgrounds.

1. Muon spallation

Radioactive isotopes produced by cosmic-ray muon-induced spallation are potential backgrounds for low energy neutrinos. Generally, the production rate depends strongly on the muon flux and the average energy, and the delayed radioactive decays cause the backgrounds in the energy region below about 20 MeV. If the lifetime of radioactive isotope is relatively short on the order of a few seconds or less, the spallation backgrounds can be mitigated by time/volume cuts based on the reconstructed muon track. Therefore, the detailed estimation of the cosmic-ray muon intensity and the spallation production rate are of great importance in demonstrating the sensitivity of Hyper-K to low energy neutrinos.

The muon intensity at the planned site can be estimated using the calculated surface muon flux

and energy, the mountain profile, the rock density and compositions. The muon flux (J_μ) and average energy ($\overline{E}_\mu$) at underground sites are estimated by the muon simulation code (`MUSIC`) [150], a three-dimensional MC tool dedicated to muon transportation in matter. In this MC, surface muons are generated according to the *Modified Gaisser Parameterization* [151] sea-level muon flux distribution. A digital map of the topological profile of Nijuugo-yama with a 5 m mesh resolution [152] is shown in Fig. 99. The Hyper-K detector will be located around the basing point, referenced in Section II.2 B corresponds to the old mountain peak before the surface mining. Based on this elevation data, we calculate slant depths as a function of zenith and azimuth angle at an arbitrary point in the mountain, and estimate the survival probability of muons after the muon transportation through the rock for each angle using the `MUSIC` simulation.

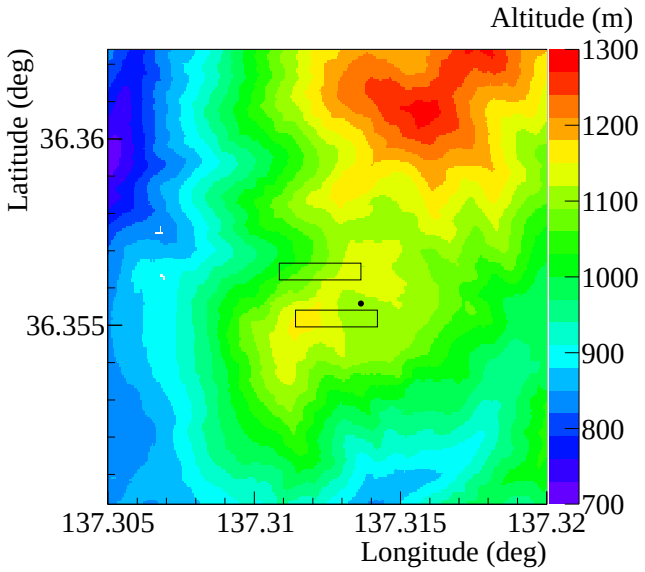

FIG. 99. Topological profile of Nijuugo-yama [152]. The black point is the basing point for the Hyper-K site, and two boxes represent the candidate locations of the two Hyper-K detector modules.

Previously, the value of J_μ and $\overline{E}_\mu$ at KamLAND in Ikeno-yama are evaluated based on the `MUSIC` simulation for various rock types [151, 153]. The value of J_μ is dependent on the type of rock. Varying the specific gravity of rock from 2.65 to 2.75 g/cm^3 in the `MUSIC` simulation yields values of J_μ that agree with the KamLAND muon flux measurement [153]. As both Nijuugo-yama and Ikeno-yama are skarn deposit, which are common characteristic in the Kamioka mine, the simulation for Hyper-K assumes the same rock type used in Ref. [153]. Figure 100 shows the

calculated J_μ and $\overline{E}_\mu$ for Hyper-K at the altitude of 508 m for 2.70 g/cm^3 specific gravity Ikenoyama rock. The values of J_μ and $\overline{E}_\mu$ vary greatly depending on the shallowest rock thickness on the west or south side, as indicated in Fig. 99, so they need to be averaged over the detector plane area at the altitude of 508 m.

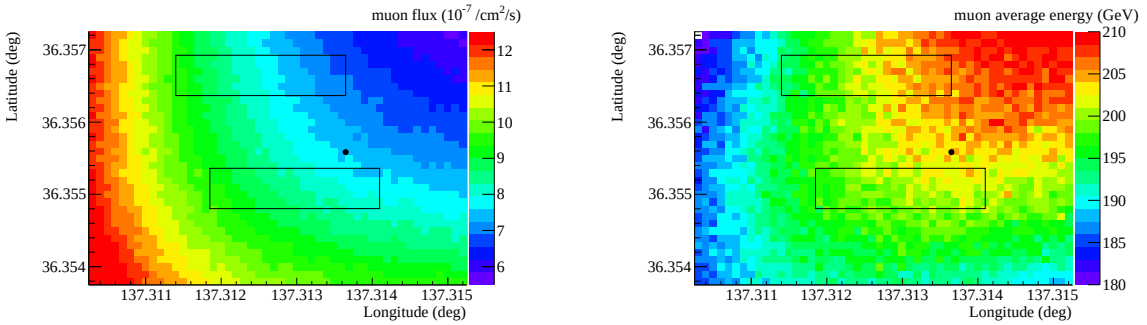

FIG. 100. Calculated muon flux (J_μ) and average energy ($\overline{E}_\mu$) at the altitude of the Hyper-K (508 m) detector. The black point is the basing point for the Hyper-K site, and two boxes represent the candidate locations of the two Hyper-K detector modules.

Table XXII summarizes the calculated J_μ and $\overline{E}_\mu$ in Hyper-K and Super-K for 2.70 g/cm^3 specific gravity. Considering the variation of J_μ for different rock types, we assume uncertainties of $\pm 20\%$ for J_μ. Because the Super-K site is deeper, the value of J_μ for Hyper-K is higher than Super-K by a factor of 4.9. On the other hand, the value of $\overline{E}_\mu$ for Hyper-K is smaller than Super-K as indicated in Fig. 101, because the relative contribution of lower energy muons becomes larger at a shallower site. Figure 102 shows the muon flux as a function of zenith angle θ (upper) and azimuth angle ϕ (lower) for Super-K and Hyper-K at the basing point. We confirmed that the `MUSIC` simulation reproduced the Super-K well. In Hyper-K, the major contribution of muon flux is introduced by the flux in the west and the south.

Based on the muon flux and energy spectrum calculated by the `MUSIC` simulation, we can estimate the isotope production rates by muon spallation in a planned detector. `FLUKA` is a good choice of code to model nuclear and particle physics processes involved in muon spallation. Previously, the measured isotope production rates in a underground detector was compared with the `FLUKA` simulation [153]. However, owing to the large uncertainties on the isotope production cross sections by muons or their secondaries, the production rate between data and MC differ by up to a factor of

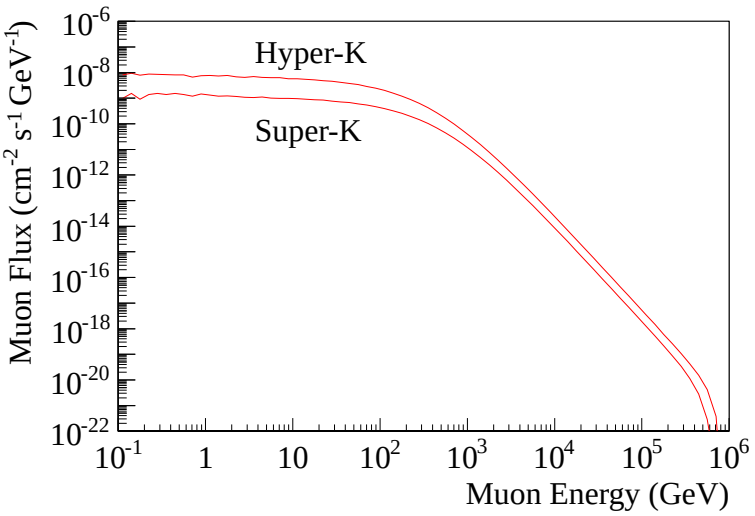

FIG. 101. Calculated muon energy spectra for Super-K and Hyper-K at the basing point based on the MUSIC simulation.

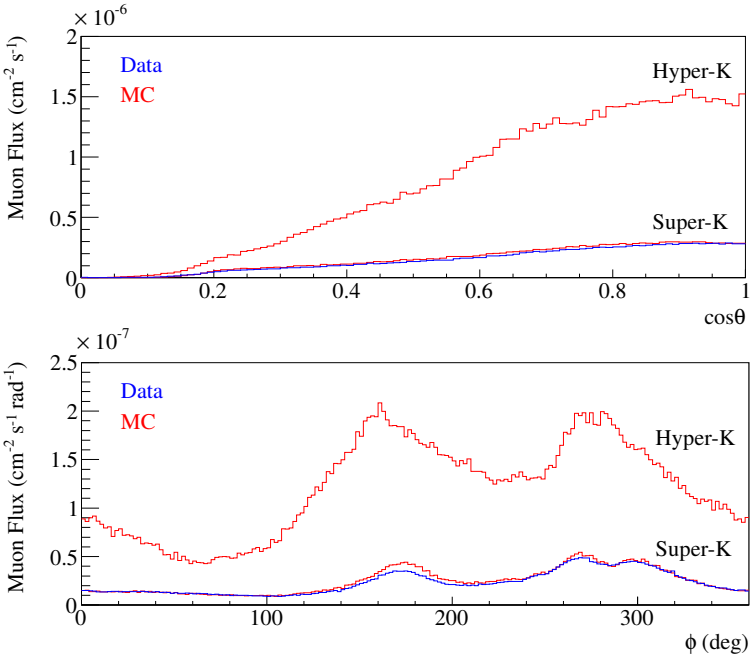

FIG. 102. Muon flux as a function of zenith angle θ (upper) and azimuth angle ϕ (lower) for Super-K and Hyper-K at the basing point. The east corresponds to the azimuth angle of zero degree. The blue lines show the data for Super-K, and the red lines show the MC predictions for Super-K and Hyper-K based on the MUSIC simulation. The absolute flux and the shape of the Super-K data, which are determined by slant depths for each angle, are well reproduced by MC.

TABLE XXII. Calculated muon flux (J_μ) and average energy ($\overline{E}_\mu$) in Hyper-K and Super-K for 2.70 g/cm^3 specific gravity Ikeno-yama rock based on the simulation method [151]. The basing point, detector 1 (north) and 2 (south) are illustrated in Fig. 99. The values for the Hyper-K detector are the average over the detector plane area at the altitude of 508 m.

Detector site	J_μ (10^{-7} cm^{-2}s^{-1})	$\overline{E}_\mu$ (GeV)
Hyper-K (basing point)	7.55	203
Hyper-K (detector 1)	8.03	201
Hyper-K (detector 2)	8.48	200
Hyper-K (detector 1 + 2)	8.25	200
Super-K	1.54	258

two, as shown in Table V of Ref. [153]. In order to minimize the uncertainties, we use the isotope production rates observed in Super-K as a basis, and the values in Hyper-K are estimated based on the muon flux ratio calculated by `MUSIC` and the isotope yield ratio by `FLUKA`,

$$R_i(\text{Hyper-K}) = R_i(\text{Super-K}) \times \frac{\Phi(\text{Hyper-K})}{\Phi(\text{Super-K})} \times \frac{Y_i(\text{Hyper-K})}{Y_i(\text{Super-K})} \tag{5}$$

where R_i is the production rate per unit volume for isotope i, Φ the muon flux (cm^{-2}s^{-1}), Y_i the isotope yield per muon track length ($/\mu$/m) for isotope i. We use `FLUKA` version 2011.2b to estimate the isotope yields in Hyper-K and Super-K. A water-filled volume of 40-m square and 40-m length is used in the simulation, and the analysis of isotope productions is limited within the inner volume of 40-m square and 20-m length in order to avoid a boundary effect. To include the muon charge and energy dependence in isotope production yields, beams of both μ^+ and μ^- with a calculated energy spectrum produced by `MUSIC` were simulated, and the isotope yields by μ^+ and μ^- are combined based on their weighted average assuming that a relative intensity of μ^+ to μ^- is 1.3. Table XXIII shows the estimation of isotope production yields for Hyper-K and Super-K, the ratio of isotope yields, Y_i(Hyper-K)/Y_i(Super-K). The ratio of the production rates, R_i(Hyper-K)/R_i(Super-K), are also calculated by multiplying the isotope yield ratio by the muon flux ratio, Φ(Hyper-K)/Φ(Super-K) $= 4.9 \pm 1.0$, which was evaluated from the `MUSIC` simulation. We assume uncertainties of $\pm$20% for the muon flux ratio considering the possibility of different rock types for the Hyper-K and Super-K sites. The resulting increase in isotope production rate per unit volume from Super-K is approximately a factor of 4 ± 1 in Hyper-K, which is used for studies of the Hyper-K physics potential in the following sections.

TABLE XXIII. Estimation of isotope production yields for Hyper-K and Super-K by muon spallation with FLUKA. The ratio of the production yields for Hyper-K compared with Super-K are also listed. The ratio of the production rates are calculated by multiplying the isotope yield ratio by the muon flux ratio of 4.9 ± 1.0, evaluated by the MUSIC simulation.

Isotope	Isotope yield by FLUKA (μ/m)		Ratio of isotope yield	Ratio of production rate
	Hyper-K	Super-K	(Hyper-K / Super-K)	(Hyper-K / Super-K)
^{12}B	8.05×10^{-5}	9.93×10^{-5}	0.811 ± 0.078	3.98 ± 0.88
^{12}N	8.70×10^{-6}	1.11×10^{-5}	0.785 ± 0.075	3.84 ± 0.85
^{9}Li	1.23×10^{-5}	1.68×10^{-5}	0.732 ± 0.070	3.59 ± 0.80
^{8}Li	8.67×10^{-5}	1.08×10^{-4}	0.805 ± 0.077	3.95 ± 0.87
^{15}C	5.12×10^{-6}	6.68×10^{-6}	0.768 ± 0.073	3.76 ± 0.83
^{16}N	2.74×10^{-4}	3.41×10^{-4}	0.804 ± 0.077	3.94 ± 0.87
^{11}Be	5.32×10^{-6}	7.76×10^{-6}	0.685 ± 0.065	3.36 ± 0.74

2. Muon spallation background reduction

The spallation products as backgrounds have their origin in the spallation reaction of the cosmic muons. Therefore, we can identify and remove these spallation products if we compare their four-dimensional correlation with corresponding muons. In this section, we will discuss about the muon spallation backgrounds using these correlations. The spallation reduction method is being used in supernova relic neutrino search at Super-Kamiokande.

2.1. Method of muon spallation background reduction

We apply a likelihood ratio test on low-energy events to reduce spallation backgrounds. The detail is discussed below.

With water Cherenkov detector, such as Super-Kamiokande or Hyper-Kamiokande, we can measure the times, positions and energies of the spallation products and their preceding muon tracks. It is also possible to measure the energy deposit per unit length dE/dx along muon tracks, by deconvoluting Cherenkov ring hits. The peak position of dE/dx distribution can be assumed as the position where muon spallation occurs.

We use following valiables for spallation background reduction.

- Time difference δt, between the low-energy event and the preceding muon.
- Transverse distance l_{trans}, which is defined as the perpendicular distance from the muon

track to the low-energy event.

- Longitudinal distance l_{long}, which is defined as the horizontal distance from the peak position of dE/dx on reconstructed muon track and the low-energy event.

- Residual charge Q_{peak}, which is the amount of light seen in *the* dE/dx distribution in a width of 4.5 m centered on the peak.

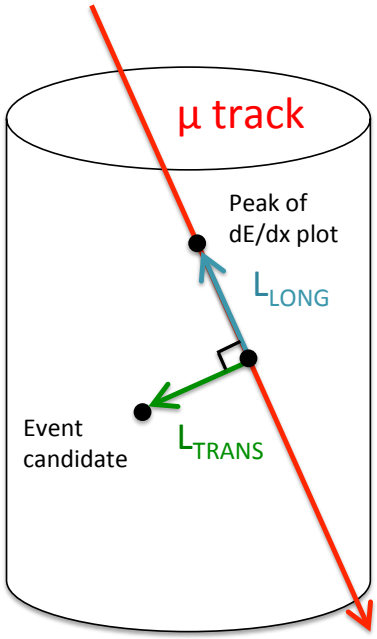

FIG. 103. Schematic figure for showing spallation distance variables[154].

A schematic figure of spallation distance variables are shown in Figure 103. Their actual distributions can be found in a reference [154]. The probability density functions PDF_{spa} and PDF_{rand} of each valuables are given from the fitting results of actual spallation candidates and non-spallation (random) event samples, respectively. The likelihood ratio Λ is defined using PDFs as follows :

$$\begin{aligned}\Lambda = -2\log[PDF_{spa}(Q_{peak}) \times PDF_{spa}(\delta t) \times L_{trans}) \times PDF_{spa}(L_{long}) \\ -log[PDF_{rand}(Q_{peak}) \times PDF_{rand}(\delta t) \times L_{trans}) \times PDF_{rand}(L_{long})\end{aligned} \tag{6}$$

Because any preceding cosmic muon can be a cause of spallation backgrounds, we calculate the likelihood ratio Λ with all muons within 30 seconds before the low energy event. The largest likelihood ratio Λ is adopted as the Λ value for the low energy event. We can arbitrarily choose the cut value for the likelihood ratio, which defines the reduction efficiency and the signal efficiency.

2.2. Estimated muon spallation background after reduction

When we have more cosmic muon flux, the number of preceding muons paired with a low-energy event will be increased. As a result, we will have more chance to have "more spallation like" Λ value for a low-energy event even if it is a non-spallation event. On the other hand the likelihood ratio is not changed for real spallation events, because they will be paired to their mother muons regardless of the number of preceding muons. Consequently we will have worse sepalation between the likelihood distribution of spallation backgrounds and that of non-spallation events with more cosmic muon flux.reduction efficiency and the signal efficiency in Hyper-Kamiokande, based on the data of Super-Kamiokande II. The spallation reduction efficiency is defined as the rate of spallation events which has survived the likelihood cut. The likelihood distribution of non-spallation event sample is also made from the data, pairing the low energy events with muons which were detected 300∼330s before these events. These muons are also applied to study increased muon flux cases, by merging these random muons into the original preceding muons.

In following, we will show two cases of spallation cuts. One is defined to keep the signal efficiency of 80%, which is applied for usual analysis, e.g. solar neutrino analysis. To estimate this cut, we use the real events of Super-Kamiokande II between 17.5 and 20 MeV. We assume the same signal efficiency and the same reduction efficiency below 17.5 MeV. As the result, the spallation reduction efficiency ($\epsilon_{reduction}$) will be 1.2% and 3.9% for the same and 5 times larger amount of the cosmic muons for this criteria, respectively. Finally, the ratio of remaining spallation events in the solar neutrino analysis is calculated as follows:

$$R_{spallation}(\text{Hyper-K/Super-K}) = \frac{R_{production}(\text{Hyper-K})}{R_{production}(\text{Super-K})} \times \frac{\epsilon_{reduction}(\text{Hyper-K})}{\epsilon_{reduction}(\text{Super-K})} \tag{7}$$

. Here, $\epsilon_{reduction}$(Hyper-K) is achieved to be 3.9% for Hyper-K at Tochibora-site as discussed above. $\epsilon_{reduction}$(Super-K) of ∼6% is taken form Super-Kamiokande II solar neutrino analysis. $R_{production}$(Hyper-K) and $R_{production}$(Super-K) are the rate of spallation isotope production per unit volume. Reffering the result of the former section, $R_{production}$(Hyper-K)/$R_{production}$(Super-K) is assumed to be 4 ± 1. Since, we conclude the ratio of remainig spallation events of Hyper-K to Super-K is $R_{spallation}$(Hyper-K/Super-K) = 2.7.

Another is applied for very low background analysis, e.g. supernova relic neutrino search. In this case, the cut value is defined to remove all spallation backgrounds or to reduce them until a few backgrounds left between 17.5 and 20 MeV or between 20 and 26 MeV. So, the signal efficiency will be affected by the increased amount of muons. The signal efficiency will be 79% (29%) for the energy range of 17.5∼20 MeV and 90% (54%) for 20∼26 MeV, for the same (5 times larger) amount

TABLE XXIV. The expected spallation background reduction efficiency, keeping signal efficiency of 80%.

Cosmic muons rate, comparing to Super-K	×1	×5 (Tochibora site)
Signal Efficiency	80%	80%
Spallation Reduction Efficiency	1.2%	3.9%

TABLE XXV. The expected spallation background reduction efficiency for very low background analysis with few spallation background.

Cosmic muons rate, comparing to Super-K	×1	×5 (Tochibora site)
Signal Efficiency (- 20 MeV)	79%	29%
Signal Efficiency (20 - 26 MeV)	90%	54%

of the cosmic muons. Because the amount of spallation backgrounds decreases exponentially in the higher energies, no spallation background is expected above 26 MeV. The results are shown in Table XXIV and Table XXV.

B. Neutron background estimation for atmospheric neutrino / proton decay study

In this subsection, we will discuss about the possible cosmic-ray backgrounds for the atmospheric neutrino or proton decay analysis, which visible energy is greater than 30 MeV. In this energy range the spallation background by cosmic muons, which is described in Section II.4 A, can be neglected.

In the Super-K detector case, thanks to the double structure of the inner and outer detector, cosmic muons entering the detector can be easily rejected by looking at hit clusters around the entering and exiting points of muons. According to Super-K's experience, the estimated background of the cosmic muons are negligible (∼0.1% in the final atmospheric neutrino fully-contained sample). Considering that Hyper-K design is basically same structure, similar level of the background rejection performance for cosmic muons by the outer detector is expected even if the cosmic muon rate is increased by several factor due to the shallower site of Hyper-Kamiokande.

One possible concern about the background due to neutral particle, such as neutrons and neutral kaons, which are produced by hadronic interaction of cosmic muons near the detector, and enter the detector without being detected by the outer detector. Such particle may penetrate deep into the detector and produce hadrons, such as π^0, by interacting with water, which could become electron-like backgrounds. Figure 104 shows a Super-K event display of the simulated neutron

TABLE XXVI. Comparison of various parameters related to neutron background estimation between Super-K and Hyper-K. The estimation of these values are based on [155]

	Super-K site	Hyper-K site
Site depth (m.w.e.)	2700	1750
Cosmic muon rate (10^{-6}/cm^2/sec)	0.13∼0.14	1.0∼2.3
Effective depth (m.w.e.)	2050	1170
$< E_\mu >$ (GeV)	219	146
Φ_n (10^{-9}/cm^2/sec)	12.3	101
(>100 MeV)	0.81	6.7
$< E_n >$ (MeV)	76	53

background events which produced π^0 particle in the detector.

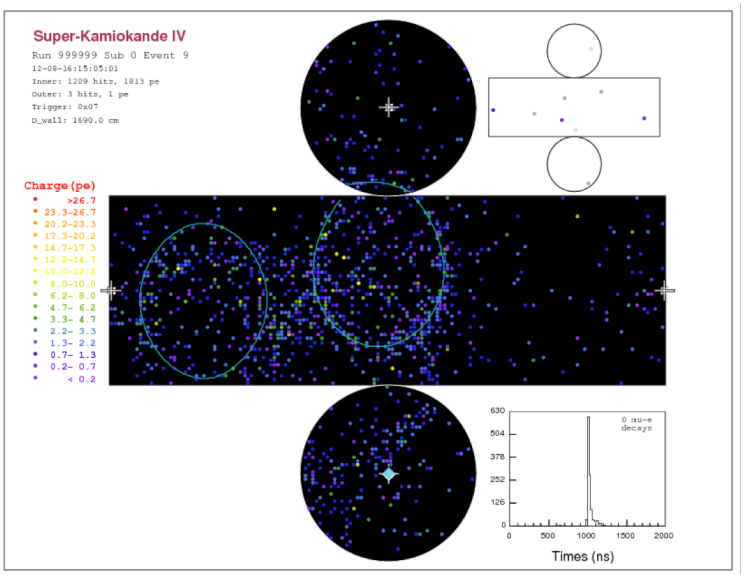

FIG. 104. Event display of a neutron background simulation. π^0 is produced by the interaction of $n + X \rightarrow X' + \pi^0$. Neutron is simulated with the energy of 1 GeV from the center of the detector.

For the study of the neutron background, the flux of cosmic neutron at the detector site are estimated based on [155] and shown in Table XXVI. According to this table, the neutron flux of $E > 100$ MeV at Hyper-K site will increase by a factor of ∼8 than that of Super-K site.

Though detecting neutron is difficult, their backgrounds can be reduced by two ways;

- Self-shielding effect due to surrounding water around fiducial volume. In Super-K case, a water volume of ∼ 4.6 m thick (2.0 m in the inner detector and 2.6∼2.8 m in the outer detector)

is surrounded around fiducial volume. Since the neutron is reduced by hadronic interactions in water in a scale of several 10 cm, neutrons is expected to be reduced significantly before reaching the fiducial volume.

- By detection of the accompanying cosmic muon. As seen in Fig 105, cosmic neutron and its parent muon are spatially correlated. This means that neutrons are reduced after traveling in several meter from muon track in the rock. Considering the detector size of the Hyper-K, when neutrons comes into the detector, it is supposed that accompanying muons go through the detector also in most case, and rejected by the signal in the outer detector.

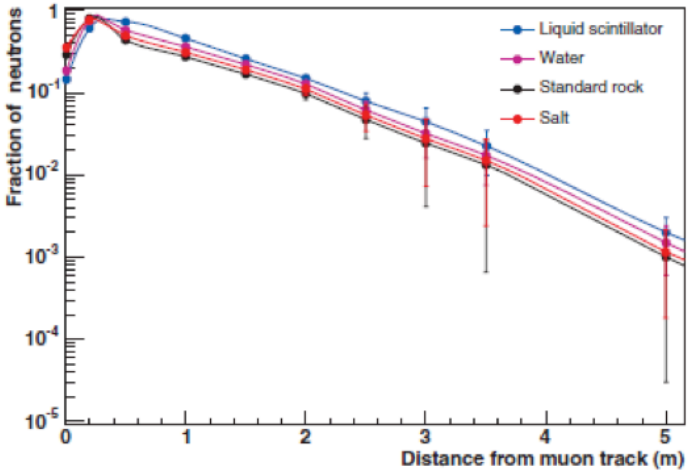

FIG. 105. Lateral distribution of cosmic neutron from parent muon track. Figure was taken from [155]

In order to estimate the amount of the neutron background in Hyper-K, we performed neutron background simulation taking into account of the effect of the accompanying muons. The detector simulation of Super-K was used. Since most of the neutrons are expected to be rejected by taking the coincidence with muon signal, as described above, simple toy Monte Carlo simulation considering the detector geometry are performed, and then events in which only neutron is entering are simulated with the Super-K simulator. The detail procedure of the simulation is described as follows:

1. Determine muon track. The starting position of muon track is in the plane about 20 meter above the top of Super-K detector and vertex is randomly determined within the region of 200 meter from the detector center.

2. Determine the neutron entering point to the detector according to the neutron lateral distribution from muon track. If the detector is enough distant from neutron vertex, this event is not counted.

3. Rejection by muon track. If muon track goes through the detector region, this event is discarded.

4. For the events which pass the previous step, neutron vector information, such as vertex, energy, direction, are fed into Super-K detector simulator and simulate neutron interactions.

5. Apply simple fully-contained (FC) reduction cut to simulated neutron events. Criterion that the number of hits in the outer detector (*nhitac*) is less than 16 and the visible energy in the inner detector (E_{vis}) is greater than 30 MeV are required.

The energy and directional angle distributions of neutrons are determined based on [155]. According to the toy simulation, 97% of events are rejected by the criteria of muon coincidence with neutron in step 3.

Fig 106 shows the distributions of the reduction parameters, *nhitac* and E_{vis}. Fig 107 shows the distribution of neutron kinetic energy for all simulated events and the remaining events after FC and fiducial volume (FCFV) cut. Fig 108 shows the vertex distribution in Z (height) vs R (radius) of the detector, D_{wall} distribution, which is the distance to the wall. In the vertex distribution events are gathering around the side wall and fewer events around top, suggesting the vertical muons passing nearby the detector produced neutrons entering the detector.

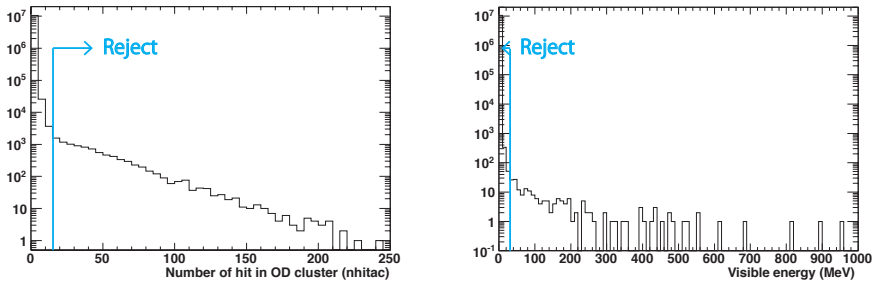

FIG. 106. Distributions of number of hits in the outer detector (*nhitac*) (left) and visible energy in the inner detector (E_{vis}) (right) for simulated neutron background events.

Table XXVII shows the summary of the neutron background MC events in each reduction step. Normalizing to the number of events per one year at Super-K detector condition, 2.1 and 0.2

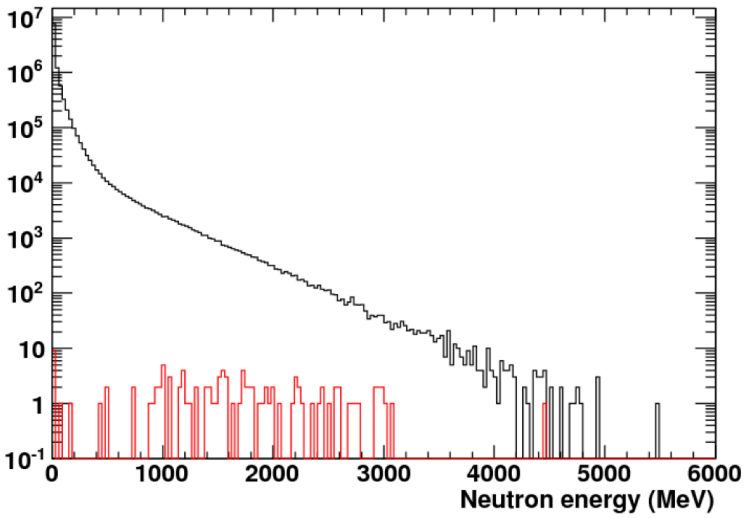

FIG. 107. Distributions of neutron kinetic energy for all simulated events (black) and remaining events after FCFV cut (red).

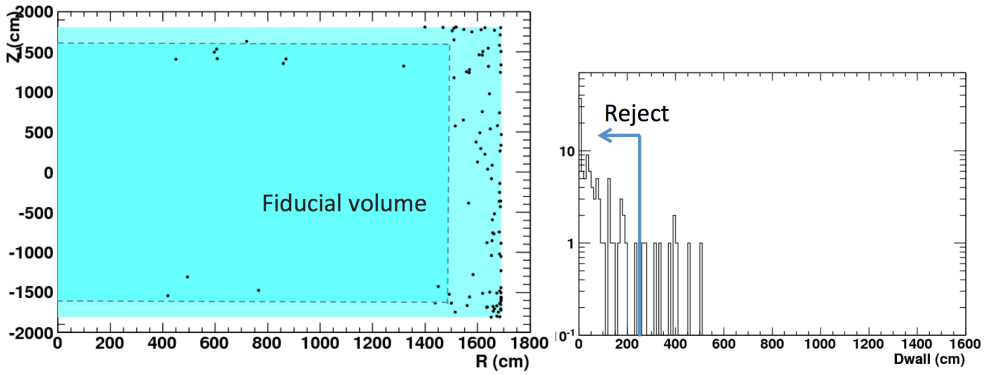

FIG. 108. Reconstructed vertex distributions of neutron background events which pass after fully-contained reduction (left), and D_{wall} distribution ,which corresponds to the distance between reconstructed vertex to the detector wall, for same event (right).

events are expected for fully-contained (FC) and fully-contained fiducial volume (FCFV) event, respectively. Considering the event rate of ∼3000 atmospheric neutrinos, this corresponds to $0.2/3000 = 7 \times 10^{-3}\%$ background rate in FCFV sample. As for the case of Hyper-K site, neutron flux is increased by about factor of eight according to Table XXVI due to the shallower overburden of detector site condition. Since the similar signal-to-background rate is expected between Super-K and Hyper-K detectors due to the same detector technology, the background rate can be simply scaled by the neutron flux, $7 \times 10^{-2}\%$ of the neutron background rate is estimated, which seems to be negligible level for physics study.

TABLE XXVII. Summary of the number of events in neutron background using Super-K detector simulation.

	All simulation	Event/1year at SK
entering neutrons	4.5×10^{8}	8.9×10^{6}
w/o muon coincidence	1.1×10^{7}	2.1×10^{5}
passed fully-contained cut (FC)	105	2.1
vertex is in FV (FCFV)	11	0.2

Another possible neutral particle which could be the background is neutral kaon. According to the calculation of neutral kaon flux in underground [156], neutral flux is estimated to be significantly smaller; 0.3% of neutron flux at 3 km m.w.e.. We estimated amount of kaon background with 0.3% flux of neutron flux and estimated energy spectrum shown in [156] for 50 year corresponding MC, and no background events are observed after FCFV selection, concluding that the background from neutral kaon is negligible.

Part III

Physics Potential

III.1. NEUTRINO OSCILLATION

A. Accelerator based neutrinos

A long baseline neutrino oscillation experiment with the J-PARC neutrino beam is one of the key elements of Hyper-K physics program. Especially, a precise study of CP asymmetry in the lepton sector is one of the major goals of Hyper-K. The existence of CP violation is one of necessary conditions to explain the matter-antimatter asymmetry of the Universe.

In the Standard Model, extended to accommodate non-zero neutrino masses, the source of CP violation is (apart from the QCD phase) attributed to irreducible complex phases in the flavor mixing matrices. In the quark sector, with more than fifty years of extensive study after the initial discovery of CP violation in kaon decays, all measurements related to CP violation are consistently explained by the Kobayashi-Maskawa phase [157]. On the other hand, in the lepton sector, experimental study of CP asymmetry has just begun. Recently, the T2K collaboration reported the first constraint on δ_{CP} [51] with θ_{13} measured by reactor experiments assuming the standard mixing framework. This is the first step in an experimental program towards the test of leptonic CP symmetry following the discovery of large value of θ_{13}. Now, it is necessary to build a next generation experiment with a definitive sensitivity to study the CP asymmetry.

For a direct and model-independent measurement of the CP asymmetry, a comparison of oscillation probabilities between neutrino and anti-neutrino will be necessary. Measurements of $\nu_\mu \to \nu_e$ and $\overline{\nu}_\mu \to \overline{\nu}_e$ oscillations are practically the only possible way to study the lepton CP asymmetry. Furthermore, it will be possible to check the consistency of the mixing framework by comparing the accelerator (ν_μ to ν_e appearance of GeV neutrino over 295 km) and reactor ($\overline{\nu}_e$ disappearance of MeV neutrino over $\sim$1 km) measurements, which are related to the same parameters in the standard framework but may receive different contribution from new physics.

The observation of CP violation in the lepton sector will open a new field of research. A quest will start to understand its origin with precision measurements, as has been done in the quark sector. A measurement of CP violating phase, together with precision measurements of mixing angles and mass differences, will provide crucial information to discriminate the fundamental physics behind mass and mixing generation. There are various models proposed based on flavor symmetries

or other methods, and many of them give testable predictions for relations among those parameters. Precision measurements of oscillation parameters require both large statistics and well controlled systematics. Combining an intense (>MW) and high quality neutrino beam from J-PARC, the huge mass and high performance of Hyper-K detector, a highly capable near/intermediate detector complex, and the full expertise obtained from ongoing T2K experiment, Hyper-K will be the best project to probe neutrino CP violation and new physics with neutrino oscillation.

1. J-PARC to Hyper-Kamiokande long baseline experiment

The neutrino energy spectrum of J-PARC neutrino beam is tuned to the oscillation maximum with the off-axis technique, which enhances the flux at the peak energy while reducing the higher energy component that produces background events. The peak energy, around 600 MeV, is well matched to the water Cherenkov detector, which has an excellent e/μ separation capability, high background rejection efficiency and high signal efficiency for sub-GeV neutrino events. Due to the relatively short baseline of 295 km and thus lower neutrino energy at the oscillation maximum, the contribution of the matter effect is smaller for the J-PARC to Hyper-Kamiokande experiment compared to other proposed experiments like DUNE in the United States. Thus the CP asymmetry measurement with the J-PARC to Hyper-K long baseline experiment has less uncertainty related to the matter effect, while other experiments with > 1000 km baseline have much better sensitivity to the mass hierarchy with accelerator neutrino beams. Hyper-K can determine the mass hierarchy using atmospheric neutrinos as described in Section III.1 B. The sensitivities for CP violation and mass hierarchy can be further enhanced by combining measurements with different baseline.

The focus of J-PARC to Hyper-K experiment is measurements of $|\Delta m^2_{32}|$, $\sin^2\theta_{23}$, $\sin^2\theta_{13}$ and δ_{CP}, while the sign of Δm^2_{32} will be determined with atmospheric neutrino measurements and other experiments. Although it is possible that new physics manifests itself in neutrino oscillation, the standard flavor mixing scenario is assumed in the following as a baseline study. The analysis presented in this report is based on [158] but with an updated treatment of systematic uncertainties.

2. Oscillation probabilities and measurement channels

In what follows, the oscillation probabilities and sensitivities to oscillation parameters with ν_e appearance and ν_μ disappearance measurements are discussed. The analysis will be performed by a combination of these two channels.

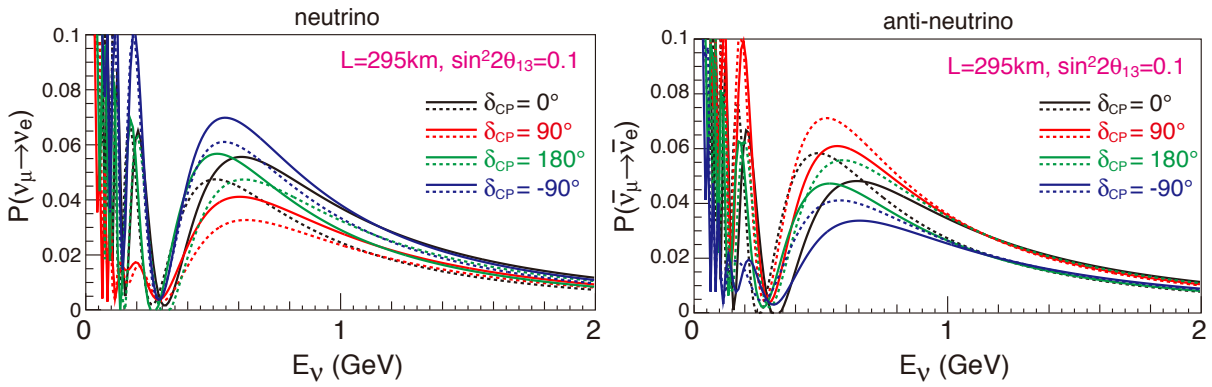

FIG. 109. Oscillation probabilities as a function of the neutrino energy for $\nu_\mu \to \nu_e$ (left) and $\overline{\nu}_\mu \to \overline{\nu}_e$ (right) transitions with L=295 km and $\sin^2 2\theta_{13} = 0.1$. Black, red, green, and blue lines correspond to $\delta_{CP} = 0°$, 90°, 180° and −90°, respectively. Solid (dashed) line represents the case for a normal (inverted) mass hierarchy.

2.1. $\nu_\mu \to \nu_e$ appearance channel The oscillation probability from ν_μ to ν_e is expressed, to the first order of the matter effect, as follows [159]:

$$\begin{aligned} P(\nu_\mu \to \nu_e) = {} & 4c_{13}^2 s_{13}^2 s_{23}^2 \cdot \sin^2 \Delta_{31} \\ & + 8c_{13}^2 s_{12} s_{13} s_{23} (c_{12} c_{23} \cos\delta_{CP} - s_{12} s_{13} s_{23}) \cdot \cos\Delta_{32} \cdot \sin\Delta_{31} \cdot \sin\Delta_{21} \\ & - 8c_{13}^2 c_{12} c_{23} s_{12} s_{13} s_{23} \sin\delta_{CP} \cdot \sin\Delta_{32} \cdot \sin\Delta_{31} \cdot \sin\Delta_{21} \\ & + 4s_{12}^2 c_{13}^2 (c_{12}^2 c_{23}^2 + s_{12}^2 s_{23}^2 s_{13}^2 - 2c_{12} c_{23} s_{12} s_{23} s_{13} \cos\delta_{CP}) \cdot \sin^2 \Delta_{21} \\ & - 8c_{13}^2 s_{13}^2 s_{23}^2 \cdot \frac{aL}{4E_\nu} (1 - 2s_{13}^2) \cdot \cos\Delta_{32} \cdot \sin\Delta_{31} \\ & + 8c_{13}^2 s_{13}^2 s_{23}^2 \frac{a}{\Delta m_{31}^2} (1 - 2s_{13}^2) \cdot \sin^2 \Delta_{31}, \end{aligned} \tag{8}$$

where $s_{ij} = \sin\theta_{ij}$, $c_{ij} = \cos\theta_{ij}$, $\Delta_{ij} = \Delta m_{ij}^2 L/4E_\nu$, and $a = 2\sqrt{2} G_F n_e E_\nu = 7.56 \times 10^{-5} [\mathrm{eV}^2] \times \rho[\mathrm{g/cm}^3] \times E_\nu[\mathrm{GeV}]$. L, E_ν, G_F and n_e are the baseline, the neutrino energy, the Fermi coupling constant and the electron density, respectively. The corresponding probability for a $\overline{\nu}_\mu \to \overline{\nu}_e$ transition is obtained by replacing $\delta_{CP} \to -\delta_{CP}$ and $a \to -a$. The third term, containing $\sin\delta_{CP}$, is the CP violating term which flips sign between ν and $\bar{\nu}$ and thus introduces CP asymmetry if $\sin\delta_{CP}$ is non-zero. The last two terms are due to the matter effect. Those terms which contain a change their sign depending on the mass hierarchy. As seen from the definition of a, the amount of asymmetry due to the matter effect is proportional to the neutrino energy at a fixed value of L/E_ν.

Figure 109 shows the $\nu_\mu \to \nu_e$ and $\overline{\nu}_\mu \to \overline{\nu}_e$ oscillation probabilities as a function of the true neutrino energy for a baseline of 295 km. The Earth matter density is assumed to be 2.6 g/cm^3. The

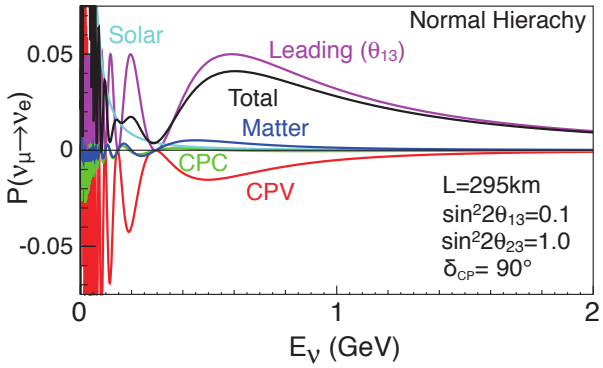

FIG. 110. Oscillation probability of $\nu_\mu \to \nu_e$ as a function of the neutrino energy with a baseline of 295 km. $\sin^2 2\theta_{13} = 0.1$, $\delta_{CP} = 90°$, and normal hierarchy are assumed. Contribution from each term of the oscillation probability formula is shown separately.

cases for 0°, 90°, 180° and −90°, are shown together. One can see the effect of different δ_{CP} values on the oscillation probabilities. For example, if $\delta_{CP} = -90°$, the appearance probability will be enhanced for neutrino but suppressed for anti-neutrino. By comparing the oscillation probabilities of neutrinos and anti-neutrinos, one can measure the CP asymmetry. The information on the CP phase can be derived from not only the total number of events but energy spectrum measurement. For example, for both $\delta_{CP} = 0°$ and 180°, CP is conserved ($\sin\delta_{CP} = 0$) and the oscillation probabilities in vacuum are the same for neutrino and anti-neutrino, however those two cases can be distinguished using spectrum information as seen in Fig. 109.

Also shown in Fig. 109 are the case of normal mass hierarchy ($\Delta m^2_{32} > 0$) with solid lines and inverted mass hierarchy ($\Delta m^2_{32} < 0$) with dashed lines. There are sets of different mass hierarchy and values of δ_{CP} which give similar oscillation probabilities, resulting in a potential degeneracy if the mass hierarchy is unknown. By combining information from experiments currently ongoing [43–45, 84, 160] and/or planned in the near future [39, 40, 46–48], it is expected that the mass hierarchy will be determined by the time Hyper-K starts to take data. If not, Hyper-K itself has a sensitivity to the mass hierarchy by the atmospheric neutrino measurements as described in the next section. Thus, the mass hierarchy is assumed to be known in this analysis, unless otherwise stated.

Figure 110 shows the contribution from each term of the $\nu_\mu \to \nu_e$ oscillation probability formula, Eq.(8), for $L = 295\,\mathrm{km}$, $\sin^2 2\theta_{13} = 0.1$, $\sin^2 2\theta_{23} = 1.0$, $\delta_{CP} = 90°$, and normal mass hierarchy. For $E_\nu \simeq 0.6\,\mathrm{GeV}$ which gives $\sin\Delta_{32} \simeq \sin\Delta_{31} \simeq 1$,

$$\frac{P(\nu_\mu \to \nu_e) - P(\bar{\nu}_\mu \to \bar{\nu}_e)}{P(\nu_\mu \to \nu_e) + P(\bar{\nu}_\mu \to \bar{\nu}_e)} \simeq \frac{-16 J_{CP} \sin\Delta_{21} + 16 c^2_{13} s^2_{13} s^2_{23} \frac{a}{\Delta m^2_{31}} (1 - 2 s^2_{13})}{8 c^2_{13} s^2_{13} s^2_{23}} \tag{9}$$

$$\simeq -0.28 \sin\delta + 0.07. \tag{10}$$

The effect of CP violating term can be as large as 28%, while that of the matter effect is 7%.

The uncertainty of the Earth's density between Tokai and Kamioka is estimated to be at most 6% [161]. Because the matter effect contribution to the total appearance probability is less than 10% for 295km baseline, the uncertainty from matter density is estimated to be less than 0.6% and neglected in the following analysis.

2.2. ν_μ disappearance channel Currently measured value of θ_{23} is consistent with maximal mixing, $\theta_{23} \approx \pi/4$ [22, 162, 163]. It is of great interest to determine if $\sin^2 2\theta_{23}$ is maximal or not, and if not, whether θ_{23} is less or greater than $\pi/4$, as it could constrain models of neutrino mass generation and quark-lepton unification [35, 164–168]. When we measure θ_{23} with the survival probability $P(\nu_\mu \to \nu_\mu)$ which is proportional to $\sin^2 2\theta_{23}$ to first order,

$$P(\nu_\mu \to \nu_\mu) \simeq 1 - 4c_{13}^2 s_{23}^2 [1 - c_{13}^2 s_{23}^2] \sin^2(\Delta m_{32}^2 \, L/4E_\nu) \tag{11}$$

$$\simeq 1 - \sin^2 2\theta_{23} \sin^2(\Delta m_{32}^2 \, L/4E_\nu), \qquad (\text{for } c_{13} \simeq 1) \tag{12}$$

there is an octant ambiguity, as for each value of $\theta_{23} \leq 45^\circ$ (in the first octant), there is a value in the second octant ($\theta_{23} > 45^\circ$) that gives rise to the same oscillation probability. As seen from Eq. 8, ν_e appearance measurement can determine $\sin^2\theta_{23} \sin^2 2\theta_{13}$. In addition, the reactor experiments provide almost pure measurement of $\sin^2 2\theta_{13}$. Thus, the combination of those complimentary measurements will be able to resolve this degeneracy if θ_{23} is sufficiently away from $\frac{\pi}{4}$ [169–171].

Measurement of $\overline{\nu}_e$ disappearance by reactor neutrino experiments provides a constraint on the following combination of mass-squared differences,

$$\Delta m_{ee}^2 = \cos^2\theta_{12} \Delta m_{31}^2 + \sin^2\theta_{12} \Delta m_{32}^2. \tag{13}$$

while ν_μ disappearance measurement with Hyper-K provides a different combination [41, 42]

$$\Delta m_{\mu\mu}^2 = \sin^2\theta_{12} \Delta m_{31}^2 + \cos^2\theta_{12} \Delta m_{32}^2 + \cos\delta_{CP} \sin\theta_{13} \sin 2\theta_{12} \tan\theta_{23} \Delta m_{21}^2. \tag{14}$$

Because the mass squared difference measurements by Hyper-K and by reactor experiments give independent information, by comparing them one can check the consistency of the mixing matrix framework, and obtain information on the neutrino mass hierarchy. In order to have sensitivity to the mass hierarchy, uncertainties of both measurements must be smaller than 1%. Future medium baseline reactor experiments, JUNO [39] and RENO-50 [40], plan to measure Δm_{ee}^2 with precision better than 1%. Thus, precision measurement of Δm^2 by Hyper-K will provide an important information on the consistency of three generation mixing framework and mass hierarchy.

3. Analysis overview

The analysis used in this report is based on a framework developed for the sensitivity study by T2K presented in [172]. A binned likelihood analysis based on the reconstructed neutrino energy distribution is performed using both ν_e ($\overline{\nu}_e$) appearance and ν_μ ($\overline{\nu}_\mu$) disappearance samples simultaneously. A full oscillation probability formula, not approximation shown in Eq. 8, is used in the analysis. Table XXVIII shows the nominal oscillation parameters used in the study presented in this report, and the treatment during the fitting. Parameters to be determined with the fit are $\sin^2\theta_{13}$, $\sin^2\theta_{23}$, Δm^2_{32} and δ_{CP}.

An integrated beam power of 13 MW$\times 10^7$ sec is assumed in this study, corresponding to 2.7×10^{22} protons on target with 30 GeV J-PARC beam. It corresponds to about ten Snowmass years with 1.3 MW. We have studied the sensitivity to CP violation with various assumptions of neutrino mode and anti-neutrino mode beam running time ratio for both normal and inverted mass hierarchy cases. The dependence of the sensitivity on the ν:$\overline{\nu}$ ratio is found not to be significant between ν:$\overline{\nu}$=1:1 to 1:5. In this report, ν:$\overline{\nu}$ ratio is set to be 1:3 so that the expected number of events are approximately the same for neutrino and anti-neutrino modes.

TABLE XXVIII. Oscillation parameters used for the sensitivity analysis and treatment in the fitting. The *nominal* values are used for figures and numbers in this section, unless otherwise stated.

Parameter	$\sin^2 2\theta_{13}$	δ_{CP}	$\sin^2\theta_{23}$	Δm^2_{32}	mass hierarchy	$\sin^2 2\theta_{12}$	Δm^2_{21}
Nominal	0.10	0	0.50	2.4×10^{-3} eV^2	Normal	0.8704	7.6×10^{-5} eV^2
Treatment	Fitted	Fitted	Fitted	Fitted	Fixed	Fixed	Fixed

Interactions of neutrinos in the Hyper-K detector are simulated with the NEUT program library [173–175], which is used in both Super-K and T2K. The response of the detector is simulated using the Super-K full Monte Carlo simulation based on the GEANT3 package [176]. The simulation is based on the SK-IV configuration with upgraded electronics and DAQ system. Events are reconstructed with the Super-K reconstruction software, which gives a realistic estimate of the Hyper-K performance.

Based on the experience with the SK-II period when the number of PMT was about half compared to other periods (corresponding to 20% photocoverage with the Super-K PMT R3600), the reconstruction performance for beam neutrino events with around 1 GeV energy is known not to degrade with reduced photocathode coverage down to 20% (with R3600). Thus, the performance for the beam neutrino is largely independent from the photocathode coverage in the range considered

for Hyper-K. There will be additional capabilities such as neutron tagging with higher coverage, but they are not yet taken into account in the current study.

In what follows, results are presented assuming ten years of running, single tank for the first six years and two tanks from the seventh year.

4. Expected observables at the far detector

The criteria to select ν_e and ν_μ candidate events are based on those developed for and established with the Super-K and T2K experiments. Fully contained (FC) events with a reconstructed vertex inside the fiducial volume (FV) and visible energy ($E_{\rm vis}$) greater than 30 MeV are selected as FCFV neutrino event candidates. In order to enhance charged current quasielastic (CCQE, $\nu_l + n \to l^- + p$ or $\overline{\nu}_l + p \to l^+ + n$) interaction, a single Cherenkov ring is required.

Assuming a CCQE interaction, the neutrino energy ($E_\nu^{\rm rec}$) is reconstructed from the energy of the final state charged lepton (E_ℓ) and the angle between the neutrino beam and the charged lepton directions (θ_ℓ) as

$$E_\nu^{\rm rec} = \frac{2(m_n - V)E_\ell + m_p^2 - (m_n - V)^2 - m_\ell^2}{2(m_n - V - E_\ell + p_\ell \cos\theta_\ell)}, \tag{15}$$

where m_n, m_p, m_ℓ are the mass of neutron, proton, and charged lepton, respectively, p_ℓ is the charged lepton momentum, and V is the mean nuclear potential energy (27 MeV).

Then, to select $\nu_e/\overline{\nu}_e$ candidate events the following criteria are applied; the reconstructed ring is identified as electron-like (e-like), $E_{\rm vis}$ is greater than 100 MeV, there is no decay electron associated to the event, and $E_\nu^{\rm rec}$ is less than 1.25 GeV. Finally, in order to reduce the background from mis-reconstructed π^0 events, additional criteria using the reconstructed π^0 mass and the ratio of the best-fit likelihoods of the π^0 and electron fits [26] are applied.

Figure 111 shows the reconstructed neutrino energy distributions of $\nu_e/\overline{\nu}_e$ events after all the selections. The expected number of $\nu_e/\overline{\nu}_e$ candidate events is shown in Table XXIX for each signal and background component. The efficiencies of selection with respect to FCFV events are also shown in Table XXIX. In the neutrino mode, the dominant background component is intrinsic ν_e contamination in the beam. The mis-identified neutral current π^0 production events are suppressed thanks to the improved π^0 reconstruction. The total rejection factor, including FCFV selection, for NC π^0 interaction is $> 99.5\%$. In the anti-neutrino mode, in addition to $\overline{\nu}_e$ and $\overline{\nu}_\mu$, ν_e and ν_μ components have non-negligible contributions due to larger fluxes and cross-sections compared to their counterparts in the neutrino mode.

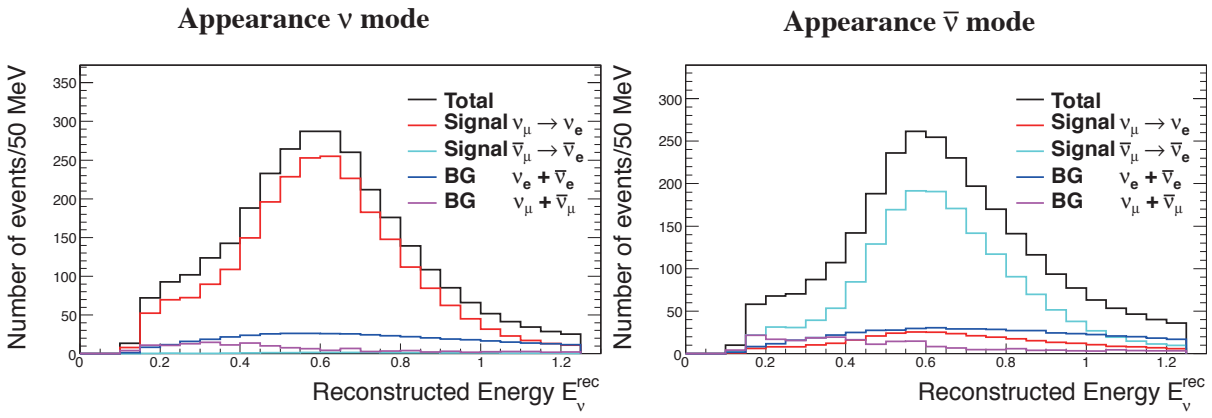

FIG. 111. Reconstructed neutrino energy distribution of the ν_e candidate events. Left: neutrino beam mode, right: anti-neutrino beam mode. Normal mass hierarchy with $\sin^2 2\theta_{13} = 0.1$ and $\delta_{CP} = 0°$ is assumed. Compositions of appearance signal, $\nu_\mu \to \nu_e$ and $\overline{\nu}_\mu \to \overline{\nu}_e$, and background events originating from $(\nu_\mu + \overline{\nu}_\mu)$ and $(\nu_e + \overline{\nu}_e)$ are shown separately.

TABLE XXIX. The expected number of $\nu_e/\overline{\nu}_e$ candidate events and efficiencies with respect to FCFV events. Normal mass hierarchy with $\sin^2 2\theta_{13} = 0.1$ and $\delta_{CP} = 0$ are assumed. Background is categorized by the flavor before oscillation.

		signal		BG						Total
		$\nu_\mu \to \nu_e$	$\overline{\nu}_\mu \to \overline{\nu}_e$	ν_μ CC	$\overline{\nu}_\mu$ CC	ν_e CC	$\overline{\nu}_e$ CC	NC	BG Total	
ν mode	Events	2300	21	10	0	347	15	188	560	2880
	Eff.(%)	63.6	47.3	0.1	0.0	24.5	12.6	1.4	1.6	—
$\bar{\nu}$ mode	Events	289	1656	3	3	142	302	274	724	2669
	Eff. (%)	45.0	70.8	0.03	0.02	13.5	30.8	1.6	1.6	—

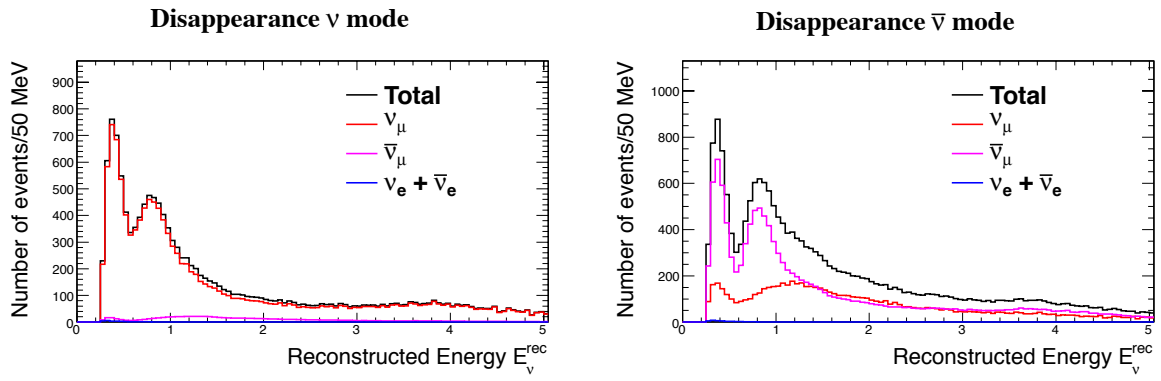

FIG. 112. Reconstructed neutrino energy distribution of the $\nu_\mu/\overline{\nu}_\mu$ candidate events after oscillation. Left: neutrino beam mode, right: anti-neutrino beam mode.

TABLE XXX. The expected number of $\nu_\mu/\overline{\nu}_\mu$ candidate events and efficiencies (with respect to FCFV events) for each flavor and interaction type.

		ν_μCCQE	ν_μCC non-QE	$\overline{\nu}_\mu$CCQE	$\overline{\nu}_\mu$CC non-QE	$\nu_e + \overline{\nu}_e$ CC	NC	$\nu_\mu \to \nu_e$	total
ν mode	Events	8460	4173	487	271	9	672	40	14110
	Eff. (%)	91.0	20.7	95.6	53.5	0.5	8.8	1.1	—
$\bar{\nu}$ mode	Events	3778	3295	8539	2745	10	844	5	19214
	Eff. (%)	88.0	20.1	95.4	54.8	0.4	8.8	0.7	—

For the $\nu_\mu/\overline{\nu}_\mu$ candidate events the following criteria are applied; the reconstructed ring is identified as muon-like (μ-like), the reconstructed muon momentum is greater than 200 MeV/c, and there is at most one decay electron associated to the event.

Figure 112 shows the reconstructed neutrino energy distributions of the selected $\nu_\mu/\overline{\nu}_\mu$ events. Table XXX shows the number of $\nu_\mu/\overline{\nu}_\mu$ candidate events for each signal and background component. In the neutrino beam mode, the purity of ν_μ CC events, after oscillation and for $E_{rec} < 1.5$ GeV, is 89%. For the anti-neutrino mode data, the contribution of wrong-sign ν_μ CC events is significant because the cross section of neutrino is about three times larger than anti-neutrino in this energy range. The fractions of $\overline{\nu}_\mu$ and ν_μ CC events in anti-neutrino beam mode data after selection, for $E_{rec} < 1.5$ GeV, are 66% and 26%, respectively.

The reconstructed neutrino energy distributions of ν_e events for several values of δ_{CP} are shown in the top plots of Fig. 113. The effect of δ_{CP} is clearly seen using the reconstructed neutrino energy. The bottom plots show the difference of reconstructed energy spectrum from $\delta_{CP} = 0°$ for the cases $\delta_{CP} = 90°, -90°$ and 180°. The error bars correspond to the statistical uncertainty. By using not only the total number of events but also the reconstructed energy distribution, the sensitivity to δ_{CP} can be improved and one can discriminate all the values of δ_{CP}, including the difference between $\delta_{CP} = 0°$ and 180° for which CP symmetry is conserved.

Figure 114 shows the reconstructed neutrino energy distributions of the ν_μ sample, for the cases with $\sin^2\theta_{23} = 0.5$ and without oscillation. Thanks to the narrow energy spectrum tuned to the oscillation maximum with off-axis beam, the effect of oscillation is clearly visible.

5. Analysis method

As described earlier, a binned likelihood analysis based on the reconstructed neutrino energy distribution is performed. Both ν_e appearance and ν_μ disappearance samples, in both neutrino

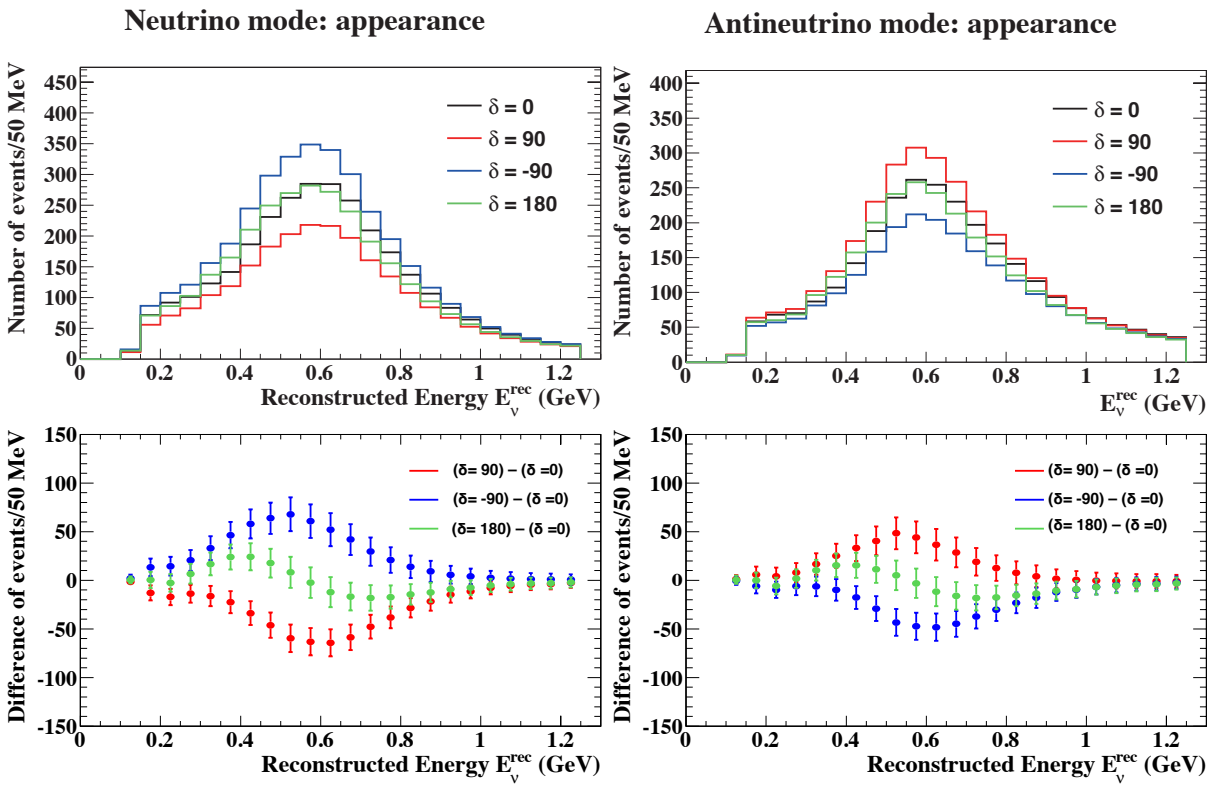

FIG. 113. Top: Reconstructed neutrino energy distribution for several values of δ_{CP}. $\sin^2 2\theta_{13} = 0.1$ and normal hierarchy is assumed. Bottom: Difference of the reconstructed neutrino energy distribution from the case with $\delta_{CP} = 0°$. The error bars represent the statistical uncertainties of each bin.

and antineutrino mode data, are simultaneously fitted.

The χ^2 used in this study is defined as

$$\chi^2 = -2 \ln \mathcal{L} + P, \tag{16}$$

where $\ln \mathcal{L}$ is the log likelihood for a Poisson distribution,

$$-2 \ln \mathcal{L} = \sum_k \left\{ -N_k^{\text{test}}(1 + f_i) + N_k^{\text{true}} \ln \left[N_k^{\text{test}}(1 + f_i) \right] \right\}. \tag{17}$$

Here, N_k^{true} (N_k^{test}) is the number of events in k-th reconstructed energy bin for the true (test) oscillation parameters. The index k runs over all reconstructed energy bins for muon and electron neutrino samples and for neutrino and anti-neutrino mode data. The parameters f_i represent systematic uncertainties.

The penalty term P in Eq. 16 constrains the systematic parameters f_i with the normalized covariance matrix C,

$$P = \sum_{i,j} f_i (C^{-1})_{i,j} f_j. \tag{18}$$

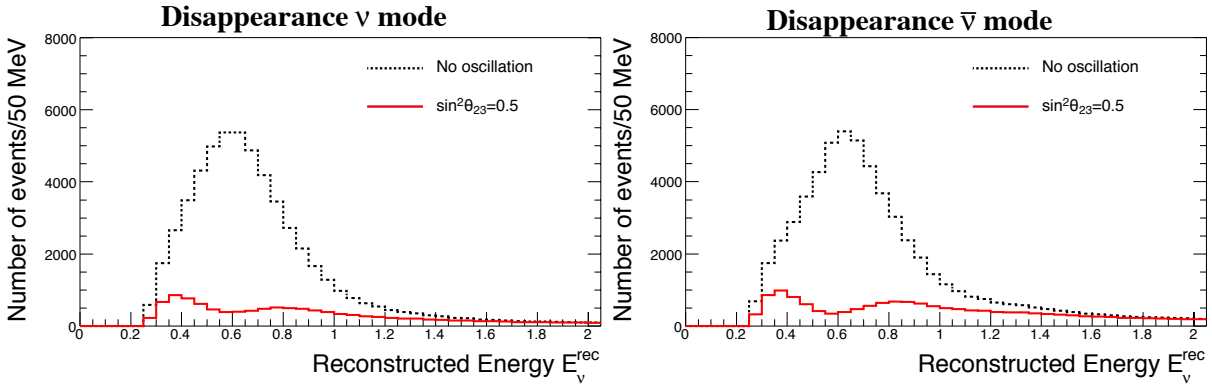

FIG. 114. Reconstructed neutrino energy distributions of ν_μ candidates. Dotted black lines are for no oscillation case, while solid red lines represent prediction with oscillation. Left: for neutrino beam mode. Right: for anti-neutrino beam mode.

In order to reduce the number of the systematic parameters, several reconstructed energy bins that have similar covariance values are merged for f_i.

We estimate the systematic uncertainties assuming the T2K neutrino beamline and near detectors, taking into account improvements expected with future T2K data and analysis improvements. A robust estimate of the uncertainties is possible based on the T2K experience. There are three main categories of systematic uncertainties. We assume improvement from the current T2K uncertainties for each category as follows.

i) Flux and cross section uncertainties constrained by the fit to near detector data:
Data from near detectors will be used in conjunction with models for the neutrino beam, neutrino interactions, and the detector performance to improve our predictions of the flux at SK and some cross-section parameters. The understanding of the neutrino beam, interaction, and detector is expected to improve in the future, which will result in reduction of uncertainties in this category. On the other hand, the near detector analysis is expected to include more samples to reduce the uncertainty for category ii), which will result in migration of some errors into this category. This category of uncertainties is assumed to stay at the same level as currently estimated by T2K.

ii) Cross section uncertainties not constrained by the fit to near detector data: This category of error stems from the cross-section parameters which are independent between the near and far detectors because of their different elemental composition and the cross-section parameters for which the near detector is insensitive. The current ND280 constraints are based on measurements on the plastic scintillator. The ongoing analysis of water target

data is expected to significantly reduce the uncertainty due to nuclear difference. Errors in this category will be reduced as more samples are added to the near detector data fit, improving the constraints on the cross section model. We assume the uncertainties arising from different target nucleus between the near and the far detectors will become negligible by including the measurement with the water target in the near detector.

iii) Uncertainties on the far detector efficiency and reconstruction modeling: Because most of the uncertainties related to far detector performance are estimated by using atmospheric neutrinos as a control sample and the current error is limited by statistics, errors in this category are expected to decrease with more than an order of magnitude larger statistics available with Hyper-K than currently used for T2K. Uncertainties arising from the energy scale is kept the same because it is not estimated by the atmospheric neutrino sample, although it could be also reduced with a larger statistics control sample and better calibration of the detector.

Compared to the systematic uncertainty used for the past publication [158], the uncertainties for anti-neutrino beam mode have been reduced to the similar level as those for neutrino beam mode, based on the experience with T2K anti-neutrino oscillation analysis. The flux and cross section uncertainties are assumed to be uncorrelated between the neutrino and anti-neutrino data, except for the uncertainty of ν_e/ν_μ cross section ratio which is treated to be anti-correlated considering the theoretical uncertainties studied in [177]. Because some of the uncertainties, such as those from the cross section modeling or near detector systematics, are expected to be correlated and give more of a constraint, this is a conservative assumption. The far detector uncertainty is treated to be fully correlated between the neutrino and anti-neutrino data.

Figures 115 and 116 show the fractional systematic uncertainties for the appearance and disappearance reconstructed energy spectra in neutrino and anti-neutrino mode, respectively. Black lines represent the prior uncertainties and bin widths of the systematic parameters f_i, while colored lines show the contribution from each uncertainty source. It should be noted that because some uncertainties are correlated between bins, the uncertainty on the total number of events is not a simple weighted sum of these errors. For example, the energy scale uncertainty of the far detector has a large contribution around the flux peak, but it does not change the total number of events. Figure 117 shows the correlation matrix of the systematic uncertainties between the reconstructed neutrino energy bins of the four samples. The systematic uncertainties of the number of expected events at the far detector are summarized in Table XXXI.

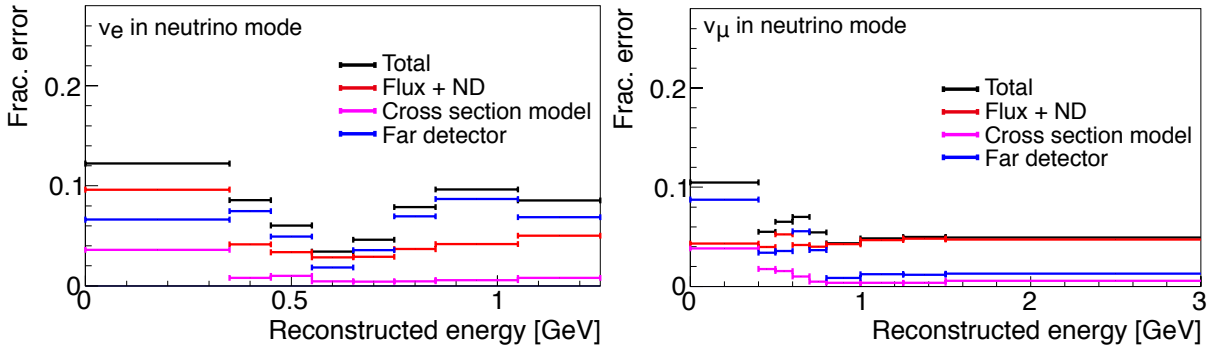

FIG. 115. Fractional error size for the appearance (left) and the disappearance (right) samples in the neutrino mode. Black: total uncertainty, red: the flux and cross-section constrained by the near detector, magenta: the near detector non-constrained cross section, blue: the far detector error.

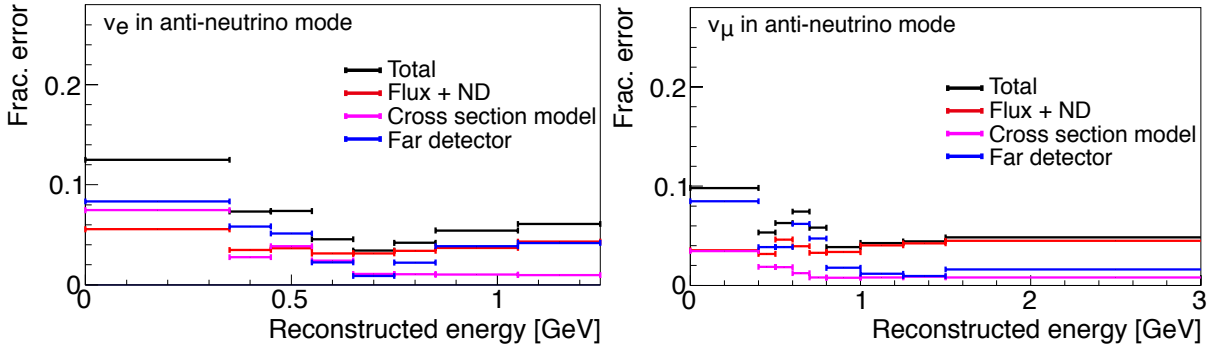

FIG. 116. Fractional error size for the appearance (left) and the disappearance (right) samples in the anti-neutrino mode. Black: total uncertainty, red: the flux and cross-section constrained by the near detector, magenta: the near detector non-constrained cross section, blue: the far detector error.

6. *Measurement of CP asymmetry*

Figure 118 shows examples of the 90% CL allowed regions on the $\sin^2 2\theta_{13}$–δ_{CP} plane resulting from the true values of $\delta_{CP} = (-90°, 0, 90°, 180°)$. The left (right) plot shows the case for the normal (inverted) mass hierarchy. Also shown are the allowed regions when we include a constraint from the reactor experiments, $\sin^2 2\theta_{13} = 0.100 \pm 0.005$. With reactor constraints, although the contour becomes narrower in the direction of $\sin^2 2\theta_{13}$, the sensitivity to δ_{CP} does not significantly change because δ_{CP} is constrained by the comparison of neutrino and anti-neutrino oscillation probabilities by Hyper-K and not limited by the uncertainty of θ_{13}.

Figure 119 shows the expected significance to exclude $\sin\delta_{CP} = 0$ (the CP conserved case). The significance is calculated as $\sqrt{\Delta\chi^2}$, where $\Delta\chi^2$ is the difference of χ^2 for the *trial* value of δ_{CP} and for $\delta_{CP} = 0°$ or $180°$ (the smaller value of difference is taken). We have also studied the

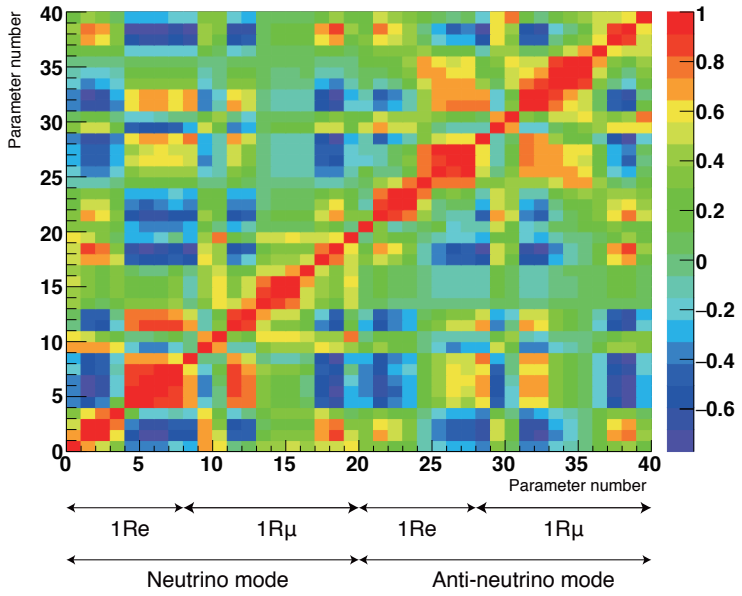

FIG. 117. Correlation matrix between reconstructed energy bins of the four samples due to the systematic uncertainties. Bins 1–8, 9–20, 21–28, and 29–40 correspond to the neutrino mode single ring e-like, the neutrino mode single ring μ-like, the anti-neutrino mode single ring e-like, and the anti-neutrino mode single ring μ-like samples, respectively.

TABLE XXXI. Uncertainties for the expected number of events at Hyper-K from the systematic uncertainties assumed in this study.

		Flux & ND-constrained cross section	ND-independent cross section	Far detector	Total
ν mode	Appearance	3.0%	0.5%	0.7%	3.2%
	Disappearance	3.3%	0.9%	1.0%	3.6%
$\overline{\nu}$ mode	Appearance	3.2%	1.5%	1.5%	3.9%
	Disappearance	3.3%	0.9%	1.1%	3.6%

case with a reactor constraint, but the result changes only slightly. Figure 120 shows the fraction of δ_{CP} for which $\sin\delta_{CP} = 0$ is excluded with more than $3\,\sigma$ and $5\,\sigma$ of significance as a function of the integrated beam power. The ratio of integrated beam power for the neutrino and anti-neutrino mode is fixed to 1:3. The normal mass hierarchy is assumed. The results for the inverted hierarchy are almost the same. CP violation in the lepton sector can be observed with more than $3(5)\,\sigma$ significance for 78(62)% of the possible values of δ_{CP}.

Figure 121 shows the uncertainty of δ_{CP} as a function of the integrated beam power. The value of δ_{CP} can be determined with an uncertainty of 7.2° for $\delta_{CP} = 0°$ or 180°, and 21° for $\delta_{CP} = \pm 90°$.

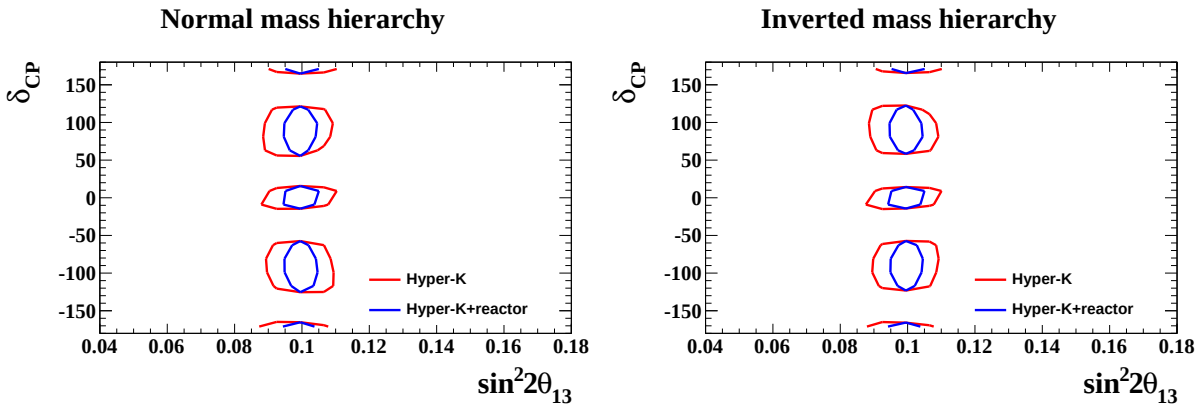

FIG. 118. The expected 90% CL allowed regions in the $\sin^2 2\theta_{13}$-δ_{CP} plane. The results for the true values of $\delta_{CP} = (-90°, 0, 90°, 180°)$ are shown. Left: normal hierarchy case. Right: inverted hierarchy case. Red (blue) lines show the result with Hyper-K only (with $\sin^2 2\theta_{13}$ constraint from reactor experiments).

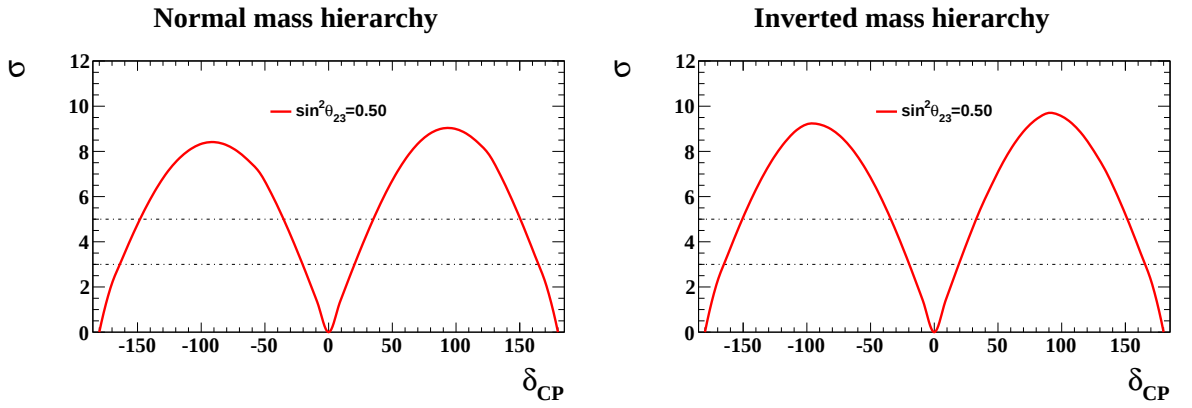

FIG. 119. Expected significance to exclude $\sin\delta_{CP} = 0$. Left: normal hierarchy case. Right: inverted hierarchy case.

As the nominal value we use $\sin^2\theta_{23} = 0.5$, but the sensitivity to CP violation depends on the value of θ_{23}. Figure 122 shows the fraction of δ_{CP} for which $\sin\delta_{CP} = 0$ is excluded with more than $3\,\sigma$ and $5\,\sigma$ of significance as a function of the true value of $\sin^2\theta_{23}$ with the 90% CL $\sin^2\theta_{23}$ range measured by T2K collaboration [22].

Table XXXII shows a comparison of several configurations for CP violation sensitivities.

7. *Precise measurements of* Δm^2_{32} *and* $\sin^2\theta_{23}$

A joint fit of the ν_μ and ν_e samples enables us to also precisely measure $\sin^2\theta_{23}$ and Δm^2_{32}. Figure 123 shows the 90% CL allowed regions for the true value of $\sin^2\theta_{23} = 0.5$ together with the 90% CL contour by T2K ν_μ disappearance measurement [22]. The expected precision of Δm^2_{32}

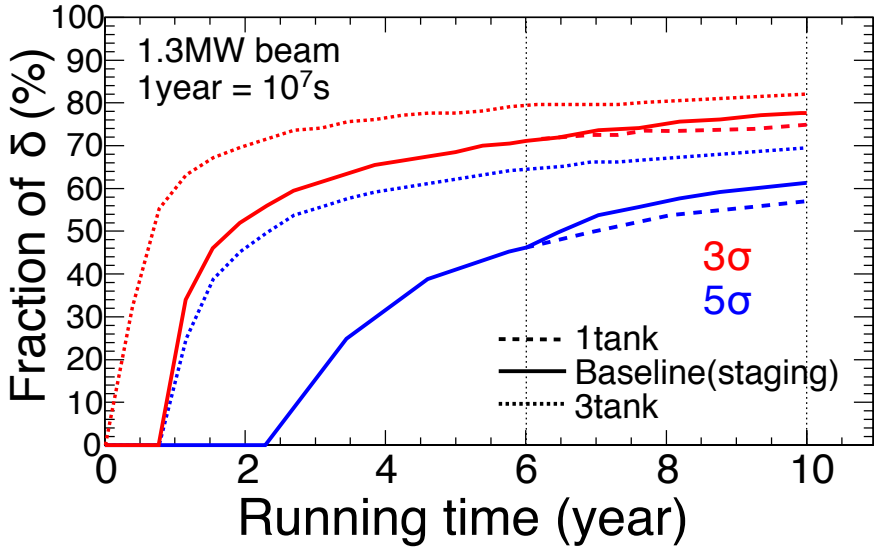

FIG. 120. Fraction of δ_{CP} for which $\sin\delta_{CP} = 0$ can be excluded with more than $3\,\sigma$ (red) and $5\,\sigma$ (blue) significance as a function of the running time. For the normal hierarchy case. The ratio of neutrino and anti-neutrino mode is fixed to 1:3.

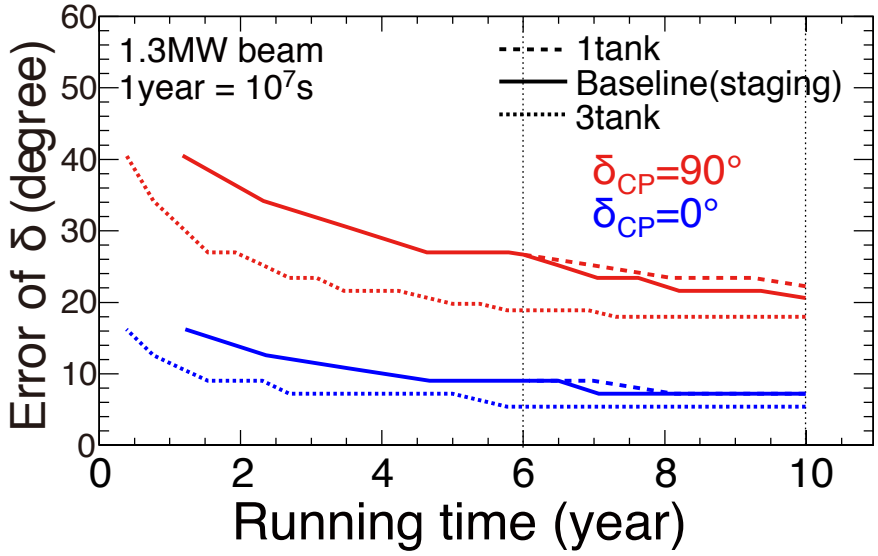

FIG. 121. Expected uncertainty (half width of 68% CL interval) of δ_{CP} as a function of running time.

and $\sin^2\theta_{23}$ for true $\sin^2\theta_{23} = 0.45, 0.50, 0.55$ with reactor constraint on $\sin^2 2\theta_{13}$ is summarized in Table XXXIII.

Figure 124 shows the 90% CL allowed regions on the $\sin^2\theta_{23}$–Δm^2_{32} plane, for the true values of $\sin^2\theta_{23} = 0.45$ and $\Delta m^2_{32} = 2.4 \times 10^{-3}$ eV^2. With a constraint on $\sin^2 2\theta_{13}$ from the reactor experiments, Hyper-K measurements can resolve the octant degeneracy and precisely determine

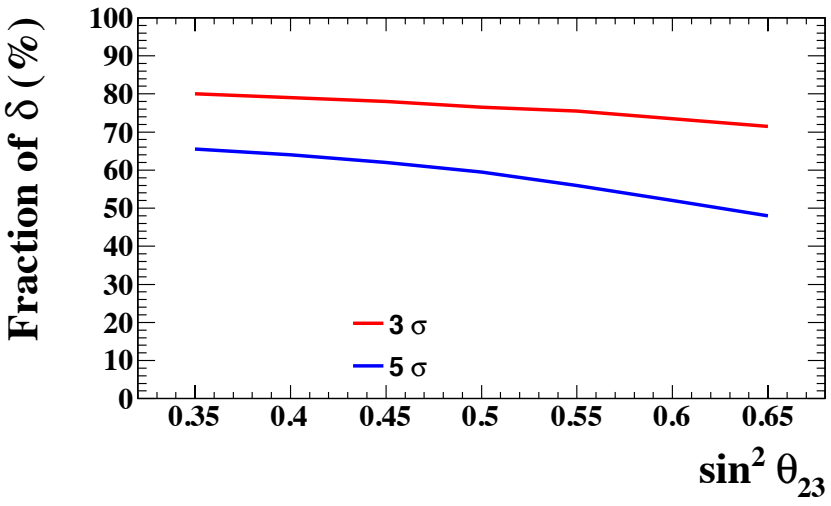

FIG. 122. Fraction of δ_{CP} for which $\sin\delta_{CP} = 0$ can be excluded with more than $3\,\sigma$ (red) and $5\,\sigma$ (blue) significance as a function of the true value of $\sin^2\theta_{23}$, for the normal hierarchy case.

TABLE XXXII. Comparison of CP sensitivity with different configurations. As a reference, former baseline result published in PTEP [158] is also shown, where 560kton fiducial volume, 7.5 MW$\times 10^7$s integrated beam power, and an old estimate of systematic uncertainty with larger anti-neutrino errors are assumed.

	$(\sin\delta_{CP} = 0)$ exclusion		68% uncertainty of δ_{CP}	
Configuration	$> 3\sigma$	$> 5\sigma$	$\delta_{CP} = 0°$	$\delta_{CP} = 90°$
Baseline	78%	62%	7.2°	21°
1 tank	76%	57%	7.2°	23°
3 tank	82%	70%	5.4°	18°
PTEP [158]	76%	58%	7°	19°

TABLE XXXIII. Expected 1σ uncertainty of Δm^2_{32} and $\sin^2\theta_{23}$ for true $\sin^2\theta_{23} = 0.45, 0.50, 0.55$. Reactor constraint on $\sin^2 2\theta_{13} = 0.1 \pm 0.005$ is imposed.

True $\sin^2\theta_{23}$	0.45		0.50		0.55	
Parameter	Δm^2_{32} (eV^2)	$\sin^2\theta_{23}$	Δm^2_{32} (eV^2)	$\sin^2\theta_{23}$	Δm^2_{32} (eV^2)	$\sin^2\theta_{23}$
NH	1.4×10^{-5}	0.006	1.4×10^{-5}	0.015	1.5×10^{-5}	0.009
IH	1.5×10^{-5}	0.006	1.4×10^{-5}	0.015	1.5×10^{-5}	0.009

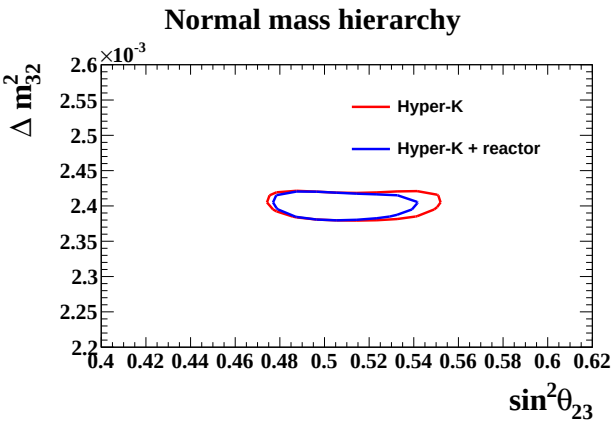

FIG. 123. The 90% CL allowed regions in the $\sin^2\theta_{23}$–Δm^2_{32} plane. The true values are $\sin^2\theta_{23} = 0.5$ and $\Delta m^2_{32} = 2.4 \times 10^{-3}$ eV^2 (red point). Effect of systematic uncertainties is included. The red (blue) line corresponds to the result with Hyper-K alone (with a reactor constraint on $\sin^2 2\theta_{13}$).

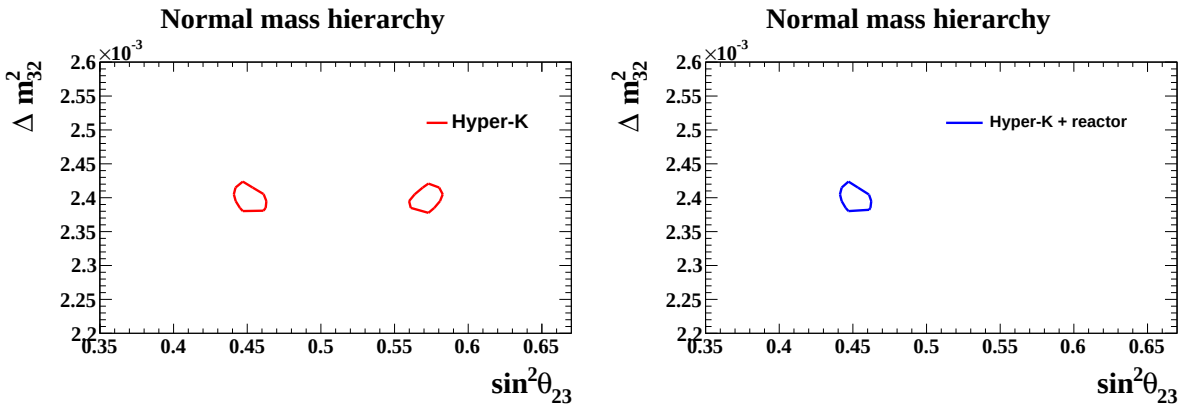

FIG. 124. 90% CL allowed regions in the $\sin^2\theta_{23}$–Δm^2_{32} plane. The true values are $\sin^2\theta_{23} = 0.45$ and $\Delta m^2_{32} = 2.4 \times 10^{-3}$ eV^2. Effect of systematic uncertainties is included. Left: Hyper-K only. Right: With a reactor constraint.

$\sin^2\theta_{23}$. Figure 125 shows the expected significance ($\sigma \equiv \sqrt{\Delta\chi^2}$) for wrong octant rejection with beam neutrino measurement alone as a function of true value of $\sin^2\theta_{23}$ in normal hierarchy case.

As discussed earlier, a precision measurement of Δm^2_{32}, compared with reactor measurements of Δm^2_{ee}, will enable a consistency check of the mixing matrix framework. The difference expected from the current knowledge of oscillation parameters is a few %. The uncertainty of Δm^2_{32} by Hyper-K is expected to reach 0.6%, while measurements by future reactor experiments are expected to achieve $< 1\%$ precision. Thus, the comparison will yield a significant consistency check.

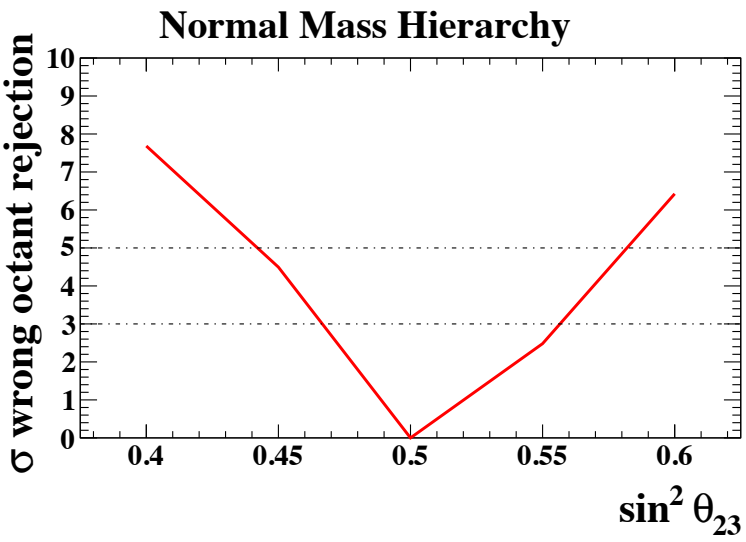

FIG. 125. The expected significance ($\sigma \equiv \sqrt{\Delta\chi^2}$) for wrong octant rejection, by beam neutrino measurement with reactor constraint, as a function of true $\sin^2\theta_{23}$ in normal hierarchy case.

8. Neutrino cross section measurements

With a set of highly capable neutrino detectors envisioned for Hyper-K project, a variety of neutrino interaction cross section measurements will become possible. The near detector suite offers a range of capabilities to probe different theoretical models for neutrino interactions: in particular data across different momenta ranges and a range of lepton emission angles. Figure 126 shows the efficiency of different detectors as a function of angle and muon momentum. The ability to measure exclusive hadronic final states, using techniques such as high pressure gas TPCs or emulsion detectors, provides valuable additional information for exclusive cross-sections. In table XXXIV we estimate the sensitivity of each proposed near detector for key selections based on a flux of 10^{21}POT.

9. Searches for new physics

In addition to the study of standard neutrino oscillation, the combination of intense beam and high performance detectors enables us to search for new physics in various ways. Examples of possible searches for new physics with Hyper-K and accelerator beam are listed below.

9.1. Search for sterile neutrino Sterile neutrino can be searched for in both disappearance and appearance channels in near and intermediate detectors. With neutrino energy of 0.1–a few GeV and baseline of 0.3–2 km, it will be sensitive to Δm^2 of $\mathcal{O}(1)$ eV^2, which is interesting region in

Detector	Selection	Nevents	Selection Characteristics
ND280 detector, 280m	ν_μCC0π	20k	FGD1 (1–3 GeV), P ≈72% [51]
ND280 detector, 280m	ν_μCC1π	6k	FGD1 (1–3 GeV), P ≈50% [51]
ND280 detector, 280m	ν_μCC inclusive	40k	FGD1 (1–3 GeV), P ≈90%[51]
INGRID	ν_μCC inclusive	17.6×10^6	ϵ >70% (1–3 GeV), P = 97% [178]
HPTPC, 8 m^3, 10 bar Ne (CF_4)	ν_μCC inclusive	5k (20k)	ϵ ≈44%, protons > 5 MeV detected
WAGASCI	ν_μCC+NC inclusive	82k	ϵ ≈84% (CC), P ≈ Y%, protons > 50 MeV detected
100kg Emulsion on-axis / 1ton Off-axis, 280m	ν_eCC inclusive	10^2–10^3	3π automated readout protons > 20-50 MeV detected
2kton WC 2 km	ν_eCC0π enhanced	14k	ϵ ≈ 41%, P ≈ 61%
2kton WC 2 km	ν_μCC0π enhanced	931k	ϵ ≈ 58%, P ≈ 90%
2kton WC 2 km	ν_eCC1π enhanced	7k	ϵ ≈ 12%, P ≈ 21%
2kton WC 2 km	ν_μCC1π enhanced	87k	ϵ ≈ 17% , P ≈ 90%
2kton WC 2 km	NCπ_0 enhanced	59k	ϵ ≈ 40%, P ≈ 88%

TABLE XXXIV. Some of the primary cross-section measurements accessible with different elements of the Near Detector Suite (see chapter 2 for details). The predicted number of events or measurement precision have been evaluated for 10^{21}POT. ϵ = efficiency = number selected / total events for given topology, P = purity = number of given topology / total events selected. For the ND280 measurements only events for a single fine grained detector (FGD1) are projected, the second FGD plus the use of other detector components as targets increases the statistics. Numbers are obtained either from independent Monte Carlo studies, or extrapolated from the cited references.

light of several anomalies reported by recent experiments. T2K has searched for sterile neutrino in ν_e appearance and ν_μ disappearance with near detectors [179, 180]. With more statistics, improved detectors, and possible two detector configuration with near and intermediate detectors, Hyper-K near detectors will have chance to improve the sensitivity for sterile neutrino searches.

Neutral current measurements at the far detector will be also sensitive to the sterile neutrino, because the neutral current channel measures the total active flavor content. By selecting two electron-like ring events with no decay electron and invariant mass consistent with π^0, neutral current events with 96% purity can be obtained. With 1.56×10^{22} protons on target and 560 kton fiducial mass, more than 12,000 π^0 events are expected after selection.

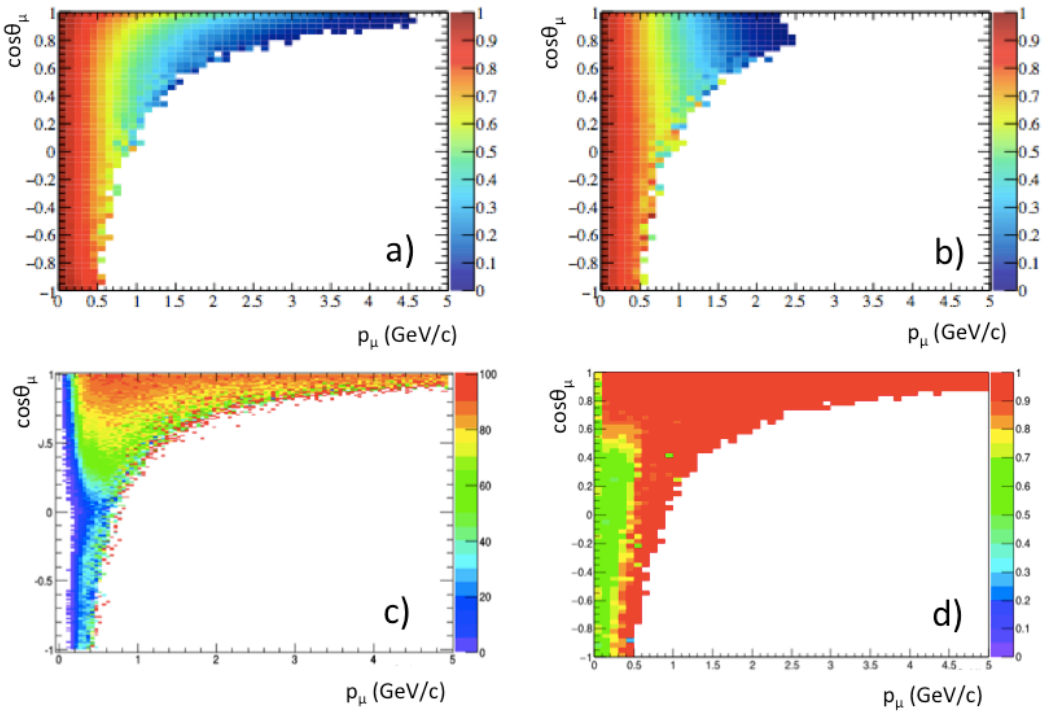

FIG. 126. Example detector efficiency in muon momentum and direction. a) A horizontally oriented 2 kton cylindrical intermediate WC detector at 2km, b) the same detector vertically oriented with respect to the beam, c) the current ND280 near detector and d) the WAGASHI detector. Good coverage of this phase space helps to constrain uncertainties in cross-section models.

9.2. Test of Lorentz and CPT invariance Lorentz Violation arises when the behavior of a particle depends on its direction or boost velocity and is predicted to occur at the Planck scale (10^{19} GeV). Searches for Lorentz Violation have been performed various experiments, including T2K, by looking for a sidereal time dependence of the neutrino event rate. Similar search can be carried out with larger statistics and improved detectors.

9.3. Heavy neutrino search The existence of heavy neutral leptons (heavy neutrinos) is predicted in many extensions of the Standard Model. Such heavy neutrinos may be produced in decays of kaons and pions from the target. Then, decays of heavy neutrinos can be detected in the near detector. The feasibility of search for heavy neutrinos in accelerator neutrino experiment, in particular with T2K, is studied in [181] and the sensitivity is expected to be better than previous searches. Because interactions of ordinary neutrinos produce background to this search, having a low density detector such as a gas TPC inside a magnetic field like ND280 is an advantage for this search. The sensitivity will be further enhanced if a larger volume of gas detector is employed.

10. Summary

The sensitivity to leptonic CP asymmetry of a long baseline experiment using a neutrino beam directed from J-PARC to the Hyper-Kamiokande detector has been studied based on a full simulation of beamline and detector. With an integrated beam power of 7.5 MW$\times 10^7$ sec and 3TankLD configuration, the value of δ_{CP} can be determined 5.4° for $\delta_{CP} = 0°$ or 180°, and 19° for $\delta_{CP} = \pm 90°$. CP violation in the lepton sector can be observed with more than 3 σ (5 σ) significance for 80% (65%) of the possible values of δ_{CP}. Using both ν_e appearance and ν_μ disappearance data, precise measurements of $\sin^2\theta_{23}$ and Δm^2_{32} will be possible. The expected 1σ uncertainty of $\sin^2\theta_{23}$ is 0.015(0.006) for $\sin^2\theta_{23} = 0.5(0.45)$. The uncertainty of Δm^2_{32} is expected to reach 0.6%.

There will be also a variety of measurements possible with both near and far detectors, such as neutrino-nucleus interaction cross section measurements and search for exotic physics, using the well-understood neutrino beam.

B. Atmospheric neutrinos

Primary cosmic ray interactions with nuclei in the atmosphere produce charged hadrons whose decays further create a continuous flux of neutrinos known as atmospheric neutrinos. Since the primary cosmic ray flux is known to be nearly isotropic about the earth, the resulting neutrino flux is present at all zenith angles observed by a terrestrial detector. Further, these neutrinos are less energetic than their cosmic ray parents by roughly an order of magnitude meaning that the range of available neutrino energies for observation spans several orders of magnitude starting near O(100) MeV. This diversity of both energy and pathlength, which ranges from O(10) to O(10^4) km, makes atmospheric neutrinos a particularly versatile tool for studying neutrino oscillations. However, these neutrinos represent the most serious background to nucleon decay searches (discussed in Section III.2 A). At the same time they form the basis for searches for exotic particles, such as dark matter (discussed in Section III.3 B), whose interactions may produce neutrinos that would subsequently appear atop the atmospheric neutrino spectrum. For these reasons a precise characterization of the atmospheric neutrino flux is key to future discoveries at Hyper-Kamiokande.

Though atmospheric neutrinos were used to make the first discovery of the neutrino oscillation phenomenon, for very large detectors like Hyper-Kamiokande, they provide excellent sensitivity to many of the remaining open questions in oscillation physics. Indeed, current neutrino telescopes have demonstrated constraints on the atmospheric mixing parameters comparable to beam measurements using atmospheric neutrinos alone. Additionally, future experiments seek to use these neutrinos to study the mass hierarchy. While both of these measurements and more are available to Hyper-Kamiokande, it offers two distinct advantages to other planned projects. First, with its exquisite ability to distinguish between charged current ν_e and ν_μ interactions, it will have improved access to the oscillation modes with the most hierarchy sensitivity, $\nu_\mu \to \nu_e$ and $\bar{\nu}_\mu \to \bar{\nu}_e$. It is indeed the asymmetry in these two probabilities for few GeV neutrinos traversing the earth that provides the cleanest signature of the mass hierarchy. Additionally, Hyper-Kamiokande will make combined beam and atmospheric neutrino oscillation measurements to yield increased sensitivity. Details of Hyper-K's physics potential using atmospheric neutrinos by themselves and in conjunction with beam neutrinos are presented in the next two subsections.

1. Neutrino oscillation studies (MH, θ_{23} octant, CP phase)

As atmospheric neutrinos span both low and high energies as well as long and short path lengths, they are in principal sensitive to all parameters in the PMNS mixing paradigm. That being said, the most apparent oscillation features are driven by the so-called atmospheric mixing parameters, θ_{23} and Δm^2_{32}, and they induce a deficit of observed upward-going ν_μ interactions at predominantly multi-GeV energies as these neutrinos oscillate into primarily unobserved ν_τ. However, now that the value of θ_{13} is known to be non-zero the presence of matter effects on atmospheric neutrinos that traverse the earth makes important contributions to this picture. Matter-induced parametric oscillations in the energy range 2-10 GeV lead to significant enhancement of the $\nu_\mu \to \nu_e$ appearance probability for upward-going neutrinos, with probabilities near 50% for the normal hierarchy. On the other hand there is no enhancement in the antineutrino channel, $\bar{\nu}_\mu \to \bar{\nu}_e$. When the hierarchy is inverted the roles are reversed and antineutrino oscillations are enhanced. For this reason the separation of atmospheric neutrino data into neutrino-like and antineutrino-like subsets can be used to extract the hierarchy signal. Importantly the features of these oscillations are also a strong function of θ_{23} and, to a lesser extent, the value of δ_{CP}. It should be noted that matter affects both the appearance and disappearance, $\nu_\mu \to \nu_\mu$, channels, enabling mass hierarchy sensitivity in both the ν_e-like and ν_μ-like data at Hyper-K.

Including these effects the flux of atmospheric ν_e at the detector may be written roughly as,

$$\begin{aligned}\frac{\Psi(\nu_e)}{\Psi_0(\nu_e)} - 1 \approx\ & P_2 \cdot (r \cdot \cos^2\theta_{23} - 1) \\ & -r \cdot \sin\tilde{\theta}_{13} \cdot \cos^2\tilde{\theta}_{13} \cdot \sin 2\theta_{23} \cdot (\cos\delta \cdot R_2 - \sin\delta \cdot I_2) \\ & +2\sin^2\tilde{\theta}_{13} \cdot (r \cdot \sin^2\theta_{23} - 1),\end{aligned} \tag{19}$$

where these three terms are identified as the "solar", "interference," and "parametric (resonance)" terms, respectively. Here P_2 is the two neutrino oscillation probability $\nu_e \to \nu_{\mu,\tau}$ driven by the solar mass splitting Δm^2_{21}. Note that the effect of δ_{CP} appears in the interference term, which is controlled by an effective mixing angle in matter, $\tilde{\theta}_{13}$, and where R_2 and I_2 denote amplitudes for CP-even and CP-odd oscillations. Antineutrino oscillations are described by changes to these amplitudes under an inversion of the sign of both the matter potential and of δ_{CP}. At sub-GeV energies the flux ratio ν_μ/ν_e, r, is ~ 2, and increases above 1 GeV until reaching ~ 3 at 10 GeV.

Figure 127 shows the expected ν_e flux at the detector normalized to the unoscillated prediction under this approximation for four configurations of the oscillation parameters and neutrinos with $cos(\theta_{zenith}) = -0.8$. At energies between 5-10 GeV the most prominent feature of the figure is the

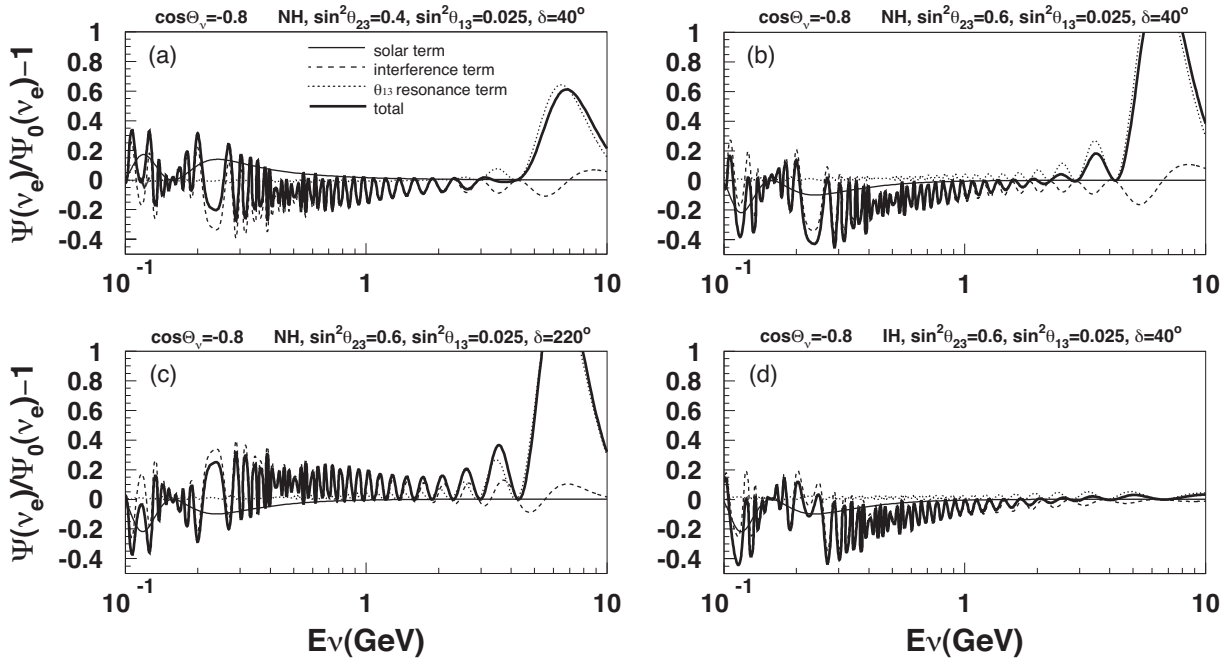

FIG. 127. Oscillated ν_e flux relative to the non-oscillated flux as a function of neutrino energy for the upward-going neutrinos with zenith angle $\cos\Theta_\nu = -0.8$. $\bar{\nu}_e$ is not included in the plots. Thin solid lines, dashed lines, and dotted lines correspond to the solar term, the interference term, and the θ_{13} resonance term, respectively (see Eq. 19). Thick solid lines are total fluxes. Parameters are set as $(\sin^2\theta_{21}, \sin^2\theta_{13}, \sin^2\theta_{23}, \delta, \Delta m^2_{21}, \Delta m^2_{32})$ unless otherwise noted. The θ_{23} octant effect can be seen by comparing (a) $(\sin^2\theta_{23} = 0.4)$ and (b) $(\sin^2\theta_{23} = 0.6)$. δ value is changed to 220° in (c) to be compared with 40° in (b). The mass hierarchy is inverted only in (d) so θ_{13} resonance (MSW) effect disappears in this plot. For the inverted hierarchy the MSW effect should appear in the $\bar{\nu}_e$ flux, which is not shown in the plot.

parametric resonance driven by $\tilde{\theta}_{13}$, whose amplitude increases with $\sin^2\theta_{23}$ (c.f. panels a. and b.). Further, this resonance becomes suppressed in the neutrino channel when the hierarchy is switched from normal to inverted (compare panels a. and d.). Though some change in the resonance can be seen via the interference term as δ_{CP} is varied, the dominant effect appears below 1 GeV (panels a. and c.). For these reasons the atmospheric neutrino oscillation analysis has been designed to maximize each of these potential effects.

Hyper-Kamiokande's reconstruction performance is expected to meet or exceed that of its predecessor, Super-Kamiokande. Nominally the size and configuration of the two detectors are similar enough that event selections and systematic errors are not expected to differ largely. Accordingly, relative to the systematic error budget present in existing Super-K analyses, no systematic error

improvements are assumed in studies presented below. The analyses proceed following those at Super-K using simulation and reconstruction tools tuned and validated for that experiment.

Atmospheric neutrino MC corresponding to a 25 year exposure of the 560 kton Hyper-K detector has been generated based on the flux model presented in [182] and using the NEUT interaction generator. The analysis is based on 19 samples optimized for sensitivity to potential oscillation signals at both high (multi-GeV) and low (sub-GeV) energies. Interactions are divided into sub-samples based upon the particle ID of their most energetic reconstructed Cherenkov ring (e-like or μ-like) and the number of such rings. Additional selections are made to the multi-GeV e-like samples to separate them into antineutrino-like and neutrino-like subsamples [183]. Event topologies with particles exiting the inner detector and depositing light in the outer veto as well as muons from neutrino interactions in the rock surrounding the detector are also included in the analysis. Further details of the sample selection are presented elsewhere [32]. Zenith angle distributions for six samples with sensitivity to the mass hierarchy are shown for both assumptions in figure 128.

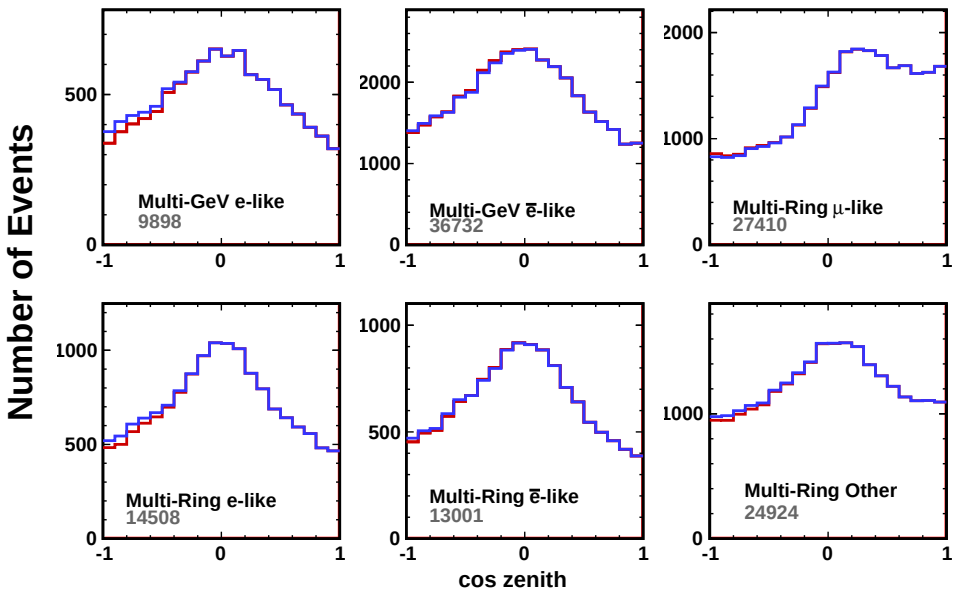

FIG. 128. Zenith angle distributions of hierarchy-sensitive analysis samples with reconstructed momenta in the range 1 to 10 GeV/c. The blue (red) line shows the expectation for a normal (inverted) hierarchy after a 5.6 Mton·year exposure. Gray numbers in each panel represent the size of the event sample.

Figure 129 shows the Hyper-K's expected sensitivity to resolving the neutrino mass hierarchy

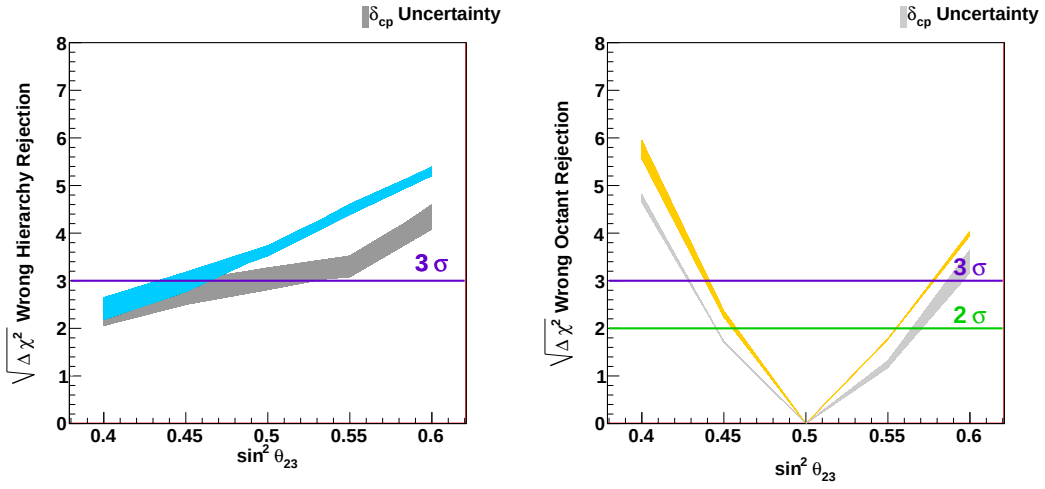

FIG. 129. Neutrino mass hierarchy sensitivity (left) and octant sensitivity (right) as a function of the true value of $\sin^2\theta_{23}$ for two 1TankHD detectors staged such that the second comes online six years after the first (a 2.6 Mton·year exposure). In both figures the colored (grey) band denotes the normal (inverted) hierarchy and the uncertainty from δ_{CP} is shown by the width of the band.

and the octant of θ_{23} assuming two 1TankHD detectors after 10 years. Here the second detector is assumed to begin taking data six years after the start of the experiment. Both panels of the figure are shown as function of the true value of $\sin^2\theta_{23}$ for the range of values allowed by recent measurements from the T2K experiment [51] and the width of the bands in the figures illustrates the uncertainty from δ_{CP}. In each panel the sensitivity is defined as $\sqrt{\Delta\chi^2}$, which for mass hierarchy resolution corresponds to $\Delta\chi^2 \equiv \chi^2_{TH} - \chi^2_{AH}$, where TH and AH refer to the true hierarchy and the alternate hierarchy hypotheses, respectively. The octant sensitivity is defined similarly. After 10 years (a 2.6 Mton·year exposure) Hyper-K is expected to resolve the mass hierarchy at $\sqrt{\Delta\chi^2} > 3$ for both hierarchy assumptions and when $\sin^2\theta_{23} > 0.45$. Similarly the atmospheric neutrino data alone can be used to determine the θ_{23} octant at $\sqrt{\Delta\chi^2} > 3$ when $|\theta_{23} - 45| > 4°$. Note further that atmospheric neutrinos can be used to measure the chemical composition of the Earth's interior. Details of Hyper-K's expected sensitivity are presented in section III.3 D.

2. *Combination with Beam Neutrinos*

Hyper-K will have improved sensitivity to neutrino oscillations by joint analysis of its atmospheric and accelerator (long-baseline beam) neutrino data sets. A particularly striking example comes in the form of mass hierarchy resolution. Since matter effects are small for the combined

Tokai-to-HK baseline and the beam neutrino data have limited sensitivity to the mass hierarchy. At the same time, though matter effects are strong in the resonance-enhanced oscillation region of the atmospheric neutrino energy spectrum, lacking precise knowledge of these neutrinos's true baseline limits their ability to constrain the atmospheric neutrino mixing parameters which govern the size of the expected enhancement namely, θ_{23}. Further, approximate degeneracies between this parameter and the sign δm^2_{32} weaken the mass hierarchy sensitivity. Note, for instance, the dramatic influence θ_{23} has on Hyper-K's atmospheric neutrino-only sensitivity in Figure 129. The off-axis angle of the beam measurement, on the other hand, provides a clean measurement of the atmospheric mixing parameters and therefore provides for a precise prediction of the expected amount of $\nu_\mu \to \nu_e$ appearance expected in the resonance region. Fitting the two data sets together in turn improves the overall mass hierarchy sensitivity as shown in the left panel of Figure 130. With five years of data with the 1TankHD detector the combined atmospheric neutrino and beam samples show better than 3σ ability to reject the inverted hierarchy hypothesis, assuming a true normal hierarchy. Similarly, the ability to resolve the θ_{23} octant improves with the combination (middle panel of the figure). While atmospheric neutrinos alone can resolve the octant at 3 σ if $|\theta_{23} - 45| > 4^\circ$, but in the combined analysis it can be resolved when this difference is only 2.5° in ten years. However, it is not just the atmospheric neutrinos that benefit from combined

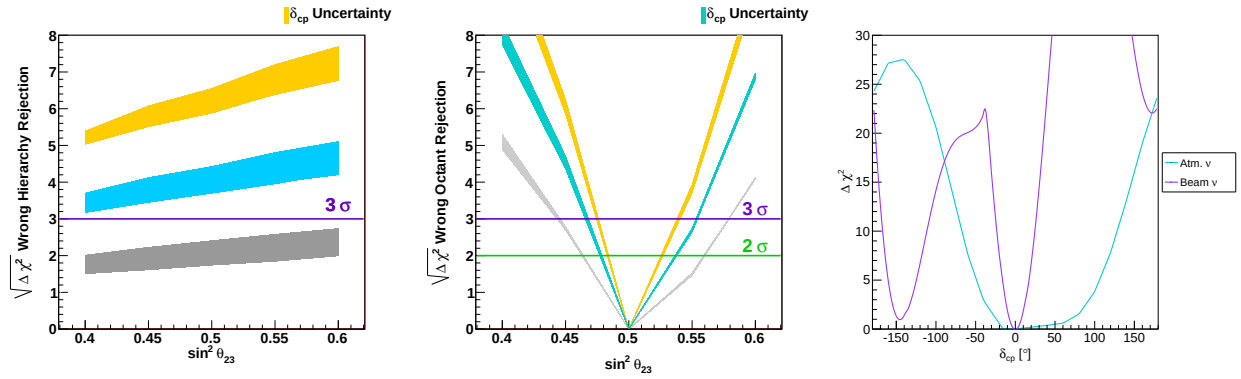

FIG. 130. Neutrino oscillation sensitivities from combined analysis of atmospheric neutrino and accelerator data at Hyper-K. The left (middle) panel illustrates the expected hierarchy (octant) sensitivity as a function of true value of $\sin^2\theta_{23}$ for three exposures: 1 year (grey), 5 years (blue), 10 years (orange). Assuming a normal mass hierarchy and $\delta_{CP} = 0$ the beam (violet) and atmospheric neutrino (cyan) constraints on δ_{CP} after a 5.6 Mton·year exposure are shown in the right panel.

measurements. Indeed, for a fixed baseline uncertainty in the mass hierarchy leads to parameter degeneracies in the the beam neutrino measurement of δ_{CP}. The atmospheric neutrino data, on

the other hand, can be used not only to resolve the mass hierarchy and subsequently these degeneracies, but they also provides complementary sensitivity to δ_{CP}. The right panel of Figure 130 shows the expected constraint on this parameter assuming its true value is $\delta_{CP} = 0$ for separate beam and atmospheric neutrino measurements. While the beam measurement (violet) shows excellent precision near the true parameter value, there is a strong degeneracy near $\delta_{CP} = \pi$ when the mass hierarchy is unknown. This false solution is not present in the atmospheric neutrino measurement (cyan), so the combination of the two measurements yields a very precise measurement. Table XXXV summarizes Hyper-K's expected sensitivity to various parameters for two different assumed fiducial volumes when using atmospheric neutrinos only and when combining them with the beam data.

Metric			Staged 1TankHD		3TankLD	
	Years	$\sin^2(x)$	Atmospheric ν	Atm + Beam	Atmospheric ν	Atm + Beam
Hierarchy	10	$\theta_{23} = 0.40$	2.2	5.3	3.8	6.9
	10	$\theta_{23} = 0.60$	5.2	6.9	8.4	9.9
Octant	10	$\theta_{23} = 0.45$	2.2	5.8	3.6	7.2
	10	$\theta_{23} = 0.55$	1.7	3.7	2.7	4.0

TABLE XXXV. Summary of Hyper-K's sensitivity in various metrics with atmospheric neutrinos only (Atmospheric) and with the combination of atmospheric neutrino and beam data (Atm + Beam) for two total fiducial volume designs. The Staged 1TankHDcolumn assumes two 186 kton detectors after 10 years, with the second coming online six years into the experiment. These numbers have assumed a normal hierarchy, $\delta m^2_{23} = 2.5 \times 10^{-3}\text{eV}^2$, $\sin^2\theta_{13} = 0.0238$, $\sin^2\theta_{23} = 0.5$, and the value of δ_{CP} that minimizes the sensitivity unless otherwise written. Entries in the table are in units of $\sqrt{\Delta\chi^2}$. See text for details.

3. Exotic Oscillations And Other Topics

Though the standard paradigm of neutrino oscillations driven by two mass differences has been well established, hints for a third mass difference with $\Delta m^2_s \sim 1\text{eV}^2$ have been seen in a variety of short-baseline experiments (c.f. [102, 103, 184, 185]). Measurements of the Z^0 decay width, however, indicate that there only three neutrinos that participate in the weak interaction and therefore explaining the short-baseline data with an additional neutrino means it cannot couple to the Z and therefore cannot participate in ordinary weak interactions. Such a state is referred to as "sterile." Even without weak interactions the existence of such sterile neutrinos can make imprints

on the atmospheric neutrino spectrum visible at Hyper-K. In addition to sterile neutrinos, other sub-dominant contributions to the standard oscillation picture, such as effects of Lorentz-invariance violating (LV) processes are expected to influence the oscillations of atmospheric neutrinos. Positive observation of LV would provide access to physics at the Planck scale, an energy regime far beyond the reach of current accelerator technology. Though Hyper-K will have an atmospheric neutrino sample of unprecedented size, its increased sensitivity to sterile and LV oscillations relative to existing measurements is hampered by current understanding of atmospheric neutrino flux and interaction uncertainties.

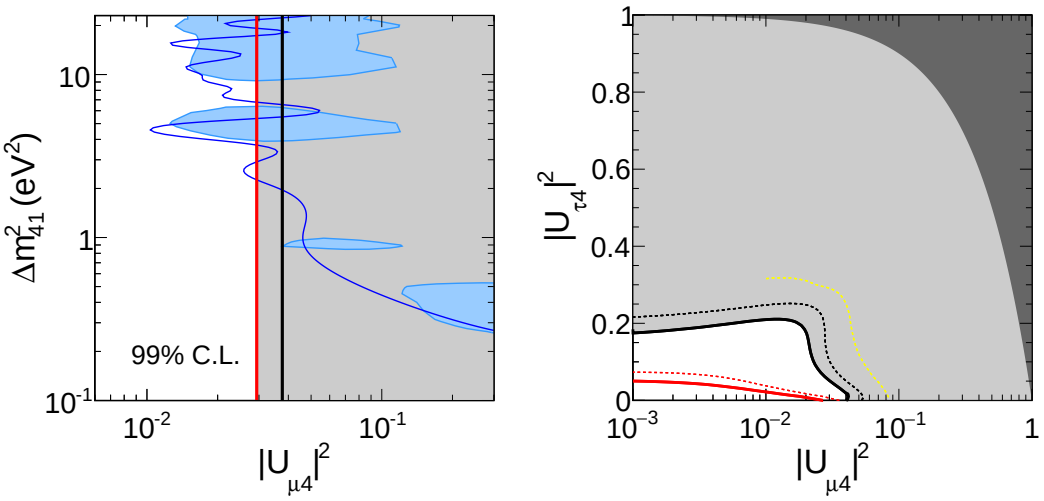

FIG. 131. Hyper-K's expected 90% C.L. upper limits on $|U_{\mu 4}|^2$ (left) and on $|U_{\mu 4}|^2$ vs $|U_{\tau 4}|^2$ (right) for a 5.6 Mton·year exposure (red) in comparison with recent limits from Super-K (black) [32]. Limits at 90% C.L. from a joint analysis of MiniBooNE and SciBooNE data [186] and light blue filled areas show the allowed regions from a joint fit to global ν_e appearance and disappearance data from [187].

Extensions of the standard (PMNS) oscillation framework to include sterile states expand the mixing matrix with additional rows and columns that include terms describing mixing between the active and sterile neutrinos, such as U_{e4}, $U_{\mu 4}$, and $U_{\tau 4}$. Interestingly, for mass differences $\Delta m^2_s > 0.1\text{eV}^2$, as suggested by short-baseline measurements, atmospheric neutrinos are not sensitive to the exact value of the splitting and further, they are essentially insensitive to the exact number of sterile neutrinos. Nonetheless, non-zero mixing of the active and sterile neutrinos is expected to produce spectral distortions of the atmospheric neutrino flux or suppress it. Sterile neutrinos lack NC interactions, which makes them subject to an additional effective potential, $V_s = \pm(G_F/\sqrt{2})N_n$ when traveling through matter. Here, N_n is the local neutron density and G_F the Fermi constant.

Due to the complications of simultaneously describing sterile matter effects and oscillations that include ν_e for atmospheric neutrinos two searches for sterile neutrinos are performed following the formalism of [188]. For the first analysis both θ_{13} and θ_{12} are set to zero, decoupling ν_e oscillations from the other active neutrinos. In so doing, atmospheric neutrinos are sensitive to the effects of $|U_{\mu 4}|$, which is expected to decrease the overall ν_μ survival probability, and $|U_{\tau 4}|$, which causes an energy dependent distortion of the ν_μ flux through the sterile matter potential. However, this comes at the expense of a slight bias in the measurement of $|U_{\mu 4}|$. Constraints on $|U_{\tau 4}|$ are possible via its effect on the PC and Upμ samples, both of which are enriched in ν_μ interactions. In the second analysis, sterile matter effects are assumed to be negligible and ν_e oscillations are reintroduced. This approximation allows for an unbiased measure of $|U_{\mu 4}|$. The results of these analyses are shown in comparison to limits from Super-K are shown in Figure 131. It should be noted that the relatively modest improvement in Hyper-K's measurement of $|U_{\mu 4}|$ is due to uncertainties in the $(\nu_\mu + \bar{\nu}_\mu)/(\nu_e + \bar{\nu}_e)$ flux and CCQE cross section below 10 GeV.

Analysis	α_{XY}^T [GeV]			C_{XY}^{TT}		
	$e\mu$	$e\tau$	$\mu\tau$	$e\mu$	$e\tau$	$\mu\tau$
Super-K	2×10^{-23}	4×10^{-23}	6×10^{-24}	2×10^{-26}	1×10^{-24}	5×10^{-27}
Hyper-K	7×10^{-24}	2×10^{-23}	2×10^{-24}	6×10^{-27}	7×10^{-25}	2×10^{-27}

TABLE XXXVI. Comparison of Hyper-K and Super-K [34] 90% C.L. limits on Lorentz-invariance violation within the context of the SME.

Atmospheric neutrino oscillations are particularly sensitive to effects of LV processes due to their interferrometric nature. Though such effects may manifest in atmospheric neutrinos as either sidereal variations in their oscillations or as distortions in the oscillated spectra, the present analysis considers only the latter. The search is performed within the context of an effective field theory which contains the standard model, general relativity, and all possible LV operators known as the standard model extension (SME) [189]. Much like the sterile oscillations described above the SME extends neutrino Hamiltonian by introducing a LV component,

$$H_{LV} = \begin{pmatrix} 0 & a_{e\mu}^T & a_{e\tau}^T \\ \left(a_{e\mu}^T\right)^* & 0 & a_{\mu\tau}^T \\ \left(a_{e\tau}^T\right)^* & \left(a_{\mu\tau}^T\right)^* & 0 \end{pmatrix} - E \begin{pmatrix} 0 & c_{e\mu}^{TT} & c_{e\tau}^{TT} \\ \left(c_{e\mu}^{TT}\right)^* & 0 & c_{\mu\tau}^{TT} \\ \left(c_{e\tau}^{TT}\right)^* & \left(c_{\mu\tau}^{TT}\right)^* & 0 \end{pmatrix}, \tag{20}$$

where $\mathrm{a}_{\alpha\beta}^T$ and $\mathrm{c}_{\alpha\beta}^{TT}$ are complex coefficients for isotropic LV operators. In general the $\mathrm{a}_{\alpha\beta}^T$ parameters produce oscillation effects proportional to the neutrino propagation distance, L, while the $\mathrm{c}_{\alpha\beta}^{TT}$

induce effects that depend on LE, where E is the neutrino energy. While atmospheric neutrinos are effective probes of such exotic oscillations due to their the large variety of pathlengths and energies, this same feature prohibits perturbative solutions to SME Hamiltonian and instead the problem must be fully diagonalized.

Event modest amounts of LV can have large effects on atmospheric neutrino oscillations, but generally they are expected to appear primarily in the multi-GeV (both e-like and μ-like), PC, and Upμ samples. Both the real and imaginary components of each of the LV coefficients found in the Hamiltonian above are then fit for in the analysis, with each coefficient considered individually while all others are held at zero. Limits from a 5.6 Mton·year exposure of Hyper-K within this framework appear in conjunction with limits from Super-K in Table XXXVI. For each of the considered coefficients the expected Hyper-K limit is roughly three or four times more stringent. Additional sensitivity may be gained by incorporating more detailed shape information into the Hyper-K analysis through finer binning.

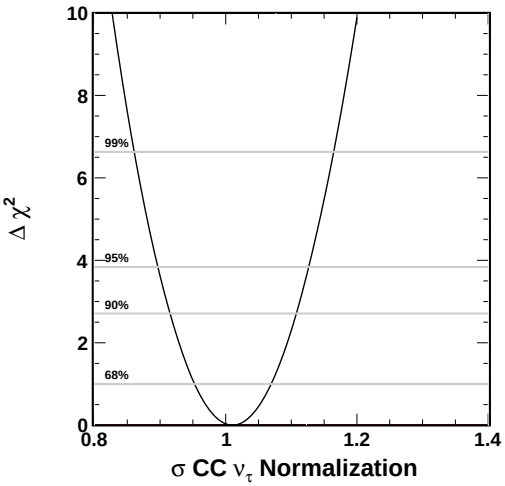

FIG. 132. Expected constraint on the CC ν_τ cross section normalization for a 5.6 Mton·year exposure of Hyper-K's to atmospheric neutrinos.

In addition to the studies presented above, Hyper-K's atmospheric neutrino sample is expected to enable measurements of several other physical phenomena, including the CC ν_τ cross section, non-standard neutrino interactions, the primary atmospheric neutrino flux, and others. The study of ν_τ interactions is a topic of particular importance, since oscillation-induced ν_τ events within the detector are often reconstructed as multi-GeV e-like interactions in the upward-going direction making them a significant background to Hyper-K's mass hierarchy sensitivity. In addition, since

creating and subsequently observing ν_τ in accelerator experiments is difficult the world data is comprised of only a handful of events (nine events from DONuT [190], and five from OPERA [191]). For this reason the uncertainty in the interaction cross section is large, with reference [32] assigning a 25% systematic error based on a survey of theoretical models. Super-Kamiokande has developed a method to extract oscillation-induced ν_τ events from the atmospheric neutrino background based on a neural network procedure trained to select CC interactions in which the τ lepton has decayed hadronically. This technique was used to successfully identify an oscillation-induced ν_τ signal of $\sim$ 40 events atop of a background of $\sim$ 448 events per 100 kton years [192]. Extrapolating to Hyper-K-level exposures this would correspond to more than 2000 CC interactions. Further, by incorporating the neural network variable into the oscillation analysis described in Section III.1 B it is possible to isolate the τ-like events and use them to measure their cross section normalization. Hyper-K's expected sensitivity to this normalization is shown in figure 132. After a 5.6 Mton·year exposure this parameter can be constrained to within 10% using the atmospheric neutrino data.

C. Solar neutrinos

The solar neutrino measurement is capable of determining the neutrino oscillation parameters between mass eigenstate ν_1 and ν_2 in the equation (2). Figure 133 shows the latest combined results of the allowed neutrino oscillation parameters, θ_{12} and Δm^2_{21} from all the solar neutrino experiments and reactor neutrino in KamLAND.[193] The mixing angle is consistent between solar and reactor neutrino, while there is about 2σ tension in Δm^2_{21}. It mainly comes from the recent result of solar neutrino day-night asymmetry observed in Super-K. In solar neutrino oscillations, regeneration of the electron neutrinos through the MSW matter effect in the Earth is expected. According to the MSW model, the observed solar neutrino event rate in water Cherenkov detectors in the nighttime is expected to be higher – by about a few percent in the current solar neutrino oscillation parameter region – than that in the daytime as shown in the Figure 133. The Super-K found the first indication of this day-night flux asymmetry at 3σ level[54], but a conclusive evidence is expected in Hyper-K. If the 2σ tension of Δm^2_{21} between solar (ν_e) and reactor ($\bar{\nu_e}$) neutrinos is a real effect, new physics must be introduced.

In addition to that, the spectrum upturn observation can be possible in the high density PMT option. The spectrum upturn is produced by the transition of the survival probability in ν_e from the matter dominant energy region to the vacuum dominant energy region in the solar neutrino oscillation, and has been observed by the comparison between ^{8}B solar neutrino flux in Super-K and SNO and ^{7}Be solar neutrino flux in BOREXINO.[194] However, the precise measurement of the spectrum shape can distinguish the usual neutrino oscillation scenario from several exotic models such as non standard interaction [195], MaVaN [196], Sterile neutrino [197], and so on. In the low density PMT option, the energy threshold is 6.5 MeV from the SK-II experience [198] and is not enough low for the measurement of spectrum upturn. While in the high density PMT option, the lowering energy threshold is possible because of better energy resolution and reduction of the radio active background.

In the following sections, the sensitivity of the day-night flux asymmetry and spectrum upturn in Hyper-K are described.

Hyper-K also could be used for variability analyses of the Sun. For example, the ^{8}B solar neutrino flux highly depends on the Sun's present core temperature. Unlike multiple scattered, random-walking photons or slow-moving helioseismic waves, free streaming solar neutrinos are the only available messengers with which to precisely investigate ongoing conditions in the core region of the Sun. Hyper-K, with its unprecedented statistical power, could measure the solar neutrino

flux over short time periods. Therefore, short time variability of the temperature in the solar core could be monitored by the solar neutrinos in Hyper-K.

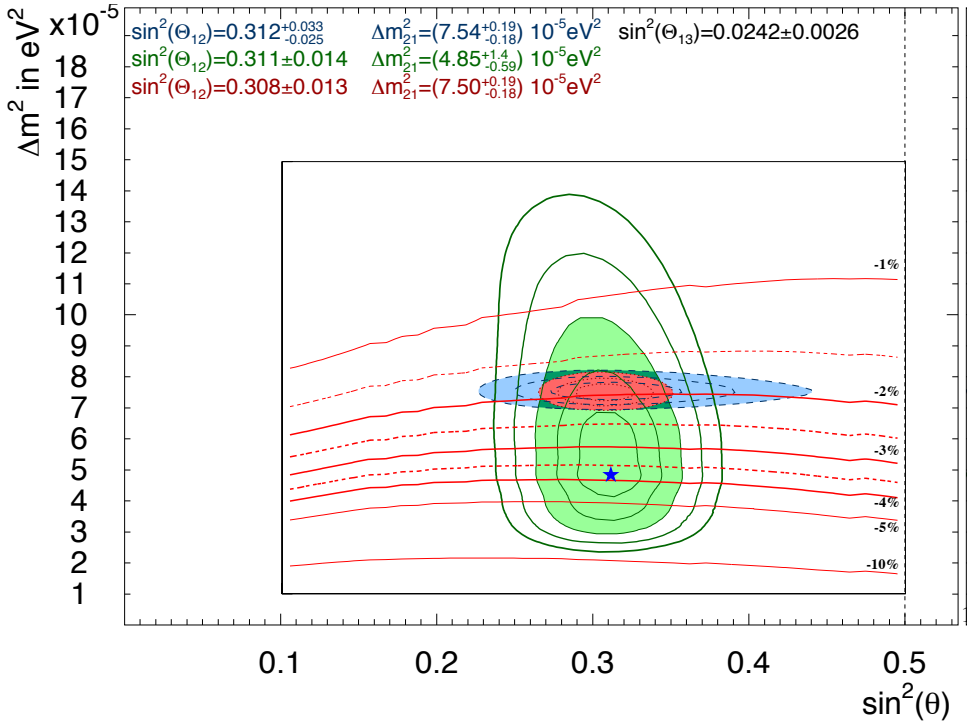

FIG. 133. Allowed neutrino oscillation parameter region from all the solar neutrino experiments (green), reactor neutrino from KamLAND (blue) and combined (red) from one to five sigma lines and three sigma filled area. The star shows the best fit parameter from the solar neutrinos. The contour of the expected day-night asymmetry with 6.5 MeV energy threshold is overlaid.

1. *Background estimation*

The major background sources for the ^{8}B solar neutrino measurements are the radioactive spallation products created by cosmic-ray muons [199] and the radioactive daughter isotopes of Rn-222 in water. The background by spallation products is discussed in detail in the paragraph II.4 A 2 2.2, and it is increased by a factor of 2.7 in Hyper-K comparing to the Super-K. Rn-222 is an essential background source for the spectrum upturn measurement. First of all, the water system has to be constructed as the Rn-222 becomes similar level as Super-K detector. Furthermore, the background level needs to be enlarge to the full fiducial volume unlike Super-K, which can use only limited volume less than 5 MeV energy. It is challenging task but we believe that this should be possible by design improvements over the next several years. Therefore, the same Rn-222 background level

as Super-K in full fiducial volume is assumed in the following calculation.

2. Oscillation studies

In order to calculate the neutrino oscillation sensitivity, the signal and background rates in each option have to be estimated. As for the day-night asymmetry analysis, the energy threshold is set to 6.5 MeV since its effect becomes bigger in higher energy region. In this energy region, only spallation background should be considered. The remaining spallation background rate in Super-K phase IV (40% photo-coverage) has been reduced factor three comparing to Super-K phase II (20% photo-coverage) because of the better energy resolution and so on. Figure 134 shows the sensitivity of the day-night asymmetry as a function of the observation time. The Δm^2_{21} separation ability between solar neutrino (HK) and reactor anti-electron neutrino (KamLAND) is expected more than 6σ level in ten years observation and 9σ in twenty years. This situation will be modified by possible JUNO results on Δm^2_{21} in future.

In the measurement of the spectrum upturn, the Rn-222 background is critical because the ^{214}Bi beta decay events (3.2 MeV end point energy) will come above the energy threshold due to the energy resolution. The detector which has good energy resolution like high density PMT case is strong to reduce such kind of background. Furthermore, the precise energy calibration has to be considered. Here, it is assumed that the same background level with full fiducial volume and the same precision of the energy calibration as Super-K are achieved in Hyper-K. Figure 135 shows the sensitivity of the spectrum upturn discovery as a function of the observation time. It is more than 5σ level in ten years and reaches 7σ in twenty years.

3. Hep solar neutrino

Hep solar neutrino has the highest energy in solar neutrinos. But, the most part of the energy region of the hep solar neutrino is overlapped with ^{8}B solar neutrinos. The expected ^{8}B solar neutrino flux is more than 100 times larger than that of hep solar neutrino in Standard Solar Model (SSM). So far, only the upper limits are reported from SNO and SK group [200, 201].

The measurement of the hep solar neutrino could provide new information on solar physics. The production regions of the ^{8}B and hep neutrinos are different in the Sun. The energy production peak of hep neutrinos is located at outermost radius among all the solar neutrinos in pp-chain [202]. So, they could be used as a new probe of the solar interior around core region. There is still solar

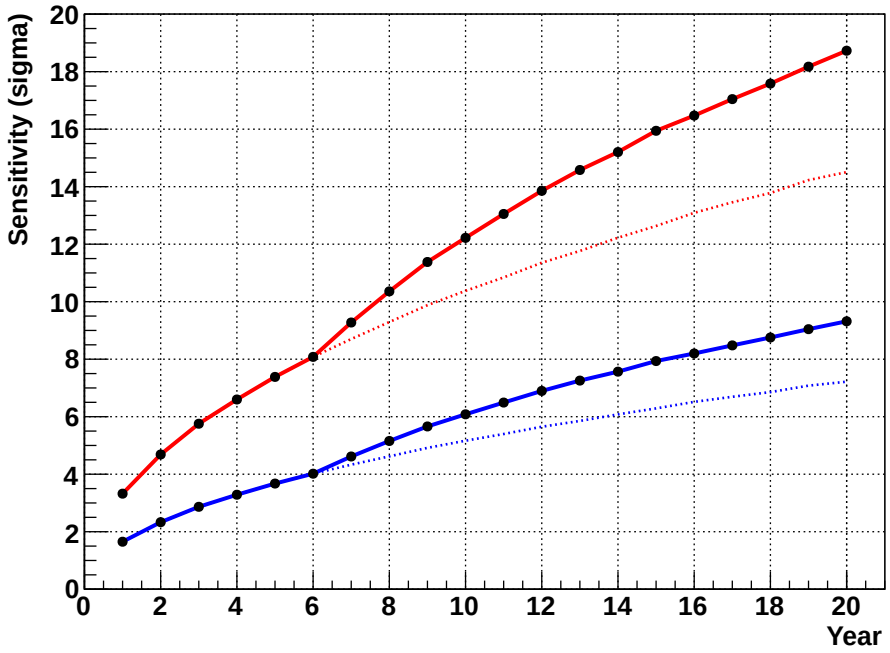

FIG. 134. Day-night asymmetry observation sensitivity as a function of observation time. The red line shows the sensitivity from the no asymmetry, while the blue line shows from the asymmetry expected by the reactor neutrino oscillation. The solid line shows the staging and the dotted line shows the single tank case.

abundance problem. ^{8}B and hep solar neutrino fluxes show different behaviour with GS98 and AGSS09 chemical compositions [203]. Theoretical calculation of hep solar neutrinos is a difficult challenge [204]. The measurement of the hep solar neutrino flux will provide a better understanding of SSM. Hep solar neutrinos could be also used to test non-standard neutrino physics in new energy region ($\sim$ 18 MeV) [205].

In Hyper-K, a high sensitivity measurements of hep solar neutrino flux would be possible, when the detector has a good energy resolution. Figure 136 shows expected solar neutrino fluxes in 1 Mton year with a 3TankLD detector and a 1TankHD detector. The separation between ^{8}B and hep solar neutrinos are highly depends on energy resolution of the detector. Table XXXVII shows a list of expected numbers of solar neutrino events in typical energy regions. A 1TankHD detector or SK-III-type photo coverage detector would be necessary to separate the hep solar neutrino flux from the ^{8}B solar neutrino flux. The high sensitive observation of the hep neutrino flux would be difficult in a 3TankLD detector.

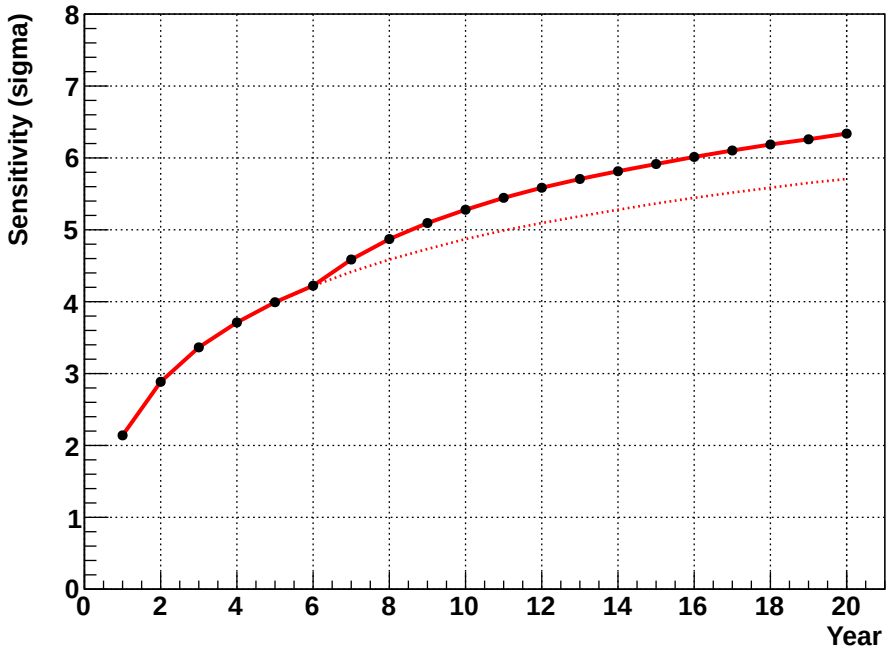

FIG. 135. Spectrum upturn discovery sensitivity as a function of observation time. The solid line shows the staging and the dotted line shows the single tank case.

TABLE XXXVII. Expected solar neutrino event rates in a water Cherenkov detector. The assumptions are same as Fig. 136.

Energy resolution	Energy range [MeV]	^{8}B [/Mton/year]	hep [/Mton/year]	hep / ^{8}B
3TankLD	22.0–22.5	0.74	0.80	1.1
SK-III	19.5–25.0	0.41	1.62	3.9
1TankHD	18.0–25.0	0.30	3.23	10.6

4. Summary

In this section, estimates of potential solar neutrino measurements are reported. The solar neutrino analysis is sensitive to the detector resolutions and background levels. We have estimated expected sensitivities in 10 years Hyper-K observation based on the current Super-K knowledge.

As a result of its shallower site, the increase of the spallation background level in Hyper-K will be up to a factor of 2.7 as compared to Super-K. However – due to its much greater size and high

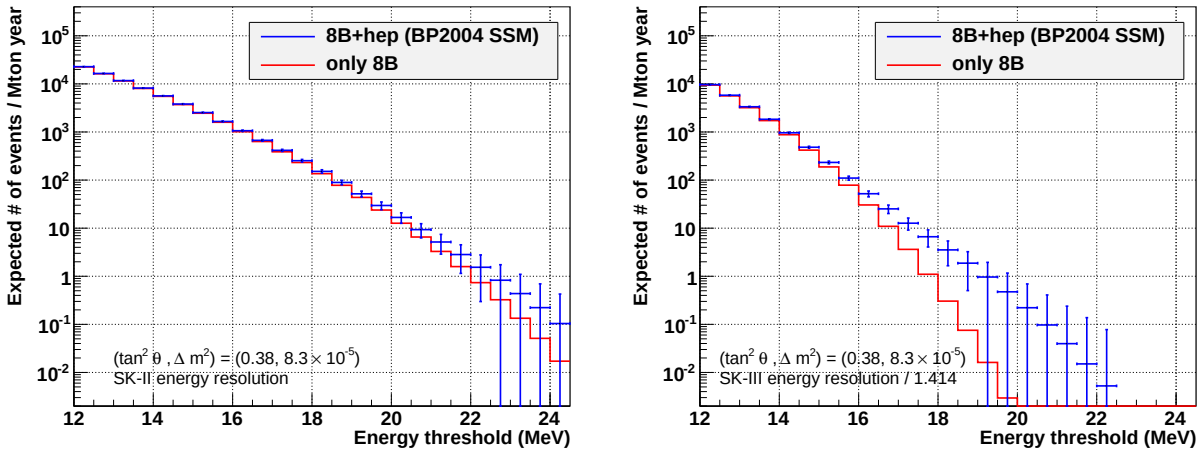

FIG. 136. Expected solar neutrino fluxes with neutrino oscillation in a water Cherenkov detector. The left (right) side plot corresponds to an estimation in a 3TankLD (1TankHD) detector. The horizontal axis is energy threshold in electron total energy and the vertical axis is expected event rate in the energy range from the threshold up to 25 MeV. BP2004 SSM fluxes are assumed. The effect of background events, reduction efficiencies, systematic uncertainties are not considered.

energy resolution in 1TankHD– the statistical uncertainties on solar neutrino measurements would actually be reduced in Hyper-K as compared to Super-K on an equal time basis.

The sensitivity of the identification of the neutrino oscillation parameters between solar and reactor neutrinos by day-night asymmetry is estimated to 5.1σ in 1TankHD and 3.5σ in 3TankLD. The possibility of spectrum upturn observation is estimated to 4.9σ level in 1TankHD, however no chance in 3TankLD due to high energy threshold.

The solar hep neutrino could be measured in a 1TankHD detector with a few Mton year data.

III.2. NUCLEON DECAYS

A. Nucleon decays

Optimizing Hyper-Kamiokande for the observation and discovery of a nucleon decay signal is one if its primary design drivers. In order to significantly extend sensitivity beyond existing limits, many of which have been set by Super-Kamiokande, Hyper-K needs both a much larger number of nucleons than its predecessor and sufficient reconstruction ability to extract signals and suppress backgrounds. While it is possible to target specific decay channels, one of the strengths of water Cherenkov technology is its sensitivity to a wide variety of modes. Using MC and analysis techniques originally developed for Super-Kamiokande, this section details Hyper-K's expected sensitivity to both the flagship proton decay modes, $p \to e^+\pi^0$ and $p \to \overline{\nu}K^+$, as well as other $\Delta(B-L)$ conserving, $\Delta B = 2$ dinucleon, and $\Delta(B-L) = 2$ decays.

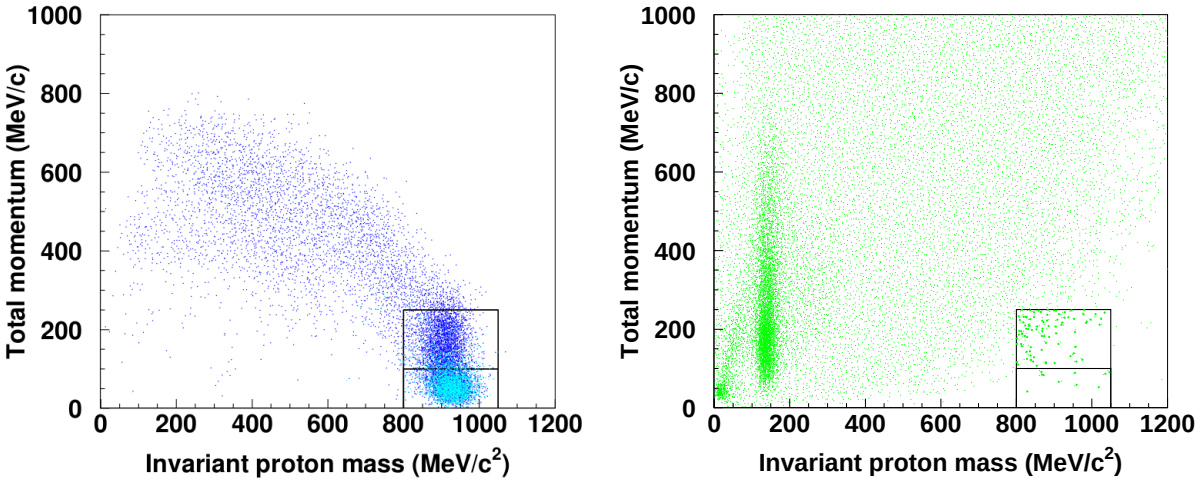

FIG. 137. Reconstructed invariant mass and total momentum distributions for the $p \to e^+\pi^0$ MC (left) and atmospheric neutrino MC (right) after all event selections except the cuts on these variables. The final signal regions are shown by two black boxes in the plane. In the signal plot decays from bound and free protons have been separated by color, dark blue and cyan respectively. Background events have been generated for a 45 Mton·year exposure and those falling in the signal regions have been enlarged for visibility.

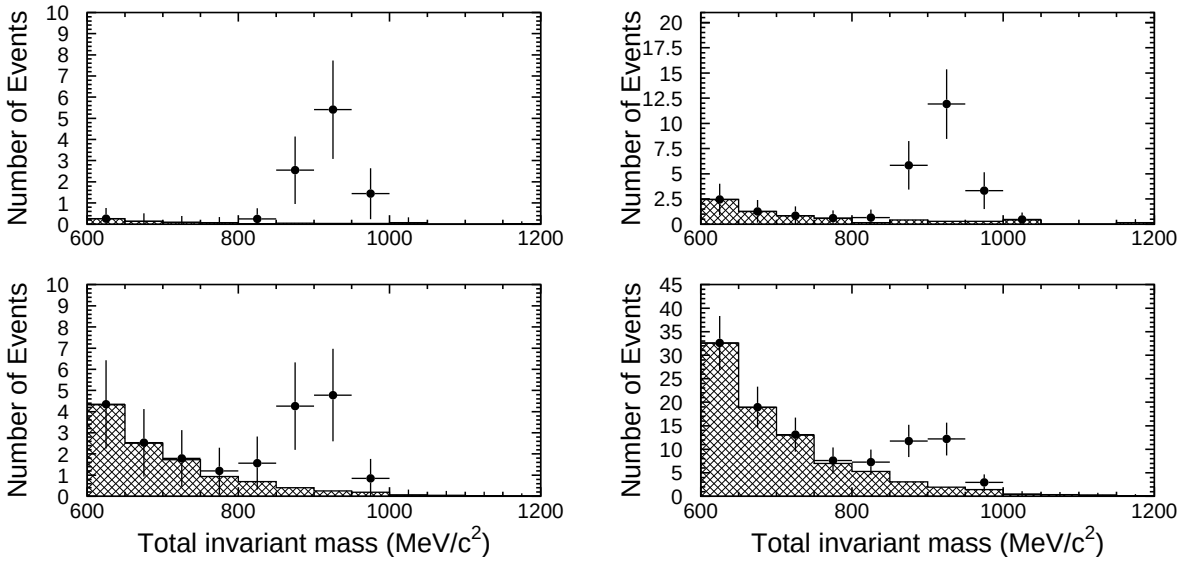

FIG. 138. Reconstructed invariant mass distribution of events passing all steps of the $p \to e^+\pi^0$ event selection except the invariant mass cut. The hatched histograms show the atmospheric neutrino background and the solid crosses denote the sum of the background and proton decay signal. Here the proton lifetime is assumed to be, 1.7×10^{34} years, just beyond current Super-K limits. The plots on the left and right show the expectation for the 1TankHD and 3TankLD designs, respectively, after a 10 year run. For the former an additional tank is assumed to come online six years after the start of the experiment. In each configuration the free (bound) proton enhanced bin appears in the upper (lower) panel of each figure.

1. *Sensitivity to $p \to e^+ + \pi^0$ Decay*

Proton decay into a positron and neutral pion is a favored mode of many GUT models. Experimentally this decay has a very clean event topology, with no invisible particles in the final state. As a result it is possible fully reconstruct the proton's mass from its decay decay products and as a two body process the total momentum of the recoiling system should be small. The event selection focuses on identifying fully contained events within the Hyper-K fiducial volume with two or three electron-like Cherenkov rings. Though the decay of the pion is expected to produce two visible gamma rays, for forward-boosted decays the two photons may be close enough in space to be reconstructed as a single ring. Atmospheric neutrino events with a muon below threshold are removed by requiring there are no decay electrons in the event. For those events with three rings, the two rings whose invariant mass is closest to the π^0 mass are labelled the π^0 candidate. An additional cut on the mass of those candidates, $85 < m_\pi < 185\mathrm{MeV/c}^2$, is applied. The signal

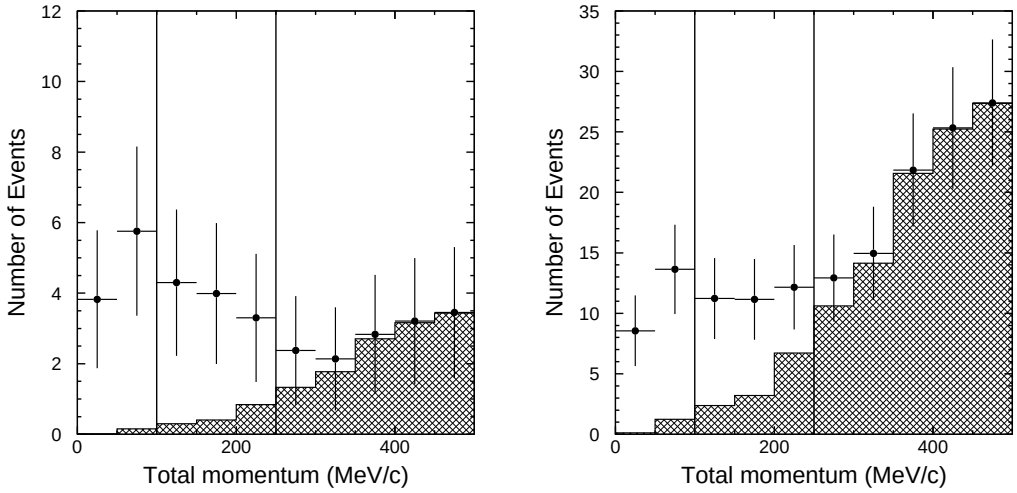

FIG. 139. Total momentum distribution of events passing all steps of the $p \to e^+\pi^0$ event selection except the momentum cut. The hatched histograms show the atmospheric neutrino background and the solid crosses denote the sum of the background and proton decay signal. Here the proton lifetime is assumed to be, 1.7×10^{34} years, just beyond current Super-K limits. The plots on the left and right show the expectation for the 1TankHD and 3TankLD designs, respectively, after a 10 year run. For the former an additional tank is assumed to come online six years after the start of the experiment. Vertical lines in each plot denote the boundaries of the free proton (farthest left) and bound proton (center) analysis bins. Events in the right side of each plot are lost to the total momentum cut.

sample is selected by requiring the total invariant mass of the event be near the proton mass, $800 < m_{inv} < 1050\mathrm{MeV/c^2}$ and that the total momentum, p_{tot}, be less than 250 MeV/c. Water is an excellent molecule for studying proton decay because in addition to providing 10 protons per molecule, two of those are unbound free protons. Decays from those protons are not subject to nuclear effects and result in final state particles with very low total momentum. At the same time, very few atmospheric neutrino interactions reconstructed with both a proton-like invariant mass and low total momentum. To optimize the analysis sensitivity, proton-decay candidates are divided into two signal regions after the invariant mass cut, a free proton decay enriched region ($0 < p_{tot} < 100\mathrm{MeV/c}$) and a bound proton decay region ($100 < p_{tot} < 250\mathrm{MeV/c}$). Finally, 1TankHD design (only) allows for neutron tagging (described in a later section), which is used to reject background events by requiring events have no neutron candidates events in the final state. Figure 137 shows the signal and background MC in the invariant mass and total momentum plane before the final signal region is defined. Signal efficiencies and background rates with corresponding

systematic errors after all selections are listed in Table XXXVIII.

	$0 < p_{tot} < 100$MeV/c				$100 < p_{tot} < 250$MeV/c			
Design	ϵ_{sig} [%]	σ_ϵ [%]	Bkg [/Mton·yr]	σ_{Bkg} [%]	ϵ_{sig} [%]	σ_ϵ [%]	Bkg [/Mton·yr]	σ_{Bkg} [%]
1TankHD	18.7	6.5	0.06	32.8	19.4	14.9	0.62	31.9
3TankLD	18.8	5.3	0.27	29.0	20.4	15.2	2.17	31.3

TABLE XXXVIII. Signal efficiency and background rates as well as estimated systematic uncertainties for the analysis $p \to e^+\pi^0$ at Hyper-K.

Monte Carlo simulation of these decays includes the effects of the nucleon binding energy, Fermi motion, and interactions within the ^{16}O nucleus. The latter represents a significant, but unavoidable, source of inefficiency as the signal π^0 may be lost to absorption or charge exchange prior to exiting the nucleus. Although the signal efficiency of free proton decays is roughly 87% these nuclear effects reduce the efficiency of bound proton decays such that the overall efficiency is only $\sim 40\%$ for $p_{tot} < 250$MeV/c.

Atmospheric neutrino interactions are the main background to proton decay sources. Not only can CC ν_e single-pion production processes produce the same event topology expected in the $p \to e^+\pi^0$, but recoiling nucleons from quasi-elastic processes can produce pion final states through hadronic scatters and mimic the signal. After the event selection above the expected background rate is 0.06 (0.27) events in the free proton enhanced bin and 0.62 (2.17) events in the bound proton enhanced bin per Mton·year for the 1TankHD (3TankLD) design. These background expectations have been experimentally verified using beam neutrino measurements with the K2K experiment's one kiloton water Cherenkov detector, which found and expected atmospheric neutrino background contamination to $p \to e^+\pi^0$ searches of $1.63^{+0.42}_{-0.33}(stat)^{+0.45}_{-0.51}(sys)$ events per Megaton·year [206].

The ability to reconstruct the proton's invariant mass is a powerful feature of this decay mode. Figure 138 shows the expected distribution of this variable for both signal events and atmospheric neutrino backgrounds after a 10 year exposure assuming the proton lifetime is $\tau_X = 1.7 \times 10^{34}$ years. Similarly, figure 139 shows the total momentum distribution of candidate events prior to the momentum selection and illustrates the marked difference in the signal and background expectations for the free proton and bound proton analysis bins.

Hyper-Kamiokande's proton decay discovery potential has been estimated based on a likelihood ratio method. A likelihood function is constructed from a Poisson probability density function for the event rate in each total momentum bin of the $p \to e^+\pi^0$ analysis with systematic errors

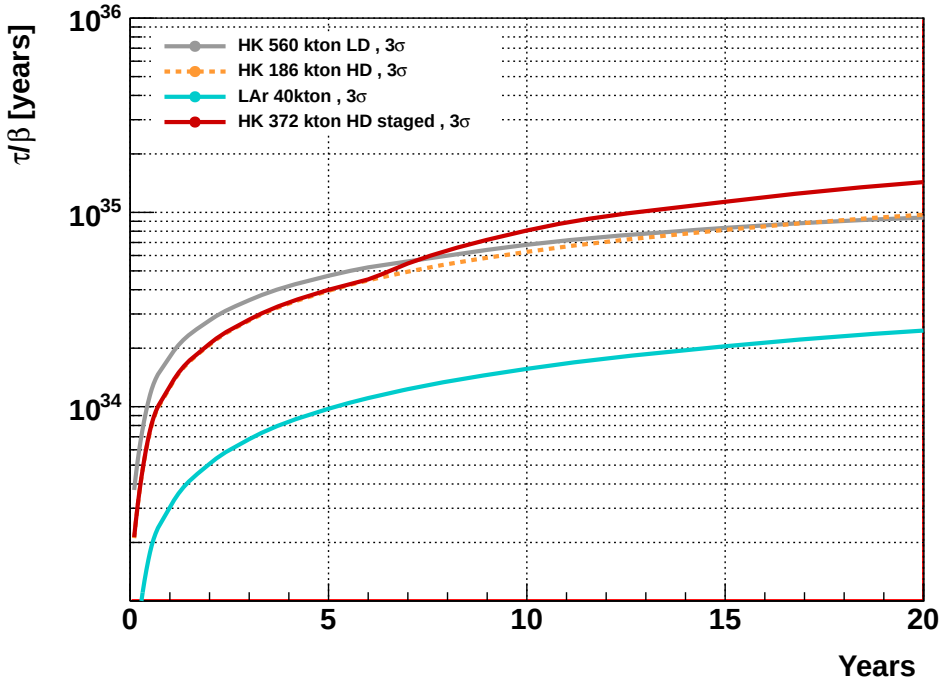

FIG. 140. Comparison of the 3 σ $p \to e^+\pi^0$ discovery potential as a function of run time of the Hyper-K 1TankHD (red solid) and 3TankLD (gray solid) designs as well as that of a 40 kton liquid argon detector (cyan solid). In the 1TankHD line an additional tank is assumed to come online six years after the start of the experiment and a dashed orange line denotes the potential of just a single tank. The 40 kton liquid argon detector is assumed to have a signal efficiency of 45% and an expected background of 1.0 events per Megaton·year. Systematic errors are included for the Hyper-K lines (c.f. Table XXXVIII) but not for the liquid argon detector.

on the selection efficiency and background rate represented by Gaussian nuisance parameters. The experiment's expected sensitivity to a proton decay signal at a given confidence level, α, is calculated as the fastest proton decay rate, Γ, whose median likelihood ratio value assuming a proton decay signal yields a p-value not larger than α from the likelihood ratio distribution under the background-only hypothesis. That is,

$$\Gamma_{disc} = \max_{\Gamma} \left[\alpha = \int_{M(\Gamma)}^{\infty} f(q_0|b) dq_0 \right], \tag{21}$$

where f is the distribution function of the likelihood ratio, q_Γ, and $M(\Gamma) = \text{median}[f(q_\Gamma|\Gamma\epsilon\lambda + b)]$. Here ϵ is the selection efficiency, λ the detector exposure, and b is the expected number of background events. For the calculated significance the corresponding proton lifetime is then

$\tau_{disc} = 1/\Gamma_{disc}$. Under this definition Hyper-K's 3σ (one-sided) discovery potential as a function of run time is shown in Figure 140. Note that if the proton lifetime is as short as τ_X its decay into $e^+\pi^0$ will be seen at this significance within one year of Hyper-K running.

Even in the absence of a signal Hyper-K is expected to extend existing limits by more than an order of magnitude. Hyper-K's sensitivity to this decay mode is computed as

$$\tau_{limit} = \sum_{n=0}^{\infty} O(n|b)/\Gamma_n, \tag{22}$$

where

$$\Gamma_n = \left[\Gamma_l : 1 - \alpha = \int_0^{\Gamma_l} P(\Gamma|n)d\Gamma\right] \tag{23}$$

and $P(\Gamma|n)$ is the probability that the proton decay rate is Γ given an observation of n events. Similarly, $O(n|b)$ is the Poisson probability to observe n events given a mean of b. The function $P(\Gamma|n)$ is obtained using Bayes' theorem and the likelihood function outlined above. Hyper-K's expected sensitivity to $p \to e^+\pi^0$ using this metric is shown in Figure 141. In both this and the discovery potential figure, systematic errors on the signal and background have been included based on the Super-K analysis; The errors are listed in Table XXXVIII. A detailed description of the systematic error estimation and the limit calculation may be found in [207].

2. Sensitivity study for the $p \to \overline{\nu}K^+$ mode

Proton decays into a lepton and a kaon are a feature of supersymmetric grand unified theories, of which $p \to \overline{\nu}K^+$ is among the most prominent. Searching for the K^+ in a water Cherenkov detector is complicated by the fact it emerges from the decay with a momentum of only 340 MeV/c, well below the threshold for light production, 749 MeV/c. As a result the K^+ must be identified by its decay products: $K^+ \to \mu^+ + \nu$ (64% branching fraction) and $K^+ \to \pi^+ + \pi^0$ (21% branching fraction). Since both of these modes are two body decays the outgoing particles have monochromatic momenta. Furthermore, the 12 ns lifetime of the kaon makes it possible to observe prompt γ ray emission produced when the proton hole leftover from a bound proton decay is filled by the de-excitation of another proton. For ^{16}O nuclei the probability of producing a 6 MeV γ from such a hole is roughly 40%, making this a powerful tool for identifying the K^+ decay products and rejecting atmospheric neutrino backgrounds.

Three methods, each targeting different aspects of the $K+$ decay, are used to search for $p \to \overline{\nu}K^+$ events [208]. The "prompt γ" method searches for a prompt nuclear de-excitation γ ray (6.3 MeV)

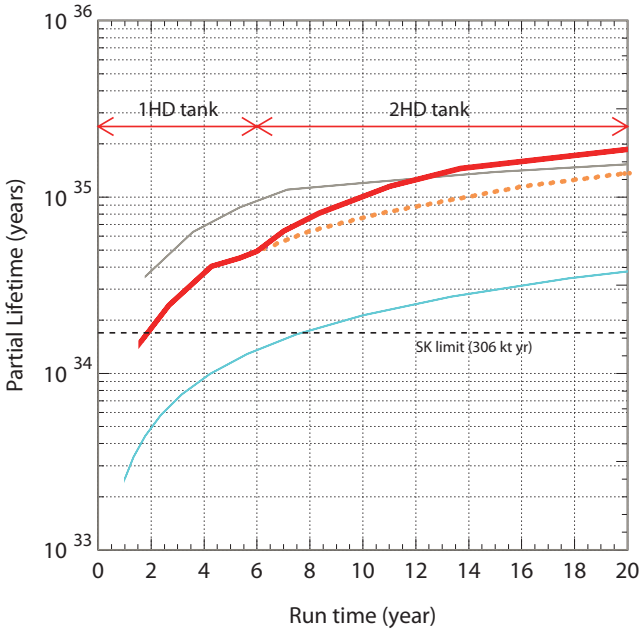

FIG. 141. Assuming no proton decay signal, Hyper-K's sensitivity to the $p \to e^+\pi^0$ decay mode at 90% C.L. as a function of run time for the 1TankHD (3TankLD) design appears in red (gray). In the red line a second detector is assumed to come online six years after the start of the experiment. The orange dotted line represents the sensitivity of just one detector. A cyan line represents the sensitivity of a 40 kton liquid argon detector assuming an efficiency of 45% and an expected background of 1.0 events per Mton·year. Super-K's current limit is shown by a horizontal line.

occurring prior to and separated in time from a 236 MeV/c muon. A schematic of this process appears in Figure 142. In the second method the same monochromatic muon is searched for but without the γ tag. Finally, the third method, or "$\pi^+\pi^0$ method", searches for a monochromatic π^0 with light from a backward π^+. Here the charged pion is only slightly above Cherenkov threshold, making it difficult to reconstruct a full ring.

The prompt γ search method proceeds by identifying fully contained fiducial volume interactions with a single μ-like ring accompanied by a Michel electron. In order to suppress atmospheric neutrino backgrounds, particularly those with an invisible muon, the muon momentum is required to be $215 < p_\mu < 260$ MeV/c and the distance between its vertex and that of the Michel electron cannot exceed 200 cm. Events with high momentum protons that create a μ-like Cherenkov ring are rejected using a dedicated likelihood designed to select in favor of genuine muons based on the PMT hit pattern and the Cherenkov opening angle. Searching backward in time from the muon candidate, de-excitation γ ray candidates are identified as the largest cluster of PMT hits

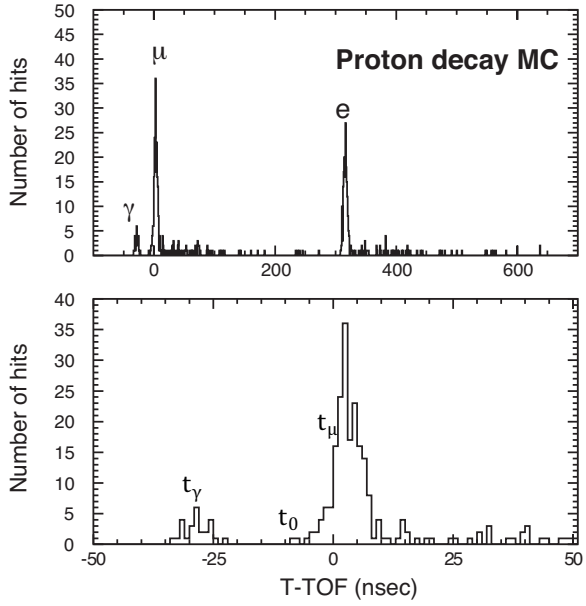

FIG. 142. Schematic view of the expected timing distribution of events in the prompt γ search method for $p \to \overline{\nu} K^+$ decays. The upper panel shows the full event time window with the μ, Michel, and γ candidate clusters. The bottom panel shows the time of flight subtracted timing distribution around the μ candidate.

within a 12 ns sliding time window. The time difference between center of the time window containing the γ candidate, t_γ, and the muon time, t_μ is then required be consistent with decay of a kaon, $t_\mu - t_\gamma < 75$ ns ($\sim 6\tau_{K^+}$). Finally, only events whose number of hits in this window, N_γ, is consistent with 6 MeV of energy deposition ($4 < N_\gamma < 30$) are kept. Figure 143 shows the expected p_μ distribution after all selection cuts have been applied assuming a proton lifetime of 6.6×10^{33} years.

The second search (p_μ spectrum) method also focuses on identifying the monochromatic muon but with relaxed search criterion. In the above only those cuts applied before the proton likelihood cut are used. A fit is the applied to the resulting muon momentum distribution to identify any proton decay-induced excess of muon events over the considerable atmospheric neutrino background.

Like the prompt γ search, the $\pi^+\pi^0$ search relies on more sophisticated event selections to identify the signal. While the momentum of both the π^+ and π^0 from the K^+ decay will be 205 MeV/c, the former does not deposit enough light to be reconstructed fully. To compensate for this the search method focuses on PMT hits opposite the direction of a π^0 at the correct momentum. Fully contained events with one or two reconstructed rings, all of which are e-like, are selected. In addition there should be one Michel electron from the charged pion decay chain. For two-ring events the invariant mass is required to be consistent with that of a neutral pion, $85 < m_{\pi^0} < 185\,\mathrm{MeV}/c^2$.

Further, the total momentum should be between 175 and 250 MeV/c. At this stage the π^+ light is identified as visible energy between 7 and 17 MeV located at an angular separation between 140 and 180 degrees from the π^0 candidate's direction. Finally a likelihood method is used to evaluate the consistency of this light pattern with that produced by a π^+. Details of the full search method are detailed elsewhere [208]. In addition, as in the $p \to e^+\pi^0$ search, a cut on the number of tagged neutrons is applied in the analysis of the 1TankHD design.

Table XXXIX summarizes the expected signal efficiency and background rates for each of the search methods. Accompanying systematic errors have been calculated based on Super-K methods [208] and are included in the table. Assuming a proton lifetime close to current Super-K limits, figures 143 and 144 show the reconstructed muon momentum from the prompt gamma search and the reconstructed kaon mass spectrum from the $\pi^+\pi^0$ search. Note that while the latter is unused in the analysis itself it provides a demonstration of the signal reconstruction since the proton mass for this decay mode cannot be reconstructed.

	Prompt γ				$\pi^+\pi^0$				p_μ Spectrum		
Design	ϵ_{sig} [%]	σ_ϵ [%]	Bkg	σ_{Bkg} [%]	ϵ_{sig} [%]	σ_ϵ [%]	Bkg	σ_{Bkg} [%]	ϵ_{sig} [%]	Bkg	σ_{fit} [%]
1TankHD	12.7	19.0	0.9	27.0	10.8	10.0	0.7	31.0	31.0	1916.0	8.0
3TankLD	7.4	19.0	2.7	25.0	6.7	10.0	3.4	29.0	31.0	1916.0	8.0

TABLE XXXIX. Signal efficiency and background rates as well as estimated systematic uncertainties for the analysis $p \to \bar{\nu}K^+$ at Hyper-K. Background rates are listed as events per Mton·yr.

3. Sensitivity study for other nucleon decay modes

Although the $p \to e^+\pi^0$ decay mode is predicted to be dominant in many GUT models, a variety of other decay modes are possible, each with a sizeable branching ratio. Table XL shows the branching ratio distribution and ratio of neutron to proton lifetimes as predicted by several GUT models. The diversity in these predictions suggests that in order to make a discovery and to subsequently constrain proton decay models, it is critical to probe as many nucleon decay modes as possible. Fortunately, Hyper-Kamiokande is expected to have an order of magnitude or more sensitivity to many decay modes beyond the two standard decays discussed above.

Hyper-Kamiokande's sensitivity to other nucleon decay modes has been estimated based in part on efficiencies and background rates from Super-Kamiokande [213]. Table XLI shows the 90 % CL

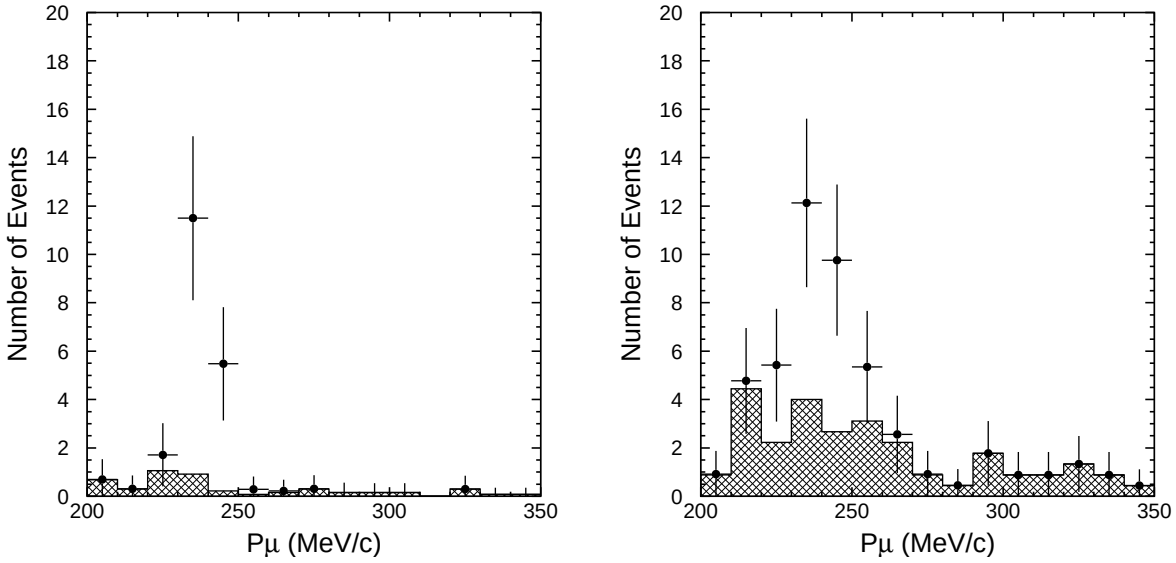

FIG. 143. Reconstructed muon momentum distributions for muons found in the prompt γ search for $p \to \bar{\nu}K^+$. The hatched histograms show the atmospheric neutrino background and the solid crosses denote the sum of the background and proton decay signal. Here the proton lifetime is assumed to be, 6.6×10^{33} years, just beyond current Super-K limits. The plots on the left and right show the expectation for the 1TankHD and 3TankLD designs, respectively, after a 10 year run. In the latter a second tank is assumed to come online six years after the start of the experiment.

sensitivities with a 5.6 Megaton·year exposure in the 3TankLD configuration. The current lifetime limits are also shown in the table for reference. Note that in all cases the sensitivity exceeds existing limits by an order of magnitude. However, several analysis improvements are anticipated for the 1TankHD design, which will result in better sensitivity for an equivalent exposure. Neutron tagging, for instance, can be used to reduce atmospheric neutrino backgrounds. Under these conditions Table XLII shows the 3σ discovery potential of Hyper-K for a selected number of decay modes after a 2.6 Mton·year exposure.

The decay modes in Table XLI all conserve baryon number minus lepton number, $(B - L)$. However, $(B + L)$ conserving mode, $n \to e^- K^+$, was also given attention and searched for by Super-Kamiokande. In $n \to e^- K^+$, the K^+ stops in the water and decays into $\mu^+ + \nu$. The final state particles observed in $n \to e^- K^+, K^+ \to \mu^+ \nu$ are e^- and μ^+. Both e^- and μ^+ have monochromatic momenta as a result of originating from two-body decays. Furthermore, the timing of μ^+ events are delayed with respect to the e^- events because of the K^+ lifetime. In SK-II, the estimated efficiencies and the background rate are 8.4% and 1.1 events/Megaton·year, respectively.

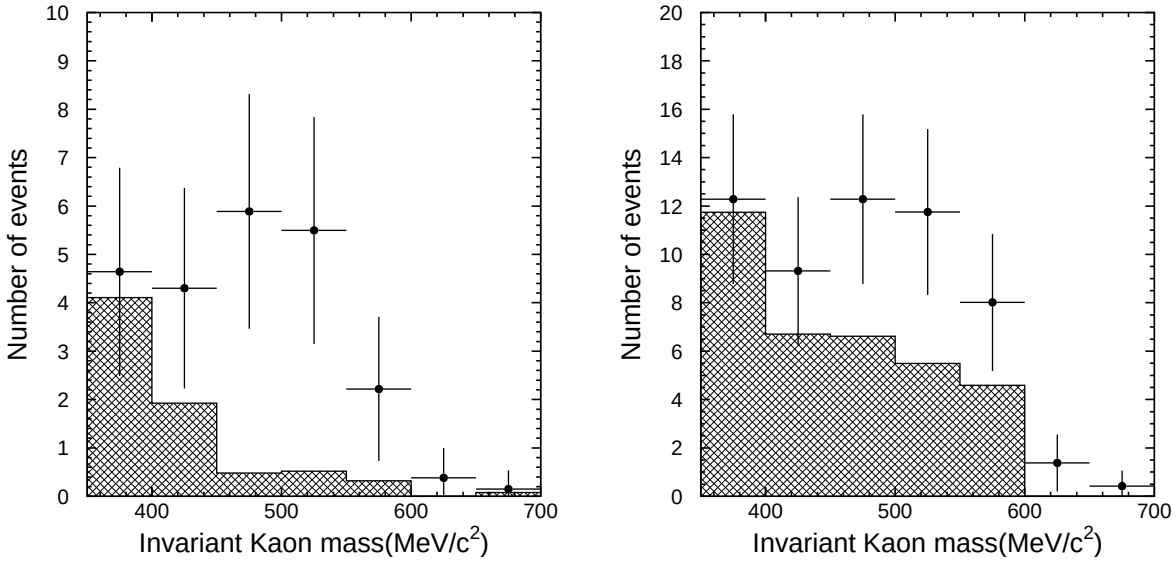

FIG. 144. Reconstructed kaon mass based on the reconstructed final in the $p \to \bar{\nu}K^+$ modes $\pi^+\pi^0$ search . The hatched histograms show the atmospheric neutrino background and the solid crosses denote the sum of the background and proton decay signal. Here the proton lifetime is assumed to be, 6.6×10^{33} years, just beyond current Super-K limits and all cuts except for the cut on visible energy opposite the π^0 candidate have been applied. The plots on the left and right show the expectation for the 1TankHD and 3TankLD designs, respectively, after a 10 year run. In the latter a second tank is assumed to come online six years after the start of the experiment.

From those numbers, the sensitivity to the $n \to e^- K^+$ mode with a 5.6 Megaton·year exposure is estimated to be $2.2{\times}10^{34}$ years.

The possibility of $n\overline{n}$ oscillation is another interesting phenomenon; it violates the baryon number (B) by $|\Delta B| = 2$. These $n\overline{n}$ oscillations have been searched for in Super-Kamiokande with a 0.09 Megaton·year worth of data [214]. Further improvement of the $n\overline{n}$ oscillation search is expected in Hyper-Kamiokande.

In addition to $(B-L)$ conserving modes several other nucleon channels are available. Unification schemes invoking left-right symmetry (c.f. [215]) predict trilepton decays such as $p \to e^+(\mu^+)\nu\nu$, which violate $(B-L)$ by two units ($|\Delta(B-L)| = 2$). Though there are two particles in the final state that are invisible to Hyper-Kamiokande, the presence of a positron or muon from such decays can, in principal, be detected. While this type of single charged lepton signature would naturally be subject to large atmospheric backgrounds, with a sufficiently large decay rate spectral information can be used to separate the two. Going one step farther, then, spectral analysis makes it possible

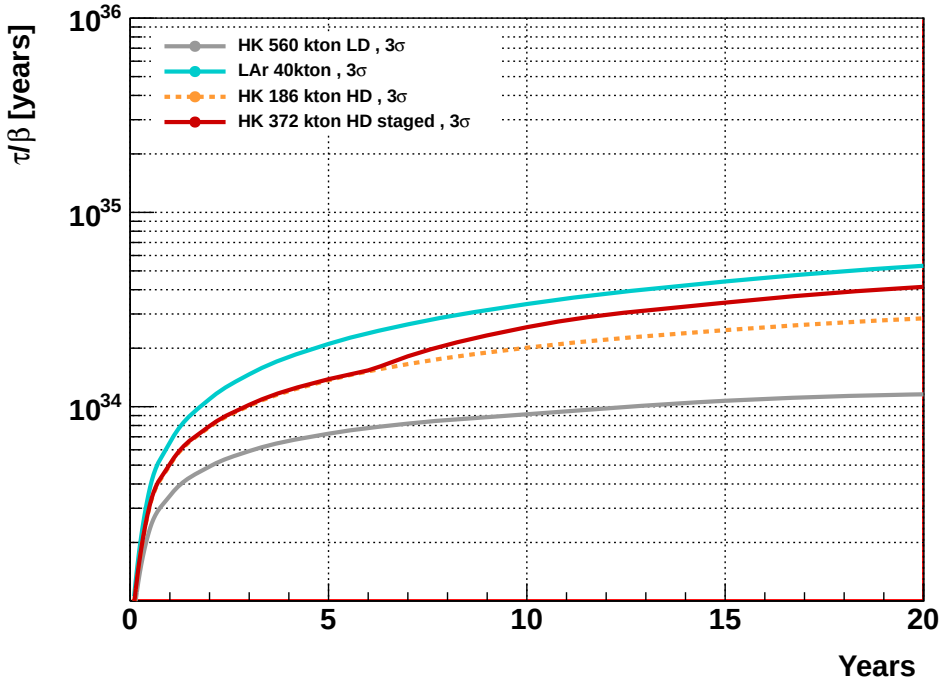

FIG. 145. Comparison of the 3 σ $p \to \bar{\nu}K^+$ discovery potential as a function of run time of the Hyper-K 1TankHD (red solid) and 3TankLD (gray solid) designs as well as that of a 40 kton liquid argon detector (cyan solid). In the 1TankHD line an additional tank is assumed to come online six years after the start of the experiment and a dashed orange line denotes the potential of just a single tank. The 40 kton liquid argon detector is assumed to have a signal efficiency of 97% and an expected background of 1.0 events per Megaton·year. Systematic errors are included for the Hyper-K lines (c.f. Table XXXIX) but not for the liquid argon detector.

to search for generic decay modes as well, such as $p \to e^+(\mu^+)X$, where X is an unknown and unseen particle.

Though only single nucleon decays have been considered up until this point it is worth noting that dinucleon processes, in which a neutron-proton (or proton-proton) pair decays into a pair of leptons, can also be studied at Hyper-Kamiokande. Modes where $\Delta B = 2$, such as $np \to l^+\nu$, appear in models with extended Higgs sectors [216] and have connections to Baryogenesis. Interestingly, these models have the additional property that the single nucleon decay modes are suppressed relative to the dinucleon decays. This wealth of predictions for possible channels further emphasizes the need to search for as many nucleon decay signatures as possible in the quest for grand unification. Table XLIII lists Hyper-K's expected sensitivity to both $|\Delta(B-L)| = 2$ and

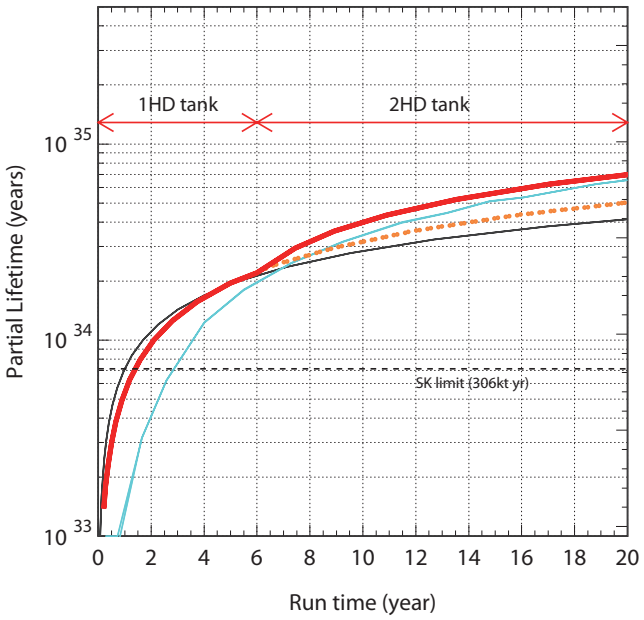

FIG. 146. Assuming no proton decay signal, Hyper-K's sensitivity to the $p \to \bar{\nu}K^+$ decay mode at 90% C.L. as a function of run time for the 1TankHD (3TankLD) design appears in red (gray). In the red line a second detector is assumed to come online six years after the start of the experiment. The orange dotted line represents the sensitivity of just one detector. A cyan line represents the sensitivity of the 40 kton DUNE liquid argon detector. Super-K's current limit is shown by a horizontal line.

$\Delta B = 2$ decays for a 5.6 Mton·year exposure. While searches for these modes are dominated by the atmospheric neutrino background, Hyper-K can be expected to extend existing limits by a factor of three to ten if no signal is observed.

B. Impact of Increased Photon Collection

Improved photon collection with larger photocathode coverages, higher quantum efficiency photosensors, or a combination of the two will have a dramatic effect on the physics sensitivity of Hyper-K. Nucleon decay searches, in particular, are expected to benefit significantly from enhanced ability to detect low levels of Cherenkov light. With the large exposures Hyper-K will provide, the atmospheric neutrino background to these searches becomes sizable, as discussed above, and inhibits the discovery potential of the experiment. However, these same backgrounds are often expected to produce neutrons either directly through the CC interaction of antineutrinos or indirectly via the secondary interaction of hadrons in the interaction. Proton decay events, in contrast, are only rarely expected to be accompanied by neutrons. Though such neutrons are ordinarily trans-

TABLE XL. Branching ratios for various proton decay modes together with the ratio of the neutron to proton lifetimes as predicted by SU(5) and SO(10) models. .

	Br.(%)				
	SU(5)				SO(10)
References	[209]	[210]	[211]	[212]	[212]
$p \to e^+\pi^0$	33	37	9	35	30
$p \to e^+\eta^0$	12	7	3	15	13
$p \to e^+\rho^0$	17	2	21	2	2
$p \to e^+\omega^0$	22	18	56	17	14
Others	17	35	11	31	31
τ_p/τ_n	0.8	1.0	1.3		

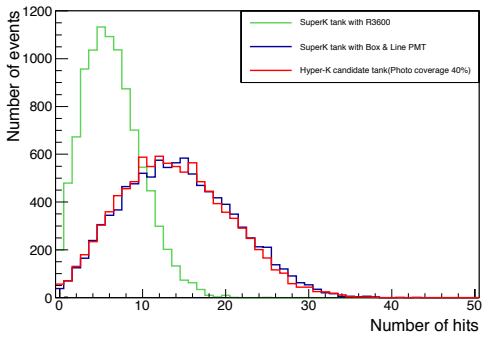

FIG. 147. Number of hit PMTs for a toy MC simulation of the 2.2 MeV γ rays emitted following neutron capture on hydrogen. Cutting at more than nine hits in the Super-K distribution yields as estimated 18% tagging efficiency.

parent to water Cherenkov detectors, Super-Kamiokande has demonstrated the ability to tag the 2.2 MeV photon emerging from neutron capture on hydrogen, $n(p,d)\gamma$. Naturally this channel is potentially available to Hyper-K.

Since 2.2 MeV is only barely visible in Super-K, the tagging algorithm makes use of a neural network to isolate signal neutrons, which are correlated spatially and temporally with the primary neutrino interaction, from background sources. Though the method achieved 20.5% tagging efficiency with a 1.8% false tag probability [53]. it is worth noting that so far it has only been successful during the SK-IV phase of the experiment. Despite 40% photocathode coverage with

TABLE XLI. Summary of Hyper-K's sensitivity to various $|B-L|$ conserving nucleon decay modes after a 5.6a,Megaton·year exposure of the 3TankLDdesign compared with existing lifetime limits. The current limits for $p \to e^+\pi^0$, $p \to \mu^+\pi^0$, and $p \to \overline{\nu}K^+$ are from a 0.22 Megaton·year exposure of Super-K, while the other modes are from a 0.14 Megaton·year exposure.

Mode	Sensitivity (90% CL) [years]	Current limit [years]
$p \to e^+\pi^0$	1.2×10^{35}	1.4×10^{34}
$p \to \overline{\nu}K^+$	2.8×10^{34}	0.7×10^{34}
$p \to \mu^+\pi^0$	9.0×10^{34}	1.1×10^{34}
$p \to e^+\eta^0$	5.0×10^{34}	0.42×10^{34}
$p \to \mu^+\eta^0$	3.0×10^{34}	0.13×10^{34}
$p \to e^+\rho^0$	1.0×10^{34}	0.07×10^{34}
$p \to \mu^+\rho^0$	0.37×10^{34}	0.02×10^{34}
$p \to e^+\omega^0$	0.84×10^{34}	0.03×10^{34}
$p \to \mu^+\omega^0$	0.88×10^{34}	0.08×10^{34}
$n \to e^+\pi^-$	3.8×10^{34}	0.20×10^{34}
$n \to \mu^+\pi^-$	2.9×10^{34}	0.10×10^{34}

TABLE XLII. Summary of Hyper-K's 3σ discovery potential for several nucleon decay modes in the 1TankHD configuration. A 2.6 Megaton·year exposure, corresponding to six years of a single detector and a subsequent four years with two, has been assumed. Current limits are summarized in Table XLI.

Mode	τ_{disc} 3σ [years]
$p \to e^+\pi^0$	8.0×10^{34}
$p \to \overline{\nu}K^+$	2.5×10^{34}
$p \to \mu^+\pi^0$	8.7×10^{34}
$p \to e^+\eta^0$	4.0×10^{34}
$p \to \mu^+\eta^0$	4.3×10^{34}
$n \to e^+\pi^-$	1.7×10^{34}
$n \to \mu^+\pi^-$	1.1×10^{34}

TABLE XLIII. Summary of Hyper-K's sensitivity to various $|\Delta(B-L)| = 2$ and $|\Delta B| = 2$ proton and dinucleon decay modes after a 5.6 Megaton·year exposure of the 3TankLD configuration compared with existing lifetime limits. The current livetime limits are taken from a 0.273 Mton·year exposure of Super-K. Limits on the dinucleon decay modes are reported per ^{16}O nucleus, whereas the single nucleon decays are displayed as limits per nucleon.

Mode	Sensitivity (90% CL) [years]	Current limit [years]
$p \to e^+\nu\nu$	10.2×10^{32}	1.7×10^{32}
$p \to \mu^+\nu\nu$	10.7×10^{32}	2.2×10^{32}
$p \to e+X$	31.1×10^{32}	7.9×10^{32}
$p \to \mu^+X$	33.8×10^{32}	4.1×10^{32}
$n \to \nu\gamma$	23.4×10^{32}	5.5×10^{32}
$np \to e^+\nu$	6.2×10^{32}	2.6×10^{32}
$np \to \mu^+\nu$	4.2×10^{32}	2.0×10^{32}
$np \to \tau^+\nu$	6.0×10^{32}	3.0×10^{32}

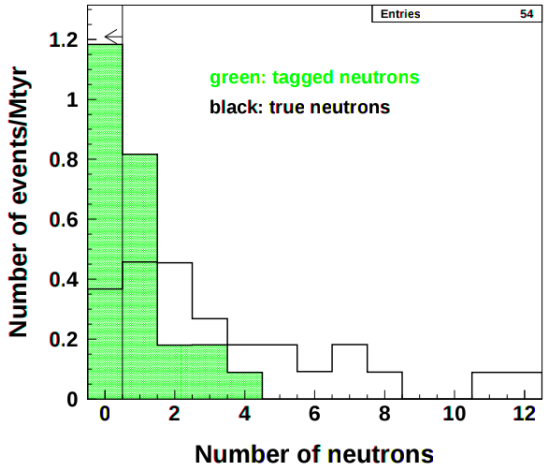

FIG. 148. Neutron multiplicity distribution for background events in the $p \to e^+\pi^0$ search at Hyper-K. The open histogram shows the distribution prior to neutron tagging and the green histogram shows the result of applying the SK-IV neutron tagging algorithm with 20.5% efficiency.

Hamamatsu R3600 50 cm PMTs, on average the neutron capture signal produces only 7 hits in the detector [53]. Since the average photon travel length in Hyper-K will be larger than that of SK-IV, in order to take advantage of the neutron signal it is essential to augment Hyper-K's photon yield

wherever possible.

While a full analysis of Hyper-K's neutron tagging capability is in development a rough estimation for a detector geometry with 40% photocathode coverage using high quantum efficiency photosensors (c.f. Section II.2 F) has been estimated in simulation. Figure 147 shows the number of hit photosensors for a simulated sample of the 2.2 MeV γ ray emitted when a neutron captures on a proton for three water Cherenkov detector configurations. The green distribution shows the response of a Super-K-sized detector with 40% photocathode coverage by Hamamatsu R3600 PMTs, while the blue line shows the effect of implementing HQE Box and Line photosensors. With the same photocatode coverage and the latter photosensors but with an enlarged tank representative of a possible design for Hyper-K (60 m diameter and 74 m height results) results in the red curve. Using these distributions the number of hit photosensors which reproduces the tagging efficiency realized in the Super-K analysis is chosen as the metric to represent the expected tagging efficiency at Hyper-K. For the Super-K distribution gamma events with more than nine PMT hits yields 18% tagging efficiency. Assuming the same 10 hit threshold can be used at Hyper-K, the equivalent distribution (red curve in the figure) suggests 73% efficiency can be achieved. In what follows sensitivity estimates are presented assuming both this and the Super-K tagging efficiency.

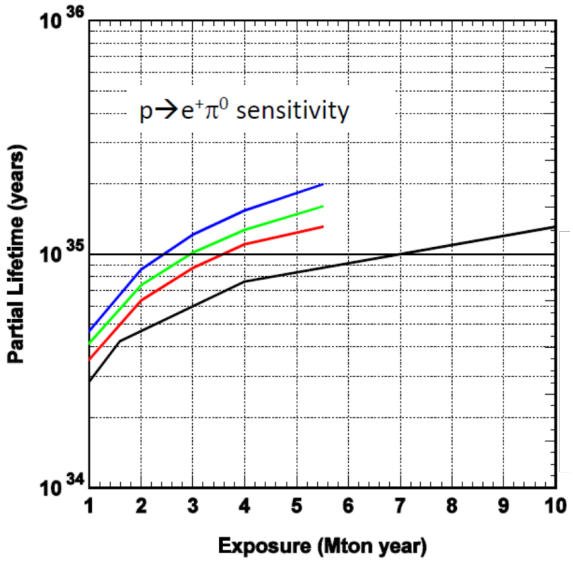

FIG. 149. Hyper-K sensitivity to proton decay for the $p \to e^+\pi^0$ mode as a function of exposure. The black curve illustrates the baseline sensitivity as presented in Section III.2 A. Improved sensitivity curves as a result of a finer binned signal region (red) in conjunction with a 50% reduction in background (green) or a 70% reduction (blue) are also shown. For the latter a null observation would produce a limit of 10^{35} with only a third of the exposure of the default analysis.

Based on MC studies, the fraction of atmospheric neutrino backgrounds to the $p \to e^+\pi^0$ search which are accompanied by at least one final state neutron is $> 80\%$. At the same time, only 4% of signal MC events have such a neutron. The multiplicity distribution for the background sample is shown in figure 148. Due to the presence of high multiplicity events, assuming the same 20.5% neutron tagging efficiency as SK, the neutron background can be reduced by approximately one half (green histogram) by rejecting events with one or more neutron tags. Reducing the background in this manner will have a large impact on the sensitivity to this decay mode, as shown in figure 149. In the figure the black cure represents the sensitivity of the default analysis as a function of exposure. If the final signal region is divided into a region where free proton decays are enhanced ($p_{tot} < 100\text{MeV/c}^2$) and a region with predominantly bound decays ($p_{tot} > 100\text{MeV/c}^2$) the resulting sensitivity is shown in the red line. Further, if the total background is then reduced by 50% (70%), by the introduction of neutron tagging, for instance, the sensitivity improves as shown in the green (blue) lines. Assuming no signal is observed Hyper-K will require a 7.0 Mton year exposure to reach lifetime limits of 10^{35} years. However, with these background reductions the exposure is reduced to 3.0 and 2.4 Mton years, respectively.

It should be noted that $p \to e^+\pi^0$ is not the only mode that is expected to benefit from a higher photon yield; Most modes are similarly expected to benefit from the atmospheric neutrino background reduction that neutron tagging affords. However the $p \to \bar{\nu}K^+$ search can also benefit from enhanced light collection to improve the signal efficiency. Its two lowest efficiency but most sensitive search modes, one in which the decay is accompanied by a prompt 6.3 MeV de-excitation γ from the recoiling nucleus and the other in which the K^+ decays into $\pi^+\pi^0$, both have components that are looking for small amounts of light. Higher photon yields are thus connected directly to potential efficiency improvements in these channels.

As discussed above the search for the prompt γ ray is done using the number of hit PMTs within a 12 nsec wide timing widow prior to the muon candidate from the $K^+ \to \mu^+\nu$ (c.f. figure 142). Figure 150 shows this distribution for the proton decay signal (red) and background from atmospheric neutrinos (blue) for the baseline Hyper-K design with 20% photocathode coverage (upper panel) and a design with 40% coverage and photosensors with improved quantum efficiency (lower panel). In the latter study the photon yield is assumed to be 1.9 times greater than that of the PMT used in the baseline design and with half of the intrinsic timing resolution of the photosensor (1 nsec at 1 p.e.). Additionally, these sensors are assumed to have a higher dark rate, 8.4 kHz. For both detector configurations the peak near zero corresponds to events in which a γ was not found and these hits are dominated by hits from the sensor dark noise. Though this peak

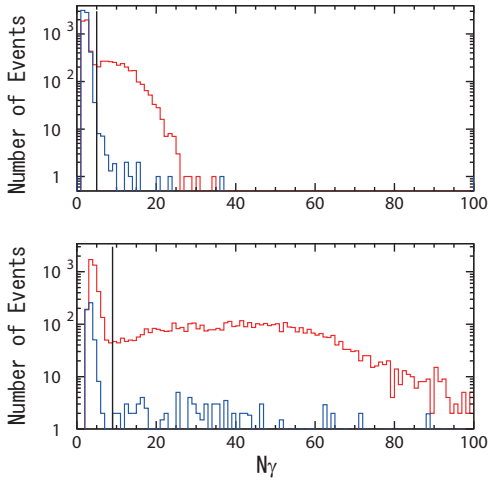

FIG. 150. Distribution of the number of hits within a 12 nsec timing window used to search for the 6.3 MeV γ from $p \to \bar{\nu}K^+$ events. The upper panel corresponds to the Hyper-K baseline design with 20% photocathode coverage and the same PMTs used in SK (Hamamatsu R3600). In the lower panel the result from an alternate design with 40% coverage and photosensors with a factor of 1.9 higher photon yield is shown. Red (blue) lines show the proton decay signal (atmospheric neutrino background) distribution. The proton decay signal region is defined as $4 < N_\gamma < 30$ hits and $8 < N_\gamma < 120$ for the baseline and alternate designs, respectively.

is not well separated from the feature at higher hits in the baseline configuration, with improved photosensors a clear distinction between the two can be seen. Further, since the γ search is designed to avoid hit contamination from the μ^+, the narrower timing resolution of the improved sensors means that the search can occur closer in time to the muon. Practically this enables K^+ with earlier decay times can be used in the analysis as shown in figure 151. Both of these effects lead to an overall increase the signal efficiency of the $p \to \bar{\nu}K^+$ mode. Based on this distribution the proton decay signal region is defined as $4 < N_\gamma < 30$ hits for the baseline design and $8 < N_\gamma < 120$ for the alternate design.

Accordingly, the signal efficiency for the prompt γ tag method to search for $p \to \bar{\nu}K^+$ increases from 6.7% in the baseline study above to 12.7% in the alternate configuration. Though not detailed here, improved tagging of the π^+ from the $K \to \pi^+\pi^0$ component of this search yields 10.2% signal efficiency in the alternate design compared to 6.7% in the baseline analysis. As in the $p \to e^+\pi^0$ study above, if neutron tagging with 70% efficiency is assumed (c.f. figure 149) the background to these $p \to \bar{\nu}K^+$ search methods can be reduced to 0.87 and 0.71 events/Mton·year, respectively. For comparison the background rates for the baseline study are 2.8 and 3.4 events/Mton·year.

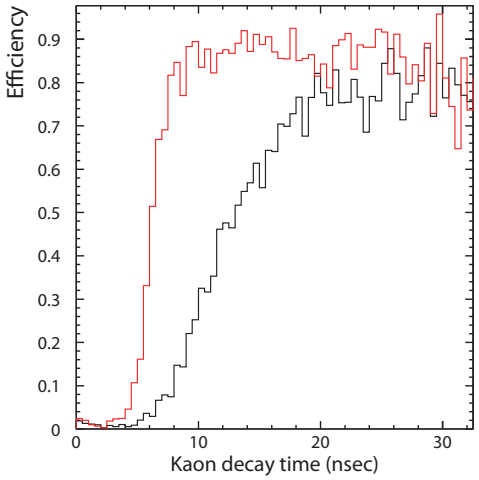

FIG. 151. Prompt γ tagging efficiency as a function of the K^+ decay time for the $p \to \bar{\nu}K^+$ decay mode. The Hyper-K baseline design is shown in black and an alternative design with 40% photocathode coverage and photosensors with 1.9 times higher photon yield is shown in red.

Figure 152 shows the corresponding sensitivity curves for both the baseline (black) and alternate (red) designs. Two vertical lines at exposures of 1.9 and 5.6 Mton·year in the figure denote positions of comparable sensitivity between the two designs. The alternative design achieves this sensitivity with only $1/3^{rd}$ the exposure of the baseline configuration.

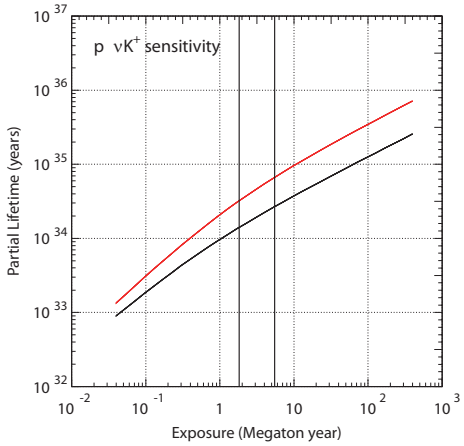

FIG. 152. Sensitivity to $p \to \bar{\nu}K^+$ at 90% C.L. for the 40% photocathode coverage and improved photosensors (see text for details) is shown in red. The black curve shows the corresponding sensitivity from the baseline design study.

It should be noted that since backgrounds for the Super-K neutron tagging algorithm are taken from its data, it is difficult to provide a realistic estimate of the potential of a similar algorithm

at Hyper-K. However assuming similar performance, Hyper-K's dramatic improvement in proton decay sensitivity makes this topic among the most fundamental to the development of it future program. It is clear that the potential for a revolutionary discovery is connected to Hyper-K's background reduction and efficiency enhancement capabilities, both of which are realizable with higher photon yields.

III.3. NEUTRINO ASTROPHYSICS AND GEOPHYSICS

A. Supernova

1. *Supernova burst neutrinos*

Core collapse supernova explosions are the last process in the evolution of massive ($> 8\mathrm{M_{sun}}$) stars. Working their way successively through periods of predominantly hydrogen fusion, helium fusion, and so on, eventually silicon fusion starts making iron. Once an iron core has formed, no more energy can be released via its fusion into still-heavier elements, and the hydrodynamic balance between gravity and stellar burning is finally and catastrophically disrupted. The sudden gravitational collapse of their iron cores – each one of which then goes on to form either a neutron star or a black hole – is the main source of energy from this type of supernova explosion. The energy released by a supernova is estimated to be $\sim 3 \times 10^{53}$ ergs, making it one of the most energetic phenomena in the universe. Since neutrinos interact weakly with matter, almost 99% of the released energy from the exploding star is carried out by neutrinos. As a result, the detection of supernova neutrinos gives direct information of energy flow during the explosion. The neutrino emission from a core collapse supernova starts with a short ($\sim$10 millisecond) burst phase of electron captures ($p + e^- \to n + \nu_e$) called the neutronization burst, which releases about 10^{51} ergs. Following that, the majority of the burst energy is released by an accretion phase ($<\sim$1 second) and a cooling phase (several seconds) in which all three types of neutrinos (including anti-neutrinos) are emitted.

The observation of a handful (25 in total) of supernova burst neutrinos from SN1987a by the Kamiokande, IMB, and Baksan experiments proved that the basic scenario of the supernova explosion was correct. However, more than three decades later the detailed mechanism of explosions is still not known. Several groups have been trying to achieve the necessary conditions for supernova explosion in computer simulations for a long time. Recently, some successes of supernova explosion in two-dimensional and three-dimensional simulations are reported. The details will be described later. Though several models are providing successful supernova explosion in computer simulation, it is necessary to detect many more supernova neutrinos to understand supernova explosions. If a supernova explosion occurs halfway across our galaxy, the Hyper-Kamiokande detector would detect approximately 52,000$\sim$79,000 neutrino events per tank. Hyper-K can also provide information for neutrinos with energy down to $\sim$3 MeV and determine their direction. The analysis threshold for supernova neutrino can be lower than other low energy neutrino analyses, such as solar neutrino. This is because supernova burst neutrinos are localized in the short time period. We can neglect the

low energy radioactive backgrounds, which limit the other analyses. Compared with the current or planned experiments, *e.g.* Super-K, an ice Cherenkov detectors like IceCube/PINGU[47] and a large liquid Ar TPC detector like DUNE, Hyper-K have several advantages on the supernova measurement. The first advantage is the volume and the large statistics. Hyper-K will have a FV of 8 times to 16 times larger than the Super-K detector, resulting in a commensurate increase in the number of detected supernova neutrinos and sensitivity to supernovae occurring in nearby galaxies. Likewise, Hyper-K will be significantly larger than currently planned large LArTPCs with mass in the tens of kt scale. For LArTPCs, the lack of free protons also means that the inverse beta reaction ($\bar{\nu}_e + p \rightarrow e^+ + n$), the most significant channel at Hyper-K, will not be observed. In comparison to large neutrino telescopes like IceCube/PINGU, Hyper-K will have a much lower energy threshold of $\sim$3 MeV , compared to 15 MeV threshold of IceCube/PINGU. Our precise measurement below 15 MeV will be essential for the comprehensive study of supernova neutrinos, especially including the energy spectrum structure below its peak (Fig. 153). With these advantages, the measurement with Hyper-K should at last reveal the detailed mechanism of supernova explosions.
The number of supernova neutrino events detected with Hyper-Kamiokande depends on the volume. In this section, we first discuss several supernova physics topics with the 2 tank configuration (latter 4 years), and then summarize with a comparison to the 1 tank (first 6 years).

Supernova neutrinos also give us an opportunity to investigate unknown properties of neutrinos. Because of their high number density at the supernova core, neutrino-neutrino self-interaction is not negligible. As described later in this section, the neutrino mass hierarchy could be determined using the time variation of the energy spectrum. The very short rise time of the outbreak of the burst enables Hyper-K to be sensitive to absolute neutrino masses. Also, a detection of neutrinos from distant sources gives us a chance to check the lifetime of neutrinos. Indeed, by far the oldest neutrinos from known sources ever seen are those of SN1987a. They were about 170,000 years old when they arrived, while the next oldest would be the solar neutrinos, seen on Earth a mere eight minutes after their birth in the heart of the Sun.

Taking into account the Mikheyev-Smirnov-Wolfenstein (MSW) matter effect through the stellar medium, the flux of each neutrino type emitted from a supernova is related to the originally produced fluxes ($F^0_{\nu_e}$, $F^0_{\bar{\nu}_e}$ and $F^0_{\nu_x}$, where ν_x is $\nu_{\mu,\tau}$ and $\bar{\nu}_{\mu,\tau}$) by the following formulas [217, 218] :

For normal hierarchy,

$$
\begin{aligned}
F_{\bar{\nu}_e} &\simeq \cos^2\theta_{12} F^0_{\bar{\nu}_e} + \sin^2\theta_{12} F^0_{\nu_x} \ , \\
F_{\nu_e} &\simeq \sin^2\theta_{12} P_H F^0_{\nu_e} + (1-\sin^2\theta_{12} P_H) F^0_{\nu_x}, \\
F_{\nu_\mu} + F_{\nu_\tau} &\simeq (1-\sin^2\theta_{12} P_H) F^0_{\nu_e} + (1+\sin^2\theta_{12} P_H) F^0_{\nu_x}, \\
F_{\bar{\nu}_\mu} + F_{\bar{\nu}_\tau} &\simeq (1-\cos^2\theta_{12}) F^0_{\bar{\nu}_e} + (1+\cos^2\theta_{12}) F^0_{\nu_x},
\end{aligned}
$$

and, for inverted hierarchy,

$$
\begin{aligned}
F_{\bar{\nu}_e} &\simeq \cos^2\theta_{12} P_H F^0_{\bar{\nu}_e} + (1-\cos^2\theta_{12} P_H) F^0_{\nu_x} \ , \\
F_{\nu_e} &\simeq \sin^2\theta_{12} F^0_{\nu_e} + \cos^2\theta_{12} F^0_{\nu_x}, \\
F_{\nu_\mu} + F_{\nu_\tau} &\simeq (1-\sin^2\theta_{12}) F^0_{\nu_e} + (1+\sin^2\theta_{12}) F^0_{\nu_x}, \\
F_{\bar{\nu}_\mu} + F_{\bar{\nu}_\tau} &\simeq (1-\cos^2\theta_{12} P_H) F^0_{\bar{\nu}_e} + (1+\sin^2\theta_{12} P_H) F^0_{\nu_x},
\end{aligned}
$$

where P_H is the crossing probability through the matter resonant layer corresponding to Δm^2_{32}. $P_H = 0 (P_H = 1)$ for adiabatic (non-adiabatic) transition. For $\sin^2 2\theta_{13} > 10^{-3}$, adiabatic transition is expected for the matter transition in the supernova envelope. The supernova neutrino spectrum is affected not only by stellar matter but also by other neutrinos and anti-neutrinos at the high density core (so-called collective effects). These collective effects, which swap the ν_e and $\bar{\nu}_e$ spectra with those of ν_x in certain energy intervals bounded by sharp spectral splits, were first discussed in [219, 220]. This has become an active field of study whose recent investigations include taking into account the possibility of multiple splits[221], computation with three neutrino flavors[222], and utilizing the full multi-angle framework[223]. The combination of the collective effects and the stellar matter effects might weaken swapping the energy spectra of $\nu_e/\bar{\nu}_e$ and ν_x. So, in the following description of the performance of the Hyper-Kamiokande detector, three cases are considered in order to fully cover the possible variation of expectations: (1) no oscillations, (2) normal hierarchy with $P_H = 0$, and (3) inverted hierarchy with $P_H = 0$. The process depends critically on θ_{12}; in what follows we assume $\sin^2\theta_{12} = 0.31$. Concerning the neutrino fluxes and energy spectra at the production site, we used results obtained by the Livermore simulation [224].

Figure 153 shows time profiles for various interactions expected at the Hyper-Kamiokande detector for a supernova at a distance of 10 kiloparsecs (kpc). This distance is a bit farther than the center of the Milky Way galaxy at 8.5 kpc; it is chosen as being representative of what we might expect since a volume with a radius of 10 kpc centered at Earth includes about half the stars in the galaxy. The three graphs in the figure show the cases of no oscillation, normal hierarchy (N.H.)

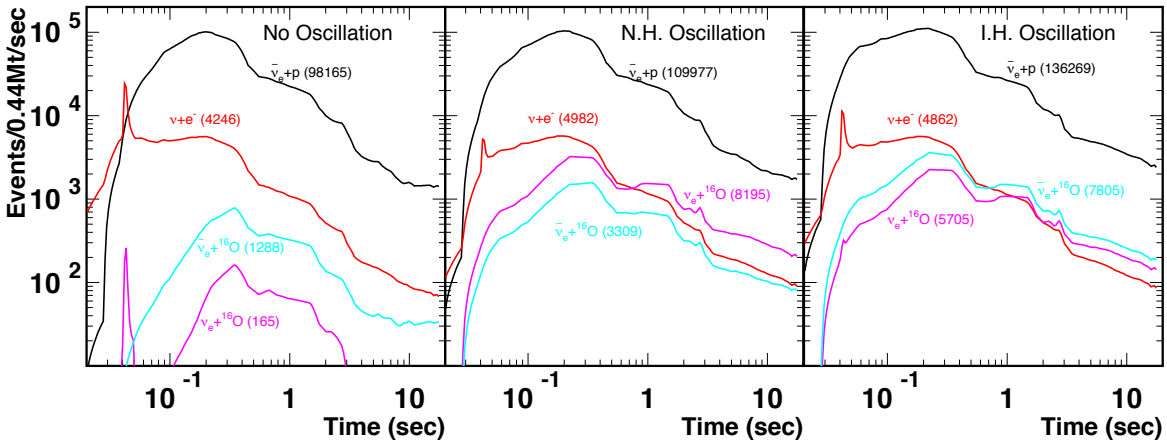

FIG. 153. Expected time profile of a supernova at 10 kpc with 2 tanks. Left, center, and right figures show profiles for no oscillation, normal hierarchy (N.H.), and inverted hierarchy (I.H.), respectively. Black, red, purple, and light blue curves show event rates for interactions of inverse beta ($\bar{\nu}_e + p \to e^+ + n$), νe-scattering($\nu + e^- \to \nu + e^-$), ν_e ^{16}O CC($\nu_e + {}^{16}\mathrm{O} \to e^- + {}^{16}\mathrm{F}^{(*)}$), and $\bar{\nu}_e$ ^{16}O CC ($\bar{\nu}_e + {}^{16}\mathrm{O} \to e^+ + {}^{16}\mathrm{N}^{(*)}$), respectively. The numbers in parentheses are integrated number of events over the burst. The fluxes and energy spectra are from the Livermore simulation [224]

and inverted hierarchy (I.H.), respectively. Colored curves in the figure show event rates for inverse beta ($\bar{\nu}_e + p \to e^+ + n$), νe-scattering($\nu + e^- \to \nu + e^-$), ν_e+^{16}O CC($\nu_e + {}^{16}\mathrm{O} \to e^- + {}^{16}\mathrm{F}^{(*)}$), and $\bar{\nu}_e$+^{16}O CC ($\bar{\nu}_e + {}^{16}\mathrm{O} \to e^+ + {}^{16}\mathrm{N}^{(*)}$). The burst time period is about 10 s and the peak event rate of inverse beta events reaches about 100 kHz. A sharp timing spike is expected for νe-scattering events at the time of neutronization, which will be discussed in more detail later. Visible energy distributions of each interaction are shown in Fig. 154, where the visible energy is the electron-equivalent energy measured by a Cherenkov detector. The distribution of inverse beta events directly gives the energy spectrum of $\bar{\nu}_e$ because the energy of the positrons (E_{e^+}) is simply $E_\nu - 1.3$ MeV. The energy spectrum of νe-scattering events has enhancement at lower energies because of the nature of the interaction.

Figure 155 shows the expected number of supernova neutrino events at Hyper-K versus the distance to a supernova. At the Hyper-Kamiokande detector, we expect to see about 98,000∼136,000 inverse beta events, 4,200∼5,000 νe-scattering events, 160∼8,200 ν_e+^{16}O CC events, and 1,300∼7,800 $\bar{\nu}_e$ + ^{16}O CC events, in total 104,000∼158,000 events, for a 10 kpc supernova. The range of each of these numbers covers possible variations due to the neutrino oscillation scenario (no oscillation, N.H., or I.H.). Even for a supernova at M31 (Andromeda Galaxy), about 17∼26 events are expected at Hyper-K. In the case of the Large Magellanic Cloud (LMC) where

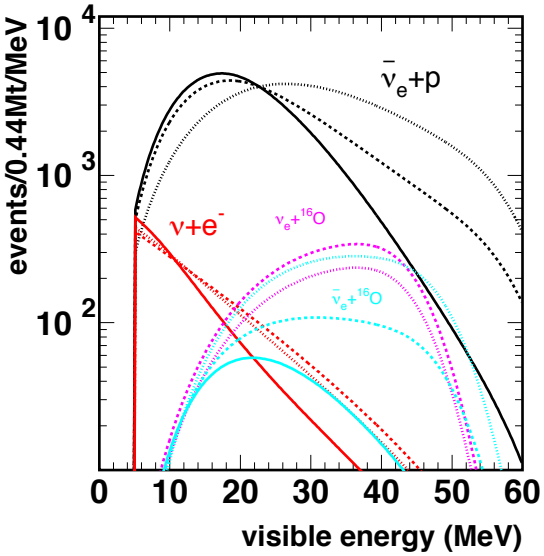

FIG. 154. Visible energy spectrum for each interaction for a supernova at 10 kpc with 2 tanks. Black, red, purple, and light blue curves show event rates for interactions of inverse beta, νe-scattering, ν_e+^{16}O CC, and $\bar{\nu}_e$+^{16}O CC, respectively. Solid, dashed, and dotted curves correspond to no oscillation, N.H., and I.H., respectively.

SN1987a was located, about 4,200∼6,300 events are expected.

From the recent computer simulation studies, new characteristic modulations of the supernova neutrino flux are proposed. These modulations are due to the motions like convection in supernovae, the key feature of successful explosions in the simulations. Such modulations of neutrino flux can be detected as a variance of the event rate in Hyper-K. One source of such modulation is Standing Accretion Shock Instability (SASI)[227][228][225]. Figure 156 shows the detection rate modulation in Hyper-K, induced by SASI. The modulation can be observed as a variance of ∼ 10% of the number of supernova events in Hyper-K detector [225]. This flux variance caused by SASI has a characteristic peak in the frequency space. The large statistics can prove the existence of SASI by performing frequency analysis.

Another source is the rotation of supernova[229][226]. The size of variation depends on the angle between the direction of earth and the rotational axis of supernova. When the supernova rotational axis is orthogonal with the direction to the earth, the detectable variance will be the maximum. In that case, Hyper-K will detect a variance of ∼50% in the number of observed signals. The observation of these modulation with Hyper-K will be good test of such simulations and also provide important information for understanding the dynamics in supernovae.

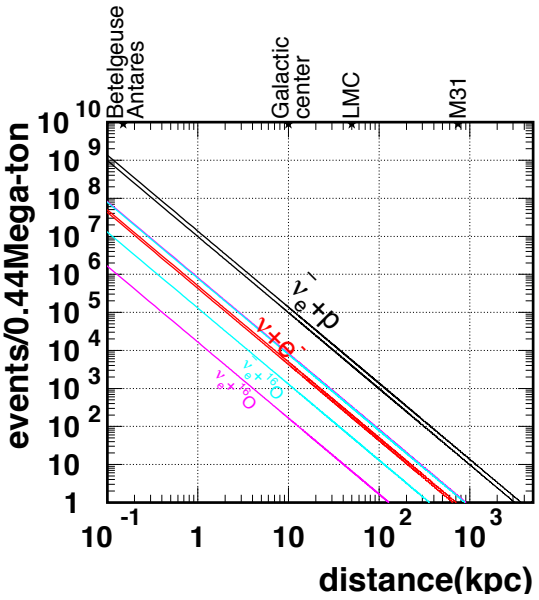

FIG. 155. Expected number of supernova burst events for each interaction as a function of the distance to a supernova with 2 tank. The band of each line shows the possible variation due to the assumption of neutrino oscillations.

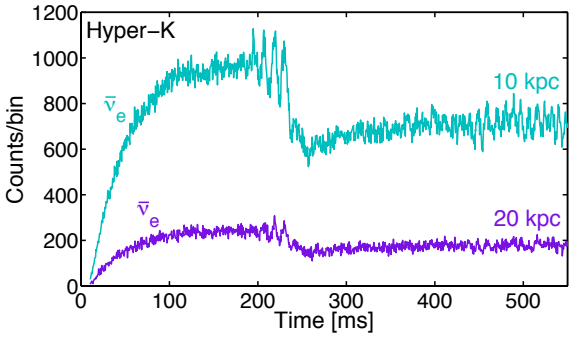

FIG. 156. Detection rate modulation induced by SASI in 5 ms bins (0.56 Mt). The SN progenitor mass is 27 solar mass. The direction to the detector is chosen for strong signal modulation. This figure is adopted from [225].

The observation of supernova burst neutrino and the directional information can be the preceding alarm for other observation experiments, e.g. optical and x-ray telescopes. It will give us the chance to understand whole process of supernova burst by integrating this information. Figure 158 shows expected angular distributions with respect to the direction of the supernova for four visible energy ranges. The inverse beta events have a nearly isotropic angular distribution. On the other hand, νe-scattering events have a strong peak in the direction coming from the supernova. Since the visible energy of νe-scattering events are lower than the inverse beta events, the angular distributions for lower energy events show more enhanced peaks. The direction of a

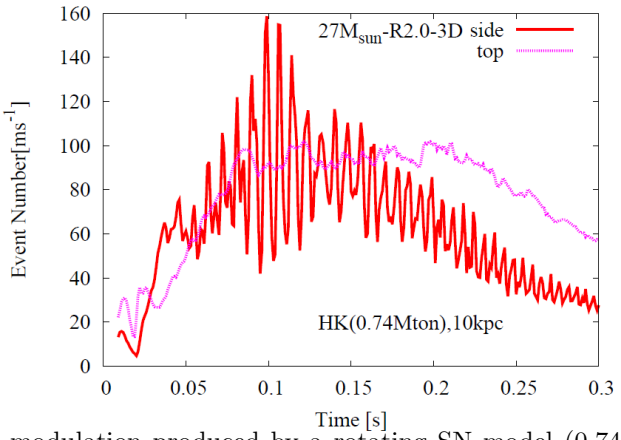

FIG. 157. Detection rate modulation produced by a rotating SN model (0.74 Mt). The SN progenitor mass is 27 solar mass. The supernova rotational axis is orthogonal (red) and parallel (magenta) with the direction to the earth. This figure is adopted from [226].

supernova at 10 kpc can be reconstructed with an accuracy of about two degrees according to these angular distributions.

In Hyper-K, we can statistically extract an energy distribution of $\nu_e + \nu_X (X = \mu, \tau)$ events using the angular distributions in much the same way as solar neutrino signals are separated from background in Super-K. Although the effect of neutrino oscillations must be taken into account, the $\nu_e + \nu_X$ spectrum gives another handle on the temperature of neutrinos. Note that inverse beta events directly provide a very precise measurement of the temperature of $\bar{\nu}_e$. Hyper-K will be able to evaluate the temperature difference between $\bar{\nu}_e$ and $\nu_e + \nu_X$. This would be a valuable input to model builders. Figure 159 shows inverse beta event rates and mean $\bar{\nu}_e$ energy distributions predicted by various models [224, 230–233] for the first 0.3 sec after the onset of a burst. The statistical error of Hyper-K is much smaller than the difference between the models, and so Hyper-K should give crucial data for comparing model predictions. The left plot in Fig. 159 shows that about 300-1000 events are expected in the first 20 millisecond bin. This means that the onset time can be determined with an accuracy of about 1 ms. This is precise enough to allow examination of the infall of the core in conjunction with the signals of neutronization (see below) as well as possible data from future gravitational wave detectors.

We can also use the sharp rise of the burst to make a measurement of the absolute mass of neutrinos. Because of the finite mass of neutrinos, their arrival times will depend on their energies. This relation is expressed as

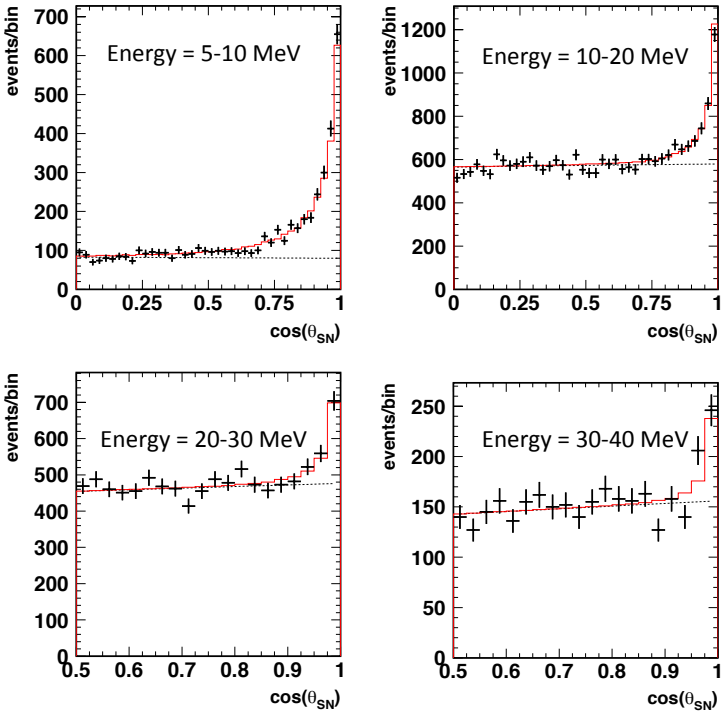

FIG. 158. Angular distributions of a simulation of a 10 kpc supernova with 2 tanks. The plots show a visible energy range of 5-10 MeV (left-top), 10-20 MeV (right-top), 20-30 MeV (left-bottom), and 30-40 MeV (right-bottom). The black dotted line and the red solid histogram (above the black dotted line) are fitted contributions of inverse beta and νe-scattering events. Concerning the neutrino oscillation scenario, the *no oscillation* case is shown here.

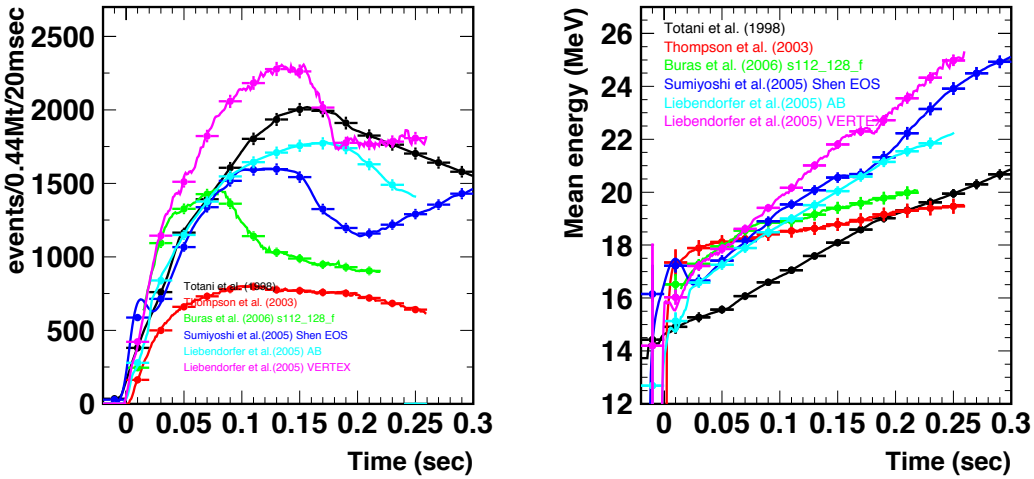

FIG. 159. Inverse beta event rate (left) and mean energy of $\bar{\nu}_e$ (right) predicted by supernova simulations [224, 230–233] for the first 0.3 seconds after the onset of a 10 kpc distant burst. (2 tanks)

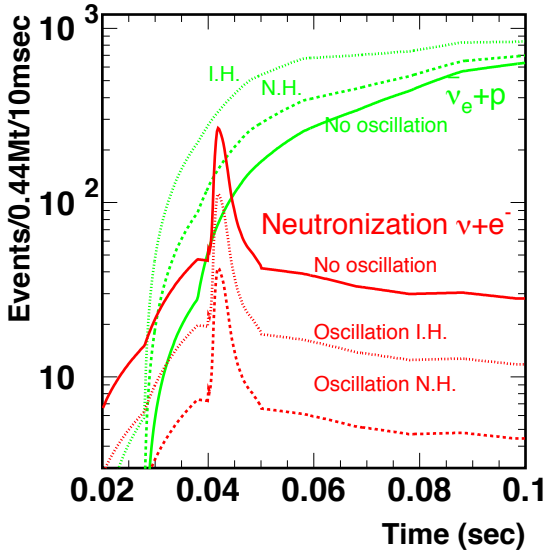

FIG. 160. Expected event rate at the time of neutronization burst for a supernova at 10 kpc with 2 tanks. Red and green show event rates for νe-scattering events originated with neutronization neutrino and inverse beta events, respectively. Solid, dotted, and dashed curved indicate the neutrino oscillation scenarios of no oscillation, N.H., and I.H., respectively.

$$\Delta t = 5.15 \text{ msec}(\frac{D}{10 \text{ kpc}})(\frac{m}{1 \text{ eV}})^2(\frac{E_\nu}{10 \text{ MeV}})^{-2} \tag{24}$$

where Δt is the time delay with respect to that assuming zero neutrino mass, D is the distance to the supernova, m is the absolute mass of a neutrino, and E_ν is the neutrino energy. Totani [234] discussed Super-Kamiokande's sensitivity to neutrino mass using the energy dependence of the rise time; scaling these results to the much larger statistics provided by Hyper-K, we expect a sensitivity of 0.5∼1.3 eV for the absolute neutrino mass [235]. Note that this measurement of the absolute neutrino mass does not depend on whether the neutrino is a Dirac or Majorana particle.

We expect ∼12, ∼33 and ∼80 νe-scattering events in the neutronization burst peak for a supernova at 10 kpc as seen in Fig. 160, for N.H., I.H., and no oscillation respectively. Although the number of inverse beta events is ∼200 (N.H.), ∼410 (I.H.), and ∼100 (no oscillation) in the 10 ms bin of the neutronization burst, the number of events in the direction of the supernova is typically 1/10 of the total events. So, the ratio of signal events (νe-scattering) to other events (inverse beta) is expected to be about 12/20 (N.H.), 33/41 (I.H.) and 80/10 (no oscillation). Thus, the νe-scattering events can be identified with high statistical significance thanks to the directionality of νe-scattering.

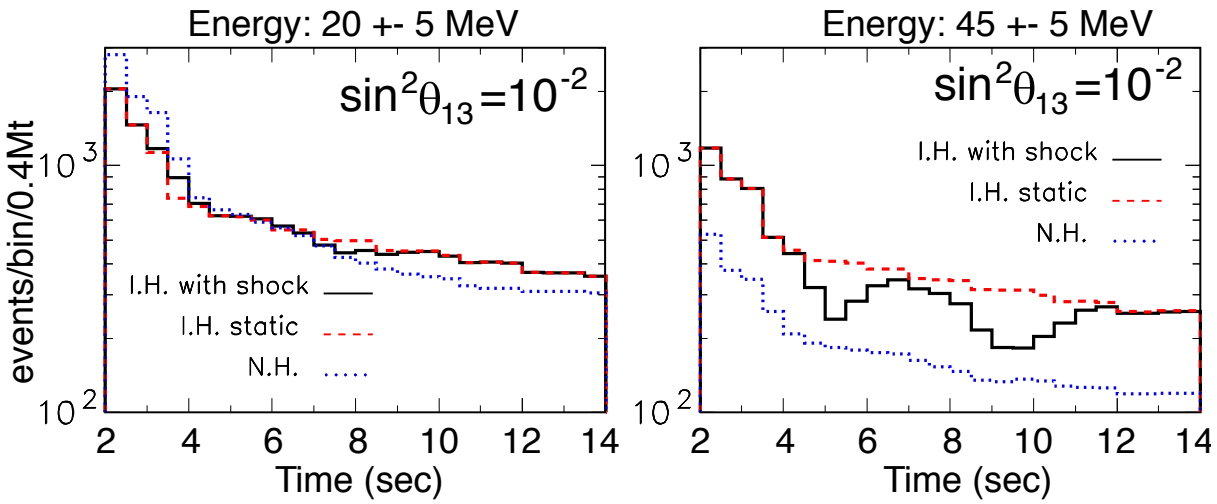

FIG. 161. Time variation of the neutrino event rate affected by neutrino conversion by matter due to shock wave propagation with 2 tanks (reproduced from [218]). Left (right) plot shows the time variation of inverse beta events for the energy range of 20±5 MeV (45±5 MeV). Solid black, dashed red, and blue dotted histograms show the event rates for I.H. with shock wave propagation, I.H. with static matter density profile, and N.H., respectively. It has been assumed that $\sin^2\theta_{13} = 10^{-2}$.

Neutrino oscillations could be studied using supernova neutrino events. There are many papers which discuss the possibility of extracting signatures of neutrino oscillations free from uncertainties of supernova models [218, 236–244]. One big advantage of supernova neutrinos over other neutrino sources (solar, atmospheric, accelerator neutrinos) is that they inevitably pass through very high density matter on their way to the detector. This gives a sizable effect in the time variation of the energy spectrum [218, 237, 245]. As an example is shown as the Figure 161[218]. The propagation of the supernova shock wave causes time variations in the matter density profile through which the neutrinos must travel. Because of neutrino conversion by matter, there may be a bump in the time variation of the inverse beta event rate for a particular energy range (*i.e.*, 45±5 MeV as shown in Fig. 161(right)) while no change is observed in the event rate near the spectrum peak (*i.e.*, 20±5 MeV as shown in Fig. 161(left)). This effect is observed only in the case of inverted mass hierarchy; this is one way in which the mass hierarchy could be determined by a supernova burst.

In Hyper-K, it could be possible to detect burst neutrinos from supernovae in nearby galaxies. As described above, we expect to observe a very large number of neutrino events from a galactic supernova. However, galactic supernovae are expected to happen once per 30-50 years. So, we cannot count on seeing many galactic supernova bursts. In order to examine a variety of supernova bursts, supernovae from nearby galaxies are useful even though the expected number of detected

events from any single such burst is small. Furthermore, in order to fully understand the spectrum of supernova relic neutrinos (see next sub-section), collecting an energy spectrum without the complications of varying red-shift effects is highly desirable. The supernova events from nearby galaxies provide a reference energy spectrum for this purpose. The supernovae in nearby galaxies was discussed in [64] and a figure from the paper is shown in Fig. 162(left). It shows the cumulative supernova rate versus distance and indicates that if Hyper-K can see signals out to 4 Mpc then we could expect a supernova about every three years. It should also be noted that the authors indicate that recent, more sensitive astronomical observations indicate that the true nearby supernova rates are probably about 3 times higher than this conservative calculation [246]. The observation of supernovae at nearby galaxy will provide the chance to prove the strange supernovae, such as dim supernovae [246]. Figure 162(right) shows detection probability versus distance for the Hyper-K detector. In this estimate, the neutrino energy is required to be greater than 10 MeV and assumes a 370 kt fiducial volume corresponding to the 2 tank configuration. If we require the number of events to be more than or equal to one(two), the detection probability is 40∼57%(10∼18%) for a supernova at 4 Mpc. If we can use a tight timing coincidence with other types of supernova sensors (e.g. gravitational wave detectors), we should be able to identify even single supernova neutrinos. Requiring the number of events to be more than or equal to one(two), we expect to observe 1.3-8.1 (0.2-3.3) supernovae in nearby galaxies during 20 years of operating Hyper-K.

Finally, the expected number of supernova neutrino events in the Hyper-Kamiokande detector is summarized in Table XLIV. In general, the number of detected neutrino events depends on the detector volume. The first 6 years with 1 tank, we will have half of neutrino events comparing with latter 4 years with 2 tanks. In both cases, it is still possible to detect large number of events for the supernovae in our galaxy, except for the neutronization burst. These events will be enough to provide detailed information about the time profile and the energy spectrum for inspecting supernova explosion mechanism. Those will also provide an opportunity for further physics topics, *i.e.* the neutrino mass, the mass hierarchy and the neutrino oscillations in the supernova. The better energy resolution of high photocoverage will help these analysis. The lower energy threshold will also help to understand the whole picture of supernova explosion. The detection of supernovae in nearby galaxies will be difficult with a single tank, because of the lower number of events. For a supernova at 4 Mpc with a single tank, the detection probability will be 22∼33% (3∼6%) if one (two) or more detected neutrinos is required. For a supernova at 2 Mpc, where we expect one supernova per 10 years, we still have the detection probability of 64∼80% (27∼47%).

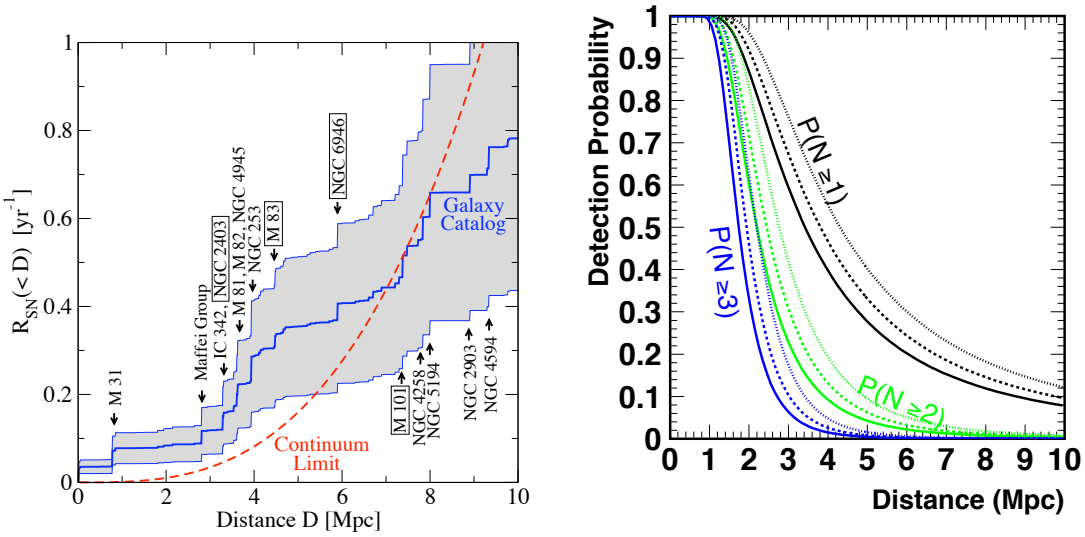

FIG. 162. (Left) Cumulative calculated supernova rate versus distance for supernovae in nearby galaxies. The dashed line is core-collapse supernova rate expectation, using the $z = 0$ limit of star formation rate measured by GALEX. The figure is reproduced from ref. [64]. (Right) Detection probability of supernova neutrinos versus distance at Hyper-K assuming a 370 kiloton fiducial volume and 10 MeV threshold for this analysis. Black, green, and blue curves show the detection efficiency resulting in requiring at least or equal to one, two, and three events per burst, respectively. Solid, dotted, and dashed curves are for neutrino oscillation scenarios of no oscillation, N.H., and I.H., respectively.

TABLE XLIV. Summary table of expected supernova neutrino events in the Hyper-Kamiokande detector. A supernova at Galactic center (10 kpc) is assumed.

Neutrino source	2TankHD (440 kt Full Volume)	1TankHD (220 kt Full Volume)
$\bar{\nu}_e + p$	98,000∼136,000 events	49,000∼68,000 events
$\nu_e + e^-$	4,200∼5,000 events	2,100∼2,500 events
$\nu_e + ^{16}O$ CC	160∼8,200 events	80∼4,100 events
$\bar{\nu}_e + ^{16}O$ CC	1,300∼7,800 events	650∼3,900 events
$\nu_e + e^-$ (Neutronization)	12∼80 events	6∼40 events
Total	104,000∼158,000 events	52,000∼79,000 events

2. *Early Supernovae*

Core-collapse supernovae are promising sources of high-energy neutrinos as well as multi-MeV neutrinos. The supernova shock propagates in the stellar material and experiences a shock breakout, which can be observed at ultraviolet or X-ray wavelengths. Before the shock breakout, the supernova shock is mediated by radiation since the photon diffusion time is longer than the expansion time. During this time, the conventional cosmic-ray (CR) acceleration is inefficient, so

associated neutrino production is not promising. However, as the shock becomes collisionless after the breakout, the CR acceleration starts to be effective [247, 248]. The situation is expected to be analogous to supernova remnants, which are almost established as CR accelerators and widely believed as the origin of Galactic CRs.

In the early phase just after the breakout, the matter density is still high, so that accelerated CRs are efficiently used for neutrino production. For type II supernovae, which are associated with red super-giants, one may expect the released energy of high-energy neutrinos to be $\mathcal{E}_{CR} \sim 10^{46}$-$10^{47}$ erg [247], emitted hours after the core collapse. We expect ∼1-10 events of GeV-TeV neutrinos for a Galactic supernova at 10 kpc, with the two tank configuration.

About 10% of core-collapse supernovae show strong interactions with ambient circumstellar material, which are often called interaction-powered supernovae. If the circumstellar material mass is ~ 0.1-$1\ M_\odot$, the released high-energy neutrino energy reaches $\mathcal{E}_\nu \sim 10^{49}$-$10^{50}$ erg [248]. For example, Eta Carinae at 2.3 kpc is an interesting candidate that showed violent mass eruptions in the past. If a real supernova occurs and the ejecta collides with the circumstellar material shell with $\sim 10\ M_\odot$, one may expect ~ 1000 events with Hyper-K. However, because of the long duration (from months to years), the signal can overwhelm the background only at early times and sufficiently high energies.

High-energy neutrinos from supernovae are detectable hours to months after the core-collapse, and detecting the signals will give us new insights into supernova physics, such as how collisionless shocks are formed and CR acceleration starts, as well as the connection to supernova remnants as the origin of Galactic CRs. We may be able to see the time evolution of multi-energy neutrino emission from the core-collapse to shock breakout and following interactions with the circumstellar material.

3. Supernova relic neutrinos

There are about 10^{20} stars in the universe (∼10^{10} galaxies in the universe, and each galaxy has about 10^{10} stars). Because about 0.3% of the stars have masses larger than 8 times the solar mass, it is estimated that 10^{17} supernova explosions have occurred over the entire history of the universe. This means that on average one supernova explosion has been occurring every second somewhere in the universe. The neutrinos produced by all of the supernova explosions since the beginning of the universe are called supernova relic neutrinos (SRN). They must fill the present universe and their flux is estimated to be a few tens/cm^2/sec. If we can detect these neutrinos, it is possible

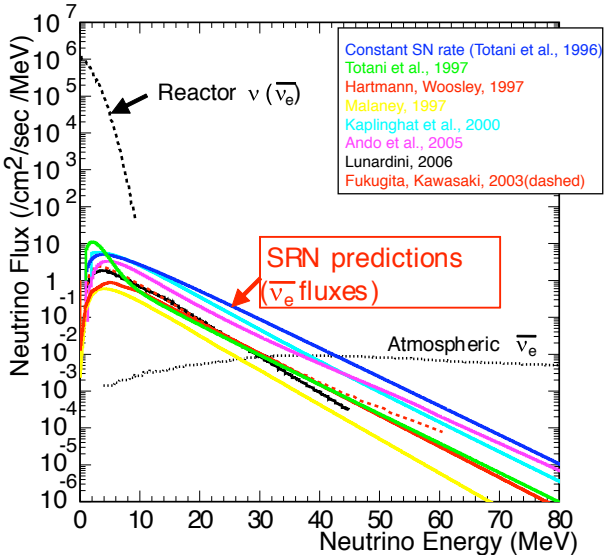

FIG. 163. Predictions of the supernova relic neutrino (SRN) spectrum. Fluxes of reactor neutrinos and atmospheric neutrinos are also shown.

to explore the history of how heavy elements have been synthesized since the onset of stellar formation. Figure 163 shows the SRN spectra predicted by various models. Although searches for SRN have been conducted at large underground detectors, no evidence of SRN signals has yet been obtained because of the small flux of SRN. The expected inverse beta ($\bar{\nu}_e p \rightarrow e^+ n$) event rate at Super-Kamiokande is 0.8-5 events/year above 10 MeV, but because of the large number of spallation products and the low energy atmospheric neutrino background (decay electrons from muons below Cherenkov threshold produced by atmospheric muon neutrinos, the so-called invisible muon background), SRN signals have not yet been observed at Super-Kamiokande. In order to reduce background, lower the energy threshold, individually identify true inverse beta events by tagging their neutrons, and thereby positively detect SRN signals at Super-Kamiokande, a project to add 0.1% gadolinium (Gd) to tank (the SK-Gd project, called GADZOOKS! project previously) was proposed by J.F. Beacom and M.R. Vagins [249]; very active R&D works for the project is ongoing.

The first observation of the SRN could be made by the SK-Gd project, but in order to measure the spectrum of the SRN and analyze the history of the universe we need a megaton-scale detector. At Hyper-K, we could measure the SRN neutrinos at E = 20∼30 MeV, while SK-Gd project concentrate on the energy of 10∼20 MeV. These measurement at different energy region can measure the contribution of extraordinary supernova bursts on the SRN, e.g. black hole formation [250][251].

Figure 164 shows expected SRN signals at Hyper-K with 10 years' livetime without tagging neu-

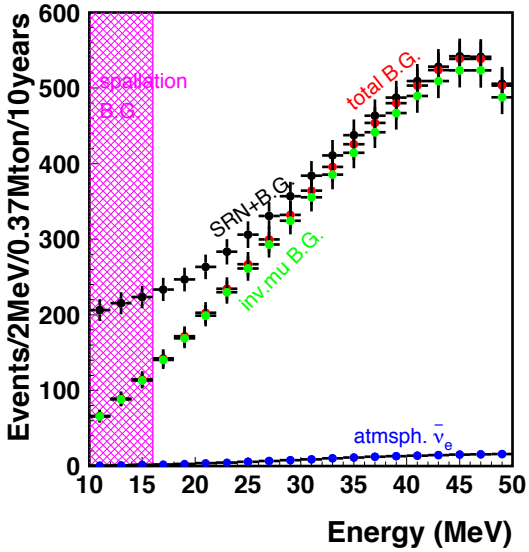

FIG. 164. Expected spectrum of SRN signals at Hyper-K with 10 years of livetime without tagging neutrons. The black dots show the sum of the signal and the total background, while the red shows the total background. Green and blue show background contributions from the invisible muon and ν_e components of atmospheric neutrinos. Without tagging neutrons, spallation background dominates below 20 MeV. The SRN flux prediction in [252] is used, and a signal selection efficiency of 90% is assumed.

trons. Because of the high background rate below 20 MeV from spallation products, the detection of SRN signals is limited to above 20 MeV, while above 30 MeV the atmospheric neutrino backgrounds completely overwhelm the signal. Considering the event selection efficiency after spallation product reduction, the expected number of SRN events in E = 16∼30 MeV is about 100 (240) after 10 (20) years with the staging construction scenario. The statistical error will be 20 (32) events, corresponding to an observation of SRN in the energy range 16∼30 MeV with 4.8 (7.5) σ significance (fig. 165). Here, we assumed the flux prediction described in [252] and neutron tagging using $n + p \rightarrow d + \gamma(2.2\,\mathrm{MeV})$ with the tagging efficiency of 70%. With 3TankLD, the number of the SRN events in E = 18.5∼30 MeV will be 210 ± 45 (430 ± 60) and the signal significance will stay 4.7 (6.6) sigma after 10 (20) years observation.

It is still important to measure the SRN spectrum down to ∼ 10 MeV in order to explore the history of supernova bursts back to the epoch of red shift (z) ∼1. Therefore, in the following discussion the expected SRN signal with gadolinium neutron tagging is considered.

Inverse beta reactions can be identified by coincident detection of both positron and delayed neutron signals, and requiring tight spatial and temporal correlations between them. With 0.1% by mass of gadolinium dissolved in the water, neutrons are captured on gadolinium with about

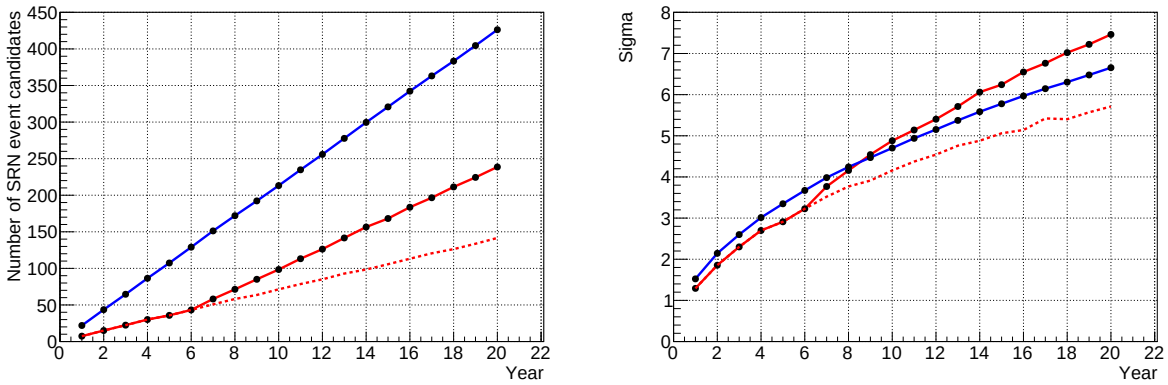

FIG. 165. The left (right) plot shows the number of observed SRN events (the discovery sensitivity) as a function of observation period. Red solid line shows the staging scenario. Red dashed line and blue solid line shows the continuous measurement with 1 tank and 3TankLD, respectively.

90% capture efficiency; the excited Gd nuclei then de-excite by emitting 8 MeV gamma cascades. The time correlation of about 20 μsec between the positron and the Gd(n,γ)Gd cascade signals, and the vertex correlation within about 50 cm are strong indicators of a real inverse beta event. Requiring both correlations (as well as requiring the prompt event to be Cherenkov-like and the delayed event to be isotropic) can be used to reduce background of spallation products by many orders of magnitude while also reducing invisible muon backgrounds by about a factor of 5. Since the 8 MeV gamma cascade of Gd(n,γ)Gd reaction produces multiple gammas, its visible energy is much lower than 8 MeV. This was measured to be 4.3 MeV as shown in Fig. 166(right). In order to reconstruct vertex and energy of such events, about 20% photocoverage is necessary. Figure 167 shows the expected observation of the SRN spectrum in the Hyper-Kamiokande detector. In this plot, a SRN flux prediction[252] was used. A signal detection efficiency of 67% and a reduction factor of 5 for the invisible muon background are also assumed. The expected number of SRN events in the energy range of 10-30 MeV is about 560 (280) with 10 years of live time with 2 tanks (1 tank). These large statistics are sufficient to start discussing the supernova history of the universe. In addition, by comparing the total SRN flux with optical supernova rate observations, a determination of the fraction of failed (optically dark) supernova explosions, currently unknown but thought to occur in not less than 5% and perhaps as many as 50% of all explosions, will be possible.

Possible backgrounds to the SRN search are (1) accidental coincidences, (2) spallation products with accompanying neutrons, and (3) the resolution tail of the reactor neutrinos. For (1) accidental coincidences, the possible source of the prompt event is the spallation products. By requiring

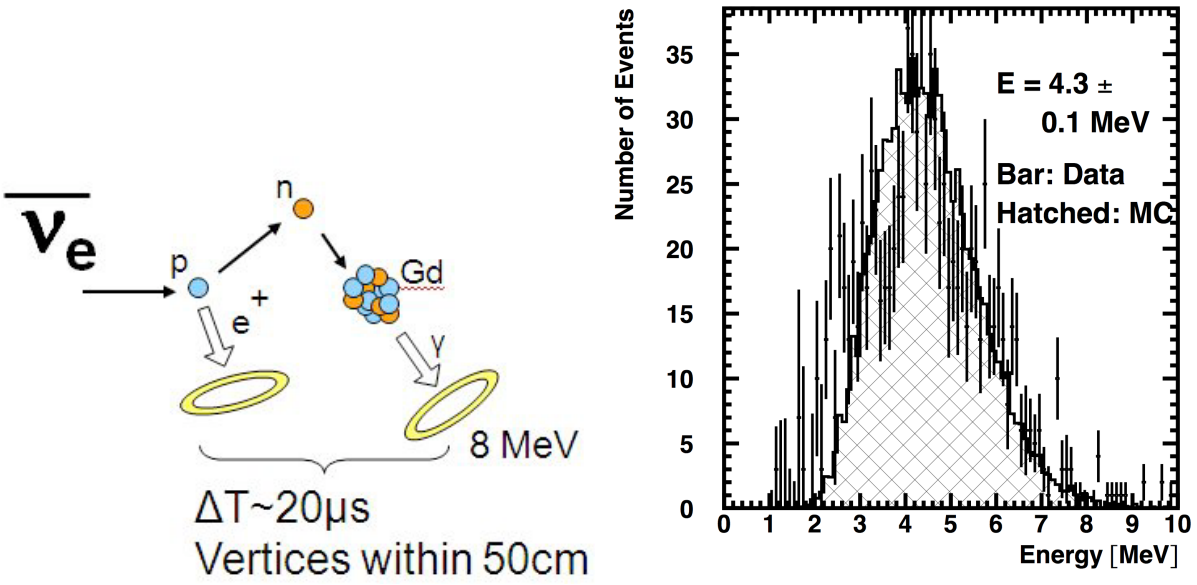

FIG. 166. The left plot shows how to tag neutrons produced by the inverse beta reaction. The right plot shows the electron-equivalent energy spectrum of the gamma cascade, which is emitted from thermal neutron capture reaction on Gd, as measured in the Super-Kamiokande detector [105]. The inverse beta reaction can be identified by detecting the delayed signal corresponding to the right plot.

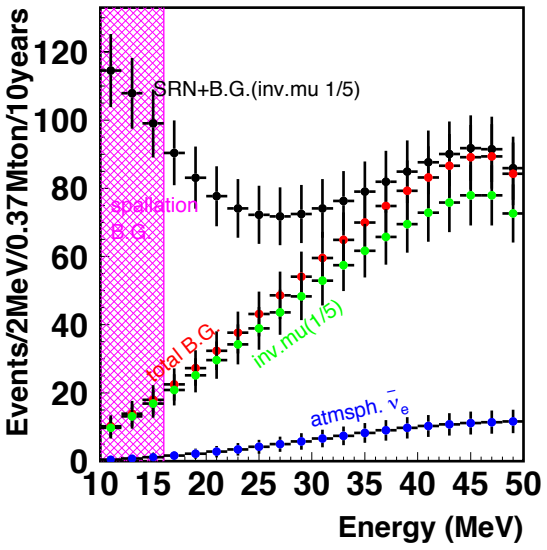

FIG. 167. Expected spectrum of the SRN signals at Hyper-K with 10 years of livetime. The black dots show signal+background (red component). Green and blue show background contributions from the invisible muon and ν_e components of atmospheric neutrinos. A SRN flux prediction[252] was used, and a 67% detection efficiency of 8 MeV gamma cascades and a factor of 5 reduction in the invisible muon background were assumed.

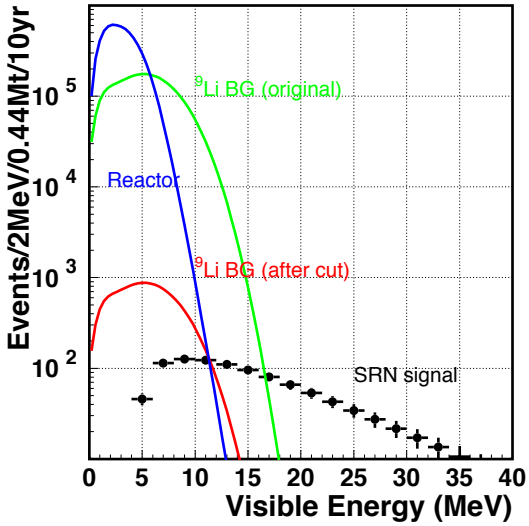

FIG. 168. Green (red) curve shows the estimated ^{9}Li production rate before (after) applying cuts based on a correlation with cosmic ray muons. Blue shows estimated background from reactor neutrinos at full intensity. Black data points show expected SRN signal based on the flux prediction in [252].

time coincidence, vertex correlation and energy and pattern of the delayed event, the accidental coincidence rate can be reduced by a factor about 5 and can be below the level of the expected SRN signal. Recording the radioactivity of PMTs and their protective cases will also improve the situation. For (2) spallation products with accompanying neutrons, the only possible spallation product is ^{9}Li and an estimation by a GEANT4 simulation is shown in Fig. 168. Because of the short half-life of ^{9}Li ($\tau_{\frac{1}{2}} = 0.18$ sec), a high rejection efficiency of $\sim$99.5% is expected. With this expectation, the ^{9}Li background is less than the signal level above 12 MeV; this could be lowered by further development of the background reduction technique.For (3) the resolution tail of the reactor neutrinos, the estimated background rate is about 200(40)/10 years above 10 MeV (11 MeV) as shown in Fig. 168 with full reactor intensity.

B. Dark matter searches

Despite overwhelming evidence for the existence of dark matter in the universe, it has yet to been definitively described or detected in terrestrial experiments. Based on astronomical observations it is known to have gravitational interactions and lacks electromagnetic interactions, but whether or not it carries the weak, strong, or some other interactions remains an open question. Assuming that dark matter is a particle with weak interactions, several direct detection experiments have looked for evidence of so-called WIMP elastic scattering off target nuclei in these detectors. It is thought though that the self-interaction or decay of dark matter particles bound in strong gravitational potentials, such as those of the milky way galaxy itself or even our sun, may produce standard model particles. Either through direct annihilation (decay) into neutrinos or through the decays of heavier particles that include neutrino final states it is possible to observe these neutrino secondaries at Hyper-Kamiokande. In this case the atmospheric neutrino sample described in Section III.1 B becomes an overwhelming background. However, a potential dark matter signal is expected to have an angular distribution peaked sharply near the center of the binding potential, which at Hyper-Kamiokande would manifest as the direction towards the galactic center or the sun. By studying the angular distance to these sources it is possible to extract the dark matter signal since the atmospheric neutrino background is expected to be uniformly distributed in this coordinate. It should be noted that the momentum distribution of the signal is important for extracting the mass of the dark matter candidate producing any observed neutrino event excess.

In the analyses below dark matter is assumed to produce standard model particles such as $\chi\chi \rightarrow W^+W^-$, $\tau^+\tau^-$, $b\bar{b}$, $\mu^+\mu^-$, and $\nu\bar{\nu}$ each with 100% branching fraction. The expected distribution of signal neutrinos is simulated and search for using the same analysis samples described in previous sections. Unlike other indirect detection experiments, such as the neutrino telescopes, Hyper-Kamiokande is expected to have superior sensitivity to lower mass (below 100 GeV/c^2) WIMPS and the ability to resolve a signal with both ν_e and ν_μ components. Hyper-K's expected sensitivity to WIMP annihilation in the galactic center and the sun after a 5.6 Mton· year exposure is resented below.

1. *Search for WIMPS at the Galactic Center*

Dark matter trapped in the gravitational potential of galaxies is said to form a halo. Halo models predict dark matter density distributions that peak sharply near the center of a given galaxy and

drop with radial distance. For example, for the Milky Way galaxy the expected density distribution at the position of our solar system, $r = 8.5$ kpc, is roughly 1000 times smaller than that at the galactic center in the NFW model [253]. When simulating the expected signal distribution expected at Hyper-Kamiokande a diffuse dark matter profile following the full NFW density distribution is assumed and accordingly the signal is expected to arise primarily from the galactic center.

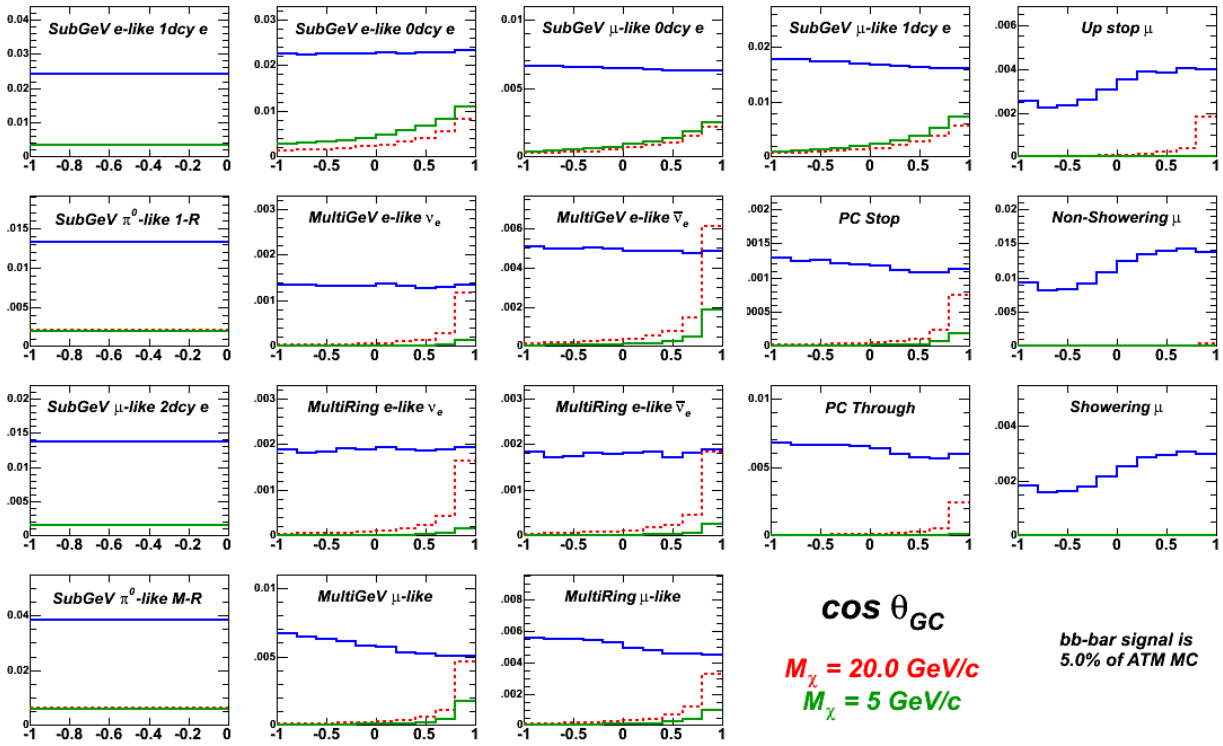

FIG. 169. Signal and background (blue) distributions used in the Hyper-K sensitivity study of dark matter annihilating via $\chi\chi \to b\bar{b}$ at the galactic center. Analysis samples are binned in $\cos\theta_{gc}$, the direction to the galactic center, with the exception of the first column, which is binned in the reconstructed momentum of the lepton candidate (only). Two WIMP hypotheses are shown: $m_\chi = 5\text{GeV/c}^2$ in green and $m_\chi = 20\text{GeV/c}^2$ in red. All distributions have been area normalized with the WIMP normalization taken to 5% of the background MC.

The differential neutrino flux arising from WIMP annihilation into the standard model particles listed above is simulated using the DarkSUSY package, and the resulting spectrum adjusted to account for oscillations on the way to the detector. An independent set of atmospheric neutrino MC is reweighted to this distribution to give a reconstructed signal MC at Hyper-Kamiokande. In

computing the sensitivity to an additional neutrino source, the analysis samples are rebinned in momentum and cosθ_{gc}, where θ_{gc} is the angle between the galactic center position (RA = 266°, Dec = -28°) and the reconstructed lepton direction. Figure 169 shows the cosθ_{gc} distributions of the atmospheric neutrino background background and two WIMP hypotheses for each of the analysis samples. During the fit MC data sets without a WIMP signal are fit against a PDF built from the atmospheric background MC plus a WIMP signal modified by a normalization parameter, β. Here the maximum value of β that is consistent with the background only model within errors is used to compute the upper limit on the amount of additional neutrinos from the galactic center allowed after a 5.6 Mton·year exposure of Hyper-K.

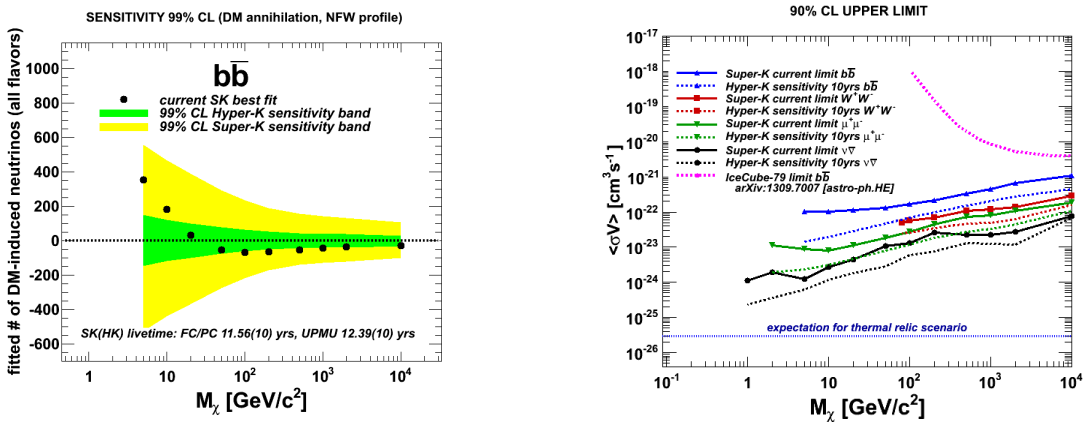

FIG. 170. Hyper-K's sensitivity to a potential dark matter-induced event excess (left) for the $\chi\chi \to b\bar{b}$ channel after a 5.6 Mton·year exposure is shown in the left panel. The right panel shows the expected limit on the WIMP velocity averaged annihilation cross section for several annihilation modes overlaid with limits from Super-K [53]. Both plots are shown as a function of the dark matter mass.

Unlike direct detection experiments this search method is insensitive to the WIMP-nucleon interaction cross section. Instead limits can be placed on the velocity averaged self-annihilation cross section, $< \sigma \times v >$, where v is the assumed velocity distribution of WIMPS in the halo. Figure 170 shows the expected sensitivity of Hyper-K to WIMP annihilations at the galactic center. The left image shows the expected 99% C.L. limit on the allowed number of neutrinos from such interactions in excess of the atmospheric neutrino background prediction for the $\chi\chi \to b\bar{b}$ annihilation channel as a function of the WIMP mass, m_χ. Note the marked constraint relative to Super-Kamiokande. Since the analysis makes use of potential signals in both ν_e and ν_μ enriched samples across the entire energy range of atmospheric neutrinos it is not just the number of allowed excess neutrinos but their distribution that determines the sensitivity. Hyper-Kamiokande's sensitivity to the WIMP

velocity averaged self-annihilation cross section is expected to exceed that of Super-Kamiokande by nearly an order of magnitude for $m_\chi > 8\text{GeV/c}^2$ for this channel. Unlike other experiments, Hyper-K's ability to reconstruct down to $O(100)$ MeV neutrino interactions gives it unparalleled sensitivity to WIMPs with masses less than ~ 100 GeV/c^2.

2. Search for WIMPS from the Sun

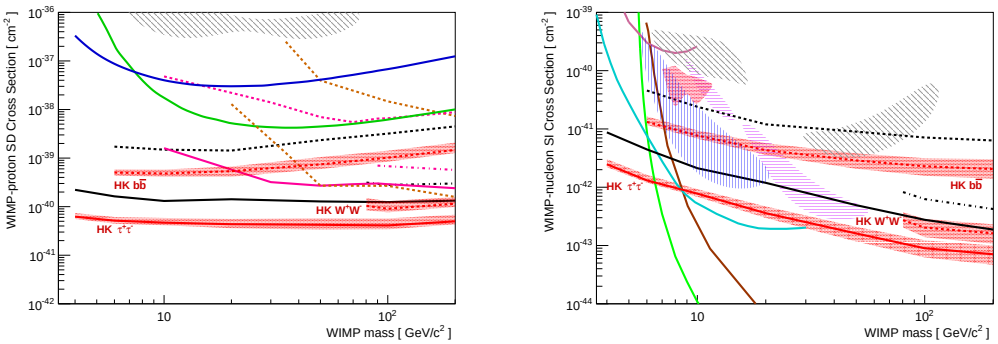

FIG. 171. The 90% C.L. upper limits on the spin-dependent (left) and spin-independent (right) WIMP-nucleon scattering cross section based on a search from WIMP-induced neutrinos coming from the direction of the sun are shown as a function of WIMP mass are shown as the red curves. Limits (lines) and allowed regions (hatched regions) from other experiments are also shown. Results from Super-Kamiokande appear in black [254]. Bands around the Hyper-K limits indicate the combined effect of uncertainties in the solar model, nuclear form factor, and assumed WIMP velocity distribution.

WIMPs bound in the halo of the galaxy may also become gravitationally trapped within the sun after losing energy via scattering processes with nuclei in its interior. If these then pair annihilate and produce neutrinos, they will escape the sun and be detectable at Hyper-Kamiokande. Assuming that the rate of WIMP capture within the sun is in equilibrium with the annihilation rate, measurements of the WIMP-induced neutrino flux can be directly translated into measurements of the WIMP-nucleon scattering cross section without the need to measure the self-annihilation cross section. Since the sun is composed of protons and heavier nuclei it is further possible to study both WIMP interactions coupled to the nuclear spin (spin dependent, SD) and interactions coupled to the target mass (spin independent, SI).

In the analysis below the local dark matter density is assumed to be 0.3 GeV/cm^3 with an RMS velocity of 270 km/s. The rotation of the solar through the halo is taken to be 220 km/s. Signal

MC has been generated by reweighting atmospheric neutrino MC events to spectra produced by the WIMPSIM package, which accounts for the passage of particles through solar matter. Oscillation between flavors as the neutrinos travel from the sun to the detector are included. An independent set of atmospheric neutrino MC is used to model the background.

The search for WIMPS bound and annihilating at the center of the sun proceeds along similar lines as the search for events from the galactic center, though events are now binned in momentum and $\cos\theta_\odot$, where $\theta_\odot$ is the angle between the reconstructed lepton direction and the direction to the sun. In these coordinates the atmospheric neutrino background is flat, while the WIMP signal MC is peaked sharply in the direction of the sun. Limits on the WIMP-induced neutrino flux are translated into limits on the WIMP-nucleon SD and SI cross sections using the DarkSUSY simulation. Hyper-K's sensitivity with a 5.6 Mton·year exposure shown in Figure 171. The left (right) plot shows the sensitivity to the WIMP-proton SD (WIMP-nucleon SI) cross section for masses $m_\chi > 4\mathrm{GeV/c}^2$ compared to allowed regions (shown as hatched spaces) and limits (shown as lines) from current experiments. These limits have been produced assuming WIMPs have only SD or SI interactions and have been estimated for $\chi\chi \to W^+W^-, b\bar{b}$, and $\tau^+\tau^-$. Hyper-K's is expected to produce limits a factor of $3 \sim 4$ times stringent than Super-K (black curves) if no WIMP signal is seen and will provide the most stringent constraints on SD interactions. Further, current hints for a positive SI (SD) dark matter signal [255–259], can be probed completely by Hyper-K's $\tau\tau$ channel (all channels). For spin independent interactions Hyper-K will provide sensitivity sub 10 GeV/c^2 masses, a region of parameter space that is difficult access with direct detection experiments using current technologies.

It is worth noting that in both the solar and galactic center analyses no improvement in systematic errors beyond Super-K's current understanding has been assumed. At Hyper-K the statistical uncertainty in the data is small enough that increase in sensitivity relative to Super-K is limited by systematic errors in the atmospheric neutrino flux and cross section model. Due to relatively high energy of the signal events and the expected directional resolution of the detector, systematic errors in the detector response, while currently less well known, are expected to be less significant. While it is uncertain how the flux and cross section model will evolve in the future, improved modeling will translate directly into better sensitivity to WIMP-induced neutrinos at Hyper-K.

C. Other astrophysical neutrino sources

1. Solar flare

Solar flares are the most energetic bursts which occur in the solar surface. Explosive release of energy stored in solar magnetic fields is caused by magnetic reconnections, resulting in plasma heating, particle accelerations, and emission of synchrotron X-rays or charged particles from the solar surface. In a large flare, an energy of 10^{33} ergs is emitted over 10's of minutes, and the accelerated protons can reach energies greater than 10 GeV. Such high energy protons can produce pions by nuclear interactions in the solar atmosphere. Evidence of such nuclear interactions in the solar atmosphere are obtained via observations of solar neutrons, 2.2 MeV gamma rays from neutron captures on protons, nuclear de-excitation gamma rays, and possible > 100 MeV gamma rays from neutral pion decays. Thus, it is likely that neutrinos are also emitted by the decay of mesons following interactions of accelerated particles. Detection of neutrinos from a solar flare was first discussed in 1970's by R.Davis [260, 261], but no significant signal has yet been found [262, 263]. There have been some estimates of the number of neutrinos which could be observed by large water Cherenkov detectors [264, 265]. According to [264], about 20 neutrinos will be observed at Hyper-Kamiokande during a solar flare as large as the one in 20 January 2005, although the expected numbers have large uncertainties. Therefore, regarding solar flares our first astrophysics goal is to discover solar flare neutrinos with Hyper-K. This will give us important information about the mechanism of the particle acceleration at work in solar flares.

2. Gamma-Ray Burst Jets and Newborn Pulsar Winds

Gamma-ray bursts (GRBs) are the most luminous astrophysical phenomena with the isotropically-equivalent gamma-ray luminosity, $L_\gamma \sim 10^{52}$ erg s^{-1}, which typically occur at cosmological distance. Prompt gamma rays are observed in the MeV range, and their spectra can be fitted by a smoothened broken power law [266]. The prompt emission comes from a relativistic jet with the Lorentz factor of $\Gamma \sim 10^2 - 10^3$, which is presumably caused by a blackhole with an accretion disk or fast-spinning, strongly-magnetized neutron star. Observed gamma-ray light curves are highly variable down to ~ 1 ms, suggesting unsteady outflows. However, GRB central engines and their radiation mechanism are still unknown, and GRBs have been one of the biggest mysteries in high-energy astrophysics.

Internal shocks are naturally expected for such unsteady jets, and the jet kinetic energy can be

converted into radiation via shock dissipation. In the "classical" internal shock scenario [267], observed gamma rays are attributed to synchrotron emission from non-thermal electrons accelerated at internal shocks. It has been suggested that GRBs may also be responsible for ultrahigh-energy cosmic rays (CRs), and TeV-PeV neutrinos have been predicted as a smoking gun of CR acceleration in GRBs [268]. One of the key advantages in GRB neutrino searches is that atmospheric backgrounds can significantly be reduced thanks to space- and time-coincidence, but no high-energy neutrino signals correlated with GRBs have been found in any neutrino detector including Super-K [269] and IceCube [270].

On the other hand, the recent theoretical and observational progress has suggested that the above classical scenario has troubles in explaining observational features such as the low-energy photon spectrum. Alternatively, the photospheric scenario, where prompt gamma rays are generated around or under the "photosphere" (where the Compton scattering optical depth is unity), has become more popular [271–273]. Indeed, observations have indicated a thermal-like component in GRB spectra [274, 275]. Energy dissipation may be caused by inelastic nucleon-neutron collisions [276–278], and neutrons can naturally be loaded by GRB central engines either blackhole-accretion-disk system or strongly-magnetized neutron star. Then, quasi-thermal GeV-TeV neutrino emission is an inevitable consequence of such inelastic nucleon-neutron collisions [279]. Since neutrinos easily leave the flow, predictions for these neutrinos are insensitive to details of gamma-ray spectra. Hyper-K will enable us to search these quasi-thermal GeV-TeV neutrinos from GRB jets, and it also has an advantage over another neutrino detector IceCube (that is suitable for higher-energy $>$ 10-100 GeV neutrinos). The GeV-TeV neutrino detection is feasible if a GRB happens at $\lesssim$ 100 Mpc, and successful detections should allow us to discriminate among prompt emission mechanisms and probe the jet composition, leading to a breakthrough in understanding GRB physics. However, GRBs are rare astrophysical phenomena, so we have little chance to expect such a nearby bright burst in the next 10-100 years. Much more promising targets as high-energy neutrino sources would be energetic supernovae driven by relativistic outflows [280–283]. A significant fraction of GRB jets may fail to puncture their progenitor star, and photon emission from the jets can easily be hidden. Indeed, theoretical studies revealed the existence of conditions for a jet to make a successful GRB. "Choked jets" or "failed GRBs" are naturally predicted when the jet luminosity is not sufficient or the jet duration is too short or the progenitor is too big. The choked jets can explain trans-relativistic supernovae or low-luminosity GRBs, which show intermediate features between GRBs and supernovae [284].

The neutrino event rate expected in Hyper-K depends on the isotropically-equivalent dissipation

energy $\mathcal{E}^{\rm iso}_{\rm diss}$, Lorentz factor Γ, and distance d. For $\mathcal{E}^{\rm iso}_{\rm diss} = 10^{53}$ erg s^{-1}, $\Gamma = 10$ and $d = 10$ Mpc, the characteristic energy of quasi-thermal GeV-TeV neutrinos is $E_\nu^{\rm qt} \sim 3$ GeV [279]. The neutrino-nucleon cross section for the charged-current interaction at 1 GeV is $\sim 0.6 \times 10^{-38}$ cm^2 (averaged over ν and $\bar{\nu}$), so the effective area of Hyper-K is $\sim 2 \times 10^{-3}$ cm^2 at 1 GeV. Then, Hyper-K will be able to detect ~ 5 signal events from such a jet-driven supernova. Successful detections enable us to probe jet physics that cannot be directly studied by electromagnetic observations. Neutrinos enable us to understand how jets are accelerated and what the jet composition is, and will give us crucial keys to the mysterious connection between GRBs and energetic supernovae [285]. Also, in principle, matter effects in neutrino oscillation could be investigated [286, 287]. Moreover, we will able to study how CR acceleration operates in dense radiation environments inside a GRB progenitor star. Whether CRs are accelerated or not depends on properties of shocks. The conventional shock acceleration mechanism can effectively operate only if the shock is radiation-unmediated collisionless [283]. On the other hand, when the shock is mediated by radiation, the so-called neutron-proton-converter acceleration mechanism can work efficiently [288, 289], which boosts the energy of quasi-thermal neutrinos produced by nucleon-neutron collisions [279].

As discussed above, relativistic outflows containing neutrons should naturally lead to GeV-TeV neutrino production, but the outflows do not have to be jets. Another interesting case may be realized when a supernova explosion leaves a fast-spinning neutron star. Neutrons are loaded in the proto-neutron star wind via neutrino heating. Around the base of the outflow, the particle density is so high that neutrons and ions are tightly coupled via elastic collisions. Neutrons should be accelerated together with ions as the Poynting-dominated pulsar wind is accelerated. Once the outflow becomes relativistic enough to exceed the pion-production threshold, inelastic collisions naturally occur as the main dissipation process of relativistic neutrons. The neutrons then interact with the material decelerated by the shock and possibly with the overlying stellar material, producing 0.1-1 GeV neutrinos [290]. Detecting this signal would probe the otherwise completely obscured process of jet acceleration and the physics of rotating and magnetized proto-neutron star birth during the core collapse of massive stars. Hyper-K may expect ~ 70 ($\mathcal{E}^{\rm iso}_\nu/10^{48}$ erg) events for a core-collapse supernova at 10 kpc. In addition, Hyper-K could also allow us to see $\sim 10 - 100$ MeV neutrinos through the $\bar{\nu}_e p \to e^+ n$ channel. However, detection of these lower energy neutrinos would be more difficult because of the smaller cross sections at lower energies and because the signal may be buried in the exponential tail of thermal MeV neutrinos from the proto-neutron star.

To detect high-energy neutrino signals from hidden GRB jets or newborn pulsar winds embedded

in supernovae, it is crucial to reduce atmospheric backgrounds using space and time coincidence, so information at other wavelengths is relevant. The atmospheric neutrino background at GeV energies is $\approx 1.3\times10^{-2}$ GeV cm^{-2} s^{-1} sr^{-1} for $\nu_e+\bar{\nu}_e$ and $\approx 2.6\times10^{-2}$ GeV cm^{-2} s^{-1} sr^{-1} for $\nu_\mu+\bar{\nu}_\mu$, respectively [291]. We may take the time window of $t_{\rm thin}\sim 10-100$ s after the explosion time that is measurable with MeV neutrinos or possibly gravitational waves. The localization is possible by follow-up observations at x-ray, optical, and infrared bands. The atmospheric background flux in the typical angular and time window is $\sim 2\times10^{-3}$ erg cm^{-2}, which can be low enough for a nearby supernova.

Note that it is critical to have large volume detectors for the purpose of detecting GeV-TeV neutrinos. The present Super-K and liquid scintillator detectors such as JUNO and RENO-50 are too small to detect high-energy signals from astrophysical objects especially if extragalactic, and much bigger detectors such as Hyper-K and PINGU are necessary to have a good chance to hunt high-energy neutrinos from GRBs and energetic supernovae. Because of the atmospheric background, sensitivities above GeV energies are typically essential but searches for neutrinos below ~ 1 GeV could also be useful for nearby events.

D. Neutrino geophysics

The chemical composition of the Earths core is one of the most important properties of the planet's interior, because it is deeply connected to not only the formation and evolution of the Earth [292] itself but also to the origin of the geomagnetic field [293]. While paleomagnetic evidence suggests that the geomagnetic field has existed for roughly three billion years, it is known that a core composed of iron alone could not sustain this magnetic field for more than 20,000 years. Explaining the continued generation of the geomagnetic field as well as its other properties requires knowledge of composition of the core matter. Based on seismic wave velocity measurements and the composition of primordial meteorites the composition of the core is presumed to be an iron-nickel alloy that additionally includes light elements, such as oxygen, sulfur, or silicone [294]. However, since no sample of the Earth's mantle has even been acquired, let alone a sample of the core, the composition of the latter, particularly its light element a abundance, remains highly uncertain. Since the deepest wellbore to date has a depth of 14 km [295], and the depth to the outer core is 2900 km it is unlikely that a core sample can be obtained within this century. As a result, addition methods of determining the chemical composition of the core are essential to understanding the Earth and its magnetic field.

As discussed in Section III.1 B, the oscillation probability of atmospheric neutrinos depends on not only the various mixing angles, the neutrino mass differences, and CP-violating phase, δ_{CP}, but also on the electron density of the media they traverse. This last property makes atmospheric neutrinos an ideal probe for measuring the electron density distribution of the Earth presuming the other oscillation parameters are well measured. Since accelerator neutrino measurements at Hyper-K itself are expected to dramatically improve on the precision of these parameters (c.f. Section III.1 A), Hyper-K may be able to make the first measurement of the core's chemical composition using its atmospheric neutrino sample.

Hyper-K's sensitivity in this regard has been studied in the context of atmospheric neutrino spectrum's dependence upon the ratio of the proton to nucleon ratio (Z/A) of material in the outer core. Constraints from the combination of measurements of the Earth's geodetic-astronomical parameters, such as its precession and nutation, with its low frequency seismic oscillation modes (free oscillations), and seismic wave velocity measurements have yielded precise knowledge of the planet's density profile [296]. Using this information the inner core and mantle layers of the Earth are fixed to pure iron (Z/A = 0.467) and pyrolite (Z/A = 0.496) and the Z/A value of the outer core is varied. The analysis uses the same analysis samples presented in Section III.1 B and focuses

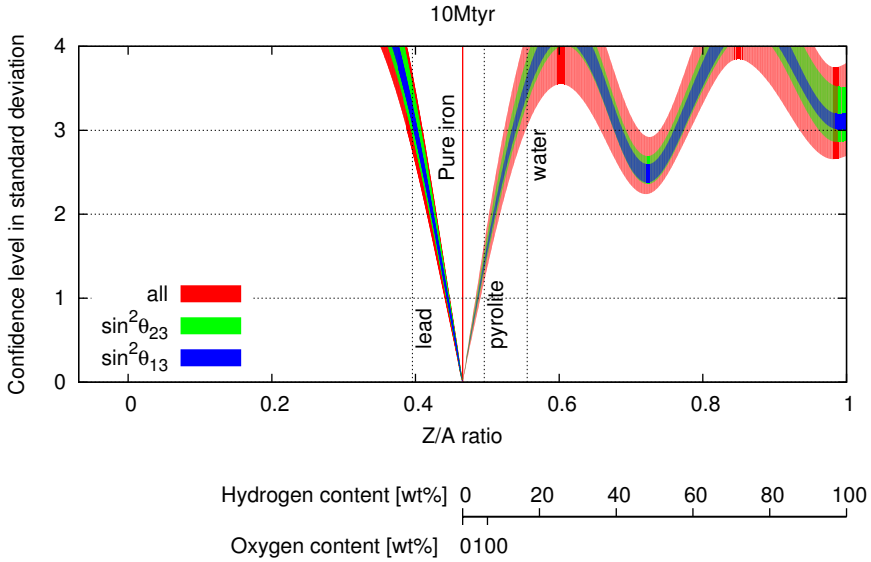

FIG. 172. Constraints on the proton to nucleon ratio of the Earth's outer core for a 10 Mton year exposure of Hyper-K to atmospheric neutrinos. Colored bands indicate the effect of present uncertainties in the neutrino mixing parameters.

on upward-going events between 1 and 10 GeV. Assuming the outer and inner core chemical compositions are the same, figure 172 shows the expected constraint on the Z/A parameter. After a 10 Mton year exposure Hyper-K can exclude lead and water (pyrolite) outer core hypotheses by approximately $\sim 3\sigma(1\sigma)$. While geophysics models will ultimately require even greater precision in such measurements, Hyper-K has the potential to make the spectroscopic measurements of the Earth's core. It is worth noting that other proposed experiments with the ability to make similar geochemical measurements, such as the next generation of neutrino telescopes, rely primarily on the muon disappearance channel. Hyper-Kamiokande's, on the other hand, is unique in that its sensitivity is derived from the electron appearance channel.

ACKNOWLEDGMENTS

This work was supported by MEXT Grant-in-Aid for Scientific Research on Innovative Areas Number 25105004, titled "Unification and Development of the Neutrino Science Frontier." In addition, participation of individual researchers has been further supported by funds from JSPS, Japan; the European Union ERC-207282, H2020 RISE-GA644294-JENNIFER and H2020 RISE-GA641540-SKPLUS; RSF, RFBR and MES, Russia; JSPS and RFBR under the Japan-Russia Research Cooperative Program.

Part IV

Appendix

Appendix A: Managerial Structure

The organization of Hyper-Kamiokande will be modeled on its very successful predecessor experiments, Super-Kamiokande, K2K, and T2K. These experiments were, in turn, modeled on the general method by which international particle physics experiments are organized, with a lead laboratory which instigates and initially approves the project with the participation of physicists from around the world. Given the rather unusual nature of Hyper-Kamiokande, with its two major installations in Tokai and Kamioka, there will be two host laboratories – ICRR for the Hyper-Kamiokande far detector and J-PARC/KEK for the beam and near detectors. Hyper-Kamiokande is currently being proposed by a proto-collaboration, the organization of which will be described below. As happened for its predecessor experiments, once the experiment is approved, the international contributions will be formalized, at which point the official Hyper-Kamiokande collaboration will be formed and its organizational structures agreed. The exact nature of that organization will be subject to that future agreement, however it is expected to be similar to the existing T2K collaboration, so this will be described to give an example of the likely organizational structures which will be present.

1. Organization of the Hyper-Kamiokande Proto-Collaboration

The idea of building a very large successor to Super-Kamiokande has been around for many years [297], however significant impetus was added by the discovery by T2K of electron neutrino appearance [25], which opened the possibility of probing CP violation with a conventional neutrino beam. The Hyper-Kamiokande proto-collaboration grew out of the Super-Kamiokande and T2K collaborations, however with a significant addition of new groups and physicists. The proto-collaboration was initiated with six open meetings, five of which were held at IPMU in Kashiwa, and one was held at the University of British Columbia, Canada. With the formal initiation of the proto-collaboration this June, the meetings are now restricted to members of the proto-collaboration, although we are still welcome anyone who wishes to make a contribution to the project.

The functional organization of the proto-collaboration is overseen by three groups.

- The Working Groups (WGs), under the directions of the Project Leader (M. Shiozawa) and Project co-Leader (F. Di Lodovico), lead all the activities of the collaboration. There is a working group associated to each main topic as shown in Fig. 173. The Working Group convenors organize their individual activities as directed by the project leaders, with communication between groups facilitated at bi-weekly convenor meetings. These meetings are also attended by members of the International Steering Committee.

- The International Steering Committee, iSC, chaired by T. Nakaya, has the responsibility for the overall strategic guidance of the proto-collaboration. The structure and current membership is shown in Table XLV.

- The International Board of Representatives, IBR, chaired by D. Wark, represents the countries of the proto-collaboration, see Table XLVI. It is charged with coordinating the approaches to funding agencies across the collaboration and with deciding on policies for governing and expanding the collaboration.

It is expected that this organizational structure will persist until the project is approved and funded, at which point a formal collaboration will be formed and a new organization instituted.

TABLE XLV. International Steering Committee structure and membership.

Internation Steering Committee.	
Role	Member
Chair	T. Nakaya
IBR chair	D. Wark
ICRR representative	M. Nakahata
KEK representative	T. Kobayashi
Project leader	M. Shiozawa
Project co-leader	F. Di Lodovico
Physics convener	M. Yokoyama
Members at large	H. Aihara, A. Blondel, G. Catanesi, E. Kearns, J.P. Poutissou

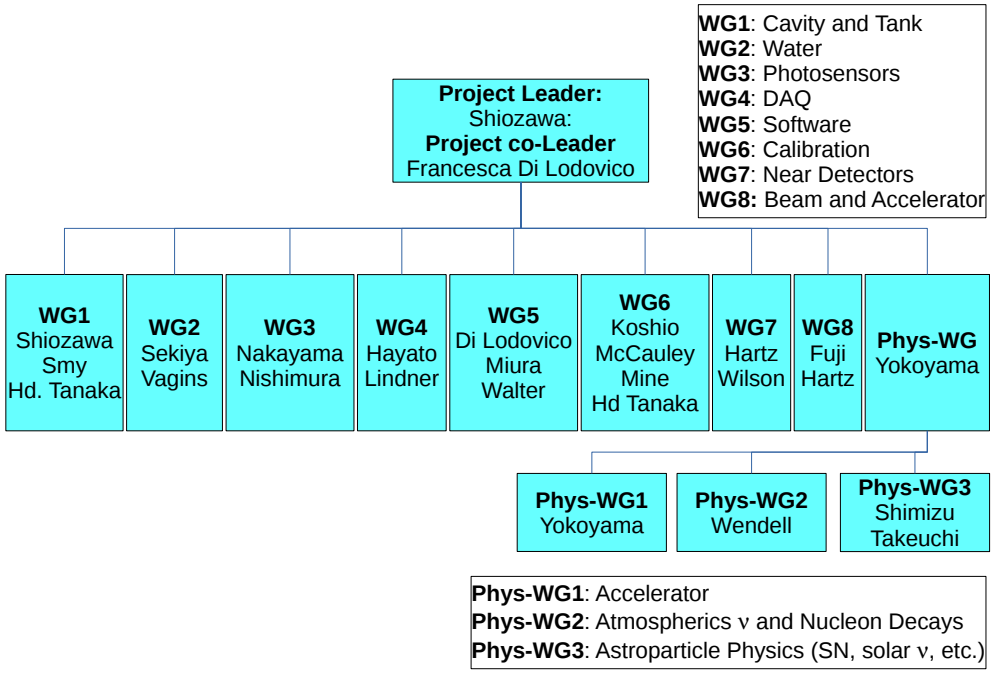

FIG. 173. The Working Group structure.

TABLE XLVI. International Board Representatives structure and membership.

Internation Board Representatives.	
Role	Member
Chair	D. Wark
Brazil	H. Nunokawa
Canada	S. Bhadra, A. Konaka
France	M. Gonin
Italy	M.G Catanesi
Japan	T. Kobayashi, T. Nakaya, M. Shiozawa
Korea	K.K. Joo
Poland	E. Rondio
Spain	L. Labarga
Switzerland	A. Blondel
UK	F. Di Lodovico, D. Wark
USA	E. Kearns, C. Walter

2. Example of the Organization of the Hyper-Kamiokande Experiment T2K

The final organization of the collaboration will inevitably be modeled on previous successful collaborations, with the T2K experiment being the most recently formed relevant example. The Hyper-Kamiokande collaboration is therefore likely to look similar to T2K (probably with some modifications to reflect its broader set of physics goals). We therefore describe the main features of the governance of T2K to lay out what structures will likely govern the Hyper-Kamiokande collaboration. The basic law of T2K is contained in its constitution, called the International Collaboration Agreement, or ICA. The ICA specifies the bodies which govern T2K and how they are elected. The collaboration is led by a Spokesperson and an International Co-Spokesperson, who have the ultimate responsibility for making decisions and who are (re)elected every two years. The senior management committee is the Executive Committee (EC), which is elected by the collaboration every other year according to rules which guarantee the host labs are well represented plus a broad geographic representation from the rest of the collaboration. The institutions are all represented on the Institutional Board of Representatives (IB), which has the final say in issues concerning personnel and overall collaboration policy towards publications, membership requirements, authorship policy, shift policy, and so forth. The EC and the IB manage a number of other committees, such as the Publications Board and the Analysis Steering Group, which execute collaboration policy. Actual experimental operations are managed by Convenors (for the apparatus) and Run Coordinators (for operations) appointed for that purpose by the EC. All significant collaboration decisions are ratified by the Collaboration General Assembly, consisting of all members of the collaboration, which meets at all collaboration meetings (currently 3 times per year).

Appendix B: Liner Sheet Tests

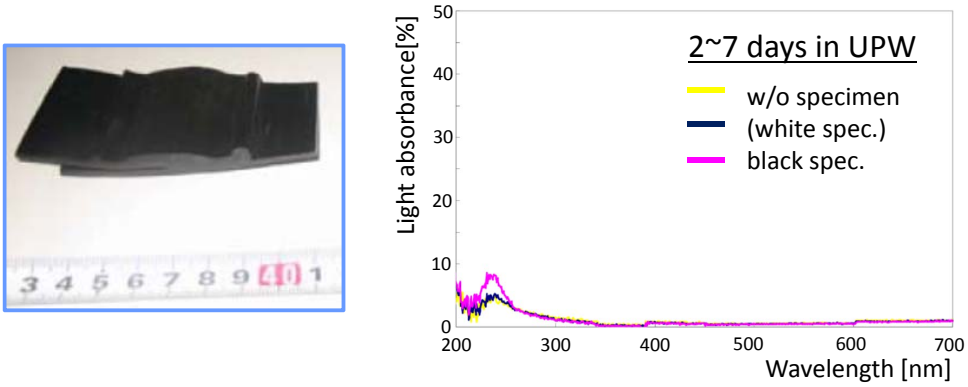

FIG. 174. A typical specimen (GSE Gundle sheet) for immersion test and typical results of light absorbance of ultra-purified water after several days with specimens soaked in it (pink line), which is compared to a control sample without specimen (yellow line).

1. Immersion test

Specimens of HDPE lining sheet (GSE Gundle sheet, whose material is identical to that for the CPL), with artificial extrusion-welded seam, were immersed into the ultra-purified water (UPW) for certain periods (1, 2 to 7, and 8 to 31 days), and absorbance was compared to a control sample without specimens. Amount of eluted materials into UPW, i.e. total organic carbon (TOC), anions and metals, were also measured. Figure 174 show the specimen and an example of measurements, where increase of the light absorbance were observed between the wavelength range of 200∼300 nm. Some amount of material elution were observed, where eluted amounts per unit area and time were significantly less for later periods. Although relation between the increase of light absorbance and the material elusion should be studied, it is noted that range of PMT-sensitive wavelength is somewhat higher (300∼650 nm), so the effect to the experiment may be limited. Similar results were obtained for Gadolinium sulfate solutions.

2. Measurements on material strength

Tension tests were carried out for the CPL to estimate yield strength, tensile strength, and Young's modulus. Since HDPE has large elongation before breaking (∼500%), 1.0% proof stress

was used as the yield strength (instead of 0.2% proof stress which is generally used for other materials). Here, varying measurement conditions were examined for tensioning velocity (0.05 mm/min and 0.5 mm/min) and for temperature (typical room temperature 23.5° Celsius and 15° Celsius simulating water temperature). It was found that measured yield strengths were smaller by a few to several tens of percent than the specification value (15.2 MPa as listed in Table VIII). In general, lower tensioning speed gives lower strength, due to large plasticity of HDPE. Strength also depends significantly on temperature: HDPE becomes harder with lowering temperature, as common properties in high-polymer materials. The measurement in 15° Celsius gave about 20% higher strengths than those at 23.5° Celsius. The tension tests were also repeated on the samples with an extrusion-welded seam. For the most cases, none of peeling, fracture, nor other troubles were observed on welded seams, but the deformation occurred at the base material. The yield/tensile strength were almost identical to the values for base material.

3. Creep test

Creep tests were performed with various tensile loads: 1/4×M, 3/8×M, or 1/2×M, where M = 18.2 MPa is the observed yield strength as 1.0% proof stress with tensioning speed of 5.0 cm/min in 20° Celsius. For the tests with load of 1/4×M (*i.e.* 4.6 MPa), creep was not observed for about 30 days. Meanwhile, for tests with load of 3/8×M (6.8 MPa) and 1/2×M (9.1 MPa), clear generation of creep was observed with 5 and 10 days, respectively.

4. Resistivity to localized water pressure

Ideally, the CPL sheet should be closely attached to the surface of flatly-backfilled concrete walls and thus firmly supported by them. However, it is probable that cracks or rough holes exist or happen in the backfill concrete wall, and thus the liner should locally stand for water pressure by itself. To simulate the situation, tests to apply localized water pressure for the lining were performed with variety of slit widths (2 to 8 mm) and hole diameters (40 to 120 mm-ϕ), as illustrated in Fig. 175. It is found that the liner survived for 0.8 MPa water pressure without breaking for all cases. Although the test load was applied only in a short period and durability for longer period should be examined, it is probable that the expected water pressure is enough lower than the critical pressure causing creep.

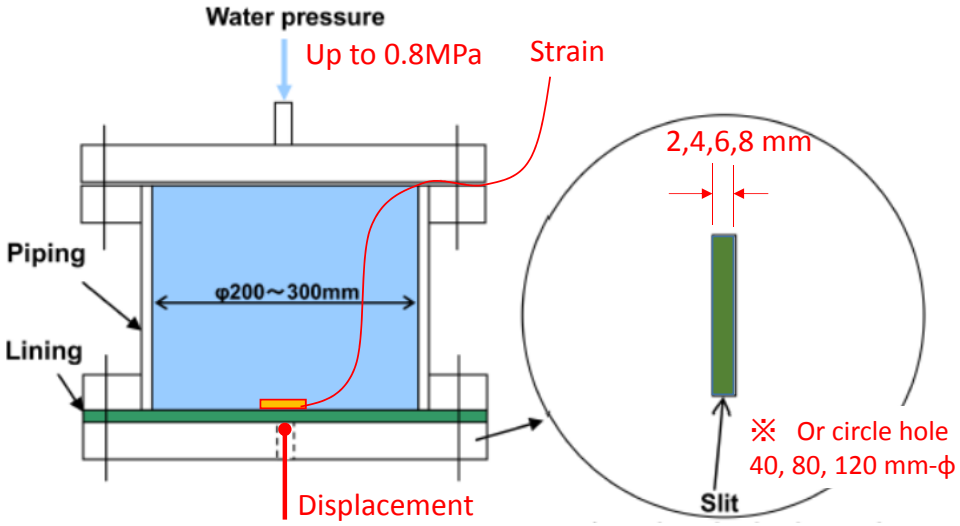

FIG. 175. Setup for the test applying localized water pressure to the lining material.

5. Water permeability

Generally, plastic materials have a property to pass water as moisture vapor through molecules. It is referred as moisture permeability, or water vapor transmission rate (WVTR), being represented with transferred mass through unit area and time (g/m^2/24-hours). The permeability was studied for the GSE geomembrane (Gundle sheet, whose material is quite simmilar to that for CPL Studliner) [298]. For the sheet with thickness t= 1.5 mm, WVTR (P_{a1}) was obtained to be 1 g/m^2/24-hours at most for standard testing temperature (40° Celsius). The water permeability coefficient (k) was then deduced to be

$$k = P_{a1} \times t \times \frac{g}{\Delta P_v} = 2.5 \times 10^{-12} cm/s,$$

where g is standard gravitational acceleration (9.8 m^2/s) and ΔP_v is difference of the water-vapor pressures of both sides of the geomembrane (90% of saturated vapor pressure at 40° Celsius, 75.22 hPa). Since the CPL is 5 mm thick, time until water permeates to backside of the CPL is:

$$0.5[\mathrm{cm}] \times \frac{1}{2.5 \times 10^{-12}[\mathrm{cm/s}]} = 2 \times 10^{11}[\mathrm{s}],$$

i.e. about 6,300 years. Since the total inner surface area of the tank is 18,259 (54,750) m^2 for 1 (3) tank options, amount of water permeation through the entire liner surface will be:

$$18,250(54,750) \times 10^4\ [\mathrm{cm}^2] \times 2.5 \times 10^{-12}\ [\mathrm{cm/s}]$$
$$= 4.6 \times 10^{-4}(1.4 \times 10^{-3})[\mathrm{cm}^3/\mathrm{s}] = 40(120)\ [\mathrm{cm}^3/\mathrm{day}],$$

thus being negligible amount.

6. Penetration structure

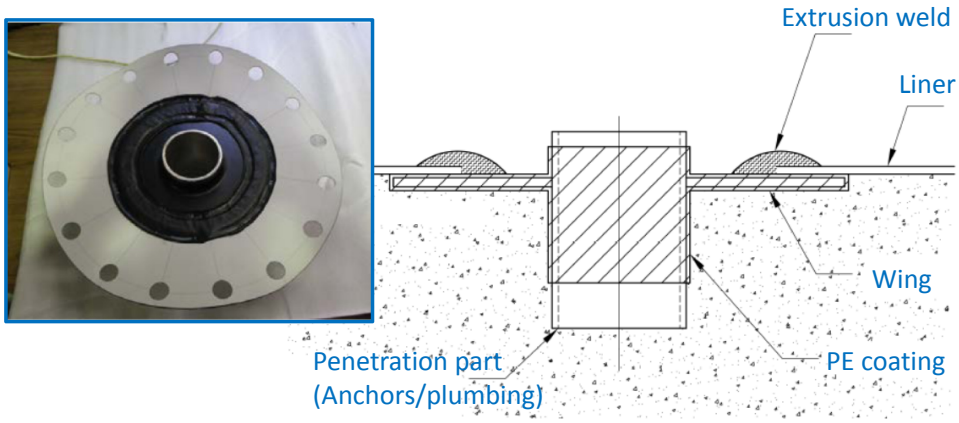

FIG. 176. Schematic drawing for the penetration structure of a water pipe and a photo of its prototype.

The leak can happen around the components which penetrate the water tank lining, such as anchors to support PMT framework columns, water supply/return pipes, and so on. A possible design of the penetration structure for the water pipes is illustrated in Fig. 176. A metal pipe with a flange is coated together with PE resin of about 1.5 mm thickness, which can be extrusion-welded to adjacent CPLs. A prototype was made for the design as shown together in the figure, and tested with pressure up to 1 MPa for 30 minutes. Tests with cyclic pressure (0.5 MPa, repeating on/off in a day for 5 days) and with continuous pressure (3 months with applying 0.5 MPa were also performed. For all of the cases, no water leak was observed.

[1] G. Aad *et al.* (ATLAS), Phys. Lett. **B716**, 1 (2013), arXiv:1207.7214 [hep-ex].

[2] S. Chatrchyan *et al.* (CMS), Phys. Lett. **B716**, 30 (2012), arXiv:1207.7235 [hep-ex].

[3] Y. Fukuda *et al.* (Super-Kamiokande), Phys. Rev. Lett. **81**, 1562 (1998), arXiv:hep-ex/9807003.

[4] Z. Maki, M. Nakagawa, and S. Sakata, Prog. Theor. Phys. **28**, 870 (1962).

[5] B. Pontecorvo, Sov. Phys. JETP **26**, 984 (1968).

[6] K. A. Olive *et al.* (Particle Data Group), Chin. Phys. **C38**, 090001 (2014).

[7] M. Kobayashi and T. Maskawa, Prog. Theor. Phys. **49**, 652 (1973).

[8] J. Schechter and J. W. F. Valle, Phys. Rev. **D22**, 2227 (1980).

[9] S. M. Bilenky, J. Hosek, and S. T. Petcov, Phys. Lett. **B94**, 495 (1980).

[10] M. Doi, T. Kotani, H. Nishiura, K. Okuda, and E. Takasugi, Phys. Lett. **B102**, 323 (1981).

[11] Q. R. Ahmad *et al.* (SNO), Phys. Rev. Lett. **89**, 011301 (2002), arXiv:nucl-ex/0204008 [nucl-ex].

[12] Q. R. Ahmad *et al.* (SNO), Phys. Rev. Lett. **87**, 071301 (2001), arXiv:nucl-ex/0106015 [nucl-ex].

[13] K. Abe *et al.* (Super-Kamiokande), Phys. Rev. **D83**, 052010 (2011), arXiv:1010.0118 [hep-ex].

[14] K. Eguchi *et al.* (KamLAND), Phys. Rev. Lett. **90**, 021802 (2003), arXiv:hep-ex/0212021 [hep-ex].

[15] T. Araki *et al.* (KamLAND), Phys. Rev. Lett. **94**, 081801 (2005), arXiv:hep-ex/0406035 [hep-ex].

[16] S. Abe *et al.* (KamLAND), Phys. Rev. Lett. **100**, 221803 (2008), arXiv:0801.4589 [hep-ex].

[17] Y. Ashie *et al.* (Super-Kamiokande), Phys. Rev. **D71**, 112005 (2005), arXiv:hep-ex/0501064.

[18] Y. Ashie *et al.* (Super-Kamiokande), Phys. Rev. Lett. **93**, 101801 (2004), arXiv:hep-ex/0404034.

[19] M. H. Ahn *et al.* (K2K), Phys. Rev. **D74**, 072003 (2006), arXiv:hep-ex/0606032.

[20] P. Adamson *et al.* (MINOS), Phys. Rev. Lett. **106**, 181801 (2011), arXiv:1103.0340 [hep-ex].

[21] K. Abe *et al.* (T2K), Phys. Rev. **D85**, 031103 (2012), arXiv:1201.1386 [hep-ex].

[22] K. Abe *et al.* (T2K Collaboration), Phys. Rev. Lett. **112**, 181801 (2014), arXiv:1403.1532 [hep-ex].

[23] K. Abe *et al.* (T2K), Phys. Rev. Lett. **107**, 041801 (2011), arXiv:1106.2822 [hep-ex].

[24] P. Adamson *et al.* (MINOS), Phys. Rev. Lett. **107**, 181802 (2011), arXiv:1108.0015 [hep-ex].

[25] K. Abe *et al.* (T2K), Phys.Rev. **D88**, 032002 (2013), arXiv:1304.0841 [hep-ex].

[26] K. Abe *et al.* (T2K Collaboration), Phys. Rev. Lett. **112**, 061802 (2014), arXiv:1311.4750 [hep-ex].

[27] Y. Abe *et al.* (Double Chooz), Phys. Rev. Lett. **108**, 131801 (2012), arXiv:1112.6353 [hep-ex].

[28] J. K. Ahn *et al.* (RENO), Phys. Rev. Lett. **108**, 191802 (2012), arXiv:1204.0626 [hep-ex].

[29] F. P. An *et al.* (Daya Bay), Phys. Rev. Lett. **108**, 171803 (2012), arXiv:1203.1669 [hep-ex].

[30] F. P. An *et al.* (Daya Bay), Phys. Rev. Lett. **112**, 061801 (2014), arXiv:1310.6732 [hep-ex].

[31] Y. Abe *et al.* (Double Chooz), Phys. Lett. **B735**, 51 (2014), arXiv:1401.5981 [hep-ex].

[32] K. Abe *et al.* (Super-Kamiokande), Phys. Rev. **D91**, 052019 (2015), arXiv:1410.2008 [hep-ex].

[33] G. Mitsuka *et al.* (Super-Kamiokande), Phys. Rev. **D84**, 113008 (2011), arXiv:1109.1889 [hep-ex].

[34] K. Abe *et al.* (Super-Kamiokande), Phys. Rev. **D91**, 052003 (2015), arXiv:1410.4267 [hep-ex].

[35] R. Mohapatra and A. Smirnov, Ann. Rev. Nucl. Part. Sci. **56**, 569 (2006), arXiv:hep-ph/0603118

[hep-ph].

[36] S. P. Mikheev and A. Yu. Smirnov, Sov. J. Nucl. Phys. **42**, 913 (1985), [Yad. Fiz.42,1441(1985)].

[37] L. Wolfenstein, Phys. Rev. **D17**, 2369 (1978).

[38] S. T. Petcov and M. Piai, Phys. Lett. **B533**, 94 (2002), arXiv:hep-ph/0112074 [hep-ph].

[39] F. An *et al.* (JUNO), (2015), arXiv:1507.05613 [physics.ins-det].

[40] S.-B. Kim, in *Neutrino Oscillation Workshop (NOW 2014) Conca Specchiulla, Otranto, Lecce, Italy, September 7-14, 2014* (2014) arXiv:1412.2199 [hep-ex].

[41] A. de Gouvea, J. Jenkins, and B. Kayser, Phys. Rev. **D71**, 113009 (2005), arXiv:hep-ph/0503079 [hep-ph].

[42] H. Nunokawa, S. J. Parke, and R. Zukanovich Funchal, Phys. Rev. **D72**, 013009 (2005), arXiv:hep-ph/0503283 [hep-ph].

[43] X. Guo *et al.* (Daya-Bay), (2007), arXiv:hep-ex/0701029.

[44] J. K. Ahn *et al.* (RENO), (2010), arXiv:1003.1391 [hep-ex].

[45] F. Ardellier *et al.* (Double Chooz), (2006), arXiv:hep-ex/0606025.

[46] S. Ahmed *et al.* (ICAL), (2015), arXiv:1505.07380 [physics.ins-det].

[47] M. G. Aartsen *et al.* (IceCube PINGU), (2014), arXiv:1401.2046 [physics.ins-det].

[48] U. F. Katz (KM3NeT), in *Proceedings of the 15th International Workshop on Neutrino Telescopes (Neutel 2013)* (2014) arXiv:1402.1022 [astro-ph.IM].

[49] V. D. Barger, K. Whisnant, and R. J. N. Phillips, Phys. Rev. Lett. **45**, 2084 (1980).

[50] S. Pakvasa, *Proceedings, 20th International Conference on High-Energy Physics*, AIP Conf. Proc. **68**, 1164 (1980).

[51] K. Abe *et al.* (T2K), Phys. Rev. **D91**, 072010 (2015), arXiv:1502.01550 [hep-ex].

[52] M. Sanchez, "Results and Prospects from the NOvA Experiment," Talk presented at the XVII International Workshop on Neutrino Factories and Future Neutrino Facilities (NuFact15), Rio de Janeiro, Brazil, August. 2015.

[53] R. Wendell (Super-Kamiokande), *Proceedings, 26th International Conference on Neutrino Physics and Astrophysics (Neutrino 2014)*, AIP Conf. Proc. **1666**, 100001 (2015), arXiv:1412.5234 [hep-ex].

[54] A. Renshaw *et al.* (Super-Kamiokande), Phys. Rev. Lett. **112**, 091805 (2014).

[55] S. P. Mikheyev and A. Y. Smirnov, Yad. Fiz. **42**, 1441 (1985).

[56] S. P. Mikheyev and A. Y. Smirnov, Nuov. Cim. **C9**, 17 (1986).

[57] S. W. Bruenn, A. Mezzacappa, W. R. Hix, E. J. Lentz, O. E. B. Messer, E. J. Lingerfelt, J. M. Blondin, E. Endeve, P. Marronetti, and K. N. Yakunin, The Astrophysical Journal Letters **767**, L6 (2013), arXiv:1212.1747 [astro-ph.SR].

[58] T. Melson, H.-T. Janka, and A. Marek, The Astrophysical Journal Letters **801**, L24 (2015), arXiv:1501.01961 [astro-ph.SR].

[59] E. J. Lentz, S. W. Bruenn, W. R. Hix, A. Mezzacappa, O. E. B. Messer, E. Endeve, J. M. Blondin, J. A. Harris, P. Marronetti, and K. N. Yakunin, The Astrophysical Journal Letters **807**, L31 (2015),

arXiv:1505.05110 [astro-ph.SR].

[60] T. Takiwaki, K. Kotake, and Y. Suwa, The Astrophysical Journal **786**, 83 (2014), arXiv:1308.5755 [astro-ph.SR].

[61] S. M. Couch and E. P. O'Connor, The Astrophysical Journal **785**, 123 (2014), arXiv:1310.5728 [astro-ph.HE].

[62] I. Tamborra, F. Hanke, B. Müller, H.-T. Janka, and G. Raffelt, Physical Review Letters **111**, 121104 (2013), arXiv:1307.7936 [astro-ph.SR].

[63] E. O'Connor and C. D. Ott, The Astrophysical Journal **762**, 126 (2013), arXiv:1207.1100 [astro-ph.HE].

[64] S. Ando, J. F. Beacom, and H. Yüksel, Phys. Rev. Lett. **95**, 171101 (2005), arXiv:astro-ph/0503321.

[65] http://lbne.fnal.gov/, LBNE collaboration.

[66] "J-PARC TDR," (2003), KEK Report 2002-13 and JAERI-Tech 2003-44.

[67] D. Beavis *et al.* (E889), "Long baseline neutrino oscillation experiment at the ags," (1995), BNL-52459.

[68] K. Abe *et al.* (T2K), Phys. Rev. **D87**, 012001 (2013), [Addendum: Phys. Rev.D87,no.1,019902(2013)], arXiv:1211.0469 [hep-ex].

[69] N. Abgrall *et al.* (NA61), JINST **9**, P06005 (2014), arXiv:1401.4699 [physics.ins-det].

[70] N. Abgrall *et al.* (NA61/SHINE), Phys. Rev. **C84**, 034604 (2011), arXiv:1102.0983 [hep-ex].

[71] N. Abgrall *et al.* (NA61/SHINE), Phys. Rev. **C85**, 035210 (2012), arXiv:1112.0150 [hep-ex].

[72] N. Abgrall *et al.* (NA61/SHINE), Nucl. Instrum. Meth. **A701**, 99 (2013), arXiv:1207.2114 [hep-ex].

[73] A. Haesler, *T2K Replica Target Hadron Production Measurements in NA61/SHINE and T2K Neutrino Flux Predictions*, Ph.D. thesis, Geneva, University of Geneva (2015), presented 22 Jun 2015.

[74] M. Otani *et al.*, *Technology and instrumentation in particle physics. Proceedings, 1st International Conference, TIPP09, Tsukuba, Japan, March 12-17, 2009*, Nucl. Instrum. Meth. **A623**, 368 (2010).

[75] S. Assylbekov *et al.*, Nucl. Instrum. Meth. **A686**, 48 (2012), arXiv:1111.5030 [physics.ins-det].

[76] D. Allan *et al.* (T2K UK), JINST **8**, P10019 (2013), arXiv:1308.3445 [physics.ins-det].

[77] S. Aoki *et al.*, Nucl. Instrum. Meth. **A698**, 135 (2013), arXiv:1206.3553 [physics.ins-det].

[78] P. A. Amaudruz *et al.* (T2K ND280 FGD), Nucl. Instrum. Meth. **A696**, 1 (2012), arXiv:1204.3666 [physics.ins-det].

[79] N. Abgrall *et al.* (T2K ND280 TPC), Nucl. Instrum. Meth. **A637**, 25 (2011), arXiv:1012.0865 [physics.ins-det].

[80] T. Koseki, "J-PARC Accelerator: status, capacity and future plan," (2014), Talk presented at the 2nd international symposium on science at J-PARC (J-PARC 2014), Tsukuba, Japan.

[81] T. Koseki, "J-PARC Accelerator: achievement and future upgrade," (2015), Talk presented at the Workshop for Neutrino Programs with Facilities in Japan, August 4, 2015 Tokai, Japan.

[82] T. Kobayashi, "Potential J-PARC beam power improvement and beam delivery before 2026," (2015), Talk presented at the Workshop for Neutrino Programs with Facilities in Japan, August 4, 2015 Tokai,

Japan.

[83] S. Igarashi, H. Harada, H. Hotchi, T. Koseki, and Y. Sato (2014), "Accelerator Concepts for the Beam Power of Multi MW with J-PARC MR," Talk presented at the 2nd international symposium on science at J-PARC (J-PARC 2014), Tsukuba, Japan.

[84] K. Abe *et al.* (T2K Collaboration), Nucl. Instrum. Meth. **A659**, 106 (2011).

[85] D. Beavis, A. Carroll, I. Chiang, *et al.*, (1995), Long Baseline Neutrino Oscillation Experiment at the AGS(Proposal E889), Physics Design Report, BNL-52459.

[86] Y. Yamada (J-PARC neutrino beamline group), "J-PARC Neutrino beamline, present limits on beam power," (2014), Talk presented at the 1st workshop on next generation accelerator-based neutrino experiment, Tokai, Japan, Feb. 2014.

[87] M. Tada (J-PARC neutrino beamline group), "Neutrino beamline for multiple MW beam," (2014), Talk presented at the 1st workshop on next generation accelerator-based neutrino experiment, Tokai, Japan, Feb. 2014.

[88] M. Martini, M. Ericson, and G. Chanfray, Phys. Rev. **D85**, 093012 (2012), arXiv:1202.4745 [hep-ph].

[89] O. Lalakulich, U. Mosel, and K. Gallmeister, Phys. Rev. **C86**, 054606 (2012), arXiv:1208.3678 [nucl-th].

[90] M. Martini, M. Ericson, and G. Chanfray, Phys. Rev. **D87**, 013009 (2013), arXiv:1211.1523 [hep-ph].

[91] E. J. Moniz and R. A. Smith, Nucl. Phys. **B101**, 605 (1972).

[92] O. Benhar and A. Fabrocini, Phys.Rev. **C62**, 034304 (2000), arXiv:nucl-th/9909014 [nucl-th].

[93] P. Coloma, P. Huber, C.-M. Jen, and C. Mariani, Phys. Rev. **D89**, 073015 (2014), arXiv:1311.4506 [hep-ph].

[94] A. Stahl *et al.*, "Expression of Interest for a very long baseline neutrino oscillation experiment (LBNO)," (2012), cERN-SPSC-2012-021, SPSC-EOI-007.

[95] T. Fukuda *et al.*, JINST **9**, P12017 (2014), arXiv:1412.4955 [physics.ins-det].

[96] R. Asfandiyarov *et al.*, (2014), arXiv:1405.6089 [physics.ins-det].

[97] A. Bonnemaison *et al.*, "A test experiment to develop a 3D grid-like neutrino detector with a water target for measurement of neutrino cross sections at the near detector hall of J-PARC neutrino beamline," (2014), Proposal to the J-PARC PAC.

[98] K. Abe *et al.* (T2K), Phys. Rev. **D90**, 052010 (2014), arXiv:1407.4256 [hep-ex].

[99] E. Kearns *et al.*, "A Proposal for a Detector 2 km Away From the T2K Neutrino Source," (2005), accessed at: http://www.phy.duke.edu/ cwalter/nusag-members/2km-proposal-05-05-30.pdf, 10-2015.

[100] A. A. Aguilar-Arevalo *et al.* (MiniBooNE), Nucl. Instrum. Meth. **A599**, 28 (2009), arXiv:0806.4201 [hep-ex].

[101] S. Bhadra *et al.* (nuPRISM), (2014), arXiv:1412.3086 [physics.ins-det].

[102] A. Aguilar-Arevalo *et al.* (LSND), Phys. Rev. **D64**, 112007 (2001), arXiv:hep-ex/0104049 [hep-ex].

[103] A. Aguilar-Arevalo *et al.* (MiniBooNE), Phys.Rev.Lett. **110**, 161801 (2013), arXiv:1207.4809 [hep-ex].

[104] S. Bhadra *et al.*, "Proposal for the NuPRISM Experiment in the J-PARC Neutrino Beamline," (2015),

Proposal to the J-PARC PAC.

[105] H. Watanabe *et al.* (Super-Kamiokande), Astropart. Phys. **31**, 320 (2009), arXiv:0811.0735 [hep-ex].

[106] J. Alonso, N. Barros, M. Bergevin, A. Bernstein, L. Bignell, *et al.*, (2014), arXiv:1409.5864 [physics.ins-det].

[107] R. Acciarri *et al.* (ArgoNeuT), Phys.Rev. **D90**, 012008 (2014), arXiv:1405.4261 [nucl-ex].

[108] U. Mosel, O. Lalakulich, and K. Gallmeister, Phys.Rev.Lett. **112**, 151802 (2014), arXiv:1311.7288 [nucl-th].

[109] K. Abe *et al.* (Hyper-Kamiokande Working Group), (2014), arXiv:1412.4673 [physics.ins-det].

[110] "Titus: the tokai intermediate tank for the unoscillated spectrum," To be published (2015).

[111] I. Anghel *et al.* (ANNIE), (2015), arXiv:1504.01480 [physics.ins-det].

[112] C. Galbiati and J. F. Beacom, Phys. Rev. **C72**, 025807 (2005), [Erratum: Phys. Rev.C73,049906(2006)], arXiv:hep-ph/0504227 [hep-ph].

[113] K. Abe *et al.*, (2011), arXiv:1109.3262 [hep-ex].

[114] A. Suzuki, M. Mori, K. Kaneyuki, T. Tanimori, J. Takeuchi, H. Kyushima, and Y. Ohashi, Nucl. Instrum. Meth. **A329**, 299 (1993).

[115] M. Fukugita and A. Suzuki, eds., *Physics and astrophysics of neutrinos* (1994).

[116] Y. Fukuda, T. Hayakawa, E. Ichihara, M. Ishitsuka, Y. Itow, *et al.*, Nucl. Instrum. Meth. **A501**, 418 (2003).

[117] K. Abe *et al.*, Nucl. Instrum. Meth. **A737**, 253 (2014), arXiv:1307.0162 [physics.ins-det].

[118] H. Tanaka, *Introduction to Geology for Civil Engineers (in Japanese)* (Sankaido, Tokyo, 1964).

[119] E. Hoek and E. T. Brown, Int. J. Rock Mech. Min. Sci. **Vol.34, No.8**, 1165 (1997).

[120] E. Hoek, P. K. Kaiser, and W. Banden, *Support of underground excavations in hard rock* (Balkema, Rotterdam, 1995) p. 215.

[121] E. Hoek, C. Carranza-Torres, and B. Corkum, in *2002 Edition, Proceedings of the 5th North American Rock Mechanics Symposium and the 17th Tunnelling Association of Canada Conference* (MARMS-TAC, Toronto, Canada, 2002) pp. 267–273.

[122] J. S. o. C. E. Concrete Committee, *Standard Specifications for Concrete Structure* (JSCE, Tokyo, 2012) p. 613.

[123] R. Becker-Szendy *et al.*, Nucl. Instrum. Meth. **A324**, 363 (1993).

[124] G. A. Inc, "4850 LBNE water cherenkov detector (WCD) conceptual liner design option," (2011),.

[125] J. W. M. Association, "Planning, design, and management of industrial waste final disposal site," (2010),.

[126] J. Babson *et al.* (DUMAND Collaboration), Phys. Rev. D **42**, 3613 (1990).

[127] I. A. Belolaptikov *et al.*, Astropart. Phys. **7(3)**, 263 (1997).

[128] P. Rapidis *et al.* (NESTOR Collaboration), Nucl. Instrum. Meth. **A602**, 54 (2009).

[129] E.G.Anassontzis *et al.* (NESTOR Collaboration), Nucl. Instrum. Meth. **A479**, 439 (2002).

[130] M. Ageron *et al.* (ANTARES Collaboration), Nucl. Instrum. Meth. **A656**, 11 (2011).

[131] P. Amram *et al.* (ANTARES Collaboration), Nucl. Instrum. Meth. **A484**, 369 (2002).

[132] J. Braun, D. Hubert, *et al.* (IceCube), *Proceedings for 31st International Cosmic Ray Conference (ICRC 2009), Lodz, Poland, 7-15 Jul 2009*, (2009), arXiv:0906.1615 [astro-ph.HE].

[133] A. Achterberg *et al.* (IceCube Collaboration), Astropart. Phys. **26(3)**, 155 (2006).

[134] KM3Net Consortium, Conceptual design for a deep-sea research infrastructure incorporating a very large volume neutrino telescope in the Mediterranean Sea, `http://www.km3net.org/CDR/CDR-KM3NeT.pdf`; Technical design report for a deep-sea research infrastructure in the Mediterranean Sea incorporating a very large volume neutrino telescope, `http://www.km3net.org/TDR/TDRKM3NeT.pdf`.

[135] V.Giordano *et al.* (KM3Net Collaboration), "The effect of Earth's Magnetic Field on 3-inch diameter photomultipliers used in KM3Net Neutrino telescope," (2015), presented at VLVnT 2015, Rome.

[136] L. Classen *et al.* (KM3Net Consortium), Nucl. Instr. Meth. A **725**, 155 (2013).

[137] A. Kappes *et al.* (IceCube-Gen2 Collaboration), "Multi-PMT Optical Module Designs for IceCube-Gen2," (2015), presented at VLVnT 2015, Rome.

[138] S. Aiello *et al.* (KM3Net Collaboration), AIP Conference Proceedings **1630**, 118 (2014).

[139] G. Bourlis *et al.* (KM3Net Collaboration), AIP Conference Proceedings **1630**, 106 (2014).

[140] R. Bormuth *et al.* (KM3Net Collaboration), AIP Conference Proceedings **1630**, 114 (2014).

[141] J. Elizondo-Decanini, D. Schmale, M. Cich, M. Martinez, K. Youngman, M. Senkow, S. Kiff, J. Steele, R. Goeke, B. Wroblewski, J. Desko, and A. Dragt, Plasma Science, IEEE Transactions on **40**, 2145 (2012).

[142] J. Goon and I. Stancu (LBNE Collaboration), (2012), arXiv:1204.2295 [physics.ins-det].

[143] M. Nakahata *et al.* (Super-Kamiokande), Nucl. Instrum. Meth. **A421**, 113 (1999), arXiv:hep-ex/9807027 [hep-ex].

[144] R. Brun and F. Rademakers, Nuclear Instruments and Methods in Physics Research Section A: Accelerators, Spectrometers, Detectors and Associated Equipment **389**, 81 (1997), new Computing Techniques in Physics Research V.

[145] C. Andreopoulos *et al.*, Nucl. Instrum. Meth. **A614**, 87 (2010), arXiv:0905.2517 [hep-ph].

[146] Y. Hayato, *Neutrino interactions: From theory to Monte Carlo simulations. Proceedings, 45th Karpacz Winter School in Theoretical Physics, Ladek-Zdroj, Poland, February 2-11, 2009*, Acta Phys. Polon. **B40**, 2477 (2009).

[147] S. Agostinelli *et al.* (GEANT4), Nucl. Instrum. Meth. **A506**, 250 (2003).

[148] R. B. Patterson, E. M. Laird, Y. Liu, P. D. Meyers, I. Stancu, and H. A. Tanaka, Nucl. Instrum. Meth. **A608**, 206 (2009), arXiv:0902.2222 [hep-ex].

[149] M.Smy (Super-Kamiokande), in *Proceedings of 30th International Cosmic Ray Conference* (Mexico, Mexico, 2007) pp. 1279–1282.

[150] P. Antonioli, C. Ghetti, E. V. Korolkova, V. A. K. udryavtsev, and G. Sartorelli, Astropart. Phys. **7**, 357 (1997).

[151] A. Tang, G. Horton-Smith, V. A. K. ev, and A. Tonazzo, Phys. Rev. D **74**, 053007 (2006).

[152] *Digital Map 5 m Grid (Elevation)*, Geographical Survey Institute of Japan (2010), unpublished.

[153] S. Abe *et al.* (KamLAND Collaboration), Phys. Rev. C **81**, 025807 (2010).

[154] K. Bays, *Search for the Diffuse Supernova Neutrino Background at Super-Kamiokande*, Ph.D. thesis, Irvine, University of California (2012).

[155] D.-M. Mei and A. Hime, Phys. Rev. D **73**, 053004 (2006).

[156] A. Bueno, A. J. Melgarejo, S. Navas, Z. Dai, Y. Ge, M. Laffranchi, A. Meregaglia, and A. Rubbia, JHEP04 **041** (2007).

[157] Y. Amhis *et al.* (Heavy Flavor Averaging Group (HFAG)), (2014), arXiv:1412.7515 [hep-ex].

[158] K. Abe *et al.* (Hyper-Kamiokande Proto-Collaboration), PTEP **2015**, 053C02 (2015), arXiv:1502.05199 [hep-ex].

[159] J. Arafune, M. Koike, and J. Sato, Phys. Rev. **D56**, 3093 (1997), arXiv:hep-ph/9703351 [hep-ph].

[160] D. S. Ayres *et al.* (NOvA), (2004), arXiv:hep-ex/0503053.

[161] K. Hagiwara, N. Okamura, and K.-I. Senda, (2011), arXiv:1107.5857 [hep-ph].

[162] P. Adamson *et al.* (MINOS Collaboration), Phys. Rev. Lett. **112**, 191801 (2014), arXiv:1403.0867 [hep-ex].

[163] A. Himmel (Super-Kamiokande), AIP Conf. Proc. **1604**, 345 (2014), arXiv:1310.6677 [hep-ex].

[164] S. King and C. Luhn, Rept. Prog. Phys. **76**, 056201 (2013), arXiv:1301.1340 [hep-ph].

[165] C. Albright, A. Dueck, and W. Rodejohann, Eur. Phys. J. **C70**, 1099 (2010), arXiv:1004.2798 [hep-ph].

[166] G. Altarelli and F. Feruglio, Rev. Mod. Phys. **82**, 2701 (2010), arXiv:1002.0211 [hep-ph].

[167] H. Ishimori, T. Kobayashi, H. Ohki, Y. Shimizu, H. Okada, *et al.*, Prog. Theor. Phys. Suppl. **183**, 1 (2010), arXiv:1003.3552 [hep-th].

[168] C. Albright and M. Chen, Phys. Rev. **D74**, 113006 (2006), arXiv:hep-ph/0608137 [hep-ph].

[169] G. L. Fogli and E. Lisi, Phys. Rev. **D54**, 3667 (1996), arXiv:hep-ph/9604415 [hep-ph].

[170] H. Minakata, H. Sugiyama, O. Yasuda, K. Inoue, and F. Suekane, Phys. Rev. **D68**, 033017 (2003), arXiv:hep-ph/0211111 [hep-ph].

[171] K. Hiraide, H. Minakata, T. Nakaya, H. Nunokawa, H. Sugiyama, *et al.*, Phys. Rev. **D73**, 093008 (2006), arXiv:hep-ph/0601258 [hep-ph].

[172] K. Abe *et al.* (T2K), PTEP **2015**, 043C01 (2015), arXiv:1409.7469 [hep-ex].

[173] Y. Hayato, Nucl. Phys. Proc. Suppl. **112**, 171 (2002).

[174] G. Mitsuka, AIP Conf. Proc. **967**, 208 (2007).

[175] G. Mitsuka, AIP Conf. Proc. **981**, 262 (2008).

[176] R. Brun, F. Carminati, and S. Giani, (1994), , CERN-W5013.

[177] M. Day and K. McFarland, Phys. Rev. **D86**, 053003 (2012), arXiv:1206.6745 [hep-ph].

[178] K. Abe *et al.* (T2K), (2015), arXiv:1509.06940 [hep-ex].

[179] K. Abe *et al.* (T2K), Phys. Rev. **D91**, 051102 (2015), arXiv:1410.8811 [hep-ex].

[180] D. Dewhurst (T2K), in *Topical Research Meeting on Prospects in Neutrino Physics (NuPhys2014) London, UK, December 15-17, 2014* (2015) arXiv:1504.08237 [hep-ex].

[181] T. Asaka, S. Eijima, and A. Watanabe, JHEP **03**, 125 (2013), arXiv:1212.1062 [hep-ph].

[182] M. Honda, T. Kajita, K. Kasahara, S. Midorikawa, and T. Sanuki, Phys. Rev. **D75**, 043006 (2007), arXiv:astro-ph/0611418.

[183] L. K. Pik, *Study of the neutrino mass hierarchy with the atmospheric neutrino data observed in Super-Kamiokande*, Ph.D. thesis, Tokyo U. (2012).

[184] P. Huber, Phys.Rev. **C84**, 024617 (2011), arXiv:1106.0687 [hep-ph].

[185] G. Mention, M. Fechner, T. Lasserre, T. Mueller, D. Lhuillier, *et al.*, Phys.Rev. **D83**, 073006 (2011), arXiv:1101.2755 [hep-ex].

[186] G. Cheng *et al.* (MiniBooNE Collaboration, SciBooNE Collaboration), Phys.Rev. **D86**, 052009 (2012), arXiv:1208.0322.

[187] J. Kopp, P. A. N. Machado, M. Maltoni, and T. Schwetz, JHEP **05**, 050 (2013), arXiv:1303.3011 [hep-ph].

[188] M. Maltoni and T. Schwetz, Phys.Rev. **D76**, 093005 (2007).

[189] V. A. Kostelecky, Phys.Rev. **D69**, 105009 (2004), arXiv:hep-th/0312310 [hep-th].

[190] K. Kodama *et al.* (DONuT), Phys. Rev. **D78**, 052002 (2008), arXiv:0711.0728 [hep-ex].

[191] N. Agafonova *et al.* (OPERA), (2015), arXiv:1507.01417 [hep-ex].

[192] K. Abe *et al.* (Super-Kamiokande), Phys. Rev. Lett. **110**, 181802 (2013), arXiv:1206.0328 [hep-ex].

[193] Presentation in Neutrino 2014 conference (2014).

[194] G. Bellini *et al.* (Borexino), Phys. Rev. Lett. **107**, 141302 (2011).

[195] P.-G. Friendland, Lunardini, Phys. Lett. **B594**, 347 (2004).

[196] M. Barger, Huber, Phys. Rev. Lett. **95**, 211802 (2005).

[197] Holand and Smirnov, Phys. Rev. **D69**, 113002 (2004).

[198] J. P. Cravens *et al.* (Super-Kamiokande), Phys. Rev. **D78**, 032002 (2008), arXiv:0803.4312 [hep-ex].

[199] Y. Zhang *et al.* (Super-Kamiokande), Phys. Rev. **D93**, 012004 (2016).

[200] B. Aharmin *et al.* (SNO), Astrophys. J. **653**, 1545 (2006), arXiv:hep-ex/0607010.

[201] J. Hosaka *et al.* (Super-Kamkiokande), Phys. Rev. **D73**, 112001 (2006), arXiv:hep-ex/0508053.

[202] J. N. Bahcall, *Neutrino Astrophysics* (Cambridge Univ. Press, 1989).

[203] A. M. Serenelli *et al.*, Astrophys. J. **734**, 24 (2011).

[204] E. G. Adelberger *et al.*, Rev. Mod. Phys. **83**, 195 (2011).

[205] K. Kubodera and T.-S. Park, Annu. Rev. Nucl. Part. Sci. **54**, 19 (2004).

[206] S. Mine *et al.* (K2K), Phys. Rev. **D77**, 032003 (2008), arXiv:0801.0182 [hep-ex].

[207] H. Nishino *et al.* (Super-Kamiokande), Phys. Rev. **D85**, 112001 (2012), arXiv:1203.4030 [hep-ex].

[208] K. Abe *et al.* (Super-Kamiokande), Phys. Rev. **D90**, 072005 (2014), arXiv:1408.1195 [hep-ex].

[209] M. Machacek, Nucl. Phys. **B159**, 37 (1979).

[210] M. B. Gavela, A. Le Yaouanc, L. Oliver, O. Pene, and J. C. Raynal, Phys. Lett. **B98**, 51 (1981).

[211] J. F. Donoghue, Phys. Lett. **B92**, 99 (1980).

[212] F. Buccella, G. Miele, L. Rosa, P. Santorelli, and T. Tuzi, Phys. Lett. **B233**, 178 (1989).

[213] H. Nishino *et al.* (Super-Kamiokande), Phys. Rev. Lett. **102**, 141801 (2009), arXiv:0903.0676 [hep-ex].

[214] J.-S. Jang, (2007), ph.D. thesis, Chonnam National University.

[215] J. C. Pati and A. Salam, Phys. Rev. **D10**, 275 (1974), [Erratum: Phys. Rev.D11,703(1975)].

[216] P. Fileviez Perez and M. B. Wise, Phys. Rev. **D88**, 057703 (2013), arXiv:1307.6213 [hep-ph].

[217] A. S. Dighe and A. Y. Smirnov, Phys. Rev. **D62**, 033007 (2000), arXiv:hep-ph/9907423.

[218] G. L. Fogli, E. Lisi, A. Mirizzi, and D. Montanino, JCAP **0504**, 002 (2005), arXiv:hep-ph/0412046.

[219] H. Duan, G. M. Fuller, J. Carlson, and Y.-Z. Qian, Phys.Rev. **D74**, 105014 (2006), arXiv:astro-ph/0606616 [astro-ph].

[220] H. Duan, G. M. Fuller, J. Carlson, and Y.-Z. Qian, Phys.Rev.Lett. **97**, 241101 (2006), arXiv:astro-ph/0608050 [astro-ph].

[221] B. Dasgupta, A. Dighe, G. Raffelt, and A. Y. Smirnov, Phys. Rev. Lett. **103**, 051105 (2009), arXiv:0904.3542.

[222] A. Friedland, Phys.Rev.Lett. **104**, 191102 (2010), arXiv:1001.0996 [hep-ph].

[223] H. Duan and A. Friedland, Phys.Rev.Lett. **106**, 091101 (2011), arXiv:1006.2359 [hep-ph].

[224] T. Totani, K. Sato, H. E. Dalhed, and J. R. Wilson, Astrophys. J. **496**, 216 (1998), arXiv:astro-ph/9710203.

[225] B.-H. G. I.Tamborra, F.Hanke, Phys.Rev.Lett. **111**, 121104 (2013).

[226] T. Takiwaki, "Neutrino signals based on supernova 3D models," Talk presented at the Workshop for Astroparticlephysics with Hyper-Kamiokande, 18 May, 2015 Hyogo, Japan.

[227] C. J.M.Blondin, A.Mezzacappa, Astrophys.J **584**, 971 (2003).

[228] T.-K. L.Scheck, H.Th.Janka, Astronomy&Astrophysics **477**, 931 (2008).

[229] Y. S. T. Tomoya, K. Kotake, "A Comparison of Two- and Three-dimensional Neutrino-hydrodynamics Simulations of Core-collapse Supernovae," (2014).

[230] T. A. Thompson, A. Burrows, and P. A. Pinto, Astrophys. J. **592**, 434 (2003), arXiv:astro-ph/0211194.

[231] R. Buras, H.-T. Janka, M. Rampp, and K. Kifonidis, Astron. Astrophys. **457**, 281 (2006), arXiv:astro-ph/0512189.

[232] K. Sumiyoshi *et al.*, Astrophys. J. **629**, 922 (2005), arXiv:astro-ph/0506620.

[233] M. Liebendoerfer, M. Rampp, H. T. Janka, and A. Mezzacappa, Astrophys. J. **620**, 840 (2005), arXiv:astro-ph/0310662.

[234] T. Totani, Phys.Rev.Lett. **80**, 2039 (1998), arXiv:astro-ph/9801104 [astro-ph].

[235] T. Totani, Private communication (2005).

[236] A. S. Dighe, M. Kachelriess, G. G. Raffelt, and R. Tomas, JCAP **0401**, 004 (2004), arXiv:hep-ph/0311172.

[237] R. Tomas *et al.*, JCAP **0409**, 015 (2004), arXiv:astro-ph/0407132.

[238] V. Barger, P. Huber, and D. Marfatia, Phys. Lett. **B617**, 167 (2005), arXiv:hep-ph/0501184.

[239] A. Mirizzi, G. G. Raffelt, and P. D. Serpico, JCAP **0605**, 012 (2006), arXiv:astro-ph/0604300.

[240] A. Esteban-Pretel, R. Tomas, and J. W. F. Valle, Phys. Rev. **D76**, 053001 (2007), arXiv:0704.0032 [hep-ph].

[241] S. Choubey, N. P. Harries, and G. G. Ross, Phys. Rev. **D76**, 073013 (2007), arXiv:hep-ph/0703092.

[242] S. Skadhauge and R. Zukanovich Funchal, JCAP **0704**, 014 (2007), arXiv:hep-ph/0611194.

[243] J. Baker, H. Goldberg, G. Perez, and I. Sarcevic, Phys. Rev. **D76**, 063004 (2007), arXiv:hep-ph/0607281.

[244] B. Dasgupta, A. Dighe, and A. Mirizzi, Phys. Rev. Lett. **101**, 171801 (2008), arXiv:0802.1481 [hep-ph].

[245] R. C. Schirato and G. M. Fuller, (2002), arXiv:astro-ph/0205390 [astro-ph].

[246] M. S. B. T. A. T. Shunsaku Horiuchi, John F. Beacom, Astrophys. J. **769**, 113 (2013), arXiv:astro-ph/1302.0287.

[247] E. Waxman and A. Loeb, Phys. Rev. Lett. **87**, 071101 (2001).

[248] K. Murase, T. A. Thompson, B. C. Lacki, and J. F. Beacom, Phys. Rev. **D84**, 043003 (2011).

[249] J. F. Beacom and M. R. Vagins, Phys. Rev. Lett. **93**, 171101 (2004), arXiv:hep-ph/0309300.

[250] C. Lunardini, "Diffuse Neutrino Flux from Failed Supernovae," (2009), Talk presented at the Workshop for Astroparticlephysics with Hyper-Kamiokande, 18 May, 2015 Hyogo, Japan.

[251] S. Horiuchi, "Search for Core-Collapse Supernovae with Neutrinos." Talk presented at the Workshop for Astroparticlephysics with Hyper-Kamiokande, 18 May, 2015 Hyogo, Japan.

[252] S. Ando, K. Sato, and T. Totani, Astropart. Phys. **18**, 307 (2003), (absolute flux revised at NNN05), arXiv:astro-ph/0202450.

[253] J. F. Navarro, C. S. Frenk, and S. D. White, Astrophys.J. **462**, 563 (1996), arXiv:astro-ph/9508025 [astro-ph].

[254] K. Choi *et al.* (Super-Kamiokande), Phys. Rev. Lett. **114**, 141301 (2015), arXiv:1503.04858 [hep-ex].

[255] R. Bernabei *et al.* (DAMA), Eur. Phys. J. **C56**, 333 (2008), arXiv:0804.2741 [astro-ph].

[256] C. Savage, K. Freese, P. Gondolo, and D. Spolyar, JCAP **0909**, 036 (2009), arXiv:0901.2713 [astro-ph.CO].

[257] R. Agnese *et al.* (CDMS), Phys. Rev. Lett. **111**, 251301 (2013), arXiv:1304.4279 [hep-ex].

[258] G. Angloher *et al.*, Eur. Phys. J. **C72**, 1971 (2012), arXiv:1109.0702 [astro-ph.CO].

[259] C. E. Aalseth *et al.* (CoGeNT), Phys. Rev. Lett. **106**, 131301 (2011), arXiv:1002.4703 [astro-ph.CO].

[260] R. Davis, in *Proc. 7th Workshop on Grand Unification, Toyama, Japan* (World Scientific, Singapore, 1986).

[261] J. N. Bahcall, Phys. Rev. Lett. **61**, 2650 (1988).

[262] M. Aglietta *et al.*, Astrophys. J. **382**, 344 (1991).

[263] K. S. Hirata *et al.*, Phys. Rev. Lett. **61**, 2653 (1988).

[264] D. Fargion and P. Di Giacomo, Nucl. Phys. Proc. Suppl. **188**, 142 (2009), arXiv:0812.4592 [astro-ph].

[265] G. E. Kocharov, G. A. Kovaltsov, and I. G. Usoskin, Nuovo Cim. **C14**, 417 (1991).

[266] P. Mészáros, Rep. Prog. Phys **69**, 2259 (2006).

[267] M. J. Rees and P. Mészáros, Astrophys. J. **430**, L93 (1994).

[268] E. Waxman and J. Bahcall, Phys. Rev. Lett. **78**, 2292 (1997).

[269] E. Thrane *et al.*, Astrophys. J. **690**, 730 (2009).

[270] R. Abbasi *et al.*, Nature (London) **484**, 351 (2012).

[271] C. Thompson, Mon. Not. R. Aston. Soc. **270**, 480 (1994).

[272] P. Mészáros and M. Rees, Astrophys. J. **530**, 292 (2000).

[273] M. J. Rees and P. Mészáros, Astrophys. J. **628**, 847 (2005).

[274] F. Ryde *et al.*, Mon. Not. R. Astron. Soc. **415**, 3693 (2011).

[275] M. Axelsson *et al.*, Astrophys. J. **757**, L31 (2012).

[276] J. N. Bahcall and P. Mészáros, Phys. Rev. Lett. **85**, 1362 (2000).

[277] P. Mészáros and M. J. Rees, Astrophys. J. **541**, L5 (2000).

[278] E. V. Derishev, V. V. Kocharovsky, and V. V. Kocharovsky, Astrophys. J. **521**, 640 (1999).

[279] K. Murase, K. Kashiyama, and P. Mészáros, Phys. Rev. Lett. **111**, 131102 (2013).

[280] P. Mészáros and E. Waxman, Phys. Rev. Lett. **87**, 171102 (2001).

[281] S. Razzaque, P. Mészáros, and E. Waxman, Phys. Rev. Lett. **93**, 181101 (2004).

[282] S. Ando and J. F. Beacom, Phys. Rev. Lett. **95**, 061103 (2005).

[283] K. Murase and K. Ioka, Phys. Rev. Lett. **111**, 121102 (2013).

[284] A. M. Soderberg *et al.*, Nature (London) **442**, 1014 (2006).

[285] T. A. Thompson, P. Chang, and E. Quataert, Astrophys. J. **611**, 380 (2004).

[286] Y. Farzan and A. Y. Smirnov, Nucl. Phys. **B805**, 356 (2008).

[287] S. Razzaque and A. Y. Smirnov, J. High Energy Phys. **3**, 031 (2010).

[288] E. V. Derishev, F. A. Aharonian, K. V. V., and V. V. Kocharovsky, Phys. Rev. D **68**, 043003 (2003).

[289] K. Kashiyama, K. Murase, and P. Mészáros, Phys. Rev. Lett. **111**, 131103 (2013).

[290] K. Murase, B. Dasgupta, and T. A. Thompson, Phys. Rev. D **89**, 043012 (2014).

[291] M. Honda, T. Kajita, K. Kasahara, and S. Midorikawa, Phys. Rev. **D83**, 123001 (2011).

[292] C. J. Allègre *et al.*, Earth Planet. Sci. Lett. **134**, 515 (1995).

[293] D. R. Fearn and D. E. Loper, Nature **289**, 393 (1981).

[294] W. McDonough and S. Sun, Chem. Geol. **120**, 223 (1995).

[295] Y. A. Popov *et al.*, Tectonophysics **306**, 345 (1999).

[296] A. M. Dziewonski and D. L. Anderson, Phys. Earth Planet. Inter. **25**, 25 (1981).

[297] Y. Itow *et al.* (T2K), "The JHF-Kamioka neutrino project," (2001), arXiv:hep-ex/0106019.

[298] H. Nakata *et al.*, "Durability Test of Geomembrane Liners Presumed to Avail Near Surface Disposal Facilities for Low-level Waste Generated from Research, Industricl and Medical Facilities," (2013),.